Compressed Sensing in MRI : optimization-based design of k-space filling curves for accelerated MRI

Carole Lazarus

NNT : 2018SACLS309

L'échantillonnage compressif en IRM: conception optimisée de trajectoires d'échantillonnage pour accélérer l'IRM

Thèse de doctorat de l'Université Paris-Saclay,
préparée à l'Université Paris-Sud, à NeuroSpin, CEA Saclay.

École doctorale n°575 Physique et ingénierie: électrons, photons, sciences du vivant (EOBE)
Spécialité de doctorat : Imagerie et physique médicale

Thèse présentée et soutenue à Gif-sur-Yvette, le 27 septembre 2018, par

CAROLE LAZARUS

Composition du Jury :

Prof. Charles Soussen CentraleSupélec (Département Signal et Statistiques)	Président du jury
Prof. Carola-Bibiane Schönlieb Cambridge University (DAMPT)	Rapporteur
Prof. Klaas Prüssmann ETH Zürich (Institute for Biomedical Engineering)	Rapporteur
Prof. Stéphane Lehéricy Université Pierre Marie Curie Paris 6 (CENIR)	Examinateur
Dr. Pierre Weiss CNRS (IMT-ITAV)	Examinateur
Dr. Robin Heidemann Siemens Healthineers (Erlangen)	Invité
Dr. Alexandre Vignaud CEA (NeuroSpin)	Co-encadrant
Dr. Philippe Ciuciu CEA (NeuroSpin)	Directeur de thèse

Thèse de doctorat

PARIS-SACLAY UNIVERSITY

DOCTORAL THESIS

Compressed Sensing in MRI: Optimization-based design of k-space filling curves for accelerated MRI

Author:
Carole LAZARUS

Supervisors:
Dr. Philippe CIUCIU
Dr. Alexandre VIGNAUD

A thesis submitted in fulfillment of the requirements for the degree of Doctor of Philosophy

in

NeuroSpin - CEA
Parietal - INRIA

October 15, 2018

"In the realm of ideas, everything depends on enthusiasm;
in the real world, all rests on perseverance."

Johann Wolfgang von Goethe

Acknowledgements

The work presented in this thesis would not have been possible without my close association with many people. I take this opportunity to extend my sincere gratitude and appreciation to all those who made this PhD thesis possible.

Firstly, I would like to express my appreciation to my supervisors, Dr. Alexandre Vignaud and Dr. Philippe Ciuciu, for the continuous support of my PhD study and related research, for their patience and motivation. Their guidance helped me in all the time of research and writing of this thesis. I appreciated the trust they had in me and the freedom they gave me to conduct my projects. I would like to especially thank Alexandre Vignaud for his priceless advice on my career.

I would also like to express my sincere gratitude and special appreciation to Dr. Pierre Weiss, who has been a tremendous mentor for me. I learned a lot by working with him and am extremely grateful for his help both with my PhD work and future career.

Besides my advisors, I would like to warmly thank Dr. Franck Mauconduit for his very valuable help on sequence development. My sincere thanks also go to Dr. Nicolas Boulant and Dr. Vincent Gras, for their insightful comments and help. I would especially like to thank the radiographers who always ensured smooth acquisitions with volunteers. I am also grateful to other colleagues at NeuroSpin who helped me occasionally: Erwan Selingue, Dr. Bottlaender and many others.

I thank my fellow labmates at NeuroSpin for the good lab atmosphere, the nice discussions during lunch and coffee times, and for all the fun we have had in general. Special thanks to the METRIC team.

Last but not the least, I would like to thank my relatives and friends for supporting me spiritually throughout this PhD thesis and my life in general.

Contents

Introduction

Magnetic resonance imaging (MRI) is one of the most powerful and safest imaging modalities for examining the human body. High-resolution MRI is expected to aid in the understanding and diagnosis of many neurodegenerative pathologies involving submillimetric lesions or morphological alterations, such as Alzheimer's disease and multiple sclerosis (Barnes et al., 2009; Pruessner et al., 2000; Kolk et al., 2013). Although high-magnetic-field systems can deliver a sufficient signal-to-noise ratio (SNR) to increase spatial resolution (Duyn, 2012), long scan times and motion sensitivity continue hindering the utilization of high resolution MRI. Despite the development of corrections for bulk and physiological motion (Maclaren et al., 2012; Federau and Gallichan, 2016; Stucht et al., 2015; Vannesjo et al., 2015), lengthy acquisition times remain a major obstacle to high-resolution acquisition, especially in clinical applications.

In the last decade, the newly developed theory of compressed sensing (CS) (Candès et al., 2006; Donoho, 2006; Lustig et al., 2007b) offered a promising solution for reducing the MRI scan time. Despite many successful applications in dynamic MRI for instance (Feng et al., 2014), the application of CS to MRI commonly relies on simple sampling patterns such as straight lines, spirals or slight variations of these elementary shapes, which do not take full advantage of the degrees of freedom offered by the hardware and cannot be easily adapted to fit an arbitrary sampling distribution. In this PhD thesis, we have introduced a method called SPARKLING, that may overcome these limitations by taking a radically new approach to the design of k-space sampling. The acronym SPARKLING stands for Spreading Projection Algorithm for Rapid K-space sampLING. This work stems from a close collaboration between mathematicians (P. Weiss, J. Kahn), physicists (A. Vignaud), engineers (F. Mauconduit, P. Ciuciu) and last but not least PhD students (C. Lazarus, N. Chauffert, L. El Gueddari) who strove to provide an elegant approach to achieve significant reductions in the scan time of segmented acquisitions in magnetic resonance imaging (MRI). It is a versatile method inspired from stippling techniques that automatically generates optimized non-Cartesian sampling patterns compatible with MR hardware constraints on maximum gradient amplitude and slew rate. These sampling curves are designed to comply with key criteria for optimal sampling: a controlled distribution of samples and a locally uniform k-space coverage.

In this PhD thesis, the SPARKLING method was developed and used for prospectively accelerated acquisitions mostly at 7 Tesla. The method was not only improved

but also extended for 3D imaging. The objectives were to evaluate the practical performance of this new design. Given the erratic aspect of the proposed trajectories, will the gradient system be able to play out these complex gradient waveforms? Is this method competitive with spiral imaging, which is considered as the most efficient sampling? How sensitive to imaging and system imperfections will these new non-Cartesian trajectories be? Are they interesting for all imaging protocols? In this dissertation, I carefully address all these concerns and provide specific answer to each point.

In addition to the SPARKLING method, which is the core of the PhD thesis, side projects in connection with this topic were investigated. On the one hand, this manuscript starts with an empirical and quantitative analysis of the maximum undersampling factor achievable with compressed sensing for T_2^*-weighted imaging. This question was investigated because we realized that a quantitative guide on the degree of acceleration applicable to a given acquisition scenario is still lacking today, leading in practice to a trial-and-error approach in the selection of the appropriate undersampling factor in CS. Finally, a model-based reconstruction accounting for analog-to-digital filtering effects was investigated to cope with artifacts that were appearing with the very first SPARKLING trajectories which happened to be too fast at some points.

Thesis outline

Chapter 1: *Background in MRI*

In this chapter, the fundamentals of MRI are reminded from the origin of the signal to its detection and sampling. The emphasis is put on the *k-space* formalism, a domain which is Fourier conjugate to the standard spatial domain that contains the object magnetization. Moreover, different pulse sequences relevant to this work are briefly presented. Then, more advanced signal description which take into account the imaging and system imperfections are considered. Furthermore, we will present some mathematical tools for image reconstruction, notably regarding non-Cartesian data. Finally, we will give an overview of the advantages and challenges of ultra high field (UHF) MRI, which concerns the main applications of this work. In particular, UHF enables to trade the gain in signal-to-noise ratio (SNR) for high resolution.

Chapter 2: *Compressed sensing in MRI: how much can we accelerate?*

In this chapter, the theory of compressed sensing (CS) is introduced and its application to MRI is presented. The limitations of the current theorems in quantifying the maximum degree of subsampling applicable to a certain acquisition scenario are discussed. Then, an empirical study of the range of applicability of CS in MRI is investigated for a T_2^*-contrast. The objective is to quantify the maximum subsampling factor R_{max} allowed for a given image size and an input SNR in order to preserve a desired image quality. On the

one hand, this study is performed on an analytical brain phantom for both iid (identically independently drawn) variable-density and radial retrospective subsampling. On the other hand, prospective experimental data were collected using a radial trajectory to verify the consistency with the retrospective results. Experimental results were found to be in good agreement with simulations.

Chapter 3: *2D SPARKLING*

In this chapter, which is the heart of this PhD thesis, we present a new method to design optimal k-space trajectories for MRI. This technique is based on the previous work done in (Boyer et al., 2016) and uses optimization to design sampling patterns which respect two key criteria: (i) a controlled distribution of the samples (e.g., a variable density for CS) and (ii) a locally uniform coverage to avoid gaps and clusters of samples. This method was named SPARKLING which stands for Spreading Projection Algorithm for Rapid K-space sampLING. Before engaging into experiments, we verified that our gradient system was capable of executing the complex gradient waveforms. We implemented the local phase measurement method described in (Schneider et al., 2011) and we observed a very good adequacy between prescribed and measured k-space trajectories. Then, SPARKLING was used to design 2D variable-density sampling patterns for a high in plane resolution of 390 μm and a T_2^*-contrast. These trajectories were used for *in vivo* brain imaging at 7 Tesla. They were also compared to standard non-Cartesian trajectories such as radial and spiral sampling.

Chapter 4: *3D SPARKLING*

In this chapter, the SPARKLING method is extended to 3D in various ways: stacks-of-SPARKLING (SOS) and fully 3D SPARKLING trajectories are explored. For SOS, two different techniques are presented: a *regular stack* and *z-variable-density stack* whose number of shots and density vary with the plane's altitude. The extension of the SPARKLING algorithm to 3D is also detailed, as well as its acceleration to limit the computation cost in the design of multi-shot trajectories. Then, experiments were performed with an *ex vivo* baboon brain at 7 Tesla to compare the different methods. Furthermore, the 3D SPARKLING method was compared to other standard 3D trajectories for an isotropic resolution of 0.6 mm. It was finally used for very high in plane resolution of 0.3 mm with the objective to perform susceptibility-weighted imaging (SWI).

Chapter 5: *Correcting the side effects of ADC filtering in MR image reconstruction*

In this last chapter, the side effects of bandlimiting filters performed during the analog-to-digital conversion (ADC) are discussed. Originally applied to prevent aliasing of the

temporal signal, we explain how and when this filtering may have deleterious consequences on image quality. We then propose a model to take into account this ADC filtering and numerical algorithms to handle the ADC filtering effect for linear and nonlinear reconstructions methods. Finally, the proposed algorithms are tested against simulated and real data, to demonstrate the potential improvements in the reconstruction quality, especially when using the novel SPARKLING trajectories designed in the framework of compressed sensing.

Contributions

Patents

- C. Lazarus, P. Weiss, N. Chauffert, J. Kahn, A. Vignaud, Ph. Ciuciu. 2017. Method and Apparatus for accelerated Magnetic Resonance Imaging. Patent submission 1000420665; Application EP17306151.

Journals

- C. Lazarus, P. Weiss, N. Chauffert, L. El Gueddari, F. Mauconduit, I. Zemmoura, C. Destrieux, A. Vignaud, P. Ciuciu. K-space filling curves for accelerated magnetic resonance imaging. Submitted to Nature Communications.
- C. Lazarus, P. Weiss, L. El Gueddari, F. Mauconduit, A. Vignaud, P. Ciuciu. 3D k-space filling curves for accelerated susceptibility-weighting. To be submitted in MRM journal.
- C. Lazarus, M. März, P. Weiss. Correcting filtering effects of receive chain in MR image reconstruction. Submitted to IEEE Transactions in Computational Imaging.
- C. Lazarus, P. Weiss, N. Chauffert, A. Vignaud, P. Ciuciu. An Empirical Study of the Maximum Degree of Undersampling in Compressed Sensing for T_2^*-weighted MRI. Accepted in *Magnetic Resonance Imaging*.

Conferences

- C. Lazarus, P. Weiss, N. Chauffert, L. El Gueddari, F. Mauconduit, I. Zemmoura, C. Destrieux, A. Vignaud, P. Ciuciu. Distribution-controlled and optimally spread non-Cartesian sampling curves for accelerated in vivo brain imaging at 7 Tesla. 26th annual meeting of the ISMRM, 2018, Paris, France.
- L. El Gueddari, C. Lazarus, H. Carrié, Alexandre Vignaud and P. Ciuciu. Self-calibrating nonlinear reconstruction algorithms for variable density sampling and parallel reception MRI. 2018 IEEE 10th Sensor Array and Multichannel Signal Processing Workshop (SAM).
- L. El Gueddari, C. Lazarus, H. Carrié, Alexandre Vignaud and P. Ciuciu. Self-calibrating nonlinear reconstruction algorithms for variable density sampling and parallel reception MRI. International Symposium on Biomedical Imaging (ISBI'18).

- H. Cherkaoui, L. El Gueddari, C. Lazarus, A. Grigis, F. Poupon, A. Vignaud, S. Farrens, J.-L. Starck, P. Ciuciu. Analysis Vs Synthesis-based Regularization for Combined Compressed Sensing and Parallel MRI Reconstruction at 7 Tesla. EUSIPCO 2018.

- C. Lazarus, P. Weiss, N. Chauffert, F. Mauconduit, M. Bottlaender, A. Vignaud, P. Ciuciu. SPARKLING: Novel non-Cartesian sampling schemes for accelerated 2D anatomical imaging at 7T using compressed sensing. 25th annual meeting of the ISMRM, 2017, Honolulu, Hawai.

- C. Lazarus, P. Weiss, N. Chauffert, A. Vignaud, P. Ciuciu. SPARKLING: nouveaux schémas d'échantillonnage compressif prospectif pour l'IRM haute résolution. GRETSI 2017.

- C. Lazarus, A. Coste, N. Chauffert, A. Vignaud, P. Ciuciu. Compressed Sensing in MRI: How the Maximum Undersampling Factor depends on the Image Size and the SNR. SFB workshop: Imaging with Modulated/Incomplete Data 2016, Graz, Austria.

- C. Lazarus, A. Coste, N. Chauffert, A. Vignaud, P. Ciuciu. Compressed Sensing in MRI: How the Maximum Undersampling Factor depends on the Image Size. ESMRMB 2016, Vienna, Austria.

Chapter 1

Background in MRI

The objective of this part is to summarize the fundamentals of MRI which will be useful for understanding the rest of the manuscript. We will start by briefly reminding the origins of the MR signal, how it is detected and processed by an MR scanner. Then, the so called *k-space* formalism will be introduced before considering more advanced phase description. Furthermore, we will present some mathematical tools for image reconstruction, notably regarding non-Cartesian data. Finally, we will give an overview of the advantages and challenges of ultra high field MRI, which concerns the main applications of this work.

1.1 NMR and MR signal

Here, we briefly remind the origins of the MR signal, which are based on nuclear magnetic resonance (NMR). We also present the different pulse sequences, which are relevant for the work. For more details on the NMR phenomenon and pulse sequences, the reader may refer to the well-known MR handbooks (Bernstein et al., 2004; Haacke et al., 1999).

1.1.1 Spins, magnetization and precession

According to quantum physics, each nucleon particle is associated with a spin quantity, which is an intrinsic property of matter such as mass and charge. Depending on the spin value, the particle may present a spin magnetic moment. For instance, the hydrogen proton has a spin of $\frac{1}{2}$ and so presents a non-zero magnetic moment μ. Interestingly for biomedical imaging, the water molecules, which are abundant in organic tissues, are composed of hydrogen nuclei.

In the absence of an external magnetic field, a set of protons has no bulk magnetization because the spin magnetic moments have independent and randomly distributed directions. However, after a short time in the presence of a magnetic field $\boldsymbol{B}_0 = B_0 \boldsymbol{e}_z$, a small static nuclear magnetization arises because the spin magnetic moments tend to align with the applied field, which decreases the system's energy. This effect is counterbalanced by thermal agitation, leading to a proportion of anti-parallel spins. Once thermal equilibrium is established, the population difference between the upper and the lower levels is given by Boltzmann statistics rules (Abragam, 1961):

$$\Delta N_p = \frac{N_p \hbar \gamma B_0}{2kT_s} \tag{1.1}$$

where N_p is the number of protons present, γ is the proton gyromagnetic ratio, $\hbar$ is the Planck's constant divided by 2π, k is Boltzmann's constant, and T_s is the absolute temperature of the sample.

Since each proton is associated with a magnetic moment given by $\mu = \gamma\hbar/2$, the total magnetic moment $\mathbf{M}_0$, whose intensity characterizes the imbalance between the two spin populations, is given by:

$$\mathbf{M}_0 = \frac{N_p \gamma^2 \hbar^2 \boldsymbol{B}_0}{4kT_s} \boldsymbol{e}_z \tag{1.2}$$

This total magnetic moment $\mathbf{M}_0$, which is aligned and proportional to the magnetic field, is referred to as the bulk magnetization.

According to the laws of motion applied to the magnetization $\mathbf{M}_0$ in the presence of the static magnetic field $\boldsymbol{B}_0$, a torque is created and leads to the clockwise precession of $\mathbf{M}_0$ around $\boldsymbol{B}_0$ at the Larmor angular frequency $\omega_0 = \gamma B_0$.

1.1.2 NMR and radiofrequency excitation

To observe the bulk magnetization $\mathbf{M}_0$, which is aligned to the static magnetic field, nuclear magnetic resonance (NMR) should be provoked. This can be achieved by applying a transversal[1] pulse $\boldsymbol{B}_1$ of electromagnetic field oscillating at angular frequency ω. When the frequency of the excitation pulse is equal to the Larmor frequency (i.e., $\omega = \omega_0$), nuclear magnetic resonance occurs: in the rotating frame, $\mathbf{M}_0$ is precessing around $\boldsymbol{B}_1$ at angular frequency $\omega_1 = \gamma B_1$. Typically, in the case of protons for which $\gamma = 42.56\ MHz/T$, the Larmor frequency lies in the radiofrequency (RF) band (i.e., in the MHz range depending on the field strength), which is why the excitation pulse is referred to as the RF pulse.

If the excitation pulse oscillates at the Larmor frequency ω_0 for a duration of T_{B_1}, the magnetization gets flipped by an angle of $\theta = \omega_1 T_{B_1}$. Therefore, an excitation pulse of duration $T_{90} = \frac{\pi}{2\gamma B_1}$ flips $\mathbf{M}_0$ from the longitudinal axis (along $\boldsymbol{B}_0$) to the transverse plane where it can be measured with maximal intensity.

1.1.3 Relaxation

After excitation, the magnetization vector $\mathbf{M}_0$ returns to the thermal equilibrium state $\mathbf{M}_0 = M_0 \boldsymbol{e}_z$, where the energy of the system of spins is minimal. This relaxation is exponential with two characteristic times: T_1 for the longitudinal magnetization $\mathbf{M}_{\shortparallel}$ and T_2 for the transverse component $\mathbf{M}_{\perp}$. In the reference frame rotating at angular frequency ω_0, the relaxation of the magnetization is modeled by the Bloch equations and is given by:

$$\frac{d\mathbf{M}_{\perp}}{dt} = -\frac{\mathbf{M}_{\perp}}{T_2}$$
$$\frac{d\mathbf{M}_{\shortparallel}}{dt} = \frac{\mathbf{M}_0 - \mathbf{M}_{\shortparallel}}{T_1}$$

which yield the Free Induction Decay (FID) signal:

[1] i.e., transversal to the main magnetic field $\boldsymbol{B}_0$.

$$\mathbf{M}_{\perp}(t) = \mathbf{M}_{\perp}(0)e^{-t/T_2}$$
$$\mathbf{M}_{\shortparallel}(t) = \mathbf{M}_{\shortparallel}(0)e^{-t/T_1} + \mathbf{M}_0(1 - e^{-t/T_1})$$

Both relaxation times are tissue-specific, which will create the contrast of MR images:

- The longitudinal relaxation time T_1 is related to the time required for the resonating protons to re-establish thermal equilibrium magnetization. It describes the rate of energy transfer from the spins to the lattice, during which a transfer of population from anti-parallel spins (higher energy) to parallel spins occurs.
- The transverse relaxation time T_2 describes the rate of desynchronization of the magnetic moments, i.e., how long the resonating protons remain coherent (i.e., in phase), following an excitation. The dephasing of magnetic moments is caused by two phenomena: spin-spin interactions and B_0 inhomogeneities. The first factor occurs at a microscopic scale where magnetic moments randomly influence each other. The second factor happens at a macroscopic scale, where slight local changes in the precession frequency cause loss in transverse magnetization as the moments dephase. The latter is characterized by a T_2^* (T_2 star) transverse relaxation time, sometimes called the apparent T_2 and is related to the spin-spin relaxation time T_2 by:
$$\frac{1}{T_2^*} = \frac{1}{T_2} + \frac{1}{T_2'} \tag{1.3}$$
where T_2' is inversely proportional to the magnetic field inhomogeneity ΔB_0 in each imaging voxel, that is, $T_2' \propto \frac{1}{\gamma \Delta B_0}$. Whereas T_2 is an intrinsic property of the tissue, T_2' and T_2^* depend not only on external factors (e.g. susceptibility variations within the patient and how well the magnet is shimmed), but also on the prescribed imaging voxel size. Although a moderate amount of T_2^* weighting can be advantageous for some applications (e.g., to image hemorrhage), excessive T_2^* weighting causes signal-loss artifacts (e.g., in regions near metallic implants) (Bernstein et al., 2004).

1.1.4 From FID to spatial encoding

The simplest MRI experiment involves measuring a *global* signal from an object (see Section 1.2 for more details on signal detection). This signal coming from all the object in the scanner is the FID and decays with the time constant T_2^*. It carries the information on the entire object in the intensity of its envelope and the relaxation times as is depicted in (Fig. 1.1).

However, without any means of spatial localization, the FID only produces a single information for the entire object and not an image of it. It is Lauterbur and Mansfield who discovered a way to separate signal from different parts of the object and laid the foundations of current MR imaging (Mansfield, 1977). By using time-varying linear magnetic *gradients*, denoted as G_x, G_y and G_z corresponding to the three Cartesian axes, one can create a magnetic field that changes in strength depending on the position, which causes the precession frequency of the protons to vary as well. For example, when G_x is applied, the magnetic field will vary with position as $B(x) = B_0 + G_x \cdot x$. This variation causes the precession angular frequency to vary linearly in space as follows:

$$\omega(x) = \gamma(B_0 + G_x \cdot x) \tag{1.4}$$

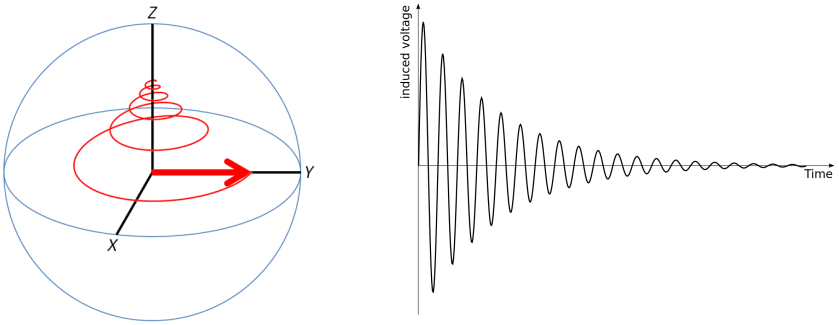

FIGURE 1.1: **Free Inducation Decay (FID)**. Following excitation, the measured transverse magnetization oscillates at the Larmor frequency but relaxes to zero. The exponential envelop decays with the time constant T_2^*.

As a result, magnetization at positive x positions will precess at a higher frequency than magnetization at negative x positions.

Hence, gradients applied during the signal acquisition enable frequency encoding, as multiple frequencies are introduced into the FID dependent on the location of the source. The same encoding principle is used with transverse phase for 2D and 3D imaging, allowing a 2D and 3D Fourier-transform-based spatial encoding. The next section, explaining how the signal is detected, will precise the origin of this Fourier encoding.

1.2 Signal detection and receive chain

Because understanding how the signal is acquired is essential to provide high quality sampling and understand anomalies, we briefly detail here the successive signal processing steps of signal detection performed by the receive chain.

The information we seek to measure is the magnetization $\mathbf{M}(\boldsymbol{r}, t)$, which is proportional to the spin density of interest. The measured MR signal is the electromagnetic force (emf) induced in a coil by the rotating magnetization $\mathbf{M}(\boldsymbol{r}, t)$ for a sample of volume V_s and is given by (Hoult and Richards, 2011)[2]:

$$S(t) = -\frac{d}{dt}\int_{V_s} (\boldsymbol{B}_1 \cdot \mathbf{M}(\boldsymbol{r}, t))\, \mathrm{d}\boldsymbol{r} \tag{1.5}$$

After interchanging the integral and partial differential operators and neglecting the derivative of the e^{-t/T_1} and e^{-t/T_2} factors compared to the derivative of the $e^{-\omega_0 t}$ factor[3], the signal is given by (Haacke et al., 1999):

$$S(t) \propto \omega_0 \int_{V_s} e^{-t/T_2(\boldsymbol{r})} |\mathbf{M}_\perp(\boldsymbol{r})||\boldsymbol{B}_\perp(\boldsymbol{r})| sin(\Phi_M(\boldsymbol{r}, t) - \Phi_B(\boldsymbol{r}))d\boldsymbol{r} \tag{1.6}$$

where $\omega_0 = \gamma B_0$ is the Larmor frequency in radians per second; $\mathbf{M}_\perp = M_x \boldsymbol{e}_x + M_y \boldsymbol{e}_y$ is the transverse component of the magnetization in the laboratory frame at time $t = 0$; $\boldsymbol{B}_\perp(\boldsymbol{r})$ is the transverse component of the receive coil B_1 field; $\Phi_M(\boldsymbol{r}, t)$ is the phase of $\mathbf{M}_\perp$, i.e. its angle with the x-axis; $\Phi_B(\boldsymbol{r})$ is the phase of $\boldsymbol{B}_\perp$ in the laboratory frame.

[2]Mathematically, it should be understood that the integration is performed over $\mathbb{R}^2$ and the magnetization has compact support.

[3]For static field at the Tesla level, the Larmor frequency ω_0 is at least four orders-of-magnitude larger than typical values of $1/T_1$ and $1/T_2$.

Then, an MRI receiver removes the Larmor precession frequency of the transverse magnetization, which is called *demodulation*. Next, the receiver does *quadrature detection*, during which the real-valued signal induced in the receive coil is converted into a complex-valued signal. Finally, the receiver performs data sampling, analog-to-digital conversion (ADC) and band-limiting to prevent aliasing (Bernstein et al., 2004). These processing steps are summarized in Fig. 1.2.

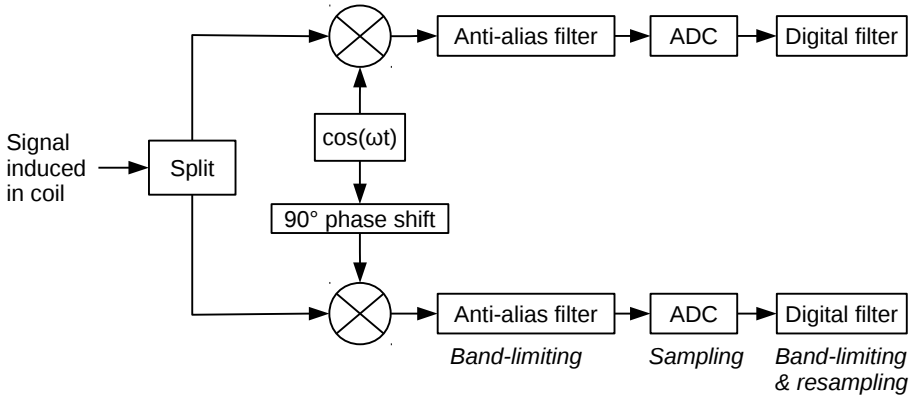

FIGURE 1.2: Diagram of MRI receive chain processing (Adapted from (Bernstein et al., 2004)).

1.2.1 Signal demodulation

Ignoring relaxation effects in Eq. (1.6), the signal $S(t)$ induced in the coil by the precessing magnetization reduces to:

$$S(t) \propto \omega_0 \int_{V_s} |\mathbf{M}_\perp(\boldsymbol{r})||\boldsymbol{B}_\perp(\boldsymbol{r})| sin(\Phi_M(\boldsymbol{r},t) - \Phi_B(\boldsymbol{r}))d\boldsymbol{r} \tag{1.7}$$

Ignoring B_0 inhomogeneities, the precession frequency of $\mathbf{M}_\perp$ is the Larmor frequency plus a frequency offset due to imaging gradients $\boldsymbol{G}(t)$, giving the resulting phase:

$$\Phi_M(\boldsymbol{r},t) = \Phi_0(\boldsymbol{r}) + \omega_0 t + \gamma \int_0^t \boldsymbol{G}(\tau)d\tau \tag{1.8}$$

where $\Phi_0(\boldsymbol{r})$ is the transverse magnetization phase at $t = 0$. So the signal $S(t)$ becomes:

$$S(t) \propto \omega_0 \int_{V_s} |\mathbf{M}_\perp(\boldsymbol{r})||\boldsymbol{B}_\perp(\boldsymbol{r})| sin(\omega_0 t + \gamma \int_0^t \boldsymbol{G}(\tau)d\tau + \Phi_0(\boldsymbol{r}) - \Phi_B(\boldsymbol{r}))d\boldsymbol{r} \tag{1.9}$$

To remove the $\omega_0 t$ term in Eq. (1.9), the signal is multiplied by a sine and a cosine oscillating at ω_0[4], followed by low-pass filtering. This yields two separate signals S_R and S_I which are combined to give a complex demodulated signal given by $S_\perp = S_R - \imath S_I$. Finally:

$$S_\perp(t) \propto \omega_0 \int_{V_s} M_\perp(\boldsymbol{r}) B_\perp(\boldsymbol{r}) e^{-\imath\gamma \int_0^t \boldsymbol{G}(\tau)d\tau} d\boldsymbol{r} \tag{1.10}$$

[4]Calibrated at the beginning of the MR exam, the demodulation frequency is equal to the frequency of the RF pulse

The Fourier encoding can be clearly identified in this equation and will take an even simpler form in the next section 1.3.

1.2.2 The analog-to-digital conversion (ADC)

Before detailing how the analog signal (i.e., continuous-time) is transformed into its digitized version (i.e., discrete-time), it is useful to remind the Nyquist-Shannon sampling theorem.

The Nyquist-Shannon sampling theorem

In the field of digital signal processing, the sampling theorem is a fundamental bridge between analog and digital signals. It establishes a sufficient condition on a sampling rate which allows a discrete sequence of samples to capture all the information from a continuous-time signal of *finite bandwidth*. The Nyquist-Shannon theorem states that the spectrum of a discretely sampled signal is replicated in the Fourier conjugate domain. It provides a prescription for the nominal sampling interval required to avoid aliasing. It may be stated as follows:

> *The sampling rate should be at least twice the highest frequency contained in the signal.*

If the signal is sampled at intervals Δt, the Fourier transform of the sampled signal is replicated at intervals $1/\Delta t$. If the frequency bandwidth of the signal is greater than $f_s = 1/\Delta t$, the replicates will overlap (i.e., aliasing results), as is illustrated in (Fig. 1.3**a**-**b**). This overlap can be prevented by windowing the spectrum before sampling so that the bandwidth is less than or equal to the replication distance $2\Omega_c \leq f_s$ (Fig. 1.3**c**-**d**). This result can be directly applied to the readout process in MRI by calculating the bandwidth of the signal resulting from spin precession in the presence of the readout gradient (Bernstein et al., 2004).

Band-limiting filtering and ADC

Many different receiver designs are possible. To allow flexibility in the choice for bandwidth, the band-limiting can be done in several steps using analog and/or digital hardware. In all designs, prior to analog-to-digital converter (ADC) sampling, the signal is band-limited with an analog anti-alias filter (hardware filter) to the maximum bandwidth allowed by the ADC sampling interval. The purpose of this anti-alias filter is to avoid spurious signals from aliasing and also prevent wide-band noise such as white noise. The ADC sampling bandwidth is denoted $\pm\text{BW}_{ADC}$ and the corresponding sampling time is denoted Δt_{ADC}. The maximum bandwidth allowed by the system $\pm\text{BW}_{max}$ can be less than $\pm\text{BW}_{ADC}$. If the operator has prescribed a bandwidth less than $\pm\text{BW}_{ADC}$, the signal is then digitally filtered (band-limiting) and resampled to the final bandwidth (Bernstein et al., 2004).

1.3 The k-space

Early in the development of MRI, it was realized that the time-varying signals detected from precessing magnetization could be analyzed by following trajectories that evolve in a 2D or 3D space. This space corresponds to a domain that is Fourier conjugate to the

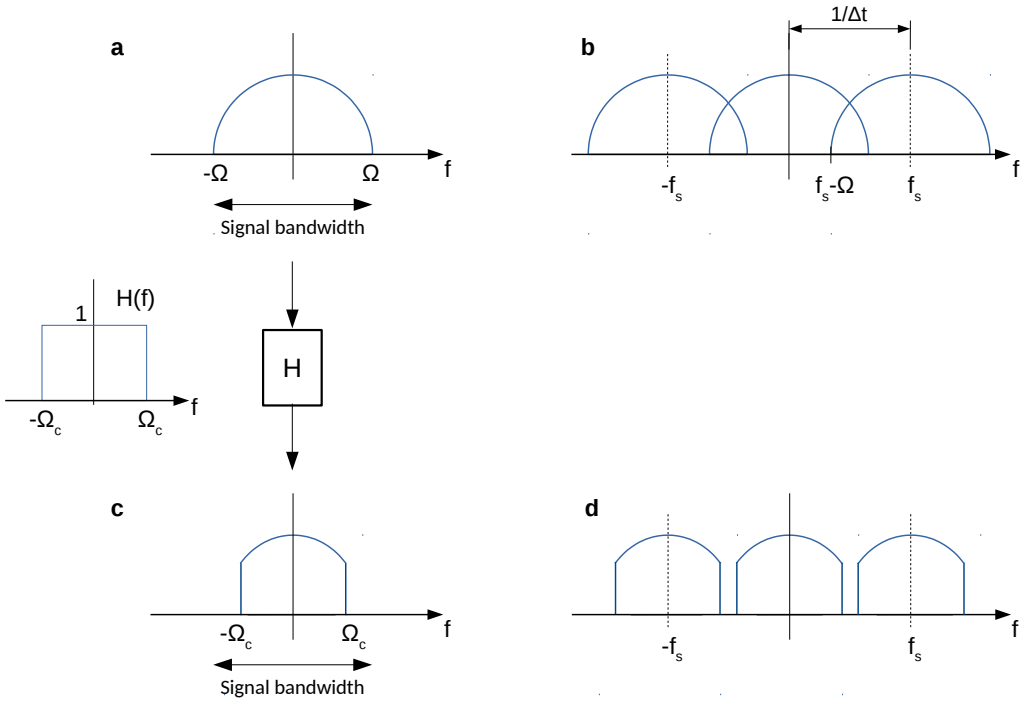

FIGURE 1.3: (a) Fourier transform of a time-domain signal (a) before sampling and (b) after discrete sampling at frequency f_s. The frequency-domain replication interval is $f_s = 1/\Delta t$. Because $f_s < 2\Omega$, the replicates overlap resulting in aliasing. (c) Fourier transform of the signal in (a) after windowing with a low-pass filter H of cut-off frequency $\Omega_c < \frac{f_s}{2}$. (d) Resulting Fourier transform of (c) after discrete sampling at frequency f_s.

standard spatial domain that contains the object magnetization (Likes, 1981; Ljunggren, 1983). The Fourier transform variables were given the symbol k, and the domain was called *k-space*. The requirements for sampling and the effects of partial sampling (e.g., parallel imaging) can be easily apprehended when viewed from the k-space perspective (Bernstein et al., 2004).

1.3.1 The k-space formalism

After demodulation, ignoring relaxation effects, the time-domain signal created by the transverse magnetization in Eq. (1.10) can be rewritten as follows:

$$S(t) = \int_{V_s} \rho(\boldsymbol{r}) e^{-\imath\Phi(\boldsymbol{r},t)} d\boldsymbol{r} \tag{1.11}$$

where $\rho(\boldsymbol{r}) = \omega_0 \Lambda M_\perp(\boldsymbol{r}) B_\perp(\boldsymbol{r})$ is the effective spin density[5], and the accumulated phase (in radians) reads:

$$\Phi(\boldsymbol{r},t) = \gamma \int_0^t \boldsymbol{r} \cdot \boldsymbol{G}(\tau) d\tau \tag{1.12}$$

Then, a function $\boldsymbol{k}(t)$, which resides in what is called the *k-space*, is introduced as follows:

[5] where Λ is introduced as a constant including the gain factors from the electronic detection system. See section 9.1.1 in (Haacke et al., 1999) for details.

$$\boldsymbol{k}(t) = \gamma \int_0^t \boldsymbol{G}(\tau) d\tau \tag{1.13}$$

With the definition of the k-space, Eq. (1.11) now reads:

$$S(t) = \int_{V_s} \rho(\boldsymbol{r}) e^{-\imath \boldsymbol{k}(t)\cdot \boldsymbol{r}} d\boldsymbol{r} \tag{1.14}$$

and the signal $S(t)$ is the Fourier transform of the spin density $\rho(\boldsymbol{r})$. The function $\boldsymbol{k}(t)$ is thus the Fourier conjugate variable to the spatial variable $\boldsymbol{r}$ and its unit is the inverse distance, as is illustrated in (Fig. 1.4). A simple inverse fast Fourier transform (FFT) reconstruction (if the k-space samples fall onto a grid) may be used to recover the image:

$$I(\boldsymbol{r}) = \int_0^T S(t) e^{\imath \boldsymbol{k}(t)\cdot \boldsymbol{r}} \mathrm{d}t \tag{1.15}$$

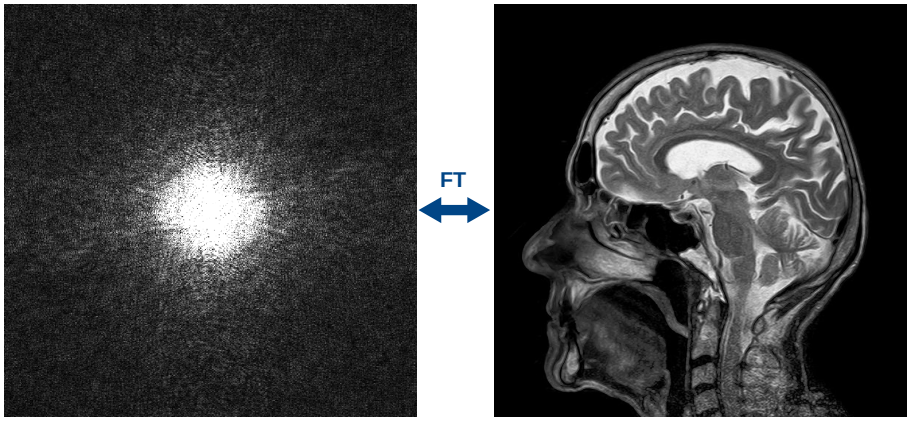

FIGURE 1.4: Correspondence between k-space (left) and image space (right) via the Fourier Transform (FT).

It is interesting here to introduce the point-spread-function (PSF), which is defined as the modulus of the Fourier transform of the sampling pattern viewed as a set of Dirac impulses:

$$PSF(\boldsymbol{r}) = \int_0^T e^{\imath \boldsymbol{k}(t)\cdot \boldsymbol{r}} \mathrm{d}t \tag{1.16}$$

The PSF is what the sampling would produce if the true object were a delta impulse located at zero, so it is a good descriptor of the sampling effect on the image. According to the convolution theorem, an image $I(\boldsymbol{r})$ reconstructed with an inverse Fourier transform will be equal to the convolution $f \star PSF$ of the actual object f with the PSF. The more closely the PSF resembles a delta impulse, the better the reconstruction.

1.3.2 K-space trajectories

The path traced out by $\boldsymbol{k}(t)$ is called the *k-space trajectory* and is determined by the gradient waveform $\boldsymbol{G}(t)$. The speed and acceleration of k-space traversal are controlled by

the gradient as well, since:

$$\dot{\boldsymbol{k}}(t) = \gamma \boldsymbol{G}(t) \tag{1.17}$$
$$\ddot{\boldsymbol{k}}(t) = \gamma \dot{\boldsymbol{G}}(t) \tag{1.18}$$

In MRI, the derivative of the gradient waveforms $\dot{\boldsymbol{G}}(t)$ is commonly called the *slew rate*. Owing to hardware and physiological constraints (e.g., peripheral nerve stimulations), these encoding gradients have a bounded amplitude and a maximum slew rate, imposing limitations of speed and acceleration on the sampling trajectories:

$$\begin{cases} \|\dot{\boldsymbol{k}}\| \leq \alpha \\ \|\ddot{\boldsymbol{k}}\| \leq \beta \end{cases} \tag{1.19}$$

These kinematic constraints make the design of trajectories more difficult, since they have to be smooth with bounded speed and acceleration. This is probably why the first and still most widely used sampling patterns are based on simple geometrical shapes such as lines or spirals. In addition, the rapid decay of the MR signal (~ 50 *ms*) usually prevents the measurement of all the needed data at once. For these reasons, k-space trajectories are generally composed of multiple segments, called *shots*, which sequentially fill the considered k-space grid in what is called a *segmented acquisition*.

The most widespread k-space trajectory is a *Cartesian raster* (Lauterbur, 1973), in which parallel and equidistant lines of the k-space grid are acquired during the frequency-encoded readout. Each Cartesian line corresponds to a given value of the phase-encoding gradient as is illustrated in (Fig. 1.5**a**).

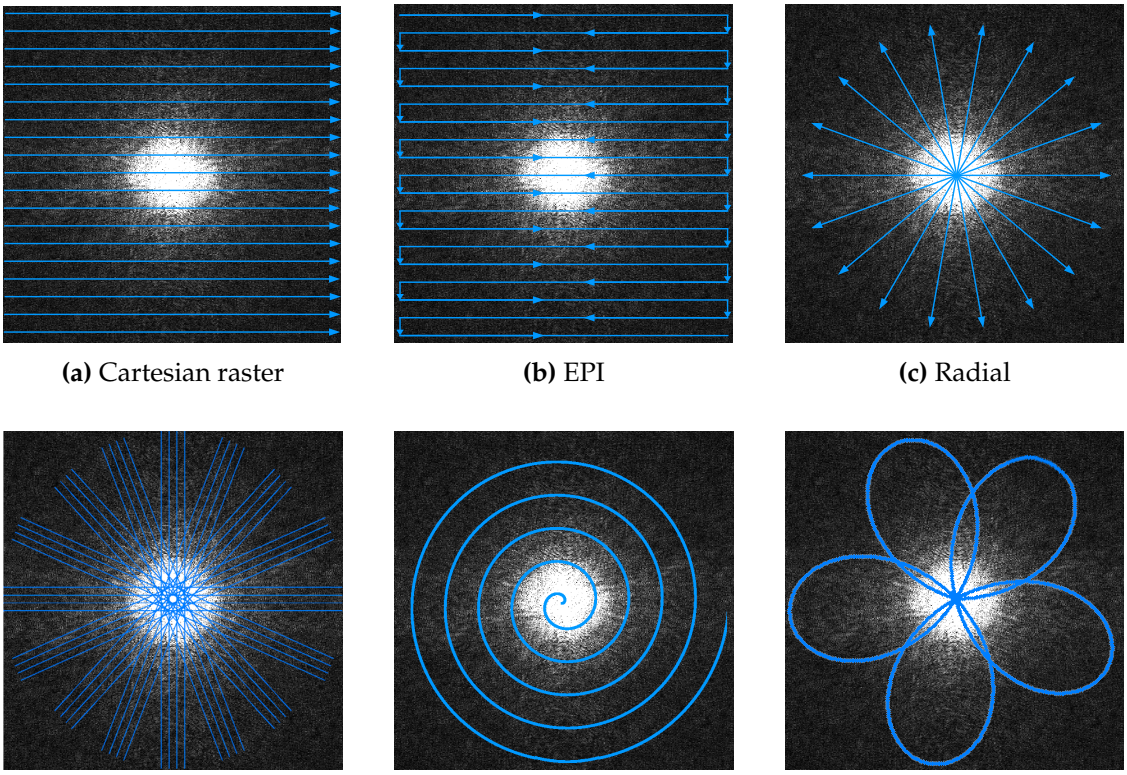

(a) Cartesian raster **(b)** EPI **(c)** Radial

(d) Propeller **(e)** Spiral **(f)** Rosette

FIGURE 1.5: A few standard 2D k-space trajectories.

One drawback of the Cartesian raster is relatively long scan times[6] because each line requires a separate RF excitation pulse (or multiple pulses, if signal averaging is used). Another Cartesian-based k-space trajectory is Echo-Planar Imaging (EPI) described by Mansfield in (Mansfield, 1977), which was developed to speed up the Cartesian raster. The idea is to collect many k-space lines in one excitation by zigzagging through the k-space, as is depicted in (Fig. 1.5**b**). This is done by using a strong frequency-encoding gradient together with a intermittently blipped low-magnitude phase-encoding gradients to switch from one line to the next.

1.3.3 2D non-Cartesian trajectories

Numerous 2D non-Cartesian trajectories were developed for MRI, mostly based on geometrical patterns that were gradually improved or optimized. Here, we present an non-exhaustive list of the most widespread sampling patterns used for 2D scans.

Projection Acquisition (PA) or radial. The first k-space trajectory used for MRI was projection acquisition (PA) (Lauterbur, 1973), which consists of radial spokes either starting from the origin of the k-space such as in (Fig. 1.5**c**) or traversing it from one border to the opposite. Its repeated sampling of k-space center results in a signal averaging over the image space, which renders radial sampling intrinsically robust to motion effects. This is why radial imaging is widely used in dynamic MRI, especially in cardiac MRI (Larson et al., 2004; Arunachalam et al., 2007). Radial imaging is also commonly used in ultra-short echo time (UTE), which allows the detection of signal components with T_2 relaxation times of only a few hundred microseconds necessary for musculoskeletal applications.

Spiral trajectories. The spiral trajectory was developed to decrease acquisition time with the idea to sweep over the k-space more efficiently than its Cartesian or radial counterparts (Ahn et al., 1986; Meyer et al., 1992). The readout is usually longer than in Cartesian sampling and in some cases sufficiently long to cover the entire k-space in a single shot. The shots composing the spiral trajectory are also called *interleaves*. These trajectories usually start at the origin of the k-space and spiral outward as illustrated in (Fig. 1.5**e**). For example, a spiral trajectory may be described as follows:

$$k_x(t) = \lambda t^{\alpha} cos(\omega t) \tag{1.20}$$
$$k_y(t) = \lambda t^{\alpha} sin(\omega t) \tag{1.21}$$

where α is the variable density parameter, $\omega = 2\pi n$ with n the number of turns in the spiral and $\lambda = N/(2\text{FOV})$ with N the matrix size and FOV the field-of-view. The Archimedean spiral characterized by a constant separation distance between successive interleaves is given for $\alpha = 1$ (uniform density).

However, the main difficulty with the design of spiral trajectories is the compliance with the hardware constraints on speed and acceleration in Eqs. (1.19). Most of the proposed designs are based on closed-form expressions, which are easy to implement on a clinical scanner. To take full advantage of the gradient hardware capabilities, two regimes are commonly defined: a slew-rate-limited regime and an amplitude-limited regime. Near the center of k-space, the trajectory is only limited by the gradient slew

[6] Unless echo train spin refocusing is used.

rate and so the slew rate is set to the maximum available slew rate S_{max}. Then, when reaching the maximal gradient amplitude, the trajectory reaches an amplitude-limited regime where the gradient is equal to the maximum available gradient amplitude G_{max} (Delattre et al., 2010).

A simple analytical solution for constant density ($\alpha = 1$) was first given in (Duyn and Yang, 1997) for the slew rate limited case only and then extended in (Glover et al., 1999) for the two regimes. It was then generalized to variable density in (Kim et al., 2003). However, the proposition given in (Kim et al., 2003) overshoots the maximum available slew rate in the first milliseconds of the trajectory which implies that the center of k-space may not be correctly sampled. Both (Glover et al., 1999) and (Zhao et al., 2008) efficiently correct for this problem at a price of lengthening the trajectory.

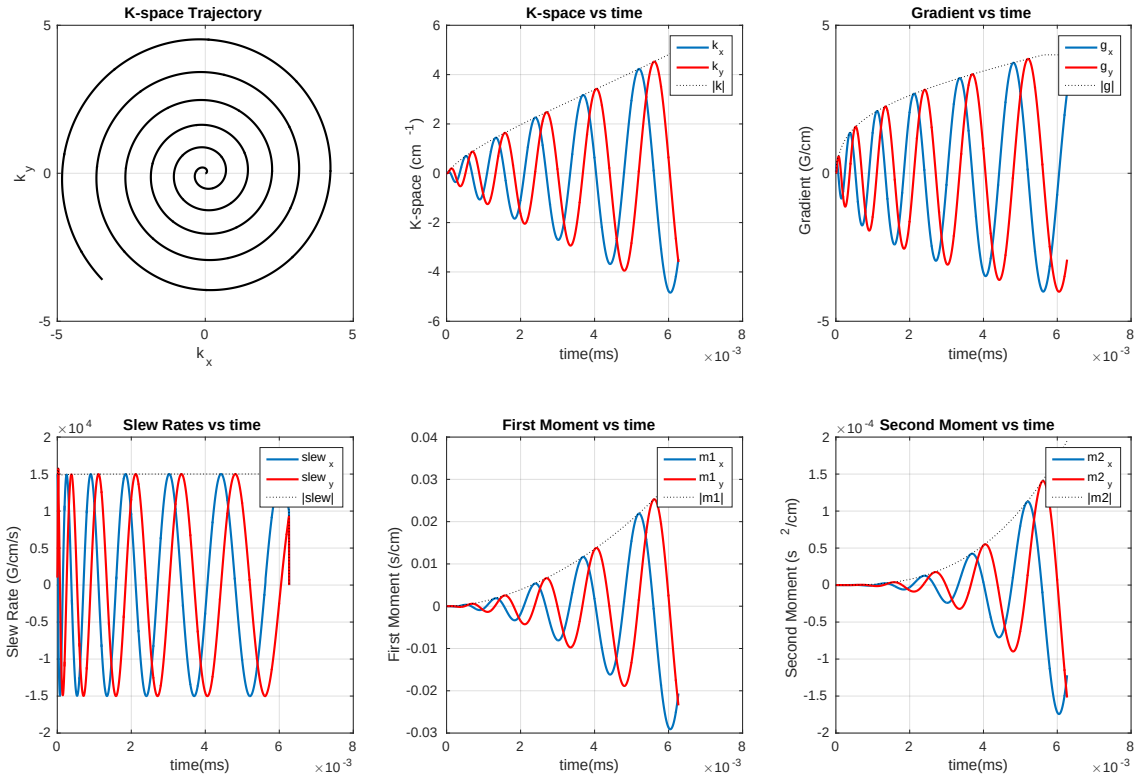

FIGURE 1.6: Variable-density design proposed in (Lee et al., 2003). L=16, resolution of 1mm, $S_{max} = 150$ T/m/s, $G_{max} = 40$ mT/m, sampling interval $\Delta t = 4$ μs, FOV varying linearly from 24 to 12 cm.

Moreover, numerical method were proposed to design variable-density spiral trajectories such as in (Lee et al., 2003), for which a Matlab toolbox is in open access[7]. In this technique, the sampling density is defined as the inverse of the sampling interval in each direction, so that a variable-density sampling is equivalent to a variable effective FOV which is used as design parameter. The effective FOV in each direction gives the following relationship that determines the rate of increase in the radial direction k_r compared with the rate of turning:

$$\frac{\Delta k_r}{\Delta \theta} = \frac{L}{2\pi \mathrm{FOV}_r(k_r)} \tag{1.22}$$

[7] http://mrsrl.stanford.edu/brian/vdspiral/

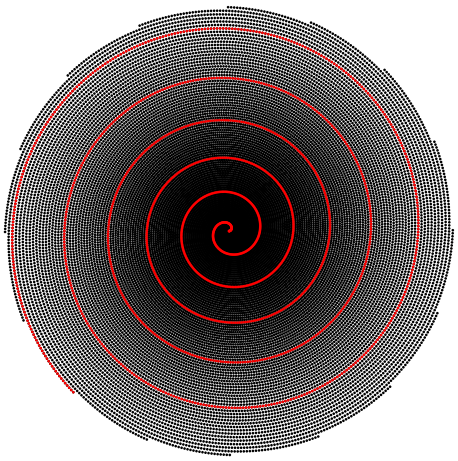

FIGURE 1.7: Multi-shot variable-density spiral proposed in (Lee et al., 2003) corresponding to the design in (Fig. 1.6).

where L is the number of interleaves. Then, the constraints imposed by the hardware and the effective FOV read:

$$\begin{cases} \|G(t)\| & \leq & \min\left(\frac{2\pi}{\gamma}\frac{1}{\mathrm{FOV}(k_r)}\frac{1}{\Delta t}, G_{max}\right), \\ \|S(t)\| & \leq & S_{max} \end{cases} \tag{1.23}$$

where Δt is the sampling interval. The trajectory that satisfies the above constraints can be solved numerically. Since the effective FOV is specified to be a monotonically decreasing function of k_r, the spirals will have increased spacing in the outer k-space region. Fig. 1.6 shows a single spiral interleaf generated with this method, and its characteristics (gradient, slew rate, ...). Finally, Fig. 1.7 displays the whole variable-density trajectory composed of 16 spiral interleaves.

Symmetric spiral trajectories which start at the border of the k-space and finish at the opposite border can simply be designed by adding the time-reversed gradient of a center-out spiral (Glover and Law, 2001).

Hybrid trajectories. Other k-space trajectories were often heuristically derived from basic geometrical patterns such as the PROPELLER (see Fig. 1.5**d**) method (Pipe et al., 1999) which allows for motion correction by using low frequencies information acquired along stacks of parallel radial spokes. Hybrids of radial and spiral patterns were also developed allowing a faster start with radial segments, such as TWIRL, which starts with a radial spoke and finishes with an Archimedean spiral (Jackson et al., 1992). The winding hybrid interleaved radial lines (WHIRL) is another example of hybrid trajectories (Pipe, 1999).

Others. The rosette trajectory (see Fig. 1.5**f**) is another example of 2D sampling patterns (Noll, 1997). Rosette trajectories cross the k-space origin many times, which enables for off-resonance phase accumulation and for the generation of an incoherent distribution of phase in the k-space data. It is also possible to calculate maps of magnetic field inhomogeneity directly from the acquired imaging data. Numerous other heuristic sampling trajectories were explore such as zigzag patterns (Breuer et al., 2008).

1.3.4 3D non-Cartesian trajectories

Various geometrical designs were explored for 3D imaging (Irarrazabal and Nishimura, 1995) and can be divided into several categories: from stack of 2D sampling patterns to fully 3D trajectories, to optimization-based sampling schemes.

Stack of 2D trajectories. Several 2D sampling patterns were used for 3D scans, by stacking the 2D trajectories along the partition direction. These sampling schemes include the "stack-of-stars" for the radial trajectory (Song and Dougherty, 2004; Lin et al., 2008; Chandarana et al., 2011; Feng et al., 2014) and the stack of spirals (Irarrazabal and Nishimura, 1995; Thedens et al., 1999; Chang et al., 2017; Valvano et al., 2016) and also the stack of EPI (Börnert and Jensen, 1995). Moreover, an hybrid radial-Cartesian 3D EPI trajectory was proposed in (Graedel et al., 2017) to enable motion correction for functional MRI. The latter trajectory is not strictly speaking a stack, but rather an assemblage of EPI planes which are rotated about the phase-encoding axis to fill out a cylinder in 3D k-space.

Variations of 3D Cartesian raster. Other designs such as Wave-CAIPI (Bilgic et al., 2015) sought to speed up the 3D Cartesian raster by acquiring a corkscrew trajectory instead of a Cartesian line in the readout direction.

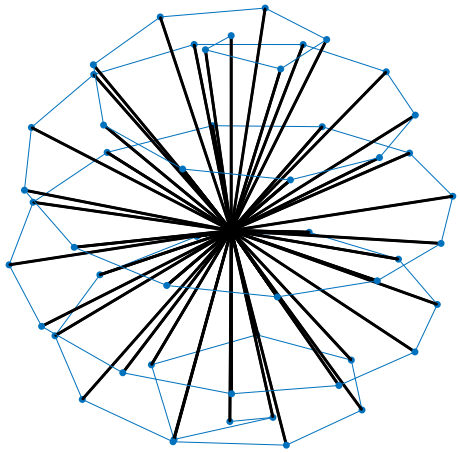

FIGURE 1.8: A spiral-based 3D radial trajectory.

Fully 3D trajectories. Fully 3D sampling patterns are also widely used, the most widespread being 3D radial trajectories. 3D radial trajectories have the same applications as 2D radial sampling, typically in dynamic MRI (Barger et al., 2000; Larson et al., 2002). There exist many ways to organize the radial spokes within the 3D k-space so as to have an approximately uniform distribution. Some of them are based on spiral patterns described on a sphere (Wong and Roos, 1994; Larson et al., 2008; Piccini et al., 2011) but other techniques exist as well (Park et al., 2016). (Fig. 1.8) displays a spiral-based 3D radial trajectory as in (Larson et al., 2008), which is going to be used in later applications of this work.

Morover, other geometrical 3D patterns were developed such as 3D cones (Gurney et al., 2006) or twisted projection imaging (TPI) which is often used in MR spectroscopy (Boada et al., 1997) (Fig. 1.9**a**). A method introduced in (Pipe et al., 2011) is

based on a Fermat spiral 2D trajectory and is called fermat looped, orthogonally encoded trajectories (FLORET) (Fig. 1.9**b**). More recently, the hybrid radial-cones (Johnson, 2017) displayed in (Fig. 1.9**c**) are another example of hybrid trajectories that were heuristically proposed to increase sampling efficiency.

Optimization-based. Optimization-driven 3D trajectory design were also explored, either derived from genetic algorithm (Sabat et al., 2003; Dale et al., 2004) (Fig. 1.9**d**) or inspired from missile-guidance ideas (Mir et al., 2004) (Fig. 1.9**e**), or so called 'heuristically-optimized' patterns (Kumar Anand et al., 2008) (Fig. 1.9**f**). In some works (Kumar Anand et al., 2008; Curtis and Anand, 2008), optimization was used to design random feasible trajectories, where the idea was to use uniformly and randomly distributed control points over a sphere. Then, a feasible trajectory passing close to the control points is generated using second order cone programming. In this way, multiple random trajectories are produced among which the most relevant one in terms of k-space coverage is selected using a genetic algorithm. Moreover, in (Seeger et al., 2010; Ravishankar and Bresler, 2011; Liu et al., 2012), the design of k-space trajectories was addressed using Bayesian methods. In (Seeger et al., 2010), the key idea was to fix a set of feasible trajectories (e.g., spiral interleaves) and to select them iteratively by picking the one that brings the largest amount of information at each step. Given the computational load of this method, other works proposed adaptive approaches based on training images (Ravishankar and Bresler, 2011; Liu et al., 2012).

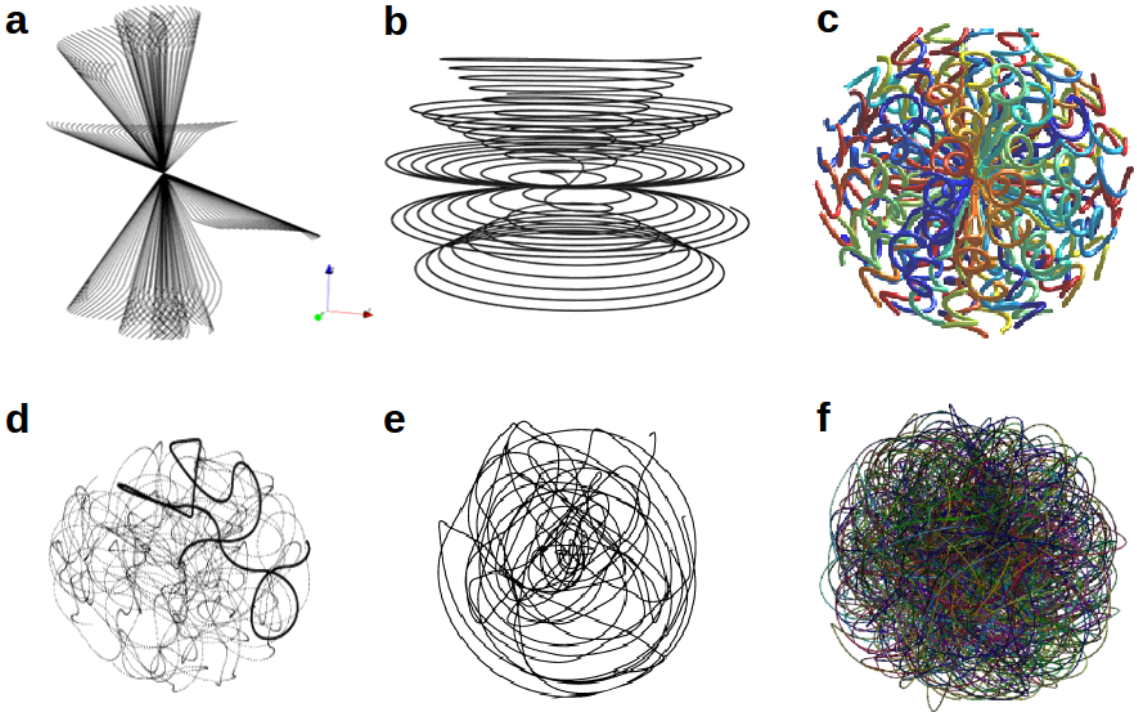

FIGURE 1.9: **Examples of 3D k-space trajectories**. Top: geometrically based 3D trajectories. **a**: TPI. **b**: FLORET. **c**: hybrid radial-cones. Bottom: optimization-based 3D trajectories. **d**: genetic (Sabat et al., 2003). **e**: missile (Mir et al., 2004). **f**: heuristically-optimized (Kumar Anand et al., 2008).

1.3.5 Sampling of k-space trajectories

The Nyquist-Shannon criterion in k-space sampling

To prevent image aliasing, also called wrap-around artifacts, the Nyquist-Shannon criterion should be applied to k-space sampling. Let's first consider the case of 2D Cartesian raster sampling, with a imaging field-of-view $\mathrm{FOV}_x \times \mathrm{FOV}_y$, a matrix size $N_x \times N_y$, one gets a resolution of $\Delta_x = \frac{\mathrm{FOV}_x}{N_x}$ and $\Delta_y = \frac{\mathrm{FOV}_y}{N_y}$. To comply with the Nyquist-Shannon criterion and get the desired resolution, the k-space sampling should respect the following relations:

$$\Delta k_x \leq \frac{1}{\mathrm{FOV}_x} \quad \text{and} \quad \Delta k_y \leq \frac{1}{\mathrm{FOV}_y}, \tag{1.24}$$

$$k_{x,max} = \frac{1}{2\Delta_x} \quad \text{and} \quad k_{y,max} = \frac{1}{2\Delta_y} \tag{1.25}$$

In the case of radial sampling, the number of equiangular spokes n_c must be adapted to the corresponding Nyquist-Shannon criteria. Assuming a matrix size of $N \times N$:

$$n_c \geq \pi N \quad \text{in the case of center-out spokes} \tag{1.26}$$

$$n_c \geq \frac{\pi}{2} N \quad \text{in the case of diametral spokes} \tag{1.27}$$

Nyquist-sampled 2D radial trajectories therefore require more views than a comparable rectilinear acquisition: about 1.57 times more for spokes spanning over π rad (diametral) and up to 3.14 times more for center-out spokes spanning over 2π rad. Artifacts from undersampling are called streaks. If streaking artifacts are not objectionable, this can result in shorter scans without sacrificing spatial resolution compared to Cartesian sampling.

Regarding spiral imaging, two criteria can be introduced: an azimuthal sampling interval Δk_θ along a spiral interleaf and a radial sampling interval Δk_r, that may cause either azimuthal or radial aliasing respectively (Bernstein et al., 2004). Because of the slew rate limit, the gradient amplitude is typically not maximal near the center of k-space, causing the distance between sampled k-space points along a spiral interleaf to be smaller near the center of the k-space than at its periphery. To reduce the readout time, it is not rare that the azimuthal sampling interval on an interleaf exceeds the Nyquist limit away from the center, causing what is called azimuthal undersampling.

Sampling along continuous curves

In most cases, discussion about MRI sampling stops at the spatial Nyquist criteria. However, one has to keep in mind that although k-space trajectories traverse a continuous path, the signal is sampled in time only at discrete intervals along the path. Because of the underlying band-limiting filters of MR receiver hardware, the measured information is essentially averaged over pieces of trajectories traversed between two sampled points (Bernstein et al., 2004; Cho, 1993; Ansorge and Graves, 2016). More precisely, as we saw in section 1.2.2, since band-limiting filters are applied to the received temporal signal before resampling at a smaller rate, this filtering is equivalent to a convolution of consecutive k-space information with a given kernel (e.g., a truncated sinc). In practice,

to avoid any artifacts, the 1D spatial Nyquist criterion should be (at least) be respected along a sampling curve.

1.4 MRI pulse sequences

An MRI pulse sequence can be defined as a preselected set of defined RF and gradient pulses, usually repeated many times during a scan, wherein the time interval between pulses and the amplitude and shape of the gradient waveforms will control NMR signal reception and affect the characteristics of the MR images (e.g., their contrast). The duration between successive excitations is called the *repetition Time* (TR) and the time arount which the signal is acquired is called the *echo time* (TE). Over the years, a multitude of imaging methods has been introduced and can be roughly divided into two categories: the Gradient-Recalled-Echo (GRE) and the Spin-Echo (SE). While SE sequences use an excitation pulse that is normally 90° followed by a 180° refocusing pulse that reverses the effect of field inhomogeneities, GRE sequences present only one excitation pulse with a flip angle that is typically less than 90°. In this thesis, we only present the two sequences most relevant to the presented work: the fast low angle shot (FLASH) and the magnetization-prepared rapid gradient-echo imaging (MP-RAGE), which both belong to the GRE family.

Gradient Recalled Echo (GRE)

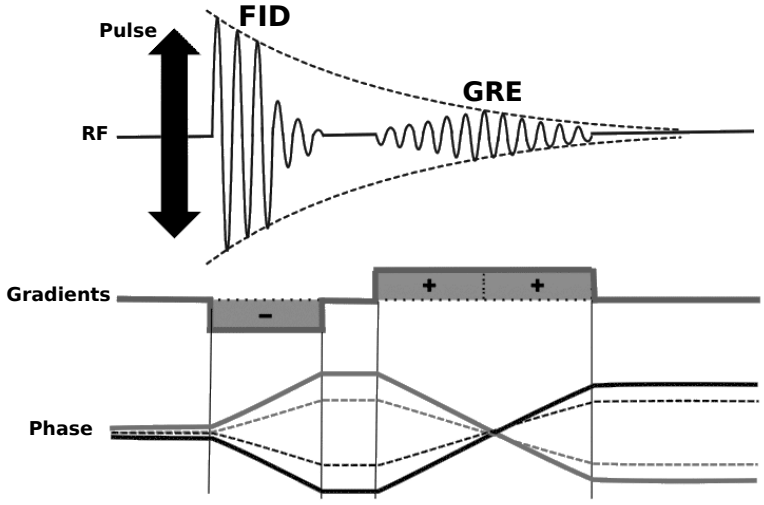

FIGURE 1.10: Pulse timing diagram of the Gradient Recalled Echo (GRE) for Cartesian acquisition. (-) and (+) gradient lobes that dephase and rephase spins respectively. The lowest line shows the phase changes of four spins in different spatial locations subjected to the (-) and (+) gradients. The peak of the gradient echo occurs when the net phase shift among spins is zero.

Gradient Recalled Echo (GRE) is a class of pulse sequences that is generally used for fast scanning (Haase et al., 1986). For instance, GRE is widely used in 3D volume imaging, cardiac imaging and acquisitions that require breath-holding. The term 'recalled

echo' refers to the magnetic field produced by the frequency-encoding gradient waveform that rephases the GRE, as depicted in (Fig. 1.10). GRE pulse sequences do not have the 180-degree RF refocusing pulse that is used to form an RF spin echo. Instead, gradient reversal on the frequency-encoded axis forms the echo. In the Cartesian setup, a readout prephasing gradient lobe first dephases the spin isochromats[8], and then they are rephased with a readout gradient that has opposite polarity, as is illustrated in (Fig. 1.10). The peak of the GRE occurs when the area under the two gradient lobes is equal. For other k-space trajectories, the echo occurs when the dephasing is minimal, i.e. when the trajectory crosses the origin of the k-space or when one of its coordinates is zero. GRE acquisitions can be fast because the flip angle α of the excitation pulse is typically less than 90 degrees so the longitudinal magnetization component is never inverted by an RF refocusing pulse. Therefore, no lengthy period of time is required for T_1 recovery, and GRE pulse sequences can use short TR (e.g., 2-50 ms).

GRE sequences can provide susceptibility-weighted images because there is no 180° pulse to refocus the phase evolution caused by local variations in the magnetic field. The phase of the spin isochromats in the transverse plane continues to accumulate during the entire echo time. Consequently, GRE images are contrast weighted by a factor e^{-TE/T_2^*} (see Fig. 1.12**c**), instead of e^{-TE/T_2} (see Fig. 1.12**b**) as in SE images.

FLASH sequence: spoiled Fast Low-Angle Shot

The basic GRE sequence described in the previous section assumes that the transverse magnetization $M_\perp$ prior to any RF pulse is zero. If so, the GRE pulse sequence is said to be *spoiled*. This is true if the TR is very long compared to the T_2 of the sample (at least four to five times T_2). Typically, spoiled GRE sequence with long TRs can be used for interleaved multi-slice acquisitions to increase the number of acquired slices per TR. However, when the TR becomes comparable or shorter than T_2, unwanted stimulated echoes may arise and corrupt the final image. It is then necessary to use other methods of spoiling such as gradient spoiling, rewinder gradients and/or RF-spoiling, which is the case of the FLASH sequence introduced by (Haase et al., 1986) and now a sequence product of SIEMENS. The pulse diagram of a 2D FLASH sequence is displayed in (Fig. 1.11), where a slice-selection gradient is applied during a low flip angle RF pulse, before the application of gradients in the phase encoding (PE) and the frequency encoding (FE) directions. A spoiler ("SP" lobe on Fig. 1.11) is applied after FE encoding. The FLASH also performs RF spoiling (not displayed on the diagram).

Magnetization-prepared rapid gradient-echo imaging (MP-RAGE)

The MP-RAGE sequence is generally done for 3D T_1-weighted imaging (Fig. 1.12**a**). A typical 3D MP-RAGE pulse sequence uses a three-step cycle: (a) magnetization preparation for contrast control (typically to maximize white matter/gray matter contrast), (b) data acquisition with a short TR gradient-echo sequence, and (c) magnetization recovery for additional contrast control (Mugler and Brookeman, 1990; Mugler and Brookeman, 1991). The diagram of a 3D MP-RAGE sequence is displayed in (Fig. 1.13). It starts with a nonselective inversion preparatory pulse whose flip angle is equal to 180°. After a inversion time denoted as TI, a T_1 contrast is introduced into the longitudinal magnetization. This T_1-prepared magnetization is excited and then read out by a series of fast gradient-echo sequences (e.g., FLASH) to sample multiple k-space lines. The maximum

[8] A microscopic group of spins, which resonate at the same frequency.

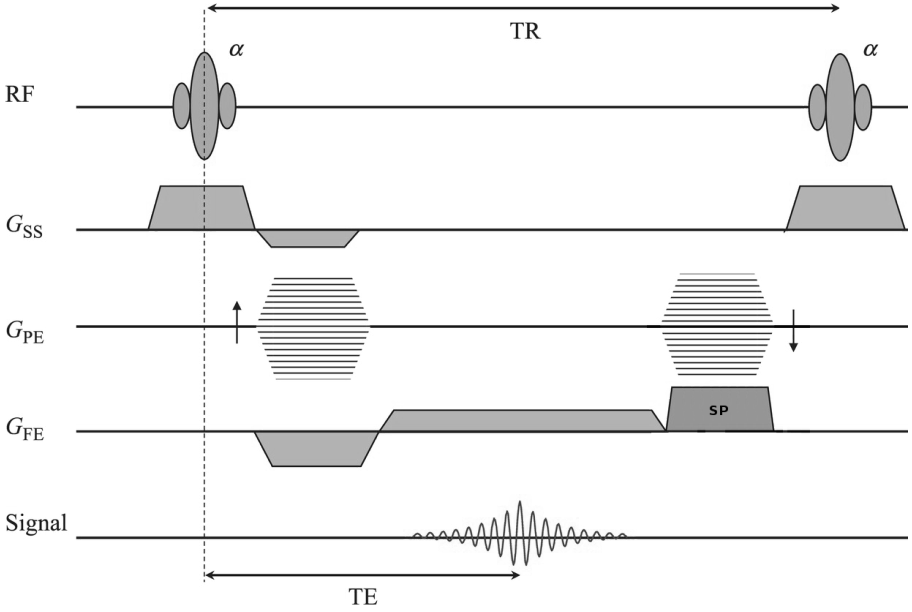

FIGURE 1.11: Unit pulse sequence of 2D FLASH and its parameters: repetition time (TR), echo time (TE) and flip angle (α). A spoiler and phase rewinders are also depicted.

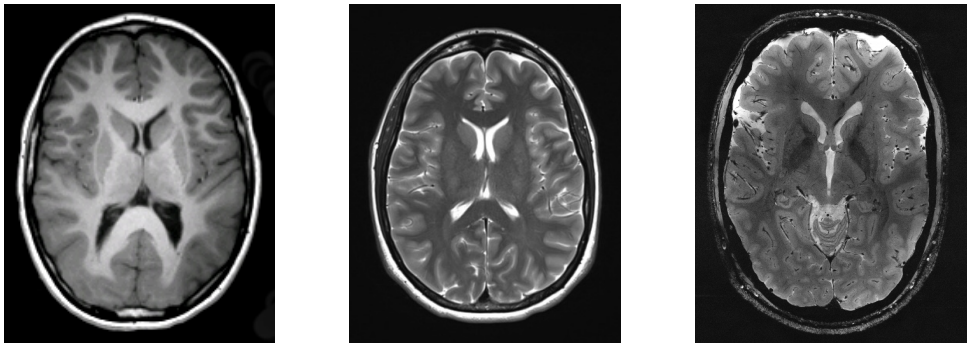

(a) T_1 constrast **(b)** T_2 contrast **(c)** T_2^* contrast

FIGURE 1.12: Different contrasts in MRI.

number of k-space lines depends on the temporal nature of the imaged object, the TR, and the degradation rate of the prepared contrast.

1.5 Advanced signal modeling

Despite hardware improvements, MRI is often subject to field perturbations that violate the traditional k-space formalism introduced above. Imperfections of gradients systems and undesired field contributions perturb the spatially encoding magnetic fields. As a result, the actual phase evolution is prone to deviate from the assumed nominal behavior, which may cause important image artifacts (Barmet et al., 2008; Vannesjo et al., 2015). Here, we list the frequently occurring technical and experimental imperfections and how they affect the signal phase.

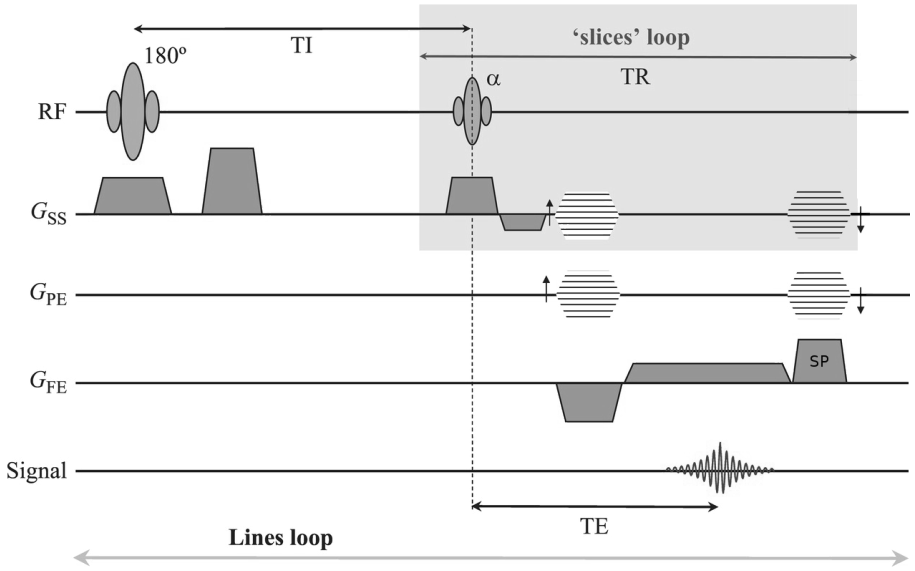

FIGURE 1.13: Unit pulse sequence of 3D MP-RAGE.

1.5.1 System and imaging imperfections

B0 variations or off-resonance effects

Despite shimming, there are spatial time-independent deviations of the field strength from the nominal value B_0. These deviations are not only due to non-perfect hardware (1ppm) but also to magnetic susceptibility (χ) differences typically occurring between soft tissues ($\chi = -9 \times 10^{-6}$) and air ($\chi = 0.4 \times 10^{-6}$). In addition, chemical shift, which refers to the frequency shift due to electron shielding effectively, reduces the resonance frequency. The most common chemical shift concerns transitions between fat and water, for which the deviations can reach 3.5ppm (220Hz at 1.5T / 440Hz at 3T). In these conditions, the local magnetic field can be modeled as a static, spatially varying deviations $\Delta B_0(\boldsymbol{r})$ from the assumed homogeneous main magnetic field B_0. After demodulation at the nominal resonance frequency $\omega_0 = \gamma B_0$, this results in a additional phase contribution compared to Eq. 1.12:

$$\begin{aligned}\Phi(\boldsymbol{r},t) &= \int_0^t (\gamma B_z(\boldsymbol{r},\tau) - \omega_0)\, d\tau \\ &= \int_0^t (\gamma \Delta B_0(\boldsymbol{r}) + \gamma \boldsymbol{G}(\tau))\, d\tau \\ &= \Delta\omega_0(\boldsymbol{r})t + \boldsymbol{k}(t)\cdot\boldsymbol{r}\end{aligned} \tag{1.28}$$

where $\Delta\omega_0(\boldsymbol{r}) = \gamma\Delta B_0(\boldsymbol{r})$ is the deviation from ω_0.
Hence, in this case, the acquired signal at time t is:

$$S(t) \approx \int f(\boldsymbol{r}) e^{-\imath\Delta\omega_0(\boldsymbol{r})t} e^{-\imath\boldsymbol{k}(t)\cdot\boldsymbol{r}} d\boldsymbol{r} \tag{1.29}$$

which is no longer a Fourier transform. The problem here comes from the term $e^{-\imath\Delta\omega_0(\boldsymbol{r})t}$, where t is not a constant and so cannot be absorbed by the $f(\boldsymbol{r}) := M_\perp(\boldsymbol{r})B_\perp(\boldsymbol{r})$ term and be quickly evaluated by a FFT.

Off-resonance will have different effects depending on the k-space trajectory. In a conventional Cartesian raster acquisition it causes displacement in the frequency-encoded (i.e., readout) direction, while in a spiral acquisition it causes displacement in all directions, which results in blurring.

Gradient imperfections

The gradient system itself suffers from inherent deficiencies such as limited coils and amplifier bandwidth. This may result in temporal delays (e.g., amplifier delays, circuit delays) and varying amplitude scaling of the generated gradient field. Overall, the gradient chains exhibit low-pass characteristics (Vannesjo et al., 2013). Moreover, nonlinear field components may arise due to limitations in the accuracy and the range of spatial linearity of the gradient fields (Bernstein et al., 2004). This is especially occurring at larger distance from isocenter.

Eddy currents

The time-varying magnetic fields from gradients induce currents in conducting structures within the magnet, gradient coils themselves and RF coils. This is a consequence of Faraday's law:

$$\nabla \times \mathbf{E} = -\frac{\partial \mathbf{B}}{\partial t} \tag{1.30}$$

These induced currents are called eddy currents and create unwanted local, spatially nonlinear transient fields. The magnetic field produced by the eddy current always opposes the change in the field causing the eddy current (Lenz's law). The rate of eddy-current buildup is proportional to the gradient slew rate. Eddy-current time constants on commercial scanners can range from a few microseconds to hundreds of seconds. Their spatial dependence is mainly classified into B_0 eddy currents which are spatially constant over the imaging volume, and linear eddy currents, which have linear spatial variation, similar to the imaging gradient fields. Higher-order spatial dependence is possible but is not commonly measured or corrected. Since eddy currents increase with higher gradient amplitude and faster slew rate, they have become a more important problem with the advent of higher performance gradients. They can be dealt with in four main ways: (a) shielded gradient coils, (b) gradient waveform preemphasis, (c) gradient waveform derating, and (d) application-specific calibrations and corrections during image acquisition or reconstruction (Bernstein et al., 2004).

Concomitant terms

According to Maxwell equations ($\nabla \times \boldsymbol{B} = \mathbf{0}$ and $\nabla \cdot \boldsymbol{B} = 0$), when linear gradients are applied in the z-direction, other magnetic field components perpendicular to B_z are produced. They also cause the amplitude of the magnetic field to exhibit higher-order spatial dependence (e.g., x^2 and y^2). The magnetic field corresponding to these spatially nonlinear time-varying terms is known as a concomitant field (Bernstein et al., 2004). This concomitant field is however negligible at high field since the characteristics parameter describing the deviations $\epsilon = B_0/(G \cdot \mathrm{FOV})$ is very small compared to 1 (Yablonskiy et al., 2005).

Others

Other experimental imperfections such as coil vibrations and thermal variations cause nonlinear time-varying phase contributions.

1.5.2 Phase modeling of growing complexity

Among the previously listed sources of phase errors, one can distinguish between static contributions (off-resonance effects), dynamic contributions (gradient imperfections and nonlinearities, eddy currents, concomitant field), and spatially linear field contributions (gradient imperfections) for which the k-space formalism holds. Regardless of the origin of phase distortions, one can consider three phase models of growing complexity (Schneider et al., 2011):

a) Only deviations *in time* or *amplitude* of linear spatial encoding magnetic fields are accounted for, which can still be described in the k-space formalism. In this case the experimentally k-space trajectory $\boldsymbol{k}^{\text{exp}}$ deviates from the nominal trajectory $\boldsymbol{k}^{\text{nom}}$:

$$\boldsymbol{k}^{\text{exp}} = \boldsymbol{k}^{\text{nom}}(t + \boldsymbol{\tau}) + \Delta\boldsymbol{k}(t + \boldsymbol{\tau}) \tag{1.31}$$

where $\boldsymbol{\tau}$ is the vector of timing delays in each gradient direction and $\Delta\boldsymbol{k}$ is the vector of deviations in k-space positions along x, y and z directions.

b) Deviations consist of spatially nonlinear but *static* fields. In this case, a static off-resonance term must be added to the magnetization phase:

$$\Phi^{\text{exp}}(\boldsymbol{r}, t) = \boldsymbol{k}^{\text{exp}}(t) \cdot \boldsymbol{r} + \Delta\omega_0(\boldsymbol{r})t \tag{1.32}$$

c) Deviations are arbitrary and contain explicit *dynamic* and spatially *nonlinear* components. The local phase evolution can then be exhaustively described by:

$$\Phi^{\text{exp}}(\boldsymbol{r}, t) = (\boldsymbol{k}^{\text{nom}}(t + \boldsymbol{\tau}) + \Delta\boldsymbol{k}(t + \boldsymbol{\tau})) \cdot \boldsymbol{r} + \Delta\omega_0(\boldsymbol{r})t + \gamma \int_0^t B_l(\boldsymbol{r}, \tau)d\tau \tag{1.33}$$

where B_l is a dynamic nonlinear spatially encoding magnetic field component.

Gradient Impulse Response functions (GIRFs)

A number of studies have shown that, to a relatively high degree of accuracy, the gradient response can be considered as a linear time-invariant (LTI) system (Alley et al., 1998; Addy et al., 2012; Vannesjo et al., 2013; Brodsky et al., 2009). Under this assumption, the gradient system's behavior is fully described by its impulse response functions, which are called the gradient impulse response functions (GIRFs):

$$\begin{aligned} G_{out}(t) &= (G_{in} * h)(t) \\ G_{out}(t) &= \int_{-\infty}^{+\infty} G_{in}(\tau) \times h(t - \tau)\mathrm{d}\tau \end{aligned}$$

Or, equivalently in the Fourier domain:

$$\mathfrak{F}(G_{out})(\omega) = \mathfrak{F}(G_{in})(\omega) \times H(\omega) \tag{1.34}$$

where $\mathfrak{F}$ denotes the Fourier transform and $H := \mathfrak{F}(h)$ is the GIRF. An advantage of this approach is that it is independent of any eddy current modeling, and it also includes effects due to gradient mechanical vibrations. Due to the low-pass characteristics of the gradient coils and amplifiers, the GIRF presents a low-pass behavior in a first approximation, as can be seen in (Fig. 1.14). Vannesjo et al. managed to measure the GIRF with unprecedented accuracy by using a gradient field camera and multiple averaging (Vannesjo et al., 2013).

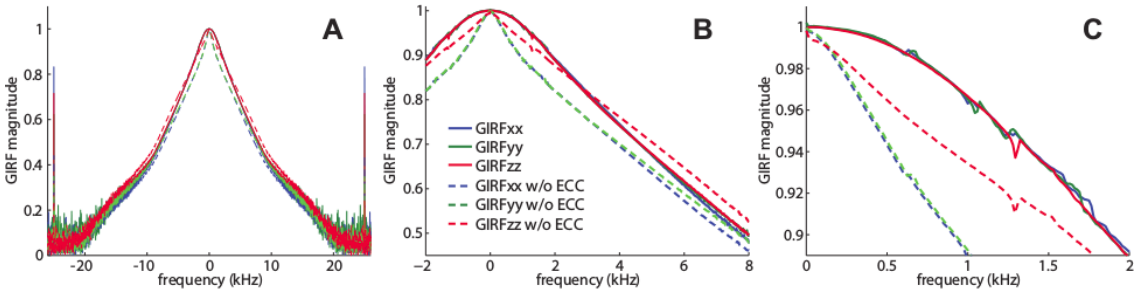

FIGURE 1.14: Magnitude of GIRFs as measured by Vannesjo et al in (Vannesjo et al., 2013) for all three gradient directions with and without built-in eddy current compensation (ECC). The low-pass characteristics of the gradient system is apparent in **(A)**. Detail of the responses in **(B)** shows how the EDD serves to broaden the response plateau and align the responses of the three different gradient channels. Several mechanical resonances are visible at low frequencies in **(C)**.

1.5.3 Measuring system imperfections

B0 field maps

A B0 field map can be estimated from different scans (at least two) acquired at different echo times. The phase difference between the acquired images is due to the different precession frequencies, which are related to the field map via a linear relation. A straightforward estimation consist of dividing the phase difference by the delay time between the acquisitions ΔTE. More sophisticated reconstructions have been proposed in the literature such as linear regression techniques (Windischberger et al., 2004), phase unwrapping techniques (Reber et al., 1998) or statistically based approaches such as (Funai et al., 2008). Once these GIRFs are determined for a given gradient system, they can be used to predict and correct gradient distortions in the image reconstruction.

Local Phase Measurement (LPM)

Many different techniques to measure deviations in the magnetization phase exist, depending on the desired degree of accuracy (phase models 1, 2 or 3). For instance, in the context of phase model 1, a simple and fast method to measure the linear deviations is proposed in (Duyn et al., 1998). However, this method cannot detect gradient coupling effects for instance.

To tackle the exhaustive phase model 3, one can for example use a gradient field camera such as (Barmet et al., 2008; Vannesjo et al., 2015) that allows to measure the actual phase up to a certain order of spherical harmonics decomposition (usually ≤ 3). If one does not possess such costly device, other (more time-consuming) methods can be used, such as the one proposed in (Schneider et al., 2011), which is an extension of method presented in (Papadakis et al., 1997). This method, called Local Phase Measurement (LPM), has the advantage of measuring all the phase contributions accumulated during the application of the gradient waveforms including coupling effects. Because this method is going to be implemented and used in the following Chapter 3, we briefly detail here its principles. Compared to (Duyn et al., 1998), the phase evolution is not only determined at two positions but is spatially resolved on a grid $N \times N$, as illustrated in (Fig. 1.15). For each grid point in the k-space, the excited spins are correspondingly spatially encoded before playing out the entire gradient waveform during the ADC. This results in N^2 time-series of complex data points, which, after Fourier transform, gives N^2 complex images representing the spatial distribution of the transverse magnetization (REP2). This sequence is repeated without any gradient waveforms to acquire a baseline (REP1).

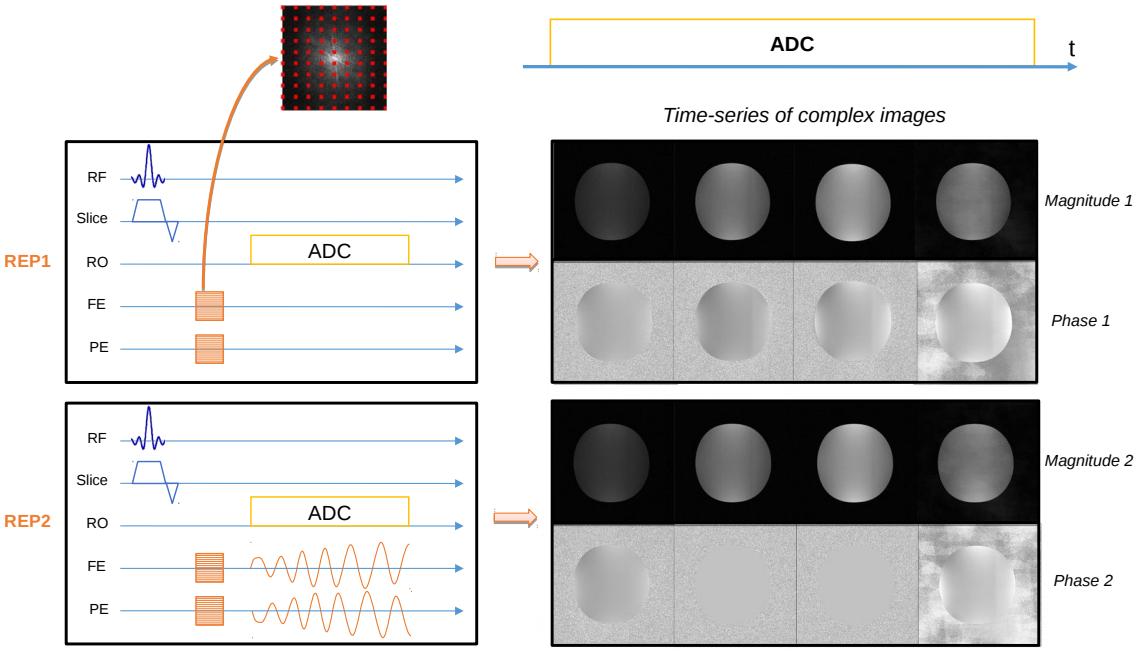

FIGURE 1.15: Principles of the Local Phase Measurement (LPM) method.

After phase unwrapping, the temporal phase can be retrieved:

$$\phi(x,y,t) = \phi_{\text{rep2}}(x,y,t) - \phi_{\text{rep1}}(x,y,t) \tag{1.35}$$

Because of this baseline subtraction, the LPM does not capture the static B_0 inhomogeneities. The time derivative of the phase divided by γ gives the effective magnetic field:

$$\begin{aligned}\frac{1}{\gamma}\frac{\partial \phi}{\partial t}(x,y,t) &= B(x,y,t) \\ &= B_0(t) + G_x(t)\cdot x + G_y(t)\cdot y + h(x,y,t)\end{aligned}$$

where $h(x, y, t)$ denotes the higher-order terms. In a discrete-time setup, the phase derivative is calculated as follows:

$$\frac{1}{\gamma}\left[\frac{\partial\phi}{\partial t}\right]_{t_i}(x,y) \approx \begin{cases} \frac{\phi(t_{i+1})-\phi(t_{i-1})}{2\gamma\Delta t}, & \text{if } i \in [2, T-1] \\ \frac{\phi(t_{i+1})-\phi(t_i)}{\gamma\Delta t}, & \text{if } i = 1 \end{cases} \tag{1.36}$$

For each time step $i \in [1, T]$, we define $f_i(x, y) := \frac{1}{\gamma}\left[\frac{\partial\phi}{\partial t}\right]_{t_i}(x, y)$. The objective is to extract the first spatial orders of the polynomial expansion of f_i. This polynomial fit was performed up to a chosen order by computing the pseudoinverse with QR decomposition of the matrix for better numerical stability (backslash operator in Matlab). The field of view used for fitting was smaller than the whole object to ensure a relative smoothness of the data. Completing the fit for all time steps then yields the global B0(t), Gx(t), Gy(t) and other higher order term time-courses.

For the LPM to work adequately, two conditions regarding the LPM phase-encoding resolution and sampling rate must be met. First, the dephasing at the border of the k-space should not exceed π for the signal not to be too weak, imposing $\Delta\phi_{max} = k_{test,max}\Delta x_{LPM} \leq \pi$, or equivalently:

$$k_{LPM,max} \geq k_{test,max} \tag{1.37}$$

where $k_{test,max}$ is the maximum spatial frequency of the tested trajectory and $k_{LPM,max}$ is the k-space extent of the LPM phase-encoding. Secondly, the dephasing between two consecutive measurements should not exceed π to enable unwrapping of the phase, i.e. $\Delta\phi_{max} = \gamma G_{test,max} r_{max} \Delta t_{LPM} \leq \pi$, which results in:

$$\Delta t_{LPM} \leq \frac{\pi}{\gamma G_{test,max} r_{max}} \tag{1.38}$$

1.6 Image reconstruction

In this section, we will present basic tools and methods to reconstruct non-Cartesian data. We will also introduce susceptibility-weighted imaging (SWI), which is a post-processing method to enhance the image contrast.

1.6.1 Reconstruction of non-Cartesian data

Gridding

One method to reconstruct images from non-Cartesian data is to resample the data onto a 2D Cartesian grid before using a 2D DFT. This technique is called 'gridding' or 'regridding' and can be done in many ways. First, we will present a 'grid-driven' approach and then a 'data-driven' approach.

Grid-driven approach. Grid-driven interpolation is the easiest method to resample the data onto a grid. The idea is to estimate the value at each grid point based on the surrounding samples as is illustrated in (Fig. 1.16**a**). One disadvantage of this approach is that it may not use all of the input data, and thus won't be as 'SNR efficient' as the data-driven interpolation. However, because it does not use all the data, the grid-driven approach does not require a density estimate, which is very convenient. The fidelity of

image reconstruction will be a trade-off between interpolator complexity and k-space oversampling. If the data is resampled onto a grid twice as finely sampled ('2X' grid), a simple bilinear interpolator yields acceptable reconstructions. In practice, this approach is seldom used due to the general convergence of the MRI community towards the data-driven interpolation. However, grid-driven interpolation can produce high-fidelity reconstructions, especially when the sampling density is difficult to compute or continually changing.

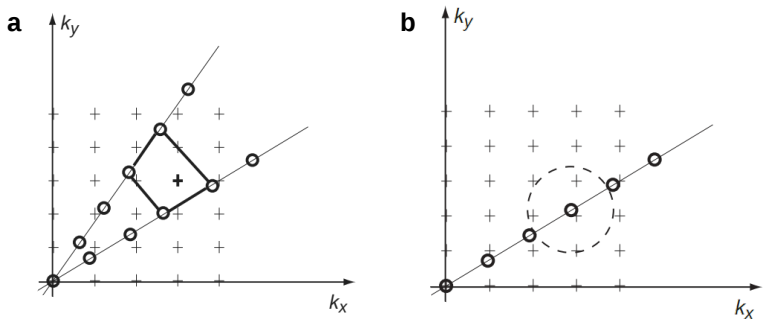

FIGURE 1.16: **Two approaches to gridding**. **a**: grid-driven approach. **b**: data-driven approach.

Data-driven approach. The idea of the data-driven approach is to take each data point and add its contribution to the surrounding grid points, as is represented in (Fig. 1.16**b**). More precisely, each sample is convolved with a small kernel, which is wide enough so as to cover the neighboring grid points. This approach has the advantage of exploiting all the data, making it more 'SNR efficient'. However, a density estimation is necessary to correct for the fact that the samples may be concentrated in particular areas of k-space, leading to an increased contribution to surrounding grid points. The third concern is the choice of the density of the reconstruction grid (i.e., the grid oversampling factor α). Following the work of (Jackson et al., 1991), the data $\hat{M}(k_x, k_y)$ after the entire gridding procedure is given by :

$$\hat{M}(k_x,k_y) = \left(\left[\left(M(k_x,k_y) \times S(k_x,k_y) \times W(k_x,k_y) \right) \star C(k_x,k_y) \right] \times \text{II} \left(\frac{k_x}{\frac{\Delta k_x}{\alpha}}, \frac{k_y}{\frac{\Delta k_y}{\alpha}} \right) \right) \star^{-1} C(k_x,k_y) \tag{1.39}$$

where $M(k_x, k_y)$ is the MR signal, $W(k_x, k_y)$ is a weighting function for density compensation, $S(k_x, k_y)$ is the non-Cartesian sampling function, $C(k_x, k_y)$ is the convolution kernel and II defines the comb function associated to the Cartesian grid. Here, $\star$ and $\star^{-1}$ are the convolution and deconvolution operators. After Fourier transform, it becomes:

$$\hat{m}(x,y) = \left(\left[\left(m(x,y) \star s(x,y) \star w(x,y) \right) \times c(x,y) \right] \star \text{II} \left(\frac{x}{\alpha \text{FOV}_x}, \frac{y}{\alpha \text{FOV}_y} \right) \right) \times \frac{1}{c(x,y)} \tag{1.40}$$

A Kaiser-Bessel kernel is often used for $C(k_x, k_y)$. The density compensation $W(k_x, k_y)$ can be calculated analytically using geometrical arguments in some cases (e.g., radial) or by using a Voronoi diagram.

The non-uniform Fourier transform

Another way to deal with non-Cartesian data is to use a non-uniform or nonequispaced Fourier transform. Several methods were proposed (Dutt and Rokhlin, 1993; Fessler and Sutton, 2003; Keiner et al., 2009b), but we will only remind the principle of the nonequispaced fast Fourier transform (NFFT) introduced by Keiner et al. in (Keiner et al., 2009b).

A d-dimensional nonequispaced discrete Fourier transform (NDFT) is defined by a set of arbitrary spatial nodes χ and a frequency bandwidth vector $\boldsymbol{N}$. Each node x_j in the nonequispaced sampling set $\chi := \left\{x_j \in T^d : j = 0, ..., M-1\right\}$ is drawn from the d-dimensional torus $T_d \cong \left[-\frac{1}{2}, \frac{1}{2}\right)^d$ with the number of nodes equal to $|\chi| = M$. For each dimension $t \in [\![0, d-1]\!]$, the bandwidth $N_t \in 2N$ is defined as a fixed even number, and collected into the vector $\boldsymbol{N} := (N_0, ..., N_{d-1})^T$. Let us define the multi-index I_N set which is a representation of all possible frequencies in a transform:

$$I_N := \left\{\boldsymbol{k} = (k_t)_{t=0,...,d-1} \in Z^d : -\frac{N_t}{2} \leq k_t < \frac{N_t}{2},\ t = 0, ..., d-1\right\} \tag{1.41}$$

Given Fourier coefficients $\hat{f}_k \in \mathbb{C},\ \boldsymbol{k} \in I_N$ as input, the NDFT is defined as the evaluation of the corresponding trigonometric polynomial $f \in T_N$ at the set of M arbitrary nodes χ as follows:

$$\forall j \in [\![0, M-1]\!], \quad f_j = \sum_{\boldsymbol{k} \in I_N} \hat{f}_k e^{-2\imath\pi \boldsymbol{k} x_j} \tag{1.42}$$

This can be rewritten as a matrix-vector product:

$$\boldsymbol{f} = \boldsymbol{A}\hat{\boldsymbol{f}} \tag{1.43}$$

with the vectors $\boldsymbol{f} := (f_j)_{j=0,...,M-1}$, $\hat{\boldsymbol{f}} := (\hat{f}_k)_{k \in I_N}$ and the nonequispaced matrix $\boldsymbol{A} := \left(e^{-2\imath\pi \boldsymbol{k} x_j}\right)_{j=0,...,M-1:k \in I_N}$

The *adjoint NDFT* is then defined by:

$$\hat{\boldsymbol{h}} = \boldsymbol{A}^H \boldsymbol{f} \tag{1.44}$$

which is equivalent to the sums:

$$\forall \boldsymbol{k} \in I_N, \quad \hat{h}_k = \sum_{j=0}^{M-1} f_j e^{2\imath\pi \boldsymbol{k} x_j} \tag{1.45}$$

The NFFT C library is a fast approximation algorithm which computes the sums in Eqs. (1.45) and (1.42). This library uses only $O\left(|I_N| log |I_N| + |log \epsilon|^d M\right)$ instead of $O\left(M|I_N|\right)$ floating point operations (ϵ is the desired accuracy of computation). The key idea of the NFFT algorithm is to use standard FFTs (fftw) in combination with an approximation scheme that is based on a window function ϕ, which should be mutually well localized in time/spatial and frequency domain. Two parameters controls the accuracy of the NFFT: an oversampling factor σ and a truncation parameter m[9].

[9]The first approximation concerns a cut-off in frequency domain, for which an aliasing error is introduced due to the use of a FFT of length $n := \sigma N$ on a smaller number of samples N. A second approximation is due to the cut-off in time/spatial domain. Assuming the window function to be well localized in

1.6.2 Post-processing: susceptibility-weighted imaging (SWI)

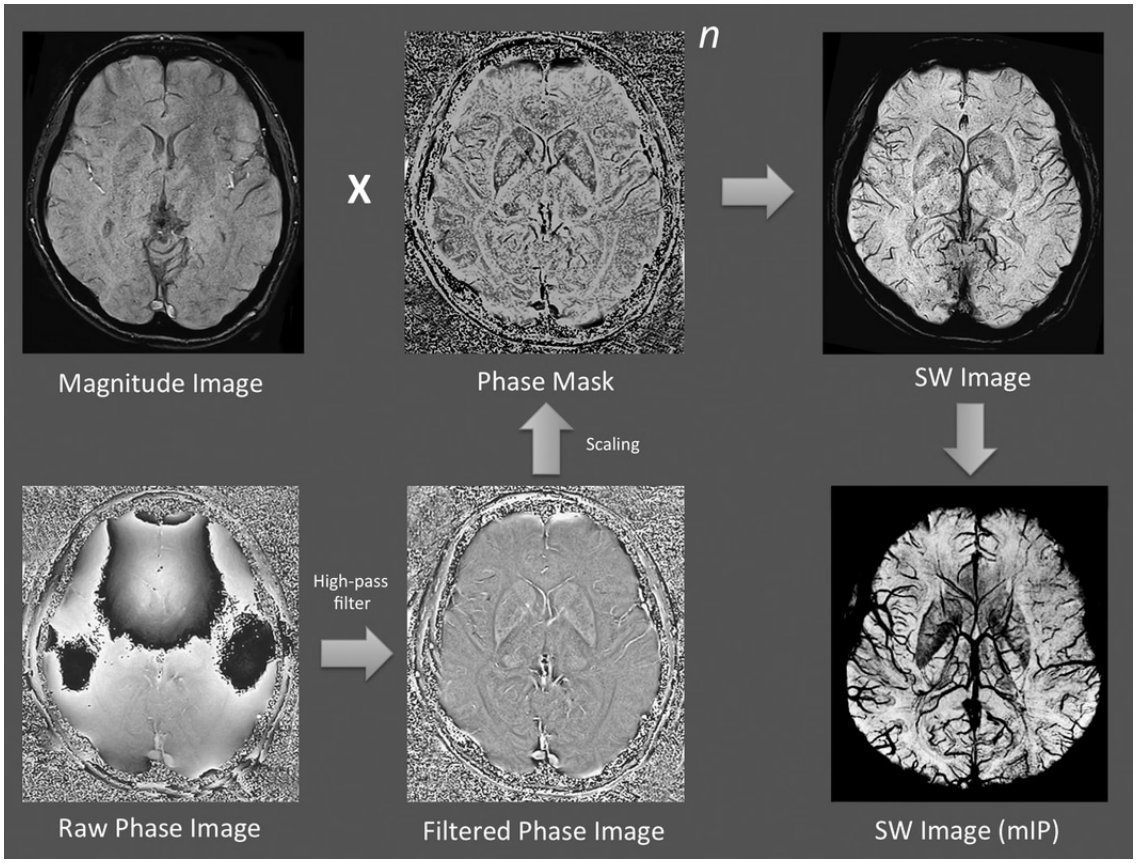

FIGURE 1.17: Processing steps of susceptibility-weighted imaging.

Once a complex image is reconstructed, it is possible to enhance its contrast by taking advantage of the phase information, thus creating a new type of contrast different from spin density, T_1-, or T_2- weighted imaging (Haacke et al., 2004). Specifically, the phase images themselves can provide excellent contrast between gray matter and white matter (Haacke et al., 1995), iron-laden tissues (Ogg et al., 1999), venous blood vessels (Reichenbach et al., 1997; Wang et al., 2000), and other tissues with susceptibilities that are different from the background tissue (Reichenbach et al., 2001). Indeed, signals from substances with different magnetic susceptibilities compared to their neighboring tissue will become out of phase with these tissues at sufficiently long echo times. One approach for combining magnitude and phase images was introduced as susceptibility-weighted imaging (SWI) (Haacke et al., 2004). SWI is typically performed using 3D gradient echo sequences with the following parameters: $TR = 25\text{-}40\ ms$, $TE = 20\text{-}40\ ms$ and a flip angle between 15° and 20°. The successive processing steps of SWI are displayed in (Fig. 1.17). The phase images are first high-pass-filtered and then transformed to a phase mask that varies in amplitude between zero and unity (Haacke et al., 2004). This mask is multiplied a few times (n times on (Fig. 1.17)) into the original magnitude image to create enhanced contrast between tissues with different susceptibilities. To further accentuate

time/spatial domain, it is approximated by a truncated version with support $\left[-\frac{m}{n}, \frac{m}{n}\right]$, $m \ll n$, $m \in \mathbb{N}$, which causes a truncation error.

the contrast of the susceptibility-weighted (SW) image, minimum intensity projection (mIP) may be used.

If SWI has become today a standardized sequence in the clinical routine at 3 Tesla, it is also more and more used at 7 Tesla with the idea to make good use of the high field advantages.

1.7 Ultra High Field MRI

Until recently, most clinical MRI scanners operated at field strengths at 1.5 Tesla. However, due in part to improvements in magnet design and shielding, 3 Tesla clinical scanners are now widely available and there is a push for even higher field whole body scanners (7-11 Tesla) throughout the industry. There seems to be a trend towards high(er)-field MRI, which is fueled by the benefits of potentially higher signal-to-noise ratio (SNR), contrast-to-noise ratios (CNR) and spectral resolution for certain applications (Duyn, 2012). Ultra high fields (UHF) ranges from 7 Tesla and above.

1.7.1 Signal-to-noise ratio

Given as certain imaging protocol, the SNR in MRI is proportional to the following parameters:

$$SNR \propto B_0 B_1^- \Delta V f_{seq}(TR, TE, \theta) \sqrt{N_{shots} T_{obs} N_{avg}} \tag{1.46}$$

where B_0 is the main magnetic field, B_1^- the receive sensitivity (RF magnetic field per unit current in the receive coil), ΔV is the voxel volume, $f_{seq}(TR, TE, \theta)$ is a factor dependent on the other sequence parameters, N_{shots} is the number of shots, T_{obs} is the observation time per shot and N_{avg} is the number of averages. Therefore, once sequence parameters and receive coils are adjusted to their optimal performance, the only options left to improve the SNR are to increase the main magnetic field B_0 or decrease the resolution. When high resolution images are desired, the only remaining possibility is to increase the main magnetic field B_0.

1.7.2 Clinical value

The SNR increase promised by UHF can typically be traded into higher spatial and/or temporal resolution MRI, which is expected to aid in the understanding and diagnosis of many neurodegenerative pathologies involving submillimetric lesions or morphological changes, such as Alzheimer's disease and multiple sclerosis (Barnes et al., 2009; Thomas et al., 2008; Pruessner et al., 2000; Kolk et al., 2013). For instance, Fluid-Attenuated Inversion Recovery (FLAIR) sequences are able to make very good use of the increased SNR at 7 Tesla, providing high CNR between brain tissue lesions and the surrounding healthy brain tissue (Visser et al., 2010). Furthermore, MR angiography, which is regularly used in clinical practice to assess all kinds of brain pathology, can be obtained with an ultra-high resolution for optimal assessment of even smaller arteries of the brain than at lower field strengths.

Besides the gain in SNR and CNR, pushing up the main magnetic field strength brings other advantages. Most importantly, susceptibility effects are increased at ultra-high field, which provide additional contrast with potential clinical utility. In particular, T_2^*-weighted sequences are very interesting at UHF for the detection of microlesions and

microbleeds and the visualization of microvasculature (Frischer et al., 2012; De Guio et al., 2014; Moenninghoff et al., 2010b; Zwanenburg et al., 2011). (Fig. 1.18) shows the enhanced visualization of microbleeds possible with a T_2^* acquisition at 7 Tesla compared to clinical standard 1.5-Tesla imaging (Conijn et al., 2010).

This increased susceptibility-induced contrast is not only beneficial for structural brain imaging, but also for Blood oxygenation level dependent (BOLD) functional imaging (Glover and Law, 2001). Indeed, the physiological noise contributions (veinous blood) are expected to decrease with increased resolutions while the BOLD signal increases with field strength (Triantafyllou et al., 2005).

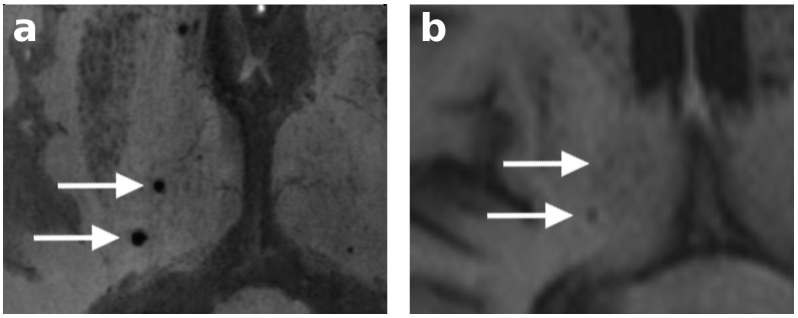

FIGURE 1.18: **Enhanced susceptibility contrast at 7 Tesla**. 77-year-old man with a history of hypertension presented with transient dysphasia based on a transient ischemic attack (TIA) of the left hemisphere. **a**: magnified region of a T_2^*-weighted brain image at 7 Tesla and **b**: standard clinical image at 1.5 Tesla. The images at 7 Tesla clearly show better visualization of the microbleeds due to the increased susceptibility effects at 7 Tesla compared to 1.5 Tesla MRI. (results published in (Conijn et al., 2010))

1.7.3 Challenges

There are, however, technological, physical and safety limitations impeding the full realization of UHF (Stafford, 2004). The most important technical challenges concern:

- **The inhomogeneous transmit field**. At high fields of 3 Tesla and above, the B_1 becomes increasingly inhomogeneous due to permittivity, conductivity and the conformation of the patients. The dielectric properties of tissues give rise to a region of hyperintensity at the center of the image referred to as 'field focusing'. This problem can be compensated with the use of parallel transmission.

- **Increased susceptibility artifacts**. Since susceptibility effects are proportional to the field strength, deleterious image distortions and signal loss are particularly detrimental in regions of air/tissue interfaces (sinus, ears) as discussed in Section 1.5.1.

- **Specific absorption rate (SAR) limitations**. The SAR is a measure of the power absorbed in tissue per unit mass and is approximately proportional to B_0^2 for fields below 4 Tesla[10]. The potential effects of heating imposes limitations on sequence pulses.

[10]This power law is somewhat reduced for higher field strengths.

Furthermore, in spite of a more favorable SNR offered by UHF, high resolution imaging is in practice hindered by motion concerns and long acquisition times. Despite the recent development of corrections for bulk and physiological motion (Maclaren et al., 2012; Federau and Gallichan, 2016; Stucht et al., 2015; Vannesjo et al., 2015), long acquisition times remain a major obstacle to high-resolution acquisition, especially in clinical applications. Hence, the development of methods to speed up MRI is still an active area of research in MRI. This issue motivates the following chapter, which presents the application of compressed sensing in MRI to accelerate the acquisition time.

Chapter 2

Compressed sensing in MRI: how much can we accelerate?

2.1 Introduction

Reducing the acquisition time in Magnetic Resonance Imaging (MRI) has been a major direction of research in recent years. Speeding up image acquisition while maintaining diagnostic quality is indeed crucial in many respects. The improvement of patient comfort together with a reduced risk of motion artifacts are examples of consequential advantages. Moreover, in dynamic imaging for instance, accelerated acquisitions are critical to visualize rapid physiological changes. Finally, the resulting gain in time can be invested in increasing the spatial and temporal resolution or in supplementary scans. In this context, considerable effort has been spent on developing methods to accelerate data acquisition while preserving image quality. One recent and most promising strategy is the Compressed Sensing (CS) theory which consists in reducing the number of measurements and thus the acquisition time (TA) by exploiting the compressibility of MR images (Lustig et al., 2007b). Using CS, data can be massively undersampled by a given acceleration factor R compared to the fully-sampled Cartesian acquisition, while ensuring conditions for optimal image recovery. Examples of recent successful applications of CS in MRI are numerous (Siemens Healthineers, 2016) especially in two-dimensional (2D) or three-dimensional (3D) dynamic MRI (Gamper et al., 2008; Jung et al., 2009). In cardiac imaging for instance, CS made it possible to perform single breath-hold and even free-breathing 2D cine MRI while including motion-correction (Vardoulis et al., 2015; Usman et al., 2013). Moreover, combining CS with golden-angle radial trajectories, the XD-GRASP method allows free-breathing cardiac cine imaging and 3D dynamic contrast-enhanced MRI of the liver (Feng et al., 2016; Feng et al., 2014).

While many efforts have been made to improve the CS methodology in MRI both on the acquisition (Haldar et al., 2011; Puy et al., 2012; Adcock et al., 2013; Adcock and Hansen, 2015; Boyer et al., 2014; Bigot et al., 2016; Chauffert et al., 2014; Chauffert et al., 2016; Boyer et al., 2016) and the reconstruction (Lustig et al., 2007b; Aelterman et al., 2011; Guerquin-Kern et al., 2011; Haldar, 2014; Florescu et al., 2014) sides, the question on the actual limitations to the acceleration rate in CS for a given experimental setup has been hardly addressed. Hence, CS could considerably benefit from a study analyzing in a quantitative way the major practical limitations to the degree of acceleration in CSMRI. Such work would provide CS users with valuable information to design their MR sequence by selecting the appropriate acceleration factor adapted to each scan instead of using a trial-and-error approach. This is however a delicate question as numerous parameters affect the quality of CS reconstructions including the image size and the

available signal-to-noise ratio (SNR) for a particular acquisition (Hollingsworth, 2015). In this work, we will offer an insight into the following question:

In CSMRI, how should the maximum acceleration factor be selected as a function of the image size and the available SNR, in order to maintain a desired image quality?

One may expect that existing theoretical sampling results would provide an analytical answer to this question. Unfortunately, if the existing literature proposes a rather comprehensive qualitative analysis of CSMRI, the constants involved in the theorems and concentration inequalities are often crudely estimated. The result is that most practically implemented sampling schemes should be considered as mere heuristics.

Following this observation which we briefly elaborate in a first theoretical part (Section 2.2), we propose to conduct an empirical analysis of the considered preceding question in the case of T_2^*-weighted imaging. Applying a generic method based on retrospective undersampling (Section 2.3), we present its results (Section 2.4) on an analytical image for two types of MR sampling schemes and a conventional ℓ^1-based non-linear reconstruction. The image quality dynamics could thus be quantitatively analyzed and threshold values were identified. The maximum acceleration factor $R_{\max}$ was also quantitatively determined as a function of the image size and the available input SNR to reach a desired image quality. Moreover, we present a retrospective and prospective experimental validation of these results based on T_2^*-weighted images acquired with a 7 Tesla scanner on an *ex vivo* baboon brain. We finally propose a method to deduce a *sequence-specific* maximum undersampling factor circumscribed by the intrinsic SNR of any given acquisition.

2.2 The theory of CS in MRI and its limitations

The theory of compressed sensing is often considered a mature field by non-specialists. While this belief proves to be quite accurate for Gaussian measurements, many important questions are still open when dealing with structured measurements and structured signal recovery, as met in MRI. In this section, we review a few major theoretical results and open questions to motivate our experimental study.

2.2.1 The case of unstructured measurements

Let

$$\sigma_s(\mathbf{z}) = \min_{\mathbf{z}' \in \mathbb{C}^n,\ \text{s-sparse}} \|\mathbf{z} - \mathbf{z}'\|_1 \tag{2.1}$$

denote the ℓ^1-tail of a vector $\mathbf{z} \in \mathbb{C}^n$. This function is often used to characterize the compressibility of a signal $\mathbf{z}$.

The following theorem ([)Theorem 9.13]foucart2013mathematical provides an accurate description of the recovery guarantees in the case of unstructured Gaussian measurements.

Theorem 1 *Assume that $\mathbf{A} \in \mathbb{C}^{m \times n}$ is a matrix with i.i.d. random Gaussian components. There exist universal constants C_1, C_2, D_1 and D_2 such that, for any $1 \leq s \leq n$, for any $\epsilon \in (0,1)$, if*

$$m \geq C_1 s(\ln(n/2) + 1) + C_2 \ln(2/\epsilon), \tag{2.2}$$

then, with probability at least $1-\epsilon$*, for all vectors* $\mathbf{z} \in \mathbb{C}^n$*, given the measurements* $\mathbf{y} = \mathbf{A}\mathbf{z} + \mathbf{e} \in \mathbb{C}^m$*, where* $\mathbf{e}$ *is a measurement error satisfying* $\|\mathbf{e}\|_2^2 \leq m\sigma^2$*, we get:*

$$\|\mathbf{z} - \hat{\mathbf{z}}\|_2 \leq D_1 \frac{\sigma_s(\mathbf{z})}{\sqrt{s}} + D_2 \sqrt{m}\sigma, \tag{2.3}$$

where

$$\hat{\mathbf{z}} = \underset{\|\mathbf{A}\mathbf{z}'-\mathbf{y}\|_2 \leq \sqrt{m}\sigma}{\arg\min} \|\mathbf{z}'\|_1. \tag{2.4}$$

The value of this theorem lies in the fact that it provides a good understanding of the reconstruction quality with respect to the signal's compressibility (captured by $\sigma_s(\mathbf{z})$) and the input SNR (captured by σ). In particular, it shows that if $s \mapsto \frac{\sigma_s(\mathbf{z})}{\sqrt{s}}$ decreases sufficiently fast with s, a small number of measurements will be sufficient to reconstruct the true signal, up to an error proportional to $\|e\|_2$. The ℓ^1-tail σ_s explains the role of resolution in the theory of CS. Fig. 2.1 shows the evolution of the normalized $\sigma_s(\mathbf{z})$ with respect to the normalized sparsity s/n for the phantom image Fig. 2.3A) at different resolutions ($n = 128\times128$, $n = 512\times512$ and $n = 2048\times2048$). Two observations can be drawn from this graph: on the one hand, the larger the relative sparsity of $\mathbf{z}$, the smaller its ℓ^1-tail $\sigma_s(\mathbf{z})$. On the other hand and more importantly, the higher the resolution, the faster the ℓ^1-tail decay. Hence, CS will allow using higher sub-sampling factors at higher resolution for an equal error. Similar phenomena are explained in more details in (Roman et al., 2014).

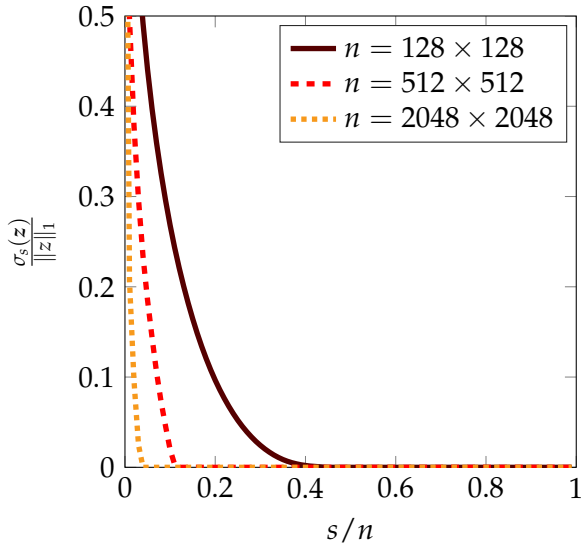

FIGURE 2.1: Normalized ℓ^1-tail $\sigma_s(\mathbf{z}) = \min_{\mathbf{z}' \in \mathbb{C}^n,\, \text{s-sparse}} \|\mathbf{z} - \mathbf{z}'\|_1$ with respect to the relative sparsity s/n for different resolutions of the brain phantom image in Fig. 2.3A): $n = 128\times128$, $n = 512\times512$ and $n = 2048\times2048$. The ℓ^1-tail decays faster at higher resolutions, thus allowing the use of larger undersampling factors for higher resolutions in the context of CS.

Let us now describe the limitations of this theorem. First, *it does not capture the denoising capabilities of* ℓ^1 *reconstructions*. The term $\sqrt{m}\sigma$ in (2.3) coincides with the amount of noise in the data and increases with the number of measurements m. In practice it is often observed that ℓ^1 minimization not only allows to recover missing information, but also serves as a regularizer able to denoise the data. Second, *the constants* C_1, C_2, D_1 *and*

D_2 are not tight and can be huge in some variants of this theorem, meaning that the lower bound on the number of measurements m may actually be quite large, or equivalently that the undersampling factor $R = n/m$ may be close to 1 or even smaller than 1.

This last criticism has to be moderated by the theoretical analysis of phase transitions in (Amelunxen et al., 2014). It is now well known that in the case of noiseless measurements, perfect recovery will occur with high probability whenever $m \geq 2s(\log(n/s) + 1) + \epsilon$ and will fail with high probability when $m \leq 2s(\log(n/s) + 1) - \epsilon$, where ϵ is a small margin. This shows that the minimum number of measurements for good recovery is very well understood in this case.

2.2.2 The case of structured measurements and structured signals

In MRI, signals are highly structured: all brain images share strong similarities and can be modeled much more precisely than arbitrary s-sparse signals. A simple model to describe this structure is the *sparsity by levels* in wavelet bases (Adcock et al., 2013): each wavelet sub-band of the image contains a number of nonzero coefficients bounded by a known quantity at each scale. (Fig. 2.2) illustrates a brain phantom image and its wavelet decompositions for four sub-bands. Moreover, the traditional way of acquiring data in MRI is far from independent Gaussian measurements: Fourier transform values of the image are probed along continuous trajectories.

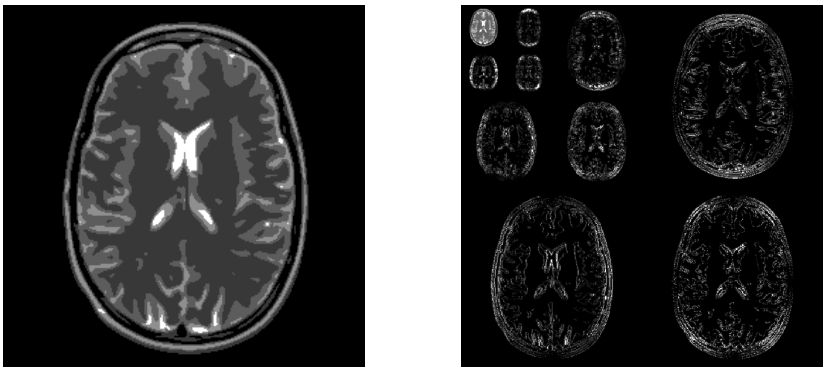

(a) Brain phantom **(b)** Wavelet representation

FIGURE 2.2: A brain phantom image of size $N = 256$ (a) and its wavelet representation (b) for a Symmlet wavelet basis and 4 leves of decomposition.

The current sampling theory in this challenging setting can safely be described as significantly less comprehensive than the case of Gaussian measurements. Let us however remark that significant advances were proposed recently (Adcock et al., 2013; Roman et al., 2014; Krahmer and Ward, 2014; Bigot et al., 2016; Boyer et al., 2017). Without introducing the theorems, let us detail the main conclusions and limitations of these studies. First, the use of incoherent sampling and reconstruction bases is not necessary if the sparsity pattern is adapted to the sampling scheme (Boyer et al., 2016). This is the case in particular for MRI, where most images are compressible in the wavelet domain. Second, one important result argues that low frequencies should be probed more often than high frequencies. The reason is subtle and not just due to the fact that there is more information in the low frequencies (Puy et al., 2011). To understand the reconstruction limits, one needs to precisely describe the links between wavelet bases, Fourier bases and *sparse by levels* signals. The current major limitations can be listed as follow:

- *The constants appearing in the theorems are usually far too large to be of any practical use.* This is due to inaccurate proof techniques, but it is currently unknown how much the constants can be lowered. Establishing phase transition results for structured sampling schemes as in the case of Gaussian measurements still requires significant mathematical advances.
- *Designing optimal sampling densities is still an open problem.* Theorems provide quantitative upper-bounds on the number of measurements necessary for perfect reconstruction, which allows designing decent densities. However, proving optimality results requires to establish tight lower bounds. In practice the design of good sampling densities is therefore heuristic.
- *The noise is not correctly handled.* The stability to noise and compressibility is established, but the dependencies are far less optimistic than those in Theorem 1.
- *Most results are only available for orthogonal wavelet transforms and ℓ^1-reconstructions.* It is now admitted that much better reconstruction results can be obtained in practice by using redundant transforms, learned dictionaries or non-convex regularizers. The understanding of CS in this setting is still very partial.
- *In the case of measurements collected along curves, very little is known*. Let us mention that the case of parallel lines as proposed in (Lustig et al., 2007b) was analyzed completely in (Boyer et al., 2017).

Overall, we see that existing theoretical results provide a good qualitative analysis of CS, allowing to guide the design of sampling and reconstruction schemes. However, to date, theorems are unable to provide quantitative conclusions on the number of needed measurements in CSMRI.

2.3 An empirical and quantitative study of the maximum degree of undersampling

While being theoretically inextricable, the proposed question[1] can be empirically addressed and its answer may provide valuable practical and quantitative information to CSMRI. Hence, we proposed the following methodology.

2.3.1 A generic method

In order to empirically quantify the effects of the image size and input SNR on the reconstructed image quality from undersampled data, we propose the following generic framework. All notations are listed in (Table 2.1).

First, a database of 2D reconstructions is constituted for a large range of image sizes, input SNR and acceleration factors. Square images are considered and characterized by their *image size*, denoted by $N \in \mathbb{N}$, which refers to the dimension of the corresponding $N \times N$ square matrix. An image of size $N \in \mathcal{N}$, where $\mathcal{N}$ is the studied range of sizes, is therefore composed of N^2 pixels. Images of different input SNR ($\mathbf{x}_N^{\mathrm{SNR}}$) were obtained by adding complex-valued zero-mean white Gaussian noise of varying standard deviation $\sigma \in \Sigma$ to the full complex k-space data of a noiseless image ($\mathbf{x}_N^{\infty}$), where Σ is the

[1] In CSMRI, how should the maximum acceleration factor be selected as a function of the image size and the available SNR, in order to maintain a desired image quality?

TABLE 2.1: Notations used throughout the paper.

Notations	Meaning
$N \in \mathcal{N}$	Image size
m	Number of measurements
$R = N^2/m \in \mathcal{R}$	Undersampling factor
$\sigma \in \Sigma$	Noise level
$\text{SNR} \in \mathcal{SNR}$	Signal-to-noise ratio
$\mathbf{x}_N \in \mathbb{C}^{N^2}$	Image of size N
$\mathbf{x}_N^{\infty}$	Noiseless image of size N
$\mathbf{x}_N^{\text{SNR}}$	Noisy image of size N characterized by its input SNR
$\widehat{\mathbf{x}}_R$	Reconstructed image from R-fold undersampled data
Q ; Q_0	Image quality metric ; image quality threshold
$R_{\max}(Q_0, N, \text{SNR})$	Maximum undersampling factor
$\mathbf{z} \in \mathbb{C}^{N^2 \times q}$	q-fold undecimated wavelet representation of image $\mathbf{x}$
$\mathbf{y} \in \mathbb{C}^m$	Measured Fourier data
$\mathbf{F}_\Omega$	Fourier Transform over the support $\Omega \subseteq \{1, \ldots, N^2\}$
$\mathbf{\Psi}$	q-fold undecimated wavelet transform ($L = 4$, $q = 3L + 1$)

studied range of noise levels. Each noise level ($\sigma \in \Sigma$) was then expressed as its corresponding input $SNR \in \mathcal{SNR}$, a quantity more commonly used in the MRI community, where $\mathcal{SNR}$ denotes the studied range of SNR. The input SNR is computed over the FFT-reconstructed fully sampled magnitude image by taking the ratio of the mean signal in a region-of-interest (ROI) in the white matter (smaller orange circle in Fig. 2.3A)) over the standard deviation in the background signal (larger yellow circle in Fig. 2.3A)). Finally, a set of undersampling schemes and image reconstruction is specified as input of the proposed pipeline 1. The undersampling or acceleration factor $R \in \mathcal{R}$ is given by $R = N^2/m$, where m is the number of measurements and $\mathcal{R}$ the studied range of undersampling factors.

Once the database is complete, it is possible to introduce the concept of a maximum acceleration factor $R_{max}(Q_0, N, \text{SNR})$ as the function of (i) the targeted image quality expressed in terms of a quality threshold Q_0 for a given image quality metric Q, (ii) the image size N and (iii) the image input SNR:

$$R_{\max}(Q_0, N, \text{SNR}) = \arg\max_R \left\{ Q(\widehat{\mathbf{x}}_R, \mathbf{x}_N^{\text{SNR}}) \geqslant Q_0 \right\}$$

where $\mathbf{x}_N^{\text{SNR}}$ is the reference image with given image size N and SNR and $\widehat{\mathbf{x}}_R$ the corresponding reconstruction retrospectively undersampled by a factor R. Similar threshold over image quality score was already used in (Zhang et al., 2014) for diagnostic utility.

Finally, to study separately the effect of either the image size or the noise level, one of these parameters was kept constant while the other was varied.

Pipeline 1 Find $R_{\max}(Q_0, N, \text{SNR})$

Input: An undersampling method *undersample* and the associated reconstruction *reconstruct*.
Input: Image quality metric Q and a threshold Q_0
for N in $\mathcal{N}$ **do**
  Take an image $\mathbf{x}_N^\infty$ of size N
  for σ in Σ **do**
    $\mathbf{x}_N^{\text{SNR}} \leftarrow \mathbf{FFT}^{-1}(\mathbf{FFT}(\mathbf{x}_N^\infty) + \mathcal{N}(0, \sigma))$.
    for R in $\mathcal{R}$ **do**
      $data \leftarrow undersample(\mathbf{x}_N^{\text{SNR}}, R)$
      $\widehat{\mathbf{x}}_R \leftarrow reconstruct(data)$
    end for
  end for
end for
Output: $R_{\max}(Q_0, N, \text{SNR})\ \forall\ \text{N} \in \mathcal{N}, \text{SNR} \in \mathcal{SNR}$

2.3.2 The studied pipeline

In this work, we applied the above method to both analytical and experimental data in the case of T_2^*-weighted imaging.

2D images

The studied images shown in Fig. 2.3A-B) are derived from the analytical brain phantom with a contrast similar to T_2^*-weighting, which was introduced by Guerquin-Kern et al (Guerquin-Kern et al., 2012b). Considered image sizes belonged to the set $\mathcal{N} = \{128, 256, 512, 1024, 2048\}$.

Input SNR

We studied a set of input SNR ranging from 3 to 110. Resulting noisy images are displayed in Fig. 2.3A)-B) for the most extreme SNR values.

Undersampling schemes

Two undersampling schemes were considered in this work: identically and independently distributed (iid) and radial samplings. First, non-Cartesian samples were iid randomly drawn according to polynomially decaying distribution of degree 2, with a plateau in the low frequencies, which provided good reconstruction performance across the different image sizes (Chauffert et al., 2013). An example of the resulting sampling schemes is depicted in Fig. 2.3C), for an image size $N = 512$ and a acceleration factor of $R = 10$. Acceleration factors from 2 up to 30 were considered.

Moreover, we also propose to evaluate the performance of radial readouts, which are widely used in CSMRI. This radial *k*-space trajectory is composed of diametrical symmetric spokes spaced by a constant angle increment. Fig. 2.3D) shows the isotropic radial trajectory for the studied image size of $N = 1024$ and $R = 15$, which results in 68 spokes composed of 1024 samples.

Both sampling patterns are implementable in practice in MRI either using 2D acquisitions in the case of radial sampling or using so called partition (i.e., the 3$^{\text{rd}}$ dimension) as

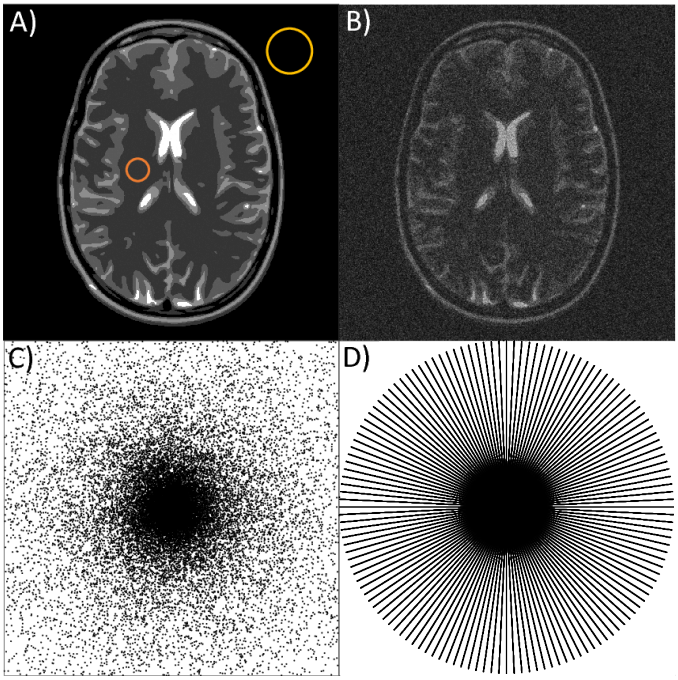

FIGURE 2.3: Guerquin-Kern analytical phantom of a brain image (Guerquin-Kern et al., 2012b) for an image size of $N = 512$ with highest studied SNR of 110 (A) and lowest input SNR of 3 (B). The smaller orange and larger yellow circles respectively represent the ROI in the white matter and the area in the background signal used to calculate the input SNR. Examples of iid sampling schemes of Fourier space along the chosen variable density is displayed for $N = 512$ and $R = 10$ in (C) and symmetric isotropic radial trajectory for $N = 1024$ and $R = 15$ in (D).

the encoding direction of a 3D acquisition for the iid sampling (Lustig et al., 2008b). For the sake of simplicity however, only slice-wise reconstructions in the orthogonal plane are considered in this work.

Reconstructions

Nonlinear non-Cartesian reconstructions were implemented to reconstruct the images by solving the ℓ^1-ℓ^2 penalized synthesis formulation of the CS reconstruction problem:

$$\widehat{\mathbf{z}} = \underset{\mathbf{z}\in\mathbb{C}^{N^2\times q}}{\arg\min} \frac{1}{2}\|\mathbf{F}_\Omega \boldsymbol{\Psi}\mathbf{z} - \mathbf{y}\|_2^2 + \lambda\|\mathbf{z}\|_1 \tag{2.5}$$

where $\mathbf{y} \in \mathbb{C}^m$ is the measured Fourier data, $\mathbf{x} = \boldsymbol{\Psi}\mathbf{z} \in \mathbb{C}^{N^2}$ is the image and $\mathbf{z} \in \mathbb{C}^{N^2\times q}$ its wavelet decomposition over a redundant wavelet basis on $L = 4$ levels ($q = 3L + 1$), $\mathbf{A} = \mathbf{F}_\Omega\boldsymbol{\Psi}$ is the sensing matrix over the support $\Omega \subseteq \{1, \ldots, N^2\}$ with $\mathbf{F}$ the discrete Fourier transform and λ the regularization parameter. The Non-equispaced Fast Fourier Transform (NFFT) (Keiner et al., 2009b) was used to handle non-Cartesian Fourier data and an undecimated wavelet transform was taken from the Rice Wavelet Toolbox (RWT version 3.0 available on `github.com/ricedsp/rwt`). A proximal accelerated gradient method (Fast Iterative Soft Thresholding Algorithm (Beck and Teboulle, 2009)) was implemented to solve the minimization problem (2.5). Finally, the regularization parameter

TABLE 2.2: Correspondence between SSIM scores and Mean Opinion Scores (MOS) between an image and a reference (Zanforlin et al., 2014).

SSIM	MOS	Quality	Impairement
≥ 0.99	5	Excellent	Imperceptible
$[0.95, 0.99)$	4	Good	Perceptible but not annoying
$[0.88, 0.95)$	3	Fair	Slightly annoying
$[0.5, 0.88)$	2	Poor	Annoying
≤ 0.5	1	Bad	Very annoying

was tuned over a range of $[10^{-6}; 10^{-2}]$ so as to select the reconstruction of best quality according to the criterion introduced below.

Image quality metrics

To quantitatively assess the image quality, we chose to work with two reference-based image quality metrics: the structural similarity (SSIM) index introduced in (Wang et al., 2004) and the Normalized Root Mean Square Error (NRMSE in %). On the one hand, the SSIM attempts to model the human visual system (HVS) and is increasingly employed in the MRI community to assess image quality (Hollingsworth et al., 2014; Mann et al., 2015; Jeromin et al., 2012), and on the other hand the NRMSE is a commonly used intensity-based metric calculated as follows (Eq. 2.6):

$$\text{NRMSE}(\widehat{\mathbf{x}}, \mathbf{x}) = \frac{\|\widehat{\mathbf{x}} - \mathbf{x}\|_2}{\|\mathbf{x}\|_2} \tag{2.6}$$

where $\widehat{\mathbf{x}}$ is the reconstructed image from Eq. (2.5) and $\mathbf{x}$ the reference. While the SSIM index, $\text{SSIM}(\widehat{\mathbf{x}}, \mathbf{x})$, varies between 0 (null correspondence with the reference) and 1 (perfect match with the reference), the NRMSE is comprised between a 0% and 100% error. For each image size, the corresponding reference was chosen as the fully sampled Cartesian image of same size presenting a SNR of 110, which is the highest studied SNR in this work. Moreover, these indexes were computed over cropped images deprived of their background with a binary mask. Since both metrics presented very similar tendencies, NRMSE performance was only shown in the first part of the results and the SSIM index was used for the rest of the study.

Furthermore, to quantitatively represent the targeted image quality, we selected an arbitrary SSIM threshold denoted by Q_0 whose value was set to 0.9 as this is considered to convey a fair image quality (Zanforlin et al., 2014). A correspondence between SSIM scores and Mean Opinion Scores (MOS) is displayed in Table 2.2.

2.3.3 Experimental validation with MRI acquisitions

MR acquisitions were performed on a 7 Tesla Siemens scanner (Siemens Healthineers, Erlangen, Germany), with a 1-channel transmit and 1-channel receive coil (InVivo Corp., Gainesville, FL, USA) to provide experimental noisy data for retrospective undersampling. An *ex vivo* baboon brain conserved in a fluorinert solution was imaged with a

TABLE 2.3: Parameters of T_2^*-weighted GRE sequence used for experiments.

Parameters	Values
Repetition time (TR)	60 ms
Echo time (TE)	30 ms
Flip angle (FA)	10°
Slice thickness (SL)	5 mm
Field of view (FOV)	205 mm
Total NEX for $N = 512$	15
Total NEX for $N = 1024$	82

2D T_2^*-weighted Gradient Recalled Echo (GRE) sequence. All animal studies were conducted in accordance with the European convention for animal care and the NIH's Guide for the Care and Use of Laboratory Animals. The acquisition was fully-sampled on the Cartesian grid for image sizes of $N = 512$ and $N = 1024$ and consisted of N lines collecting N Fourier samples (no oversampling). Parameters of the sequence are summarized in Table 2.3. To get a wide range of input SNR, data averaging over several measurements was performed in the Fourier domain. To reach an input SNR of 110, image sizes $N = 512$ and $N = 1024$ needed respectively a number of 15 and 82 averages, referred as to NEX (Number of EXcitations) hereafter. The resulting magnitude images of various input SNR were then retrospectively undersampled with the presented iid and radial sampling patterns.

Moreover, prospective radial acquisitions were performed for an image size of $N = 1024$ and a acceleration factor of $R = 15$ using the trajectory displayed in Fig. 2.3D). Imaging parameters were the same as for the fully-sampled Cartesian acquisition at $N = 1024$, including the NEX to vary the input SNR.

2.3.4 Dependence of SSIM scores on reference SNR

Furthermore, the influence of the reference should also be mentioned as SSIM scores are likely to change with the input SNR of the reference notably. We evaluated the impact of this parameter here, and showed that this effect is of minor concern for the considered SNR. To evaluate the influence of the input SNR of the reference $\mathbf{x}$ on the scores $\mathrm{SSIM}(\widehat{\mathbf{x}}, \mathbf{x})$ scores, the reference SNR was varied in the computation of the SSIM for a fixed reconstruction $\widehat{\mathbf{x}}$ of the analytical brain phantom with iid sampling schemes. Two cases were tested and are presented in Fig. 2.4 for (i) $N = 512$, $R = 5$ and an input SNR of 46 (black line) and (ii) $N = 1024$, $R = 10$ and an input SNR of 110 (orange line). Both curves present a stationary value as the input SNR of the reference increases. This graph shows that above an input SNR of approximately 100, the SNR of the reference no longer influences the value of SSIM scores. Noisier references do not match as well the reconstructed images probably because of the denoising effect of the nonlinear reconstructions. This result supports the use of a reference presenting an input SNR of 110 for the calculation of SSIM scores.

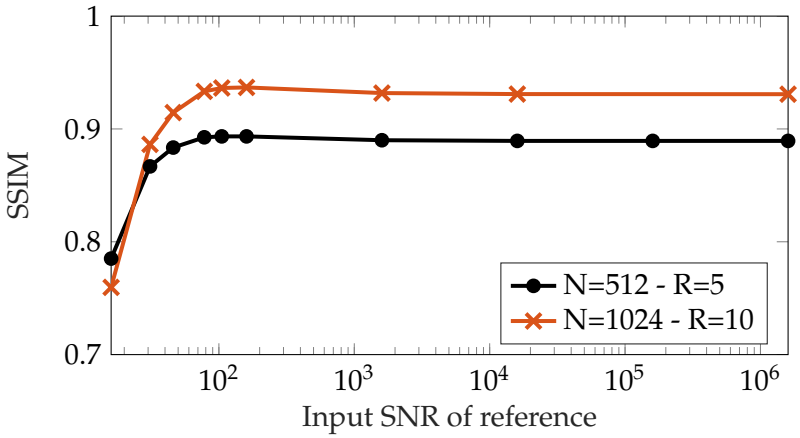

FIGURE 2.4: Influence of input SNR of the reference on the SSIM scores calculated for fixed reconstructions in the case of a 5-fold undersampled image size of $N = 512$ for an input SNR of 46 (black line) and of a 10-fold undersampled image size of $N = 1024$ for an input SNR of 110 (orange line). The logarithmic scale was used for the x-axis.

2.4 Results

2.4.1 Influence of SNR

Fig. 2.5A)-B) respectively show the SSIM and NRMSE scores as a function of the input SNR for four increasing undersampling factors, under a constant image size of $N = 1024$. For a given acceleration factor, as the input SNR gets larger the SSIM increases to an asymptotic value corresponding to the maximum score denoted by $\text{SSIM}_{lim}(N, R)$ (Fig. 2.5A). More precisely, the image quality reaches a *plateau*, as soon as the input SNR is sufficiently high. Hence, the concept of a minimum input SNR required to attain the asymptotic image quality score can be defined: once this SNR is reached, there is no gain in image quality anymore.

For the presented case $N = 1024$ and $R \in \{5, 10, 20, 30\}$, the values of $\text{SSIM}_{lim}(N, R)$ are reported in Table 2.4. As the undersampling factor grows, the corresponding asymptotic SSIM value drops. A similar but reversed trend can be observed on Fig. 2.5B) for the NRMSE index where a plateau is visible as well.

TABLE 2.4: Asymptotical SSIM values, $\text{SSIM}_{lim}(N = 1024, R)$, for $R \in \{5, 10, 20, 30\}$.

R	5	10	20	30
SSIM_{lim}	0.97	0.93	0.89	0.85

2.4.2 Influence of image size

Fig. 2.6 shows the SSIM scores as a function of the image size for four undersampling factors, under a constant intermediate input SNR of 81. For a given acceleration factor, as the image size gets larger the SSIM index increases in a concave manner. Moreover, two regimes can be identified in the dynamics of image quality scores: a high-resolution regime corresponding to large image sizes and a low-resolution regime corresponding

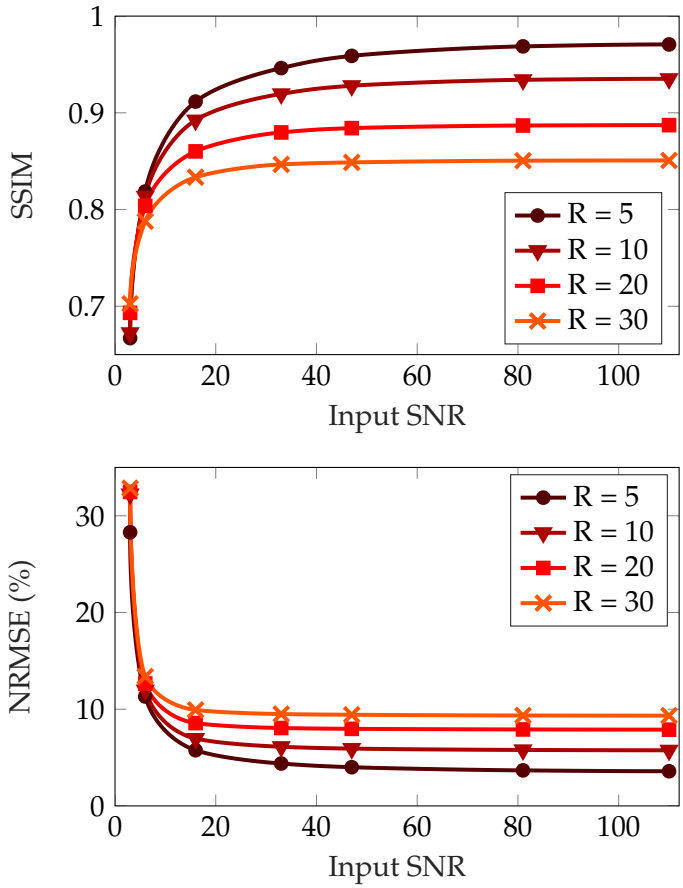

FIGURE 2.5: For a constant image size $N = 1024$, evolution of A) SSIM scores and B) NRMSE scores as a function of input SNR, for different acceleration factors of 5, 10, 20 and 30, in the case of analytical images reconstructed from iid-undersampled data. For both metrics, as the input SNR increases, the image quality improves and approaches its limit. A stationary regime is reached for high input SNR, where SSIM and NRMSE scores are approximately equal to their maximum and minimum values respectively for a given acceleration factor.

to small image sizes (the FOV is kept constant). On the one hand, for large image sizes above $N = 512$ the image quality scores are quasi invariant by change in image size and are close to their maximum value for each acceleration factor. On the other hand, for small image sizes the image quality rapidly drops to severely low scores.

Furthermore, Fig. 2.6 allows to determine the combinations of image size and acceleration factor (N, R) guaranteeing a SSIM threshold of $Q_0 = 0.9$ (dashed line) at the studied input SNR. While any undersampling factor up to $R = 30$ can be applied to an image of size $N = 2048$ and still ensure SSIM scores above 0.9, an image size of $N = 256$ cannot be accelerated more than 5 times in order to meet $Q_0 = 0.9$.

2.4.3 Maximum acceleration factor

The previous results on image size and SNR influences can be combined to determine the maximum acceleration factor allowed in a given situation, $R_{\max}(Q_0, N, \mathrm{SNR})$.

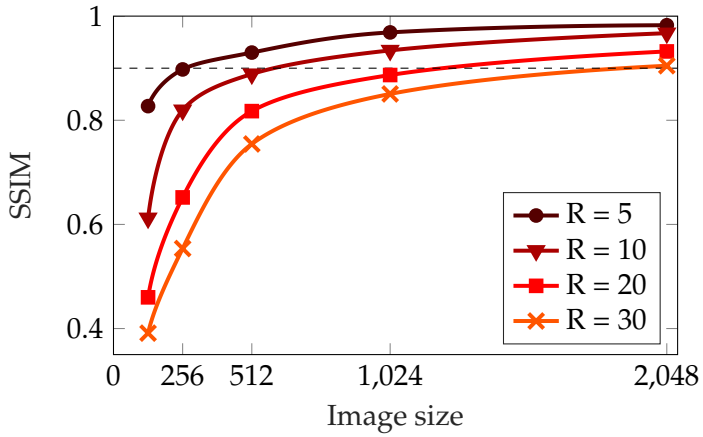

FIGURE 2.6: For a constant input SNR of 81, evolution of SSIM scores as a function of image size, for different acceleration factors of 5, 10, 15 and 30, in the case of analytical images reconstructed from iid-undersampled data. SSIM scores increase in a concave manner as the image size gets larger. Two dynamics can be distinguished: a low-resolution regime where image quality rapidly diminishes as the image size decreases and a high resolution regime where image quality remains stable as the image size gets larger. The dashed black line represented the chosen quality threshold $Q_0 = 0.9$ and highlights the combinations (N, R) of image sizes and acceleration factors which allow to maintain the targeted image quality.

A 3D map of the maximum undersampling factor allowing SSIM scores higher than $Q_0 = 0.9$ is shown in Fig. 2.7A) for the analytical phantom, as a function of image size N and input SNR. The flat aspect of the surface along the input SNR direction conveys the image quality reaching the previously observed stationary state once a specific minimum SNR has been attained. In contrast, as can be seen on the 2D projection of the surface on Fig. 2.7B), the maximum acceleration factor keeps growing as the image size increases, reaching values of 5, 8, 16 and 30 for images sizes of 256, 512, 1024 and 2048 respectively. Moreover, the natural logarithmic scale on the image size direction used on this view indicates a super-linear growth rate of $R_{\max}$ as a function of image size.

2.4.4 Acquisition intrinsic SNR and $R_{\max}$

We propose to further specify the aforementioned functional $R_{\max}$ defined on all the possible combinations of studied input SNR and image sizes, by taking into account the *acquisition intrinsic SNR* available in practice which depends on the image resolution and the considered MR sequence. Indeed, any acquisition is characterized by its sequence relaxation parameters (TR, TE, FA), resolution parameters (N, FOV, SL), the MR scanner itself and its transmitting/receiving chain including the coils, and the imaged object relaxation properties (T_1, T_2). Hence, for a particular acquisition and fixed FOV, there exists a unique relationship between the image size N and the input SNR. Graphically, this N-SNR relation can be projected onto the $R_{\max}$ surface to delineate where the maximum undersampling factor of the sequence of interest lives in practice. Fig. 2.7 shows this experimental N-SNR level line (in orange) in the case of the presented GRE sequence (see Table 2.3) which was projected on the studied domain. The 2D view of this line is depicted in Fig. 2.7B) and illustrates where the maximum acceleration factor for each image

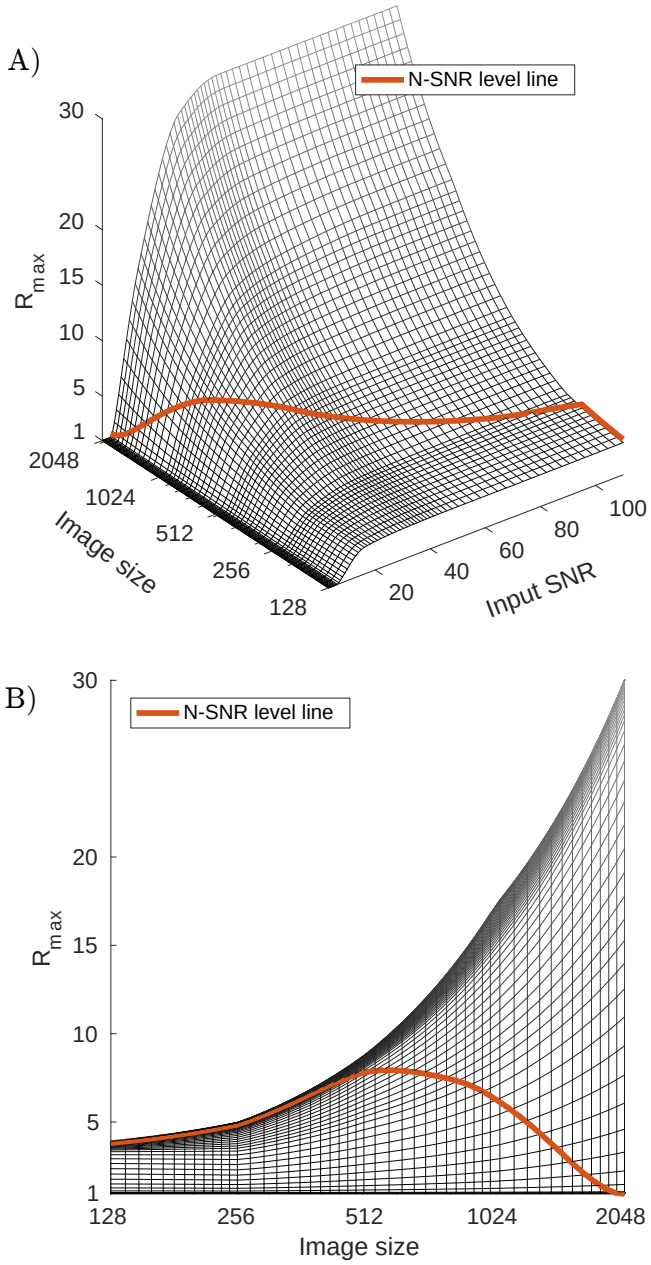

FIGURE 2.7: Analytical phantom $R_{\max}$ results in the case of iid undersampling. A) 3D view of the maximum undersampling factors allowing SSIM scores above $Q_0 = 0.9$ as a function of image size N and input SNR. B) Its 2D projection on the $(R_{\max}, N)$ plane. Knowing the image size and the available input SNR of any acquisition, the corresponding maximum undersampling factor allowing to reach the targeted image quality $Q_0 = 0.9$ can thus be derived. The experimental $N-$SNR level line (orange line) of the presented T_2^*-weighted GRE acquisition (see section III.C) was added on both graphs. It represents the projection onto the $R_{\max}$ surface of the relationship between the intrinsic SNR available in practice for this particular acquisition and the image size. For the considered sequence, only acceleration factors below the $N-$SNR level line will thus meet or exceed the targeted image quality (see B).

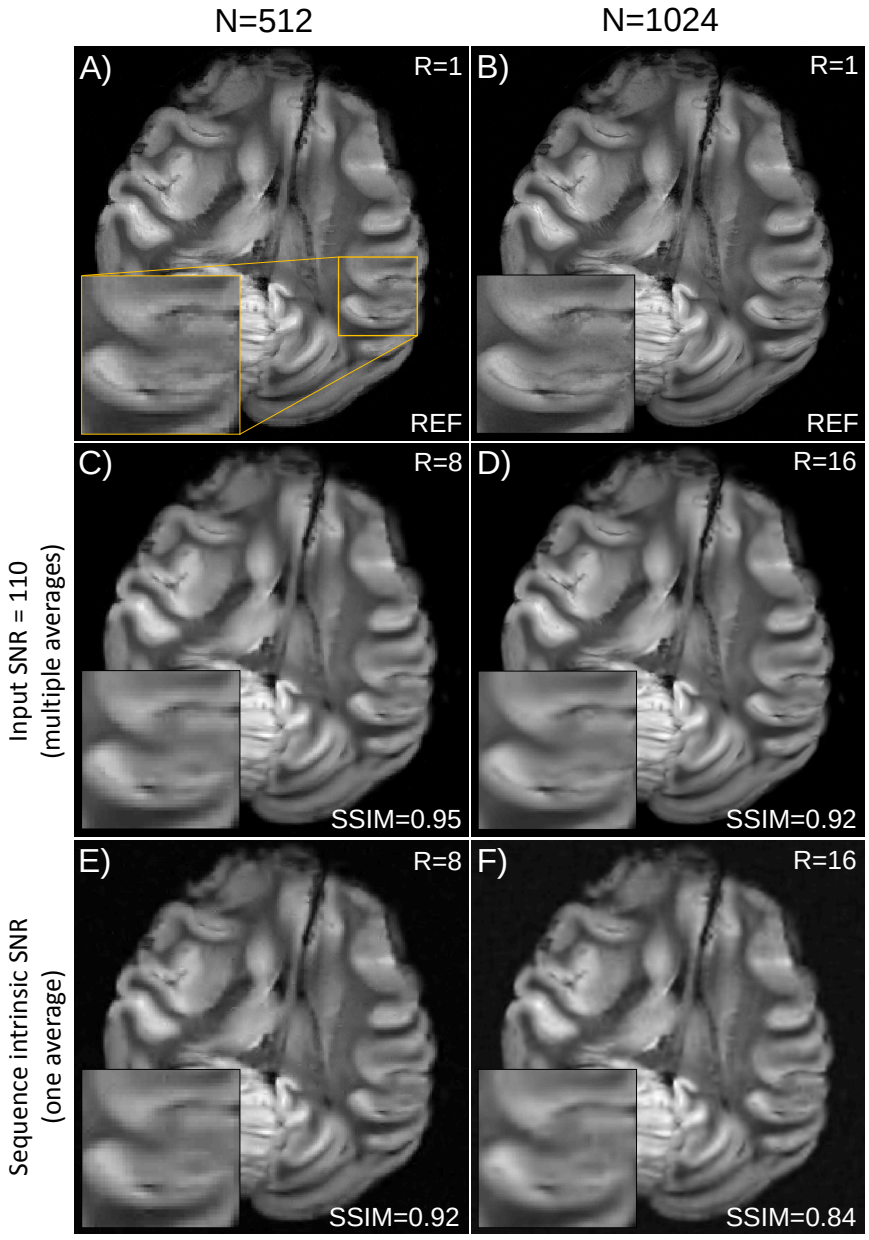

FIGURE 2.8: Results of retrospective iid-undersampling performed on experimental data acquired with a T_2^*-weighted GRE sequence (see sections III.C). Fully-sampled Cartesian reference images presenting an input SNR of 110 for $N = 512$ (A) and $N = 1024$ (B). A 2x-zoom displaying a folded pattern in the baboon cortex of visual interest has been added in the bottom left-hand corner for each image. For the intrinsic SNR of the considered acquisition (no average), reconstructions for images sizes $N = 512$ (E) and $N = 1024$ (F), which were undersampled respectively by a factor $R = 8$ and $R = 16$, are shown together with their SSIM scores calculated against their respective reference. In the case of an increased input SNR of 110 which was obtained by multiple averaging (82 and 15 NEX for $N = 1024$ and $N = 512$ respectively), reconstructions for images sizes $N = 512$ (C) and $N = 1024$ (D), accelerated respectively by a factor $R = 8$ and $R = 16$ are displayed likewise.

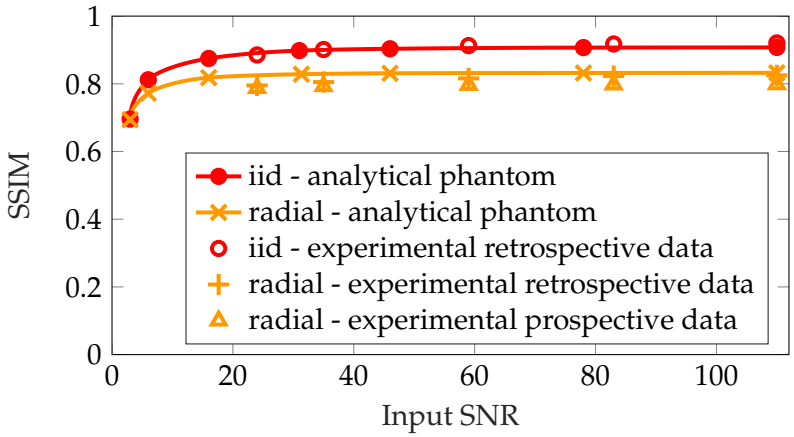

FIGURE 2.9: For an image size $N = 1024$ and an acceleration factor of $R = 15$, SSIM performance of iid (in red) and radial (in yellow) sampling schemes. Results obtained for the analytical phantom are represented by continuous lines while the experimental data on the *ex vivo* baboon brain are symbolized by discrete symbols. For radial sampling, prospectively acquired results are represented with triangles, while retrospective reconstructions on experimental data are displayed with cross signs.

size is located in practice for this particular sequence to reach the targeted image quality $Q_0 = 0.9$. This N-SNR level line interestingly presents a maximum of 8 reached for an image size of $N = 512$. More precisely, between $N = 256$ and $N = 512$, we observe that the N-SNR level line begins to deviate from the envelope of the $R_{\max}$ projection, which represents the point at which the acceleration starts to be limited by the available SNR. Hence, given the intrinsic SNR of the studied acquisition for one NEX, an 8-fold accelerated reconstruction of an image size $N = 512$ should maintain a SSIM score above 0.9 which is verified experimentally in Fig. 2.8E), whereas this is no longer ensured for a 16-fold undersampled image of size $N = 1024$ as can be seen in Fig. 2.8F). Nevertheless, if the input SNR is important enough (e.g., SNR $= 110$ as this was experimentally obtained by computing multiple averages), an acceleration factor of 16 would be feasible for an image size of $N = 1024$ and the same threshold Q_0 (Fig. 2.8D)). The increase of the input SNR to 110 for the image size of $N = 512$ expectedly increases the SSIM score up to 0.95 (Fig. 2.8C)).

2.4.5 2D radial sampling trajectories

Finally, we present the performance of conventional radial trajectories for an image size of $N = 1024$ and an undersampling factor of $R = 15$. SSIM scores are reported in Fig. 2.9 for both iid (red) and radial sampling (yellow) patterns, in the case of the analytical phantom (continuous line) and of the experimental data of the baboon brain image (discrete symbols). In the case of radial sampling, prospectively acquired results are represented with triangles, while retrospective reconstructions on experimental data are displayed with cross signs. It can be noted that retrospective and prospective quality scores are almost overlapping. Moreover, experimental scores are in good agreement with the simulated results for both retrospective and prospective data. As expected, radial trajectories are performing worse than iid sampling, with a difference of approximately 0.1 in the asymptotic SSIM scores for both experimental and simulated results.

Nevertheless, as the input SNR falls to lowest values, the gap between the two different sampling schemes shrinks to zero. Theses results illustrate how iid sampling schemes can produce near upper bounds to other 2D MR-feasible sampling trajectories such as radial readouts.

2.5 Discussion

In this empirical study, we showed how to quantitatively derive the maximum undersampling factor preserving a targeted image quality as a function of the image size and the input SNR. Hence, our results for T_2^*-weighted MRI provide quantitative guidelines on how to select subsampling factors and resolution in the framework of compressed sensing. On the one hand, our analysis quantitatively confirmed the benefits of going higher in resolution and is therefore in agreement with the presented theoretical results of CS (Section II - Fig. 2.1). By increasing the image size, larger acceleration factors can indeed be used while allowing to recover high-resolution details. Nevertheless, this enhanced performance at high resolution is in practice limited by the available SNR of the considered acquisition. We thus showed the existence of a minimum SNR that has to be reached in order to meet the expected image quality, a key feature which is not always clearly stated in previous studies in CSMRI. This $R_{\max}$ function is theoretically defined over all possible combinations of image sizes and SNRs in the studied domain, but in practice remains confined to a more restricted area owing to the intrinsic SNR limitations of a particular MR acquisition. We introduced this constraint by means of a characteristic relationship between image size and SNR. In situations where the intrinsic SNR is limiting, it may be more favorable to use a smaller accelerating factor on a lower resolution scan for optimal results.

Regarding the practical utilization of this work, our experimental results appeared to be in good agreement with simulations performed on the analytical brain phantom, which corroborates the validity of our approach to derive a maximum undersampling factor for a given acquisition-reconstruction setup. Our work may thus aid the design of undersampled 3D acquisitions using CS and even 4D MRI, even though prospective performance of compressed MR acquisitions may be slightly lower than predicted due to unconsidered MR system imperfections (e.g., eddy currents). Moreover, our comparison with experimental radial sampling performance suggests that our results may be extended to 2D acquisitions insofar as they provide close upper bounds on the maximum undersampling factor which may be approached with spiral readouts (Boyer et al., 2016). Although in practice it is not always possible to acquire the fully-sampled Cartesian image to compute the available input SNR, MR physicists could estimate their acquisition intrinsic SNR by probing the noise and signal strength in the k-space directly.

Since this study assumes a particular acquisition and reconstruction pipeline, SSIM scores generated with another setup (e.g., parallel imaging and multi-channel CSMRI reconstruction, see for instance (Liang et al., 2009; Chaari et al., 2011; Chun et al., 2016)) may lead to slightly different quality scores. However, we expect the observed tendencies and dynamics to remain similar with other methods (e.g. changes in sparsifying dictionary or algorithm), with possibly minor up- or down-shifts of the SSIM curves. If the arbitrary choice of the SSIM quality threshold is not an issue itself since any user should be able to determine the image quality of interest against a chosen reference, some limitations of the SSIM index should be pointed out. First, the comparison of scores between

different image sizes should be done carefully since the SSIM metric is not resolution-invariant: an image of size $N = 1024$ presenting a SSIM of 0.92 may look better than an image of size $N = 512$ presenting a SSIM of 0.95, as can be observed on Fig. 2.8B)-C). The explanation lies in the fact that matching a reference of higher resolution is inherently more demanding. This issue can be bypassed by adjusting the desired image quality (i.e. the threshold) to the resolution via a threshold function $Q_0(N)$. The structural characteristics of different images are also expected to influence the SSIM scores since this metric was designed to be sensitive to structural features. Nevertheless, our experimental results on a brain baboon showed SSIM scores very close to those of the analytical brain phantom despite significant structural differences between these two types of images (Fig. 2.8 and 2.9), which supports the consistency of the presented study. Although this study uses T_2^* data, it is not unreasonable to expect the same behavior and quantitative estimations for other contrast such as T_2 and T_1, but this should be confirmed with further experiments. Finally, the code and data used for this study are freely accessible on the website `cosmic.cosmostat.org/code`.

2.6 Conclusion

In the case of T_2^*-weighted MRI, our study empirically and quantitatively showed how the image quality measured with the SSIM index is affected by both input SNR and image size when Compressed Sensing alone is used to speed up MRI acquisition and how this information can be used to determine a maximum acceleration factor depending on the targeted image quality. On the one hand, our results confirmed the benefits of going higher in resolution since increasing the image size allows the use of larger acceleration factors. Nevertheless, this enhanced performance at high resolution is in practice limited by the available SNR in the considered acquisition. We showed the existence of a minimum SNR required to meet the expected image quality. Once this minimum SNR is reached, increasing the input SNR does not improve the image quality anymore. Most interestingly, we showed how to quantitatively derive the maximum undersampling factor $R_{\max}$ preserving a targeted image quality as a function of the image size and the input SNR. When the input SNR is high enough, typical $R_{\max}$ values were found to be 5, 8, 16 and 30 for image sizes 256, 512, 1024 and 2048 respectively for the considered ℓ^1-based reconstruction. In practice, this $R_{\max}$ function is however constrained by SNR limitations inherent to a particular MR acquisition and we demonstrated how our results enable to take this a priori knowledge into account. These results were corroborated by experiments performed on a 7 Tesla scanner both retrospectively and prospectively on radial data. They illustrate how the use of CS in acquisitions can be virtually limited by the available SNR when exploring very high resolution. Finally, our proposed SSIM-based method to determine the maximum acceleration factor for a particular acquisition can easily be adapted to any acquisition-reconstruction pipeline and may thus be of interest to other techniques such as parallel imaging.

Chapter 3

2D SPARKLING: k-space filling curves for accelerated MRI

In this Chapter, the SPARKLING method and results will be presented for 2D imaging. This will be preceded by a short review on existing sampling strategies used in CSMRI. In addition, we will show the results of the Local Phase Measurement (LPM) that was used on a SPARKLING shot and allowed to estimate trajectory errors on our 7 Tesla scanner.

3.1 Introduction

Magnetic resonance imaging (MRI) is one of the most powerful and safest imaging modalities for examining the human body. High-resolution MRI is expected to aid in the understanding and diagnosis of many neurodegenerative pathologies involving sub-millimetric lesions or morphological changes, such as Alzheimer's disease and multiple sclerosis (Barnes et al., 2009; Pruessner et al., 2000; Kolk et al., 2013). Although high-magnetic-field systems can deliver a sufficient signal-to-noise ratio (SNR) to increase spatial resolution (Duyn, 2012), long scan times and motion sensitivity continue hindering the utilization of high resolution MRI. Despite the development of corrections for bulk and physiological motion (Maclaren et al., 2012; Federau and Gallichan, 2016; Stucht et al., 2015; Vannesjo et al., 2015), long acquisition times remain a major obstacle to high-resolution acquisition, especially in clinical applications.

As explained in Chapter 1, the k-space is sampled along a set of parameterized curves generated by varying magnetic field gradients which have a bounded amplitude and a maximum slew rate. Hence, filling the entire k-space array may require a long time especially for high-resolution imaging. In this work, we make significant progress in accelerating the acquisition time of segmented MR acquisitions with minimum deterioration of image quality, by limiting the number of shots using efficient sampling patterns combined with compressed sensing. The proposed strategy can be used in combination with parallel imaging (Pruessmann et al., 1999; Griswold et al., 2002), yielding even more important acceleration factors.

Most MRI sampling methods are currently based on the Shannon-Nyquist theory, which relies on the use of Cartesian sampling, with the number of required samples increasing with the resolution. The newly developed theory of compressed sensing (Candès et al., 2006; Donoho, 2006; Lustig et al., 2007b) offers a promising solution for reducing the MRI scan time, since it theoretically allows for subsampling of the k-space while guaranteeing exact reconstructions. While early theoretical results were based

on concepts such as coherence or restricted isometry properties, more recent developments (Adcock et al., 2017; Boyer et al., 2016) suggest compliance with two criteria for optimal sampling:

(i) The sampling pattern should be distributed along a given variable density. In the case of MRI, low frequencies should be sampled more densely than high frequencies.

(ii) Coverage of the k-space should be locally uniform to avoid large gaps and clusters of samples.

Although seemingly unrelated, the Shannon-Nyquist and compressive sampling theories advocate for the same criteria since both methods promote *locally uniform sampling patterns* and differ only in the target density (uniform density for the Shannon-Nyquist theory and variable density for compressed sensing theory). Methods to generate sampling patterns satisfying (i) and (ii) have been extensively studied and range from simple dart throwing to Poisson disk sampling or more elaborate optimal transportation-based techniques (Dippé and Wold, 1985; De Goes et al., 2012). Nevertheless, since they do not account for hardware constraints and produce discontinuous samples, these algorithms are unable to provide sampling curves for MRI.

This limitation may explain why the 2D sampling patterns used in practice are essentially made of simple analytical models such as Cartesian lines (spin-warp imaging or EPI) (Edelstein et al., 1980; Mansfield, 1977), non-Cartesian radial spokes (Lauterbur, 1973; Bergin et al., 1991; Glover and Pauly, 1992), spiral interleaves (Ahn et al., 1986; Meyer et al., 1992) and variations of these patterns (Pipe et al., 1999; Jackson et al., 1992; Bilgin et al., 2008; Lustig et al., 2005; Wang et al., 2012). Although these geometrical curves may enable relatively rapid scanning, they do not take advantage of all the degrees of freedom offered by the hardware and lack flexibility to comply with the above optimal criteria. They may therefore be significantly improved to reduce MRI scan time.

Here, we introduce a method called SPARKLING, that may overcome these limitations by taking a radically new approach to the design of k-space sampling. SPARKLING stands for Spreading Projection Algorithm for Rapid K-space sampLING. To optimally spread the samples (criteria (i)-(ii)), our method relies on optimization to automatically generate k-space trajectories under the aforementioned hardware constraints by minimizing a tailored distance between the sample distribution and any prescribed density (for details, see Materials and Methods). Finally, to maximize sampling efficiency (i.e., the k-space coverage per unit time), we apply our algorithm to highly-sampled trajectories in the same manner as for spiral imaging (Tan and Meyer, 2009). Hence, for a given MR protocol with defined imaging parameters (TR, TE and readout duration), this method is able to enhance sampling performance.

The proposed sampling patterns were prospectively validated both *ex vivo* and *in vivo* in healthy volunteers on a 7-Tesla MR scanner for T_2^*-weighted imaging. The versatility of the method was demonstrated for various setups and target densities. In comparison to standard fully-sampled Cartesian acquisitions, our strategy significantly reduced the scan time while maintaining good image quality. Moreover, SPARKLING-generated acquisitions were compared to acquisitions obtained with two non-Cartesian sampling methods widely used in anatomical MRI, namely, radial and spiral trajectories. Using the same equally accelerated gradient echo sequence (GRE) and without additional equipment, we show that our method achieves enhanced image quality. The stability of

SPARKLING-generated acquisitions was also tested for very high in-plane acceleration factors of up to 20.

3.2 Related works: compressed sensing and sampling patterns

3.2.1 Compressed sensing and undersampled k-space trajectories

The two main ideas which guided previous designs of MRI sampling for compressed sensing were randomness or *incoherence* and variable density. This is clearly stated in the original paper of Lustig et al.: *Realistic designs for CS in MRI should have variable-density sampling with denser sampling near the center of k-space, matching the energy distribution in k-space. Such designs should also create k-space trajectories that are somewhat irregular and partially mimic the incoherence properties of pure random sampling, yet allow rapid collection of data*. Note that the original search for randomness is different from our criterion of local uniform distribution (criterion (ii)). We summarize here the most important sampling patterns developed for CSMRI.

Resorting to 3D acquisitions

If acquiring a random distribution of point-wise samples using a 2D acquisition is generally impractical, the situation improves when considering 3D acquisitions. (Fig. 3.1) displays the idea introduced by Lustig et al. to use the partition encoding dimension to acquire 3D lines whose cross-section would be the desired 2D random sampling distribution. This trick has the advantage of avoiding the design of feasible trajectories for MRI but forces to resort to 3D imaging. Practical implementations of this method were used for dynamic MRI using a Poisson disk distribution with a fully-sampled central region of the k-space as is shown in (Fig. 3.1**b**) (Vasanawala et al., 2010; Menzel et al., 2011). Note that Poisson disk sampling which yields a *locally uniform coverage* was rapidly preferred over *random* sampling. Nevertheless, this strategy has several limitations. First, from a 3D perspective, the 3rd encoding direction is sampled at least at Nyquist rate and so does not take full advantage of the potential acceleration offered by undersampling all available dimensions. Second, the efficiency of this strategy decreases as the readout duration of each shot increases. Indeed, if quickly acquiring a set of lines can be effective for short readouts and short TRs, it however becomes inefficient for longer readouts since sticking to the support of a line prevents the exploration of other parts of the k-space which could have been sampled and thus limits the amount of collected information. We will illustrate this limitation in the following chapter which deals with 3D MRI (Chapter 4).

Radial trajectories

Among all k-space trajectories, radial patterns are the most widely and successfully used in CSMRI. Radial sampling has a particular appeal for compressed sensing since the spokes of a radial acquisition naturally lead to a variable density sampling, measuring low frequencies more frequently than high frequencies. In dynamic imaging, radial spokes are typically ordered according to a golden ratio profile (Winkelmann et al., 2007), where the angle between consecutive shots is set to 111.25°. This ensures that any consecutive selection of radial spokes that are retrospectively selected yields a very good k-space coverage. In addition, each new acquisition explores a direction not covered by

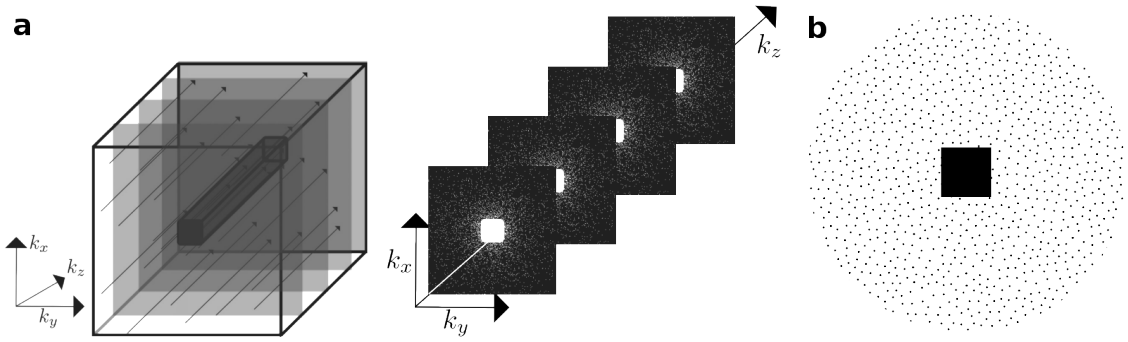

FIGURE 3.1: Lustig's method of acquiring along the 3rd direction (**a**) to perform a Poisson disk sampling (**b**) in cross-sections.

the previous profiles. Such properties not only permit robustness to motion, but allows to select a spatial and temporal resolution *after* the acquisition by varying the number of consecutive shots per image to reconstruct. This method was successfully applied in free-breathing dynamic contrast-enhanced MRI (Chandarana et al., 2013), volumetric abdominal and cardiac imaging (Feng et al., 2016; Feng et al., 2014).

Spiral trajectories

Undersampled spiral trajectories were also used for compressed sensing, as they can be designed to respect a variable density sampling. This enables to use the data collected near the k-space center for motion correction. In addition to sampling efficiency, they also present non-aliased artifacts. In clinical imaging, spiral sampling has been applied in 4D flow imaging with CS-PI reconstruction (Dyvorne et al., 2014) and fMRI (Holland et al., 2013).

Adding randomness to existing trajectories.

Following Lustig's idea that randomness was desirable for compressed sensing, a few works sought to add 'random-like' perturbations to existing sampling patterns such as radial (Bilgin et al., 2008; El-Metwally et al., 2008) or spiral (Lustig et al., 2005; Lustig et al., 2008a; Wang et al., 2012; Pang et al., 2014) trajectories. Some of them are displayed in (Fig. 3.2). For instance in (Lustig et al., 2008a), the spiral is perturbed in the radial direction by a randomly generated smooth waveform (see Fig. 3.2**c**). Then, the gradient waveform is found by solving a time-optimal control problem subject to hardware constraints. One drawback of this method is that the k-space trajectory and the gradient waveforms are designed separately, so that the final sampling distribution is not truly controlled. It has however the advantage of being simple and rather fast when not too many samples are used.

3.2.2 Previous optimization-driven sampling designs

In the literature of sampling trajectories for MRI, a few works addressed the problem of optimizing k-space coverage using computational techniques. These methods must be distinguished from two-step approaches which design the k-space trajectory and the gradient waveform separately such as the time-optimal control method we just mentioned (Lustig et al., 2008a). These optimization-driven sampling design were already

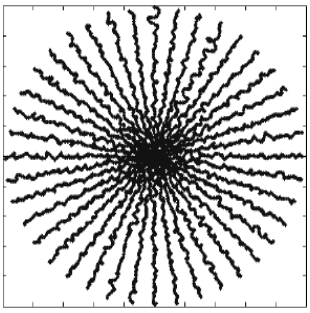

(a) El metwalli et al. (El-Metwally et al., 2008)

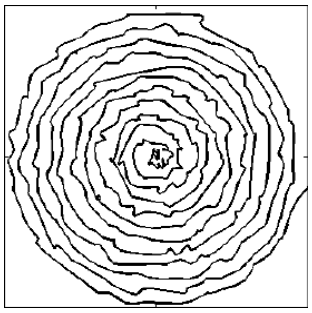

(b) Pang et al. (Pang et al., 2014)

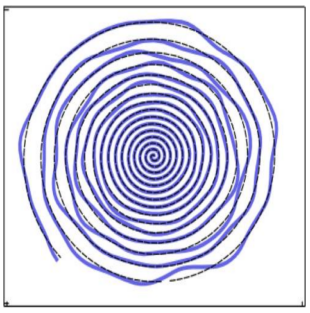

(c) Lustig et al. (Lustig et al., 2008a)

FIGURE 3.2: Different examples of "random-like" perturbations applied to radial and spiral trajectories.

presented in Chapter. 1. We highlight here the limitations of these approaches and how they differ from the proposed SPARKLING method (Boyer et al., 2016).

In the works of (Kumar Anand et al., 2008; Curtis and Anand, 2008), as the authors state themselves, this method is *heuristically-optimized* as it is not established on any clear sampling theory and advocates randomness in contrast to the SPARKLING approach. Furthermore, the algorithms relying on techniques used for missile guidance (Mir et al., 2004; Spiniak et al., 2005) sought to satisfy Shannon's sampling theorem, i.e., to cover the k-space uniformly and is therefore not adapted to variable-density sampling. Finally, the Bayesian methods proposed in (Seeger et al., 2010; Ravishankar and Bresler, 2011; Liu et al., 2012), also present some limitations. First, these methods use a set of predefined trajectories, and so are unable to produce original trajectories which differ from the chosen preset. Moreover, these techniques deviate from existing sampling theories in contrast to the SPARKLING method.

3.3 Design of SPARKLING trajectories

The flowchart describing our method is depicted in (Fig. 3.3). Any segmented pattern (feasible or not) may serve as an initialization of the proposed pipeline and be transformed into a feasible k-space trajectory with a truly controlled density and optimized k-space coverage. Gradient waveforms are defined as a set of discrete gradient amplitudes that are spaced across a given gradient sampling period, defined as the *raster time*. The latter is fixed and typically equal to $dt = 10\ \mu s$ on the actual MR gradient coils. The support of a k-space trajectory is thus determined by its gradients steps and will be sampled at the desired sampling rate, also referred to as the readout bandwidth (rBW $= \frac{1}{\Delta t}$, where Δt is the interval between digitized samples, also called the dwell time in the MRI field). The key aspect of our method is optimization, in which the samples are optimally distributed in the non-Cartesian k-space, following criteria (i)-(ii). When using compressed sensing, since the selection of the target density proved to be important for optimal results, we incorporated in our method a density generator that adapts to the resolution and the number of samples. Finally, the method allows for handling of additional linear constraints such as passage through the origin of the k-space at a given time (the *echo time*), which is crucial for controlling the image contrast.

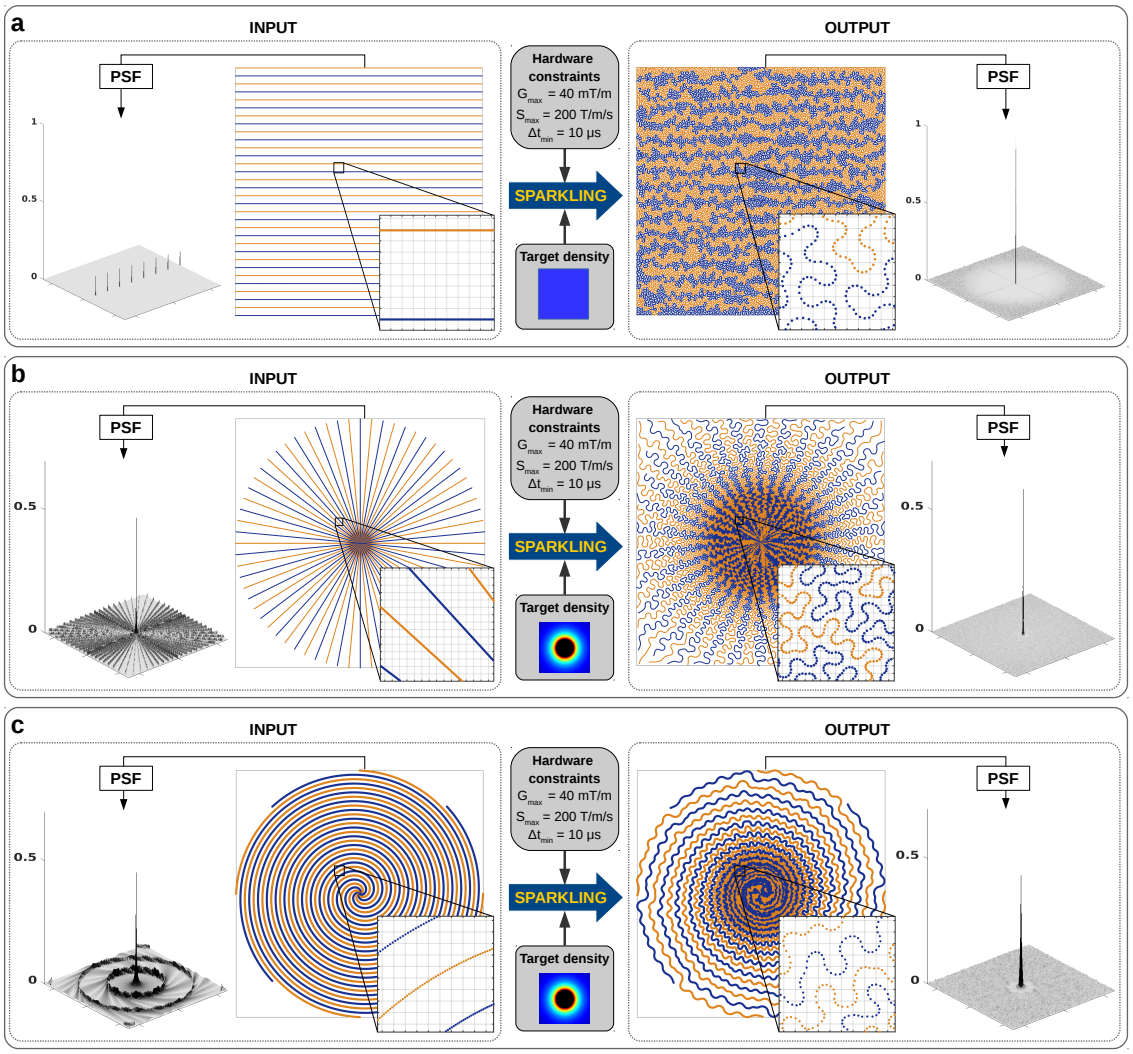

FIGURE 3.3: **Generation of SPARKLING trajectories for different initializations and target densities**. The maximum gradient amplitude and slew rate were $G_{max} = 40\,\mathrm{mT/m}$ and $S_{max} = 200\,\mathrm{T/m/s}$, respectively. The duration of each segment was 30.72 ms, and the readout bandwidth was taken equal to the gradient bandwidth (rBW = $\mathrm{BW}_{\mathrm{gradient}} = 100$ kHz). **a**, The SPARKLING method applied to Cartesian lines with uniform density for $N = 256$ and 32 segments ($AF = 8$, $R = 0.66$). **b**, The SPARKLING method applied to radial spokes with variable radial density for $N = 512$ and 34 symmetric segments ($AF = 15$, $R = 2.5$). **c**, The SPARKLING method applied to centered-out Archimedean spiral initialization with variable radial density for $N = 256$ and 8 segments ($AF = 32$, $R = 2.66$).

3.3.1 A projection algorithm on measure sets

The algorithm of SPARKLING trajectories is based on the theoretical work presented in (Chauffert et al., 2017; Chauffert et al., 2016), from which an iterative algorithm was

derived to comply with criteria (i)-(iii). A k-space trajectory is usually composed of several segments $\boldsymbol{k}(t)$, also referred to as shots, which are controlled by magnetic field gradients $G(\tau)$ as follows :

$$\boldsymbol{k}(t) = \frac{\gamma}{2\pi} \int_0^t G(\tau) d\tau \tag{3.1}$$

Hardware constraints on the maximum gradient amplitude (G_{max}) and slew rate (S_{max}) induce limitations in trajectory speed and acceleration. These limits can be expressed as inequality range constraints on each of the time points of the discrete waveform $\boldsymbol{k}[i]_{1 \leq i \leq N}$:

$$\|\dot{\boldsymbol{k}}[i]\| = \left\| \frac{\boldsymbol{k}[i] - \boldsymbol{k}[i-1]}{\delta t} \right\| < \frac{\gamma}{2\pi} G_{max} \tag{3.2}$$

where δt is the gradient raster time. Note that the gradient raster may be different from the dwell time Δt but, in what follows, we set $\Delta t = \delta t$. The constraint on the discrete trajectory acceleration is expressed likewise:

$$\|\ddot{\boldsymbol{k}}[i]\| = \left\| \frac{\boldsymbol{k}[i-1] - 2\boldsymbol{k}[i] + \boldsymbol{k}[i+1]}{\delta t^2} \right\| < \frac{\gamma}{2\pi} S_{max} \tag{3.3}$$

Following our previous work (Boyer et al., 2016; Chauffert et al., 2017), our objective is to minimize the distance between a target density π and a sample distribution $\boldsymbol{k}$ under the aforementioned constraints :

$$\min_{\boldsymbol{k} \in \mathcal{Q}_p} dist(\pi, \nu(\boldsymbol{k})) = \min_{\boldsymbol{k} \in \mathcal{Q}_p} \frac{1}{2} \|h \star (\nu(\boldsymbol{k}) - \pi)\|_2^2 \tag{3.4}$$

where h is a continuous interpolation kernel, $\nu(\boldsymbol{k})$ is the probability measure supported by the curve $\boldsymbol{k}$ and $\mathcal{Q}_p$ is the set of admissible curves, i.e., respecting the aforementioned constraints.

The distance in Eq. (3.4) can be conveniently rewritten by expanding the L^2-norm into (details not shown):

$$\min_{\boldsymbol{k} \in \mathcal{Q}_p} \underbrace{\frac{1}{N^2} \sum_{1 \leq i,j \leq N} H(\boldsymbol{k}[i] - \boldsymbol{k}[j])}_{F_r(\boldsymbol{k})} - \underbrace{\frac{1}{N} \sum_{i=1}^{N} \int_\Omega H(x - \boldsymbol{k}[i]) \pi(x)\, dx}_{F_a(\boldsymbol{k})} \tag{3.5}$$

where H is a well-chosen radial function (e.g. $H(x) = \|x\|_2$) (Boyer et al., 2016; Schmaltz et al., 2010). (Problem 3.5) can be interpreted as the minimization of a potential energy $F = F_r - F_a$ containing an attractive term F_a (bringing together samples according to the target density) and a repulsive term F_r (avoiding the formation of gaps and clusters of samples). After calculation of the derivatives of these two terms giving a gradient f_i at iteration i, this non-convex cost function can be minimized by a projected gradient descent of the type $\boldsymbol{k}_{t+1} = \Pi_{\mathcal{Q}_p} (\boldsymbol{k}_t - \beta_t \nabla F(\boldsymbol{k}_t))$, which alternates between a non-convex distance minimization part and a projection onto the convex MR constraints. See Appendix A for more mathematical details or refer to (Boyer et al., 2016; Chauffert et al., 2017).

The SPARKLING algorithm's bottleneck lies in the calculation of repulsive term F_r between the samples in Eq. 3.5 and its gradient, where there is a summation over all the samples. The naive approach to compute this gradient is to directly use the explicit formula, at the cost of a high complexity in $O(m^2)$, where m is the total number of samples.

Here in 2D, this summation is performed via a fast NFFT-based summation (Potts and Steidl, 2003; Keiner et al., 2009a; Teuber et al., 2011), that allows to significantly accelerate the computation. Compared to the previous works (Chauffert et al., 2017; Chauffert et al., 2016), we accelerated the convergence by using a Barzilei-Borwein (BB) step size rule (Barzilai and Borwein, 1988), allowing to double the algorithm speed. This method is motivated by Newton's method but does not compute the Hessian. At nearly no extra cost over the standard gradient method, the BB method is often found to significantly outperform the standard gradient method just using a special steps size β_i at iteration i of the form:

$$\beta_i = \frac{< \Delta \boldsymbol{k}, \Delta \boldsymbol{f} >}{< \Delta \boldsymbol{f}, \Delta \boldsymbol{f} >}, \tag{3.6}$$

where $\Delta \boldsymbol{k} = \boldsymbol{k}_t - \boldsymbol{k}_{t-1}$ and $\Delta \boldsymbol{f} = \boldsymbol{f}_t - \boldsymbol{f}_{t-1}$, where $\boldsymbol{f}_t = \nabla F(\boldsymbol{k}_t)$.

Importantly, all segments of an output SPARKLING trajectory are generated simultaneously using a multi-scale algorithm, which first decimates the number of samples by a dyadic factor (e.g., a factor 4), spread these fewer samples before interpolating them by a factor, and so on until reaching the desired number of samples. This multi-scale approach proved to fasten and stabilize the algorithm, as its runs faster with fewer samples and fewer iterations are needed for the last scales.

Altogether, this non-Cartesian algorithm was implemented on Matlab (Release 2015b, the MathWorks Inc., Natick, MA, USA). Typically, to generate the k-space trajectory in (Fig. 3.3a) (N=256, 32 shots, 3072 gradient points per shot, 5 decimation levels), the computation time was about 10 minutes on a Intel dual Core i7-5600U CPU running at 2.60 GHz with 16GB RAM.

The considered hardware constraints were $G_{max} = 40$ mT/m and $S_{max} = 200$ T/m/s for the gradient and the slew rate respectively. For T_2^*-weighted imaging, the readout time was set to 30.72 ms, corresponding to 3072 gradient samples. (Fig. 3.12a) displays the SPARKLING trajectory composed of 16 spokes of 3072 samples used to produce the brain image in Fig. (3.14b), corresponding to a 16-fold acceleration for an image size of 256×256.

3.3.2 High receiver sampling rate

To take full advantage of the curves' flexibility and maximize sampling efficiency, it seems natural to sample at least at the same rate as the gradient bandwidth. The same idea guides spiral acquisitions, where a high sampling rate is used to rapidly sweep over a large portion of the k-space (Cline et al., 2001; Tan and Meyer, 2009). Although a higher readout bandwidth practically increases the amount of noise per sample, the resulting additional information collected is theoretically more advantageous (Daubechies and DeVore, 2003).

More importantly, one has to keep in mind that although k-space trajectories traverse a continuous path, the signal is sampled only at discrete intervals along the path. Because of the underlying bandlimiting filters of MR receiver hardware, the measured information is essentially averaged over pieces of trajectories comprised between two sampled points (Bernstein et al., 2004; Cho, 1993; Ansorge and Graves, 2016). This explains why the per sample SNR increases as the bandwidth decreases, but it comes at the expense of a lower resolution in the k-space. Hence, it is necessary to incorporate a third criterion in our trajectory design to minimize these filtering effects:

(iii) For each individual shot, assuming a certain sampling rate rBW, the k-space path between two consecutive samples should be smaller than the size of a k-space pixel $\Delta k = \frac{1}{\text{FOV}}$, where FOV is the field-of-view.

Criterion (iii) can easily be incorporated into the algorithm by adjusting the speed limitation to:

$$\|\dot{\boldsymbol{k}}[i]\| < \min\left(\frac{\gamma}{2\pi} G_{max}, \frac{1}{\text{FOV} \cdot \Delta t}\right) \tag{3.7}$$

This additional requirement tends to straighten the trajectories, since they are designed so that consecutively acquired samples remain close to each other in the k-space. To relax this side effect, the readout sampling rate should therefore be chosen as large as possible. Indeed, as the sampling rate increases, more and more circumvolutions are permitted to fill the k-space, as is illustrated in (Fig. 3.4). Hence, using a high sampling rate allows for improvement of the resolution in the k-space, which is critical in the case of our non-Cartesian winding trajectories (see more discussion in Materials and Methods).

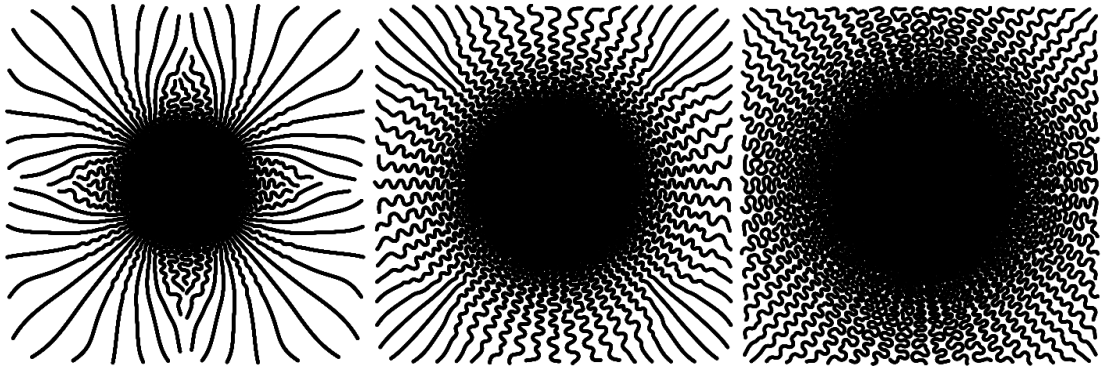

FIGURE 3.4: **Evolution of SPARKLING patterns as a function of the readout sampling rate**. Radial-initialized SPARKLING trajectories composed of 34 shots were generated for three growing readout sampling rates. From left to right, the readout bandwidth (rBW) is equal to 25 kHz, 50 kHz and 100 kHz respectively. Because the k-space path between two consecutive samples acquired along an individual shot is constrained to be smaller than the size of a k-space pixel ($\Delta k = 5\ m^{-1}$), the trajectories become more flexible and space-filling as the rBW increases. Excluding the readout sampling rate, all other parameters were kept constant and the same radially decaying target density was used. The readout duration was 30.72 ms, corresponding to 3072 gradient steps (displayed on the figures) per individual shot ($\text{BW}_{\text{gradient}} = 100$ kHz). The considered imaging matrix was 512×512, corresponding to a resolution of 390 μm $\times$ 390 μm.

The selection of the readout bandwidth is traditionally based on the Shannon-Nyquist criterion. Although matching Shannon's rate exactly does not convey stable reconstructions, it is well known that a small oversampling allows to design improved and stable linear reconstructions (Aldroubi and Gröchenig, 2001). This explains why Cartesian trajectories for instance are usually sampled at twice the Shannon's rate. In the framework of linear reconstructions, using a higher bandwidth would arguably be unproductive because of the resulting higher computational burden. However, in the context of non-Cartesian sampling and nonlinear reconstructions, one faces the following dilemma: is it better to use a large sampling period, allowing to increase the per sample SNR or a

shorter sampling period, yielding a larger number of noisier samples? In view of recent theoretical findings (Daubechies and DeVore, 2003), we argue below that the latter solution should be preferred, especially in the case of our optimized trajectories. Although it is not clearly stated, the same idea seems to drive spiral acquisitions, where a high sampling rate is often used to rapidly sweep over a large portion of the k-space (Cline et al., 2001; Tan and Meyer, 2009). First, by increasing the bandwidth, the total number of samples is also larger, bringing additional valuable information for nonlinear reconstructions. More importantly, although the path traced out by k-space trajectories is continuous, the signal is sampled only at discrete intervals along the path. Because of the underlying bandlimiting filters of MR receiver hardware, the measured information is essentially averaged over short pieces of the continuous trajectories (Bernstein et al., 2004; Cho, 1993; Ansorge and Graves, 2016). The question is then: should SNR be preferred over k-space resolution? In view of the recent progresses in the field of nonlinear denoising (Chatterjee and Milanfar, 2010), the answer seems to favor k-space resolution: it is usually much easier to denoise data than solve complex deconvolution problems. There are however two practical reasons which may limit the bandwidth. First, a higher bandwidth produces more data which are harder to store and analyze. Fortunately, this aspect is mitigated by the use of massively parallel architectures such as GPUs. Second, since the ADC produces quantized data, it is critical to remain above the quantization step. In view of these arguments, we therefore set the sampling bandwidth equal to the gradient bandwidth, allowing to take full advantage of our erratic trajectories. Altogether, in all our experiments, we acquired the ADC samples at a rate of 100 kHz, which is equal to the gradient bandwidth: ADC samples and gradient samples are thus superimposed. Because MR data are sampled at a high rate and samples are optimally spread along a variable density adapted to compressed sensing, the proposed method allows to maximize the amount of information measured per shot, and thus to reduce the large number of shots needed for high resolution imaging. Hence, very high acceleration factor AF can be achieved while maintaining a relatively low subsampling factor R. R and AF are defined with respect to the fully sampled Cartesian acquisition (ground truth image), leading to the formulas $R = n/m$ and $AF = N/n_c$, where $n = N \times N$ is the number of pixels in the image, m is the number of collected Fourier samples and n_c is the number of shots.

3.3.3 Target density

In this work, we address radially symmetric densities for the most part. The rationale for this choice is that we aimed to design sampling patterns that are *rotation and translation invariant*, i.e., that are capable of reconstructing images independently of arbitrary rigid transforms. This choice might be arguable since i) the organs (e.g., brain) are usually oriented in a unique position and ii) the sparsifying transform that we chose is not rotation invariant. However, the invariance requirement seems important for the design of *universal* sequences adapted to any organ.

In the situation in which all segments of a k-space trajectory pass through the origin at a given echo time, the sample density at the origin is excessively high. Our objective was to provide a method to generate target densities that mitigate this effect.

Considering n_c segments crossing the origin with a maximum speed α, the minimal density in the center of the k-space is that of the radial trajectories at the maximum speed (see Fig. 3.5a). The density of the radial curves at a constant speed is of type $f(k) = \frac{c}{|k|}$ for a certain c (at least asymptotically as n_c increases). However, this is only true

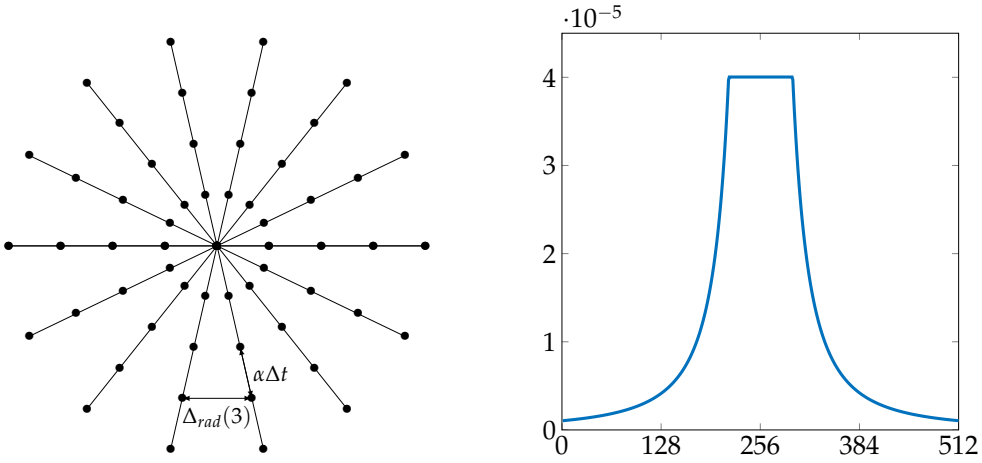

FIGURE 3.5: **Design of the target density**. (Left), The most rapidly vanishing density in the center of the k-space corresponds to the radial trajectories at the maximal speed. (Right), A representative density generated by our algorithm for N=512, $n_c = 34$, $d = 2$, $\tau = 0.5$, $\Delta t = 10$ µs, $\alpha = \gamma G_{max}$ and $G_{max} = 40$ mT/m.

within a given disk D_{r_0} of radius r_0 that we wish to determine. In practice, the distance between two circularly adjacent samples (denoted $\Delta_{rad}(j)$ for the j_{th} sample from the center) should be smaller than $\tau\Delta k_0$, where $\tau \in (0, 1]$ and $\Delta k_0 = \frac{1}{FOV}$ is the size of a k-space pixel. Nyquist's theorem suggests taking $\tau = 1$, but selecting a lower value ensures more stability, as it allows the use of smooth interpolation functions (Daubechies and DeVore, 2003). The condition on two circularly adjacent samples $\Delta_{rad}(\bar{j}) \leq \tau\Delta_{k_0}$ therefore gives $r_{\min} = \bar{j}\alpha\Delta t$, where Δt is the sampling interval and the index $\bar{j}$ is given by:

$$\bar{j} = \left\lceil \frac{\tau\Delta_{k_0}}{\alpha\Delta t_{min}\sqrt{2 - 2\cos(\pi/n_c)}} \right\rceil . \tag{3.8}$$

Furthermore, to determine the density inside the disk D_{r_0}, we use the fact that the total mass of the density inside the disk should be $\frac{n_c(\bar{j}+1)}{m}$, where m is the total number of samples. The value of constant c defining the density f should be such that:

$$\int_{B_0^{r_{\min}}} f(k)\, dk = \frac{n_c(\bar{j}+1)}{m}, \tag{3.9}$$

i.e.,

$$c = \frac{n_c(\bar{j}+1)}{m \int_{B_0^{r_{\min}}} \frac{1}{|k|}\, dk}. \tag{3.10}$$

Finally, we get:

$$f(k) = \frac{n_c(\bar{j}+1)}{m 2\pi r_{\min}|k|}. \tag{3.11}$$

Given, an initial target density $\nu : k \mapsto \frac{1}{|k|^d}$, a value τ and the parameters describing the trajectory α, n_c and Δt, we generate an algorithm that returns a new target density π complying with the following three constraints:

1. Inside the disk D_{r_0}, $\pi = f$. Since the analytic expression of f was derived, it suffices to set $\pi(I) = f(I)$, where I is the set of indices with $|k| \leq r_{\min}$.

2. Two samples outside this disk should be separated by a distance greater than $\tau\Delta k_0$. The mean number of samples inside a pixel x of edge length Δ_{k_0} is $n_s\pi(x)$. If the samples are uniformly distributed in the pixel, the mean distance between adjacent pixels is $\frac{\Delta_{k_0}}{\sqrt{n_s\pi(x)}}$; we aimed for this distance to be greater than $\tau\Delta_{k_0}$. This means that π should satisfy:
$$\pi(x) \leq \frac{1}{n_s\tau^2} = \pi_{\max}. \tag{3.12}$$

3. π should be proportional to ν when possible. To satisfy this criterion, we designed an iterative algorithm as follows:

   - While $\max(\pi(I^c)) > \pi_{\max}$
     - Find $J = \{k \in I^c, \pi(k) > \pi_{\max}\}$.
     - Set $\pi(J) = \pi_{\max}$.
     - Normalize π in $I^c \setminus J$.

For simplicity, we assumed that π is constant on each pixel of edge size Δk_0.

3.3.4 Resulting trajectories

Uniform sampling

To illustrate the versatility of the proposed approach, we first consider a uniform density without undersampling for an acceleration factor of $AF = 8$ and an imaging matrix of 256×256. Classically, the fully sampled Cartesian acquisition would measure 512 samples (oversampling factor of 2) along 256 Cartesian lines to fill the k-space grid. (Fig. 3.3a) displays how our process transforms an initial Cartesian trajectory composed of 32 parallel lines, which corresponds to $AF = 8$. Here, the considered readout duration is 30.72 ms, corresponding to 3072 samples (rBW = $\text{BW}_{\text{gradient}} = 100$ kHz), with the idea to perform T_2^*-weigthed acquisitions (Mainero et al., 2009). Our optimization algorithm deforms these straight lines and uniformly scatters the non-Cartesian samples along highly sinuous curves. In this case, despite high acceleration ($AF = 8$), the acquisition is not subsampled ($R = 0.66$).

Variable-density sampling

Above all, the most important benefit of our strategy where the largest acceleration factors are attained lies in the use of variable densities. Hence, in the context of compressed sensing, our approach can substantially improve robustness to subsampling by complying with criteria (i)-(ii). The results of such variable-density k-space trajectories are presented for a radial initialization in (Fig. 3.3b) and for an Archimedean spiral initialization in (Fig. 3.3c). In both cases, the input initializations did not originally comply with the gradient hardware constraints, the target density was radially decreasing, and the considered readout duration was also 30.72 ms. (Fig. 3.3a-c) also displays the point spread functions (PSFs) of both the input and output k-space trajectories, defined as the modulus of the Fourier transform of the sampling pattern viewed as a set of Dirac impulses. This result shows how the proposed method improves the PSF properties by

transforming coherent patterns that are sources of artifacts into incoherent noise, which is easily removed with nonlinear reconstructions. The output central peak is also better defined than initially and is surrounded by a low-energy annulus, yielding higher image quality (Nayak and Nishimura, 1998; Tsai and Nishimura, 2000).

3.4 Is the gradient system able to accurately perform these complicated waveforms?

Before engaging into prospective image acquisitions using the SPARKLING trajectories, we wanted to verify that the gradient system would be able to play out such complex gradient waveforms. Fig. 3.6 displays the gradient and slew rate waveforms for a SPARKLING trajectory.

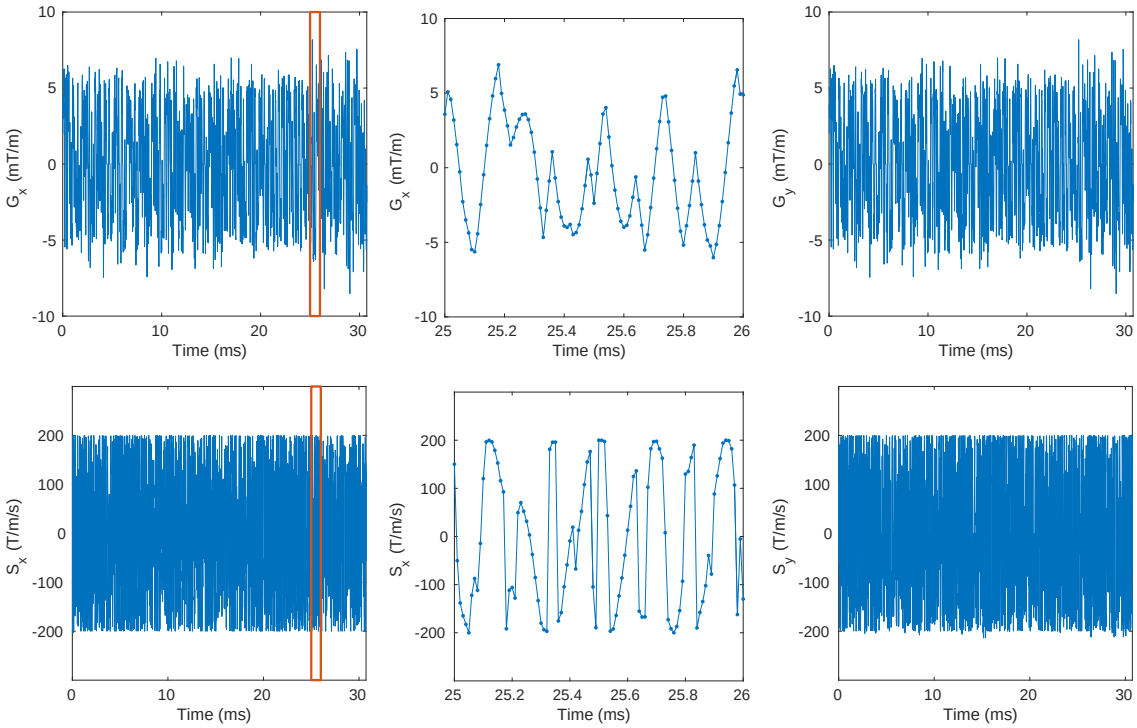

FIGURE 3.6: Gradient (left) and slew rate (right) in the x-axis of a uniform-density SPARKLING trajectory composed of 32 shots.

3.4.1 Simple estimation using a GIRF

To have an idea of how well the gradient system will be able to perform the SPARKLING trajectories, it is reasonable to model the gradient system as linear and time-invariant (LTI) (Brodsky et al., 2009). Under this assumption, the gradient system's behavior is fully described by its impulse response functions, which are called the gradient impulse response functions (GIRF) (Vannesjo et al., 2013). Given the general low-pass characteristics of gradient coils and amplifiers, the self-term GIRFs ($x-x$, $y-y$, $z-z$) can be approximated by low-pass filters.

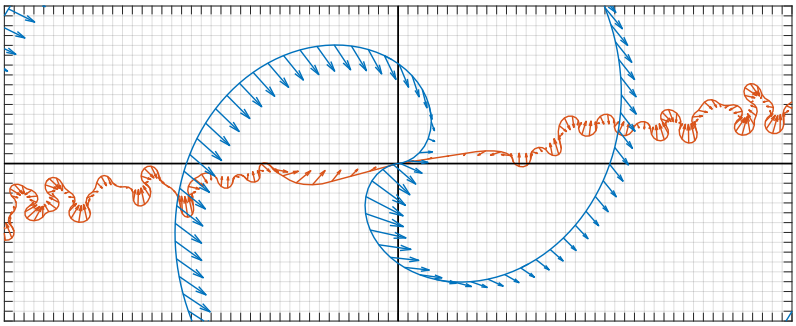

FIGURE 3.7: **Effects of low-pass filtering on spiral and radial-initialized SPARKLING shots**. To simulate trajectory errors, the gradients corresponding to an individual segment of a spiral trajectory (in blue) and a sparkling trajectory (in orange) were filtered with the same low-pass filter. A magnified region of the center of the k-space shows the nominal trajectories and the corresponding error vectors represented as arrows. Compared to the simulated trajectory errors of the spiral, the ones of SPARKLING are of smaller magnitude and present random directions. The gridded background corresponds to the Cartesian grid for the considered FOV.

Fig. 3.7 shows the effects of low-pass filtering on one shot of the spiral (in blue) and the radial-initialized SPARKLING (in orange) trajectories. These shots were selected from the 20-fold accelerated trajectories used for the *in vivo* prospective experiments (Fig. 3.16). After bilateral zero-padding of the corresponding gradient waveforms in the time domain, a low-pass constant kernel of width 20 was applied to the input gradients by multiplication in the Fourier domain as described in (Vannesjo et al., 2015). After inverse discrete Fourier transform, the output trajectories were obtained by time integration. The simulated errors are represented as arrows departing from the nominal trajectories in a magnified region of the k-space center. The error vectors tend to point in the direction of the inward-pointing normal. Compared to the spiral errors, the SPARKLING ones are not only smaller in magnitude but also present random directions. This simple experiment provides an insight on why the SPARKLING patterns may be less sensitive to gradient errors than spiral patterns, even though a full validation would require a dynamic field camera such as (De Zanche et al., 2008).

3.4.2 Trajectory measurement with a Local Phase Measurement (LPM)

To get an even better appraisal of the practical trajectory, we used the LPM method described in Section 1.5.3 for one shot of a particular SPARKLING trajectory.

Materials and Methods

A SIEMENS mini-FLASH sequence was adapted to perform the LPM. All acquisitions were done on a 7-Tesla MR scanner (Siemens Healthineers, Erlangen, Germany) with a single-receiver coil. The considered trajectory displayed in Fig. 3.8 corresponds to a matrix size of 256×256 and field-of-view of 205 cm. It is composed of 8 shots, each lasting 32.76 ms. We applied the LPM method to one of the shots highlighted in orange in Fig. 3.8. Remembering the requirements of the LPM, a matrix size of 512×512 was considered for a field-of-view of 256 cm. Repetition time was 40 ms, echo time 4.44 ms,

flip angle 30° and dwell time of 4 μs. A marcol ball phantom of diameter 20 cm was used and the acquisition was in the coronal plane. Regarding the phase reconstruction, a mask of radius 6 cm was applied to the complex images before polynomial expansion of the phase up to an order 4 as explained in Chapter 1.

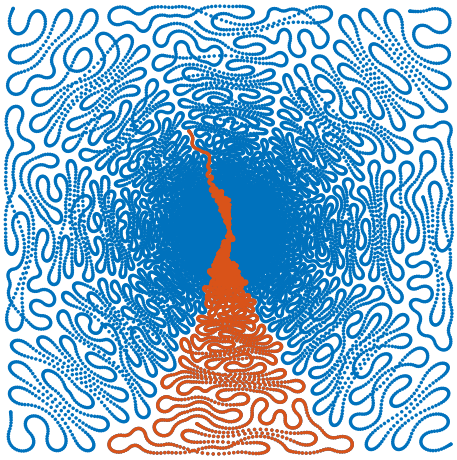

FIGURE 3.8: SPARKLING trajectory. The individual shot used for the LPM is highlighted in orange.

Results

The result of the LPM acquisition for the linear term x, which corresponds to the gradient waveform along the x-axis, is displayed in Fig. 3.9**a** for the total duration. On this scale, the prescribed gradient (blue continuous line) and the measured gradient (orange dashed line) seem to be superimposed on each other. On the same figure, a black window delineates the extent of the magnified region displayed in (Fig. 3.9**b**). Now, it is possible to observe the differences between prescribed and measured waveforms. The measured gradient never reaches the local extrema of the prescribed gradient, conveying the low-pass characteristics of the gradient system. Moreover, very small variations present in the prescribed waveform are smoothed out in the measured one.

Then, the k-space trajectory was reconstructed using the measured gradient information and is displayed (orange dashed line) in (Fig. 3.10). The measured and prescribed (blue continuous line) trajectories are almost overlaid. Highest deviations are observed where the curvature is the most important and the measured trajectory is inside the prescribed one. In the end, as observed in the previous low-pass filtering experiment, the trajectory errors seem to somehow compensate since the NRMSE[1] on the total shot is of 0.92% and 0.22% in the x and y directions respectively.

Furthermore, the zeroth-order field term B_0 is displayed in (Fig. 3.11**a**) and reaches a maximum magnitude of 0.02 mT. Finally, (Fig. 3.11**b**) displays the second-order field term whose oscillations reach a maximum amplitude of 1 μT/cm^2.

[1] $\text{NRMSE}(\widehat{\mathbf{x}}, \mathbf{x}) = \dfrac{\|\widehat{\mathbf{x}} - \mathbf{x}\|_2}{\|\mathbf{x}\|_2}$

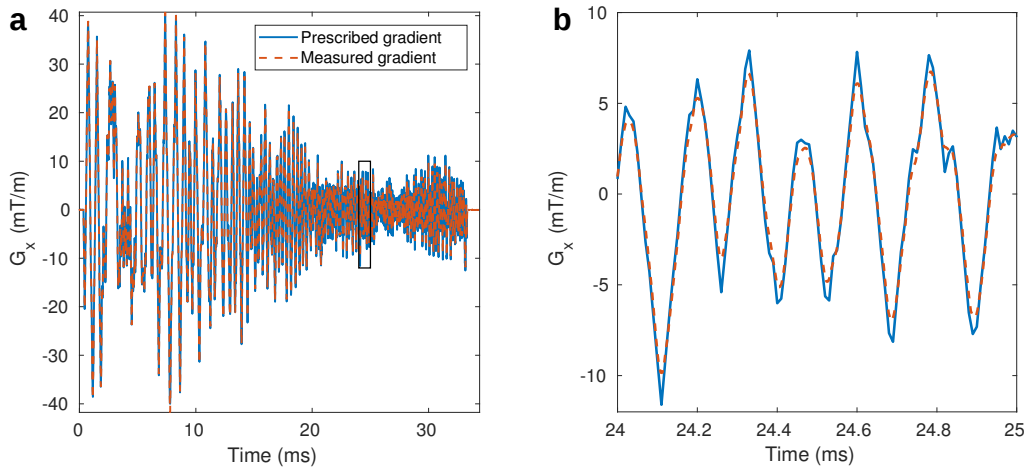

FIGURE 3.9: Prescribed (in blue continuous line) and measured (in orange dashed line) gradient waveforms along x-axis for the total duraction (**a**) and a magnified region (**b**) which corresponds to the black window in (**a**).

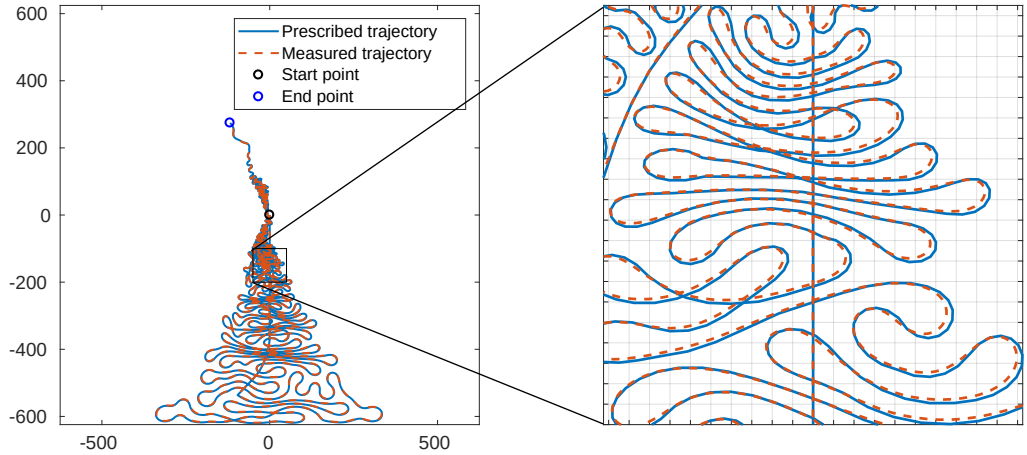

FIGURE 3.10: Prescribed (in blue continuous line) and measured (in orange dashed line) trajectory.

3.5 SPARKLING prospective acquisitions for T2* 2D imaging

After having ensured that the gradient system on our 7-Tesla scanner was capable of playing out the SPARKLING trajectories, we performed a series of prospective acquisitions using the SPARKLING trajectories and compared them to fully-sampled Cartesian, iPAT, variable-density spiral and radial sequences. In this section, we acquired T_2^*-weighted images, which permits the use of long observation times (~ 30 ms).

3.5.1 Materials and Methods

Design of spiral trajectories

Variable-density spiral trajectories were designed using a variable effective FOV as described in (Lee et al., 2003), with a maximum gradient amplitude of $G_{max} = 40$ mT/m, a maximum slew rate of $S_{max} = 200$ T/m/s. A symmetric segment was obtained by joining two opposing center-out spiral interleaves (Law and Glover, 2009) in order for

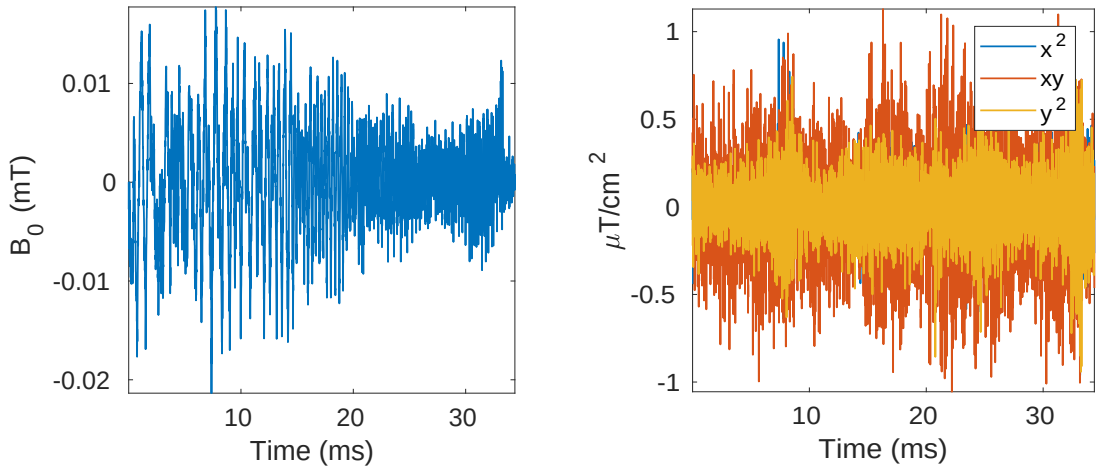

(a) 0th order **(b)** 2nd order

FIGURE 3.11: Zeroth-order field coefficient (**a**) and second-order field coefficients (**b**).

the echo time to be half of the readout time. The total duration of one interleaf was set to 30.72 ms by tuning the parameters controlling the linear variable-density trajectory. (Fig. 3.12b) displays the variable-density spiral sampling composed of 16 interleaves of 3072 samples used to produce the brain image in (Fig. 3.14c), corresponding to a 16-fold acceleration for an image size of 256×256.

Design of radial trajectories

Radial trajectories were designed using a trapezoid gradient waveform, with a ramp time of 0.1 ms until reaching a plateau amplitude of 0.98 mT/m and 1.96 mT/m for images sizes of $n = 256 \times 256$ and $n = 512 \times 512$, respectively, such that the readout time was 30.72 ms. Radial spokes crossed the origin of the k-space at their middle time point and were designed to reach the corners of the k-space. (Fig. 3.12c) displays the radial sampling composed of 16 spokes of 3072 samples each, which were used to produce the brain image in (Fig. 3.14d), corresponding to a 16-fold acceleration for an image size of 256×256.

Acquisitions

All acquisitions were performed on a 7-Tesla MR scanner (Siemens Healthineers, Erlangen, Germany) with a 1Tx/32Rx head coil (Nova Medical, Wilmington, MA, USA). The maximum gradient amplitude and slew rate for this system were 50 mT/m and 333 T/m/s, respectively. For the T_2^*-weighted acquisitions, a 2D GRE sequence was modified to allow execution of arbitrary gradient waveforms complying with the hardware constraints. All non-Cartesian trajectories were acquired using this sequence and the same parameters. The repetition time, echo time and observation time were 550 ms, 30 ms and 30.72 ms, respectively. The FOV was 20 cm, and the flip angle was 25 degrees. Two resolutions were investigated: 390 μm $\times$ 390 μm $\times$ 3 mm and 780 μm $\times$ 780 μm $\times$ 1.5 mm, corresponding to matrix sizes of 512×512 and 256×256, respectively. Standard shimming was performed on the studied slice for *ex vivo* acquisitions and on the

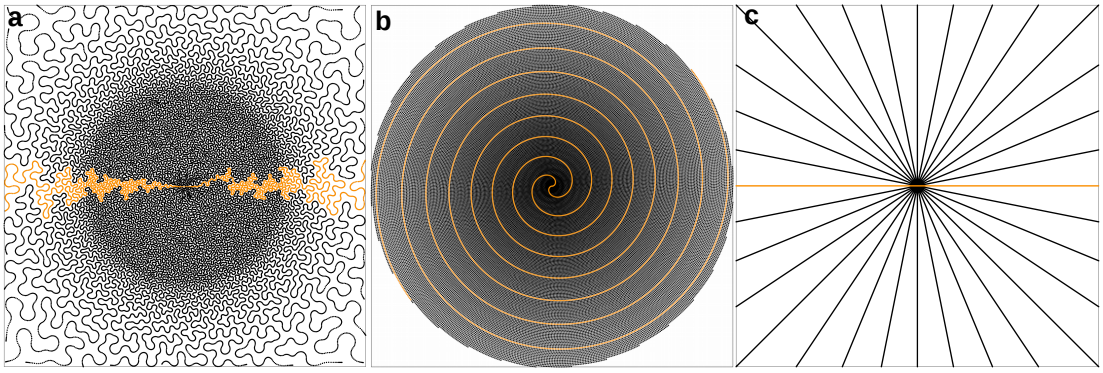

FIGURE 3.12: **Sampling trajectories used for (Fig. 3.14)**. The SPARKLING (**a**), variable-density spiral (**b**) and radial (**c**) trajectories used for *ex vivo* comparisons in (Fig. 3.14). The considered imaging matrix was 256×256, corresponding to a resolution of $780\ \mu m \times 780\ \mu m$. Each trajectory is composed of 16 symmetric segments of 3072 samples (an individual shot is highlighted in yellow), resulting in an acceleration factor of $AF = 16$ and a subsampling factor of $R = 1.33$. An individual segment is highlighted in yellow.

whole brain volume for *in vivo* experiments. The sampling bandwidth was equal to the gradient bandwidth: $\text{rBW} = \text{BW}_{\text{gradient}} = 100$ kHz.

For the 8-fold accelerated Cartesian acquisition using online GRAPPA reconstruction (Fig. 3.13d-h), the same GRE sequence was used with Integrated Parallel Acceleration Technology. This sequence acquires 24 reference lines for auto-calibration. Sequence parameters were the same as above and the default oversampling factor of 2 was used for a base resolution of 256.

***Ex vivo* experiments.** The human brain used for this study was obtained via the body donation program of University of Tours, France from a donor who gave his written consent before death. The brain was extracted and fixed in formalin (formaldehyde solution at 37 % m/m, Cooper, Melun, France) diluted in tap water to obtain a formalin concentration of 10 %). The *ex vivo* phantom was then immersed in a proton-free perfluorinated liquid before the acquisitions.

***In vivo* experiments.** The *in vivo* human experiments were approved by a national ethics committee (CPP IDF 7 Kremlin-Bicêtre) under the protocol registration number 07-042. All volunteers signed a written informed consent form.

Self-calibrating nonlinear reconstruction

2D MR image reconstructions were performed by iteratively minimizing a sparsity promoting regularized Compressed Sensing SENsitivity Encoding (CS-SENSE) criterion introduced in (Wu et al., 2008; Liu et al., 2008; Boyer et al., 2012). We adopted a synthesis formulation composed of one ℓ_2-norm data consistency term and one ℓ_1-norm penalty

term, which reads as follows:

$$\widehat{\mathbf{z}} = \underset{\mathbf{z}\in\mathbb{C}^{N\times N}}{\arg\min}\, \frac{1}{2}\sum_{\ell=1}^{L} \|F_\Omega \mathbf{S}_\ell \mathbf{\Psi}\mathbf{z} - \mathbf{y}_\ell\|_2^2 + \lambda \|\mathbf{z}\|_1. \tag{3.13}$$

This function estimates the image decomposition ($\widehat{\mathbf{z}}$) in a sparsifying domain before projecting the values back to the image domain, i.e., $\widehat{\mathbf{x}} = \mathbf{\Psi}\widehat{\mathbf{z}}$ with $\widehat{\mathbf{x}} \in \mathbb{C}^{N\times N}$, where $\mathbf{\Psi}$ was chosen as an orthogonal wavelet transform using the Symmlet of order 8 as the mother wavelet basis function $\Psi(t)$. We used $J = 4$ levels of decompositions, i.e., 12 sub-bands of detail coefficients for encoding horizontal, vertical and diagonal details on top of the low-frequency approximation. The sum of squares term in (3.13) encodes parallel reception over the $L = 32$ channels of our phased array coil. $\mathbf{y}_l \in \mathbb{C}^m$ represents the measured Fourier values of the ℓ^{th} coil. To handle non-Cartesian Fourier samples, the non-equispaced fast Fourier transform (NFFT, version 3.2.3) (Keiner et al., 2009b) was therefore used to compute F_Ω. The NFFT takes non-uniformly sampled k-space measurements as input data and returns an image on the Cartesian grid. Matrix $\mathbf{S}_\ell \in \mathbb{C}^{n\times n}$ ($n = N \times N$) in (3.13) is diagonal and represents the sensitivity map associated with the ℓ^{th} coil that enhances the specific spatial domain of the desired image $\widehat{\mathbf{x}}$. To estimate the sensitivity maps $\{\mathbf{S}_\ell\}_{\ell=1:L}$, we extended a self-calibrated method used in SAKE (Shin et al., 2014) or IRGN (Uecker et al., 2008) to the non-Cartesian setting, as explained below. First, for each coil, a low-resolution $N \times N$ image was reconstructed using the central surface representing 20 % of the collected k-space completed by zero-filling: $\mathbf{x}_\ell^{\text{LR}} = F^\star_{[\Omega_{|20\%},\mathbf{0}]}\mathbf{y}_\ell$, where LR stands for low resolution and F^* defines the adjoint operator of the NFFT. Second, the square root of the sum of squares (SSOS) was computed: $\mathbf{w} = \sqrt{\sum_{\ell=1}^{L} \|\mathbf{x}_\ell^{\text{LR}}\|^2}$. Third, the sensitivity maps were given by the pixelwise ratio of the low-resolution image coils and the SSOS: $[\boldsymbol{s}_\ell]_i = \text{diag}[\mathbf{S}_\ell]_{ii} = \left[\mathbf{x}_\ell^{\text{LR}}\right]_i / \mathbf{w}_i$, $\forall \ell = 1:L, (i = 1:n)$. Because of this SSOS operation, our method is less dependent on the threshold (i.e., 20 %) over the central surface of the k-space than the method of (Yeh et al., 2005), who directly exploits the $\mathbf{x}_\ell^{\text{LR}}$ images as sensitivity map information. Once the sensitivity maps were estimated, an accelerated proximal gradient method (Taylor et al., 2017) was implemented to solve (3.13). The regularization parameter λ controls the trade-off between data consistency and confidence in the sparsity prior, and this parameter was tuned manually over a discrete grid of values within the interval $[10^{-7}; 10^{-4}]$. In practice, we conducted image reconstructions for each value over this grid and retained the setting with the highest visual quality.

3.5.2 Prospective *ex vivo* and *in vivo* results

The proposed method was prospectively validated on a 7-Tesla MR scanner with a modified gradient echo (GRE) sequence, allowing to execute any feasible gradient waveform. All acquisitions were prospectively performed with this sequence. For both *ex vivo* and *in vivo* acquisitions, a 32-channel receiver coil was used. The first set of experiments involved an *ex vivo* human brain, which allowed assessing the performance of the proposed strategy independently from motion and physiological considerations. Second, acquisitions were also performed *in vivo* on four healthy volunteers to validate the clinical potential of the approach. Following typical high-field sequence specifications (Mainero et al., 2009), we considered a T_2^* contrast with an echo time of 30 ms and a readout of 30.72 ms for both *in vivo* and *ex vivo* experiments. The long repetition time

(550 ms) allows to acquire 11 interleaved slices per excitation, but in what follows, reconstructions are only displayed for one slice. To assess the performance of our method, we compared it with the two most widespread non-Cartesian trajectories in MRI: radial and variable-density spiral trajectories (Materials and Methods, Fig. 3.12). The collected mutli-channel non-Cartesian data were reconstructed using a ℓ^1-based nonlinear reconstruction algorithm suggested in compressed sensing, which does not account for distortions (Smith and Nayak, 2010; Jezzard, Clare, et al., 1999).

Ex vivo experiments

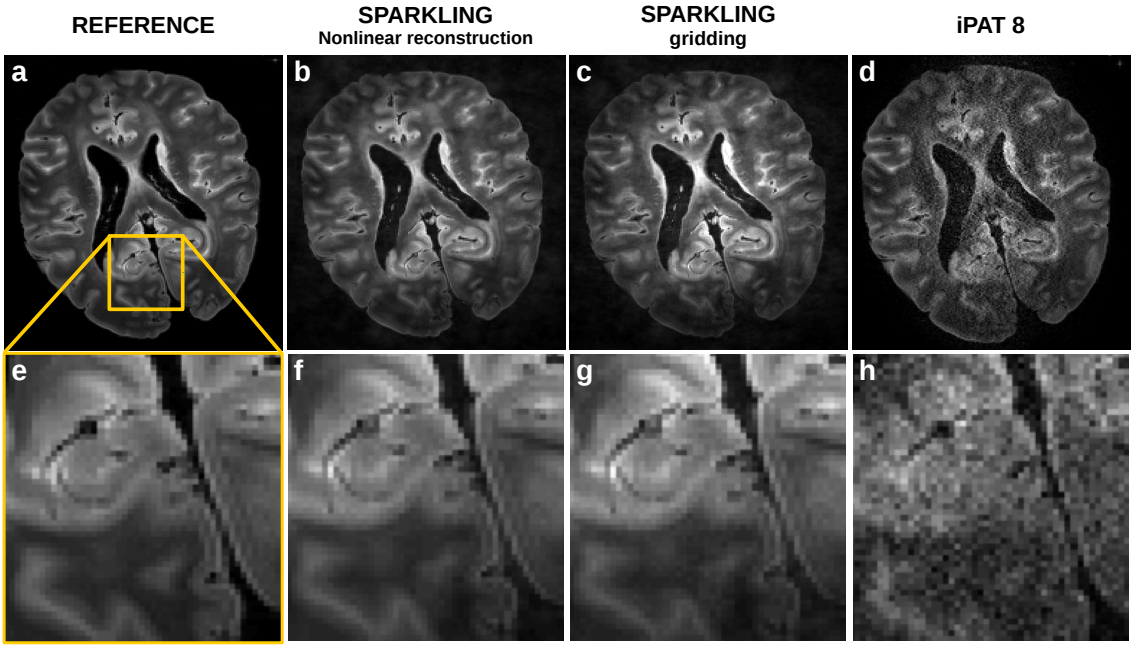

FIGURE 3.13: **Prospective validation of SPARKLING trajectories**. Acquisitions performed on a *ex vivo* human brain for uniform-density SPARKLING sampling (Fig. 3.3a output) at a resolution of 780 μm $\times$ 780 μm $\times$ 1.5 mm and an acceleration factor of $AF = 8$ without subsampling ($R = 0.66$). **a**, A fully sampled Cartesian reference lasting 2 min 20 s for 11 slices. **b**,**f**, Image reconstructed using nonlinear methods from SPARKLING acquisition lasting 16 s. **c**, Image reconstructed from the same SPARKLING acquisition using a gridding method. **d**, Image acquired with the input Cartesian trajectory of (Fig. 3.3a) and reconstructed with a GRAPPA method available on a Siemens scanner (integrated parallel acceleration technology with a factor of 8), whose acquisition time was 16 s. **e**,**f**,**g**,**h**, Magnified region of interest in the medial part of the parieto-occipital cortex (delimited by a yellow square in **a**) of images **a**,**b**,**c**, and **d**, respectively. Image reconstructions did not include any correction of system imperfections.

Prospective results of the SPARKLING strategy initialized with Cartesian lines for a T_2^*-weighted contrast are displayed in (Fig. 3.13) in the case of the uniform-density output shown in (Fig. 3.3a). The acquisition performed with the SPARKLING trajectories thus lasted 16 s, which is 8 times shorter than the fully sampled Cartesian acquisition

with an acquisition duration of 2 min 20 s for 11 slices. SPARKLING images reconstructed with nonlinear compressed sensing reconstructions are displayed in (Fig. 3.13b-f). We also show in (Fig. 3.13c-g) the results of a simple gridding method to reconstruct the SPARKLING data. Both reconstructions show very little difference from the fully sampled Cartesian reference (Fig. 3.13a-e), although the gridding reconstruction may be slightly noisier (Fig. 3.13g) than the nonlinear reconstruction (Fig. 3.13f). The data corresponding to the input trajectory of 32 Cartesian lines (oversampled by a factor of 2) in (Fig. 3.3a) can be typically processed online with a GRAPPA reconstruction (Griswold et al., 2002) available on the MR scanner to produce the image in (Fig. 3.13d-h). The degradation of the image quality, along with a significant decrease in the SNR, is clearly observed (Fig. 3.13h).

The radially initialized SPARKLING strategy similar to that in (Fig. 3.3b) was also compared to widely used radial and variable-density spiral trajectories for an in-plane resolution of 780 μm and a slice thickness of 1.5 mm (Fig. 3.14). All three acquisitions lasted 8.8 s and involved 16 segments, corresponding to a 16-fold acceleration relative to the fully sampled Cartesian reference with an acquisition duration of 2 min 20 s for 11 slices. The subsampling factor was in that case $R = 1.33$, as the long readout duration of 30.72 ms allowed the measurement of many samples per shot (3072 samples

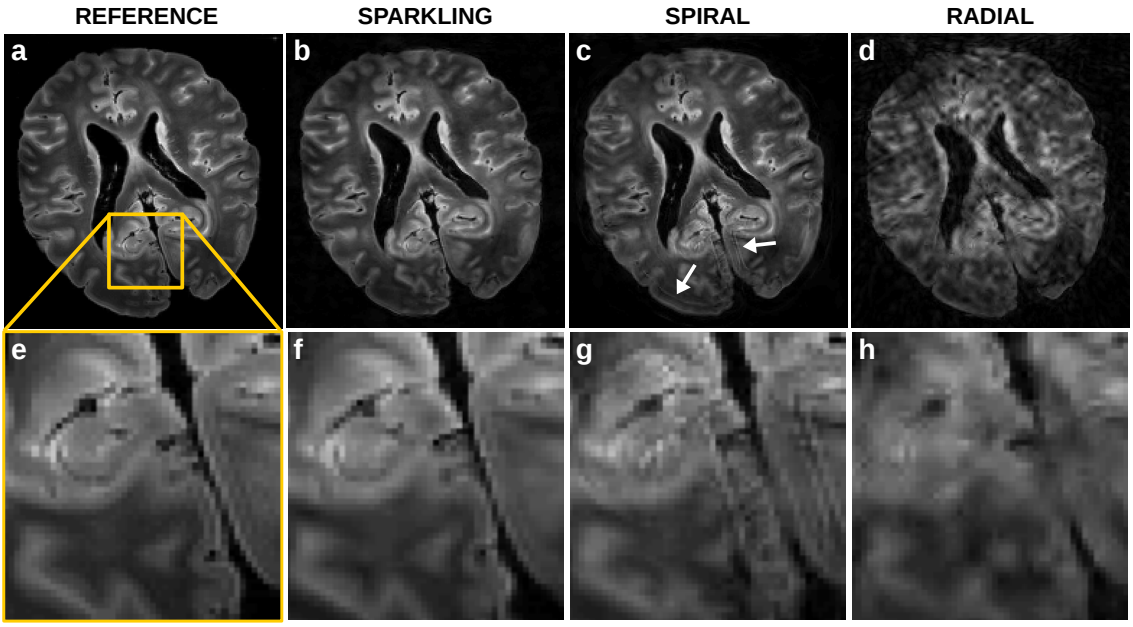

FIGURE 3.14: **Comparison of SPARKLING sampling with variable-density spiral and radial trajectories**. *Ex vivo* acquisition presenting a resolution of 780 μm $\times$ 780 μm $\times$ 1.5 mm, an acceleration factor of $AF = 16$ and a subsampling factor of $R = 1.33$. **a**, T_2^*-weighted reference image and a magnified region of interest in the parieto-occipital cortex in **e** acquired with a fully sampled Cartesian acquisition lasting 2 min 20 s for 11 slices. **b**,**f**, Image reconstructed from a 16-fold-accelerated SPARKLING-generated acquisition lasting 8.8 s. **c**,**g**, Image reconstructed from a 16-fold-accelerated variable-density spiral acquisition lasting 8.8 s. **d**,**h**, Image reconstructed from a 16-fold accelerated radial acquisition lasting 8.8 s. Image reconstructions did not include any correction of system imperfections. Image reconstructions did not include any correction of system imperfections.

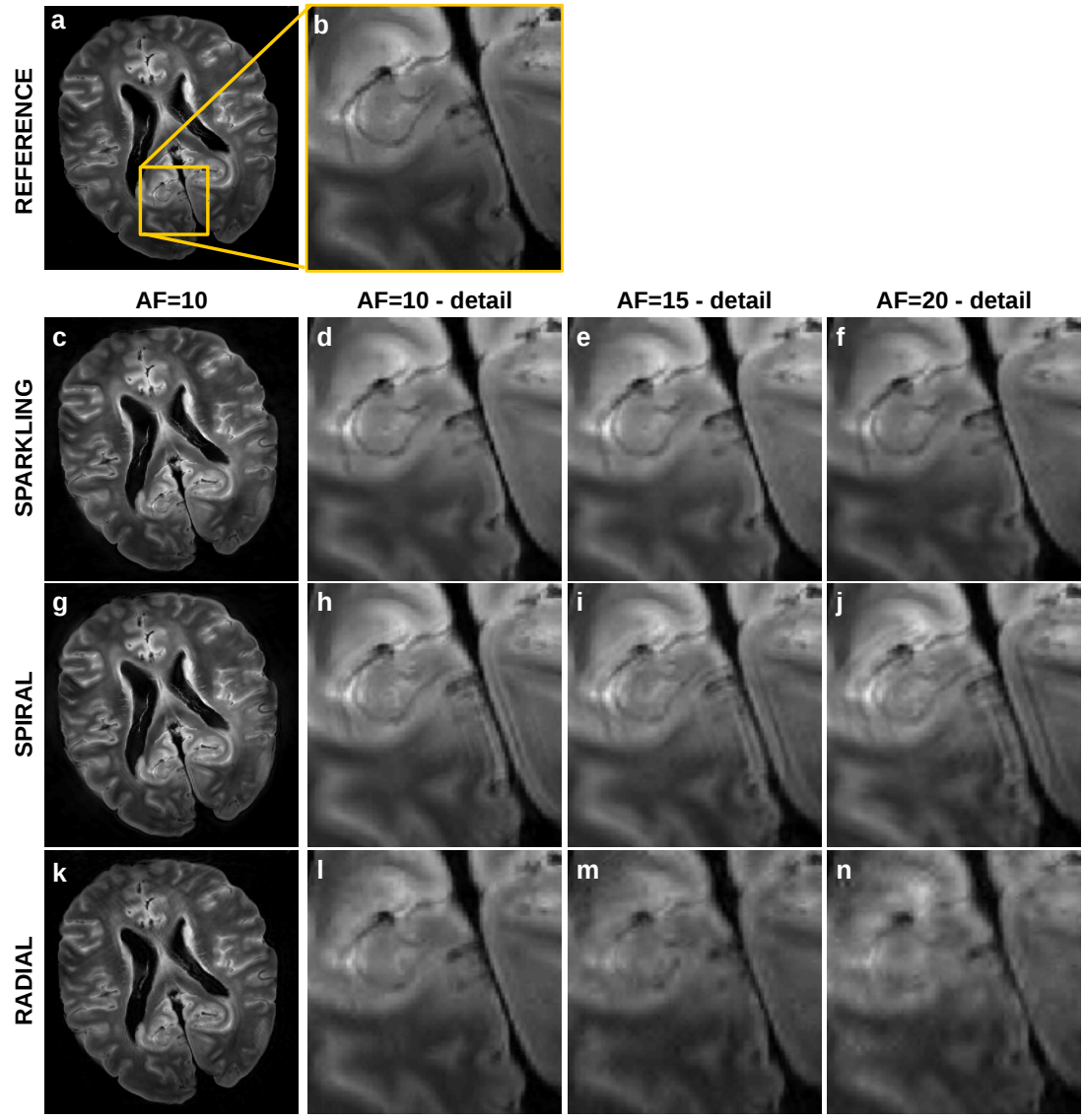

FIGURE 3.15: **Robustness of radial-initialized SPARKLING to very high acceleration factors**. Acquisitions performed on an *ex vivo* human brain for an image resolution of 390 μm $\times$ 390 μm $\times$ 3 mm and with acceleration factors ranging from $AF = 10$ to $AF = 20$. **a**,**b**, T_2^*-weighted reference image acquired with a fully sampled Cartesian acquisition lasting 4 min 42 s for 11 slices and a magnified region of interest in the parieto-occipital junction (delimited by the yellow box). Image reconstructed from 10-fold accelerated acquisitions (28 s) and magnified region of interest are respectively displayed in **c**,**d** for SPARKLING sampling, **g**,**h** for variable-density spiral sampling and **k**,**l** for radial sampling. Magnified images reconstructed from 15-fold accelerated acquisitions (18 s) are displayed in **e** for SPARKLING sampling, **i** for spiral sampling and **m** for radial sampling. Magnified images reconstructed from 20-fold accelerated acquisitions (14 s) are displayed in **f** for SPARKLING sampling, **j** for spiral sampling and **n** for radial sampling. Image reconstructions did not include any correction of system imperfections.

per shot). Using the same nonlinear reconstruction pipeline, the resulting images (top row) and corresponding magnified images of a region of interest in the medial parieto-occipital cortex (bottom row) are shown in (Fig. 3.14b-f) for the SPARKLING trajectory, (Fig. 3.14c-g) for the variable-density spiral trajectory and (Fig. 3.14d-h) for the radial trajectory. While the SPARKLING reconstruction remains similar to the fully sampled Cartesian reference (Fig. 3.14a-e), the high acceleration factor severely impairs the results of the variable-density spiral and radial reconstructions. The accelerated radial trajectory generates a blurry image, illustrating the inefficiency of oversampling radial spokes. The more efficient variable-density spiral trajectory produces a higher-quality image; however the image contains notable off-resonance artifacts along the cortical surface of the brain (Fig. 3.14c) as well as in finer structures visible in the magnified image (Fig. 3.14g).

Acquisitions were also performed with a higher in-plane resolution of 390 μm and three acceleration factors $AF = 10, 15, 20$. The SPARKLING trajectories were initialized with radial patterns; the 15-fold accelerated SPARKLING trajectory corresponds to the output of (Fig. 3.3b). The resulting SPARKLING images and corresponding magnified images are displayed in (Fig. 3.15c-d) for $AF = 10$, (Fig. 3.15e) for $AF = 15$ and (Fig. 3.15f) for $AF = 20$. When focusing on fine brain structures in the medial parieto-occipital cortex, the stability of image quality using SPARKLING trajectories with increasing acceleration factors is observed. In addition, the images produced with the SPARKLING sequence, despite their very short acquisition times, e.g. 14 s for the highest acceleration factor (Fig. 3.15f), maintain high similarity to the fully sampled Cartesian reference, which was obtained with an acquisition time of 4 min 42 s for 11 slices (Fig. 3.15a-b). Likewise, variable-density spiral and radial acquisitions with increasing acceleration factors are displayed in (Fig. 3.15g-h,i,j) and (Fig. 3.15k-l,m,n), respectively. In contrast to the SPARKLING reconstructions, the spiral acquisition yielded substantially more distortions due to off-resonance effects and the undersampled radial patterns produced an overly smoothed image presenting streaking artifacts at $AF = 20$.

In vivo experiments

T_2^*-weighted acquisitions were also performed *in vivo* on four healthy volunteers at an image resolution of 390 μm $\times$ 390 μm $\times$ 3 mm. Consistent with the *ex vivo* results, the *in vivo* results showed that the proposed SPARKLING strategy outperformed the conventional variable-density spiral and radial trajectories in all cases. The results from one subject are presented in (Fig. 3.16) for the highest studied acceleration factor, $AF = 20$. (Fig. 3.16b) shows the image reconstructed from the SPARKLING acquisition lasting 14 s, and this image is nearly indistinguishable from the reference (Fig. 3.16a), which was obtained in an acquisition time of 4 min 42 s for 11 slices. However, the spiral acquisition at the same acceleration factor (Fig. 3.16c,g) has notably more off-resonance artifacts, and the 20-fold-accelerated radial reconstruction (Fig. 3.16d,h) appears blurry and presents streaking artifacts.

3.6 Short-readout SPARKLING for T1-weighting

Finally, T1-weighted SPARKLING acquisitions with a shorter readout time were obtained on our 7-Tesla scanner at an image resolution of 780 μm $\times$ 780 μm $\times$ 3 mm. The acquired trajectory was generated from a Cartesian initialization and a 1D-variable density to obtain the appropriate T1 contrast (Deichmann et al., 2000). The readout time

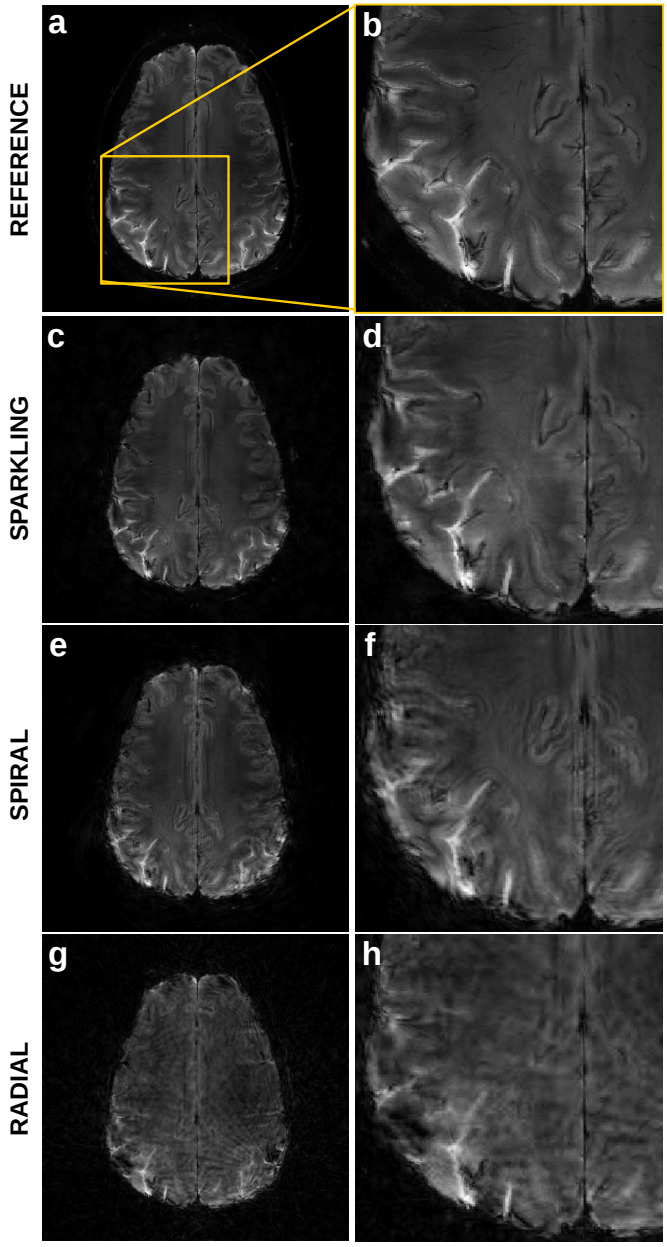

FIGURE 3.16: ***In vivo* validation of radial-initialized SPARKLING trajectories at an acceleration factor of 20 and comparison with spiral and radial sampling**. T_2^*-weighted GRE acquisition on a 7-Tesla scanner at an image resolution of 390 μm $\times$ 390 μm $\times$ 3 mm. **a**,**e**, Fully sampled Cartesian reference with an acquisition time of 4 min 42 s for 11 slices and a magnified region of interest in the parieto-occipital cortex (yellow box). **b**,**f**, Image and magnified image reconstructed from a 20-fold-accelerated variable-density SPARKLING acquisition lasting 14 s for 11 slices. **c**,**g**, Image and magnified image reconstructed from a 20-fold accelerated variable-density spiral acquisition lasting 14 s. **d**,**h**, Image and magnified image reconstructed from a 20-fold accelerated radial acquisition lasting 14 s. Image reconstructions did not include any correction of system imperfections.

was set to 5.12 ms, corresponding to 512 gradient samples and 1024 ADC samples were measured along each shot. (Fig. 3.17a) displays the resulting 128 shots of 1024 samples, each of which lasted 5.12 ms, corresponding to an acceleration factor of $AF = 2$. A 2D MP-RAGE sequence was used with an inversion time of TI=2000 ms, a flip angle of 9°, an echo-spacing of 9.4 ms and a repetition time of 10 s (Deichmann et al., 2000). With these sequence and trajectory, a T1-weighted image was acquired as displayed in (Fig. 3.17b).

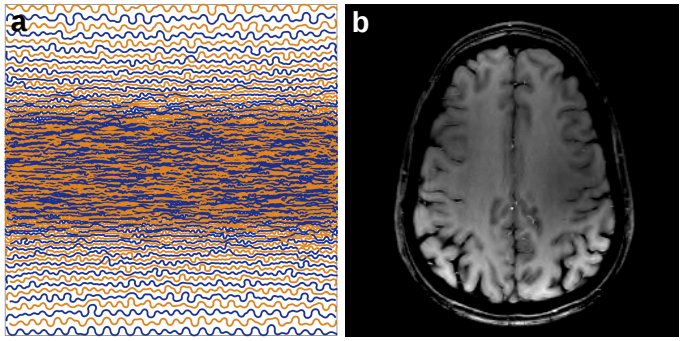

FIGURE 3.17: **T1-weighted *in vivo* SPARKLING acquisitions**. Experiments performed on a 7-Tesla scanner at an image resolution of 780 μm $\times$ 780 μm $\times$ 3 mm. **a**, The SPARKLING trajectory used for the acquisitions, composed of 128 shots of 1024 samples with a readout time of 5.12 ms each, and generated for a 1D-variable density and a Cartesian initialization. **b**, Image reconstructed from the SPARKLING trajectory in **a**.

3.7 Discussion and Conclusion

In this work, we demonstrated that gradient performance allows the successful use of more complex and efficient variable-density sampling patterns which are optimal for compressed sensing (Lustig et al., 2008b). Using the non-Cartesian SPARKLING framework, it is hence possible to generate optimized sampling trajectories fulfilling the aforementioned key criteria of truly controlled sampling density, locally uniform coverage and controlled k-space path between consecutive samples. Given any MR protocol characterized by its echo time (TE) and readout duration (Tobs), the presented optimization-driven method is thus able to enhance MR sampling performance and reduce the number of shots in segmented acquisitions.

In this study, prospective accelerated acquisitions using SPARKLING trajectories were performed on a 7-Tesla scanner. The quality of these images was maintained at high in-plane resolutions of 390 μm and 780 μm both *ex vivo* and *in vivo*. The stability of this method was established even for very high acceleration factors of up to 20, at which fine structural details of T_2^*-weighted images were adequately preserved. The versatility of the SPARKLING approach in terms of initialization and density inputs was corroborated in practice with the implementation of both uniform and variable-density sampling initialized either with Cartesian lines or radial spokes.

Moreover, our sampling strategy was 5 to 7 times faster than the standard acceleration techniques available on the scanner (IPAT) to achieve acceptable image quality for T_2^* weighting. Compared with conventional non-Cartesian spiral and radial 2D trajectories, the SPARKLING sampling yielded perceptually higher image quality. The similar

results of *ex vivo* and *in vivo* imaging prove that motion was not a discriminating element in these cases. Despite the long readout duration for the T_2^*-weighted acquisition (30.72 ms), our method seemed to be relatively less sensitive to system imperfections such as magnetic field inhomogeneity or trajectory errors, while spiral acquisitions presented important artifacts, as often reported in the literature (Yudilevich and Stark, 1987; Mason et al., 1997; Börnert et al., 1999; Tan and Meyer, 2009). In spite of its sinuous appearance, SPARKLING patterns did not seem to suffer much from trajectory distortions which usually lead to severe image artifacts especially in non-Cartesian scanning. As we saw previously, this relative robustness may be explained by considering a simple linear and time-invariant model of the gradient system. Using a simple low-pass filter to model the GIRF self-terms (Vannesjo et al., 2013), we observed that trajectory errors were more important in the studied spiral patterns that in the SPARKLING curves.

There may be two obstacles to the enhanced performance of the proposed strategy for 2D imaging. First, the modest SNR associated with 2D acquisitions may reduce the effectiveness of our method, as for any other subsampled trajectory. Although our experiments benefited from relatively good SNR conditions owing to a strong magnetic field and the use of a multiple receiver coil, SNR limitations appeared beyond the highest presented in-plane resolution of 390 μm. The second potential limitation is the hardware capacity, namely, the maximum gradient amplitude, the maximum slew rate and the gradient and readout bandwidths, which together control the flexibility and thus, the efficiency of the k-space trajectory. In particular, the gradient raster time plays a critical role and should be as short as possible. Assuming a readout bandwidth larger or equal to the gradient bandwidth, the following practical rule for best SPARKLING use should be observed: the ratio of the number of gradient steps per shot to the image size should be as high as possible. As regards high resolution, long-readout scenarios will maximize this ratio and thus optimize SPARKLING performance, while short-readout acquisitions allow for less departure from simple geometric trajectories. When considering lower resolutions however, our method remains applicable and promising. Moreover, in view of the considerable efforts that are currently being invested to push the limits of gradient systems (Weiger et al., 2018), it is reasonable to expect further improvement of SPARKLING performance.

The SNR limitation should be considerably mitigated by the use of 3D SPARKLING acquisitions, which benefit from improved SNR conditions. Although our demonstration focused on 2D sampling as a proof of concept, the presented method can be extended to 3D imaging, for which further gains in terms of acceleration factors are anticipated. Additional improvements may be achieved by incorporating corrections for field inhomogeneities and trajectory deviations into the reconstruction algorithms (Sutton et al., 2003); these possibilities have yet to be investigated. Most interestingly, in contrast to radial or spiral sampling methods, our technique is able to handle any arbitrary density and therefore permits implementation of anisotropic trajectories, which may lead to improved image reconstructions (Kutyniok and Lim, 2015; Baldassarre et al., 2016).

Our findings may be of value in numerous MRI applications including T_2^* (Frischer et al., 2012; De Guio et al., 2014), proton-density (Kasper et al., 2017), susceptibility-weighted imaging (SWI) (Haacke et al., 2004) and also reconsquantitative susceptibility mapping (Langkammer et al., 2015), as our method paves the way to increases in spatial and temporal resolution under conditions compatible with clinical time constraints. Our approach also allows to design optimized multi-echo acquisitions, which may be of interest for T_2^*-mapping (Bittersohl et al., 2009; Denk and Rauscher, 2010). By properly adjusting the initialization and target density of the proposed algorithm, any arbitrary

sampling trajectory might be improved and potentially replaced. Given the advantage of SPARKLING sampling over radial sampling, substituting radial trajectories for patterns produced with our strategy would potentially enhance image quality or allow further acceleration. Furthermore, since each segment can be constrained to pass through the origin of the k-space at a given time, our SPARKLING trajectories possess valuable properties such as robustness to motion and potential for self-navigation (e.g., respiratory self-navigation), while remaining efficient. Most interestingly, our method can be readily used for lower magnetic field imaging available in the clinic just by adapting the imaging protocol.

Chapter 4

3D SPARKLING

4.1 Introduction

In the previous chapter, we saw that the SPARKLING strategy yielded significantly higher image quality compared to standard geometrical patterns such as radial or spiral trajectories, while allowing very high acceleration factors up to 20 for T2*-weighted *in vivo* 2D high resolution imaging of the brain.

Most interestingly, the SPARKLING method can be readily extended to design optimal 3D trajectories, thus allowing to perform 3D imaging which benefits from more favorable SNR conditions than 2D imaging. On the one hand, 3D imaging can be directly achieved using stacks of 2D SPARKLING trajectories, in the same way as stack-of-stars or stack-of-spirals. On the other hand, the SPARKLING algorithm may be extended to 3D and hence permit to produce fully 3D sampling patterns. Fully 3D trajectories have the potential to respect a true 3D variable density presumably necessary for an optimal use of compressed sensing in 3D. Additionally, they are not concerned with limitations in the undersampling factor along the partition direction, which in practice rarely exceeds 4.

Introduced in Chapter 1, susceptibility-weighted imaging (SWI), which is usually performed in 3D, may significantly benefit from the efficiency of the SPARKLING method, since SWI allows the use of long TE (15-20 ms), TR (28-40 ms) and readouts (15 ms). Indeed, in the previous Chapter 3, it was understood that the advantages of the SPARKLING method are enhanced for longer readouts that allow a more important departure from the initial support. Moreover, our method could be an interesting alternative to EPI in this application. Indeed, as well explained in (Holdsworth et al., 2015), although 3D GRE-EPI trajectories are an attractive faster alternative to 3D GRE, they are prone to off-resonance artifacts such as signal drop-out, image blurring, and geometric distortion even when coupled with parallel imaging. Interleaved ('multi-shot') EPI (iEPI) approaches can help reducing distortion artifacts (at the expense of scan time), however (like standard GRE) even small head motion can cause phase errors that typically result in ghosting artifacts and unreliable phase maps. Navigator-based phase correction can help mitigate image ghosting; however, residual non-equidistant sampling in k-space may require excessive oversampling or averaging (Atkinson et al., 2000). In the literature of SWI at 7 Tesla, imaging protocols targeted either a very high in plane resolution (0.2-0.4 mm) with thicker slices (1.5 mm) (Moenninghoff et al., 2010a; Moenninghoff et al., 2015; Theysohn et al., 2011) or high isotropic resolution (0.6-0.8 mm) (Abosch et al., 2010; Schmidt et al., 2017; Moenninghoff et al., 2015). In this chapter, we will therefore focus on such applications and resolutions for 3D imaging.

Here, we will introduce and assess different sampling designs of the 3D SPARKLING approach: stacks and fully 3D trajectories. Imaging and sampling parameters were selected with the objective to perform SWI at 7 Tesla. The study was mostly performed *ex vivo* on a baboon brain. Preliminary *in vivo* results are shown as well.

4.2 Materials and Methods

4.2.1 Stack-of-SPARKLING

Having designed and implemented 2D SPARKLING trajectories, the most straightforward way to perform 3D imaging is to stack these 2D trajectories along the partition direction denoted here as z.

Regular stack-of-SPARKLING

Fig. 4.1**a** shows a stack of 10 identical SPARKLING trajectories, which will be referred to as *regular stack-of-SPARKLING* or *regular SOS*. To respect the Nyquist criterion along the partition direction, the N_z stacks should be spaced by a FOV_z^{-1}-distance until reaching the desired maximum spatial frequency.

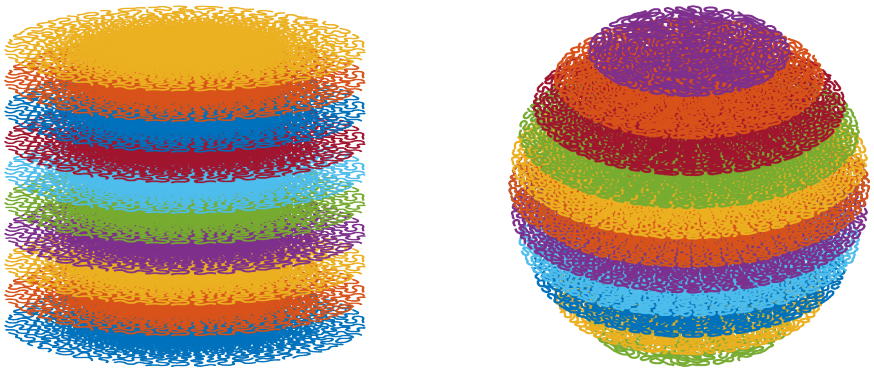

(a) Regular SOS **(b)** z-variable-density SOS

FIGURE 4.1: Stack of 10 identical SPARKLING trajectories filling a cylinder (left) and stack of 11 variable SPARKLING trajectories filling a 3D ball (right). (Colors are just for visualization purposes)

Z-variable-density stack-of-SPARKLING

More interestingly, to obtain a fully 3D variable density, the target density may be changed according to the plane's altitude k_z. Given a 3D density $\pi \in \mathbb{R}^{N\times N\times N_z}$, a trajectory at altitude k_z will be generated with the density $\pi_{2D}(k_z) = \frac{p(:,:,k_z)}{\int p(:,:,k_z)}$. In addition, once the number of shots in the central stack $n(0)$ is chosen, the mass of each plane can be adapted to the plane density by reducing the number of shots per altitude, as k_z increases:

$$n(k_z) = n(0)\frac{\int \pi(:,:,k_z)}{\int \pi(:,:,0)}, \tag{4.1}$$

where $n(k_z)$ is the number of shots in the plane of altitude k_z. Fig. 4.1**b** shows such a stack for an isotropic density (defined on a 3D ball) for 10 SPARKLING trajectories. This

design will be referred to as *z-variable-density stack-of-SPARKLING* or *z-vd SOS*. Further acceleration may be reached by subsampling the number of planes and using parallel imaging along this direction.

4.2.2 Fully 3D SPARKLING

The SPARKLING method was adapted to 3D imaging, with the objective to generate admissible non-Cartesian segmented trajectories filling a ball of radius k_{max}, where k_{max} is the maximum radial extent in 3D k-space.

Computation time and memory load

As explained in Chapter 3, the SPARKLING algorithm's bottleneck lies in the repulsive term F_r between the samples in Eq. (3.5), where there is a summation over all the samples. In 3D, this summation is calculated directly in C++ via a mex file, which gives a complexity of $O(m^2)$, where m is the number of samples. This method to calculate the summation was chosen for time concerns, since developing the NFFT-based fast summation in 3D is a considerable work (probably requiring a few months of development). For 3D sampling, the total number of samples is of the order of 10 million. On a standard computer, it takes about 10 minutes to generate one single shot of 3000 samples, for a matrix size of 256, on one core. Hence, to generate 1000 such shots together, the computation time should be multiplied by 1000^2, which corresponds to about 26 years. Using multiple cores, the computation time could admittedly be reduced, but probably not to a reasonable time... Hence, in our design, each shot of the segmented trajectory was generated independently from the others.

Regarding memory load, there also exist constraints that limit the parallelization of the 3D algorithm over the number of shots, when using large 3D matrices. In practice, on a standard (good) PC with 128 Go RAM, this parallelization was typically limited to 7 shots of 3000 samples for $N = 256$ in parallel.

Using a regular sphere tessellation to accelerate the process

Since each shot must be generated separately, the target density was truncated into n_s volumetric sectors filling the considered k-space, where n_s is the desired total number of shots. To further accelerate the process, we sought to reduce the number of SPARKLING-processed shots by taking advantage of a semi-regular partition of the sphere. We used an equal-area tessellation which divides the sphere into regions of equal area (Leopardi, 2006), as is displayed in (Fig. 4.2**a**) for $n_s = 100$. The property of equal area is important insofar as it ensures that all 3D sectors have equal mass in the case of a radial density. Furthermore, for a constant elevation angle (highlighted in blue on (Fig. 4.2**a**)), all tiles are exactly identical and can be obtained from one another using a simple rotation. Hence, only a small fraction of the desired total number of shots needs to be generated (one per latitude), leading to a reduction in computation time by a factor 20 to 30. In the case of center-out shots, a 3D sector is created by connecting the four summits of a spherical tile to the origin of the k-space. If symmetric shots for which the echo time is at the middle of the segment are desired, the latter sector constitutes one half of total symmetric sector and the other half is obtained by rotating the latter about the origin, as displayed in (Fig. 4.2**b**). To avoid discontinuity between the two halves, the sector is slightly thickened near the origin. For example, with this strategy, only 7 symmetric

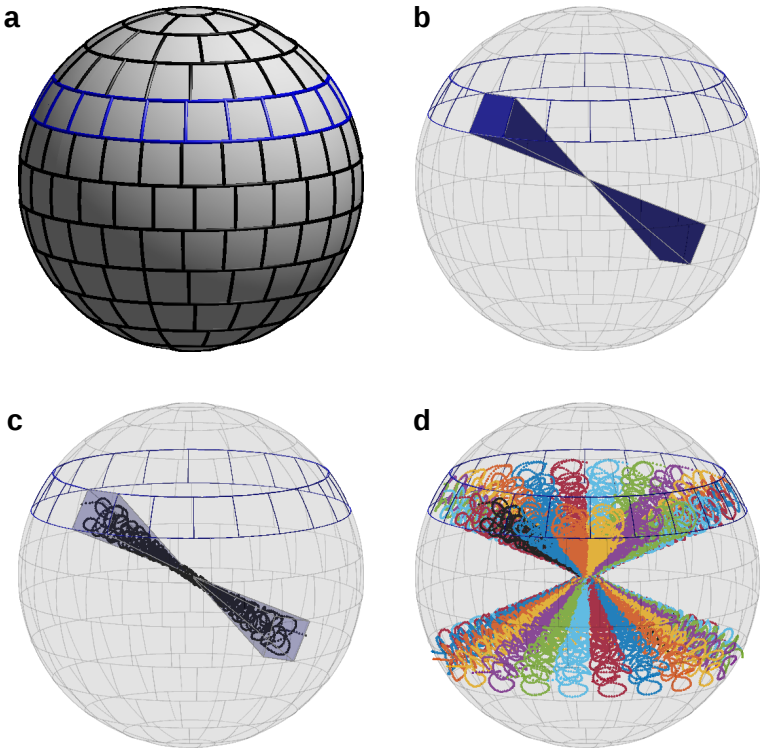

FIGURE 4.2: 3D SPARKLING process. (**a**): Partition of the sphere into 100 regions of equal area. Regions along a constant elevation angle were highlighted in blue: they are identical up to a rotation. (**b**): One 3D density sector. $N = 128$, $k_{max} = 320\,\mathrm{m}^{-1}$, 100 symmetric shots. 7 shots to generate (6 + 1 conic cap).

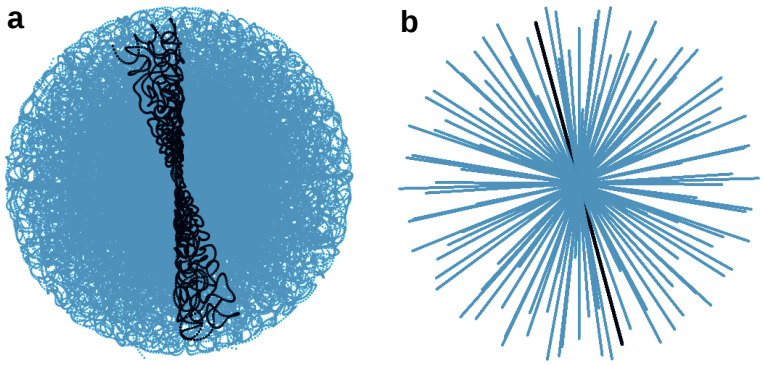

FIGURE 4.3: A 3D SPARKLING trajectory composed of 60 symmetrical shots for a matrix size of $128 \times 128 \times 128$, $k_{max} = 320\,\mathrm{m}^{-1}$, $G_{max} = 40$ mT/m and $S_{max} = 200$ T/m/s. The target density was a variable radially decaying density. An individual segment is highlighted in black.

shots need to be produced by the SPARKLING algorithm for $n_s = 100$. (Fig. 4.2**c**) shows one SPARKLING shot, corresponding to the sector in (Fig. 4.2**b**) with a radially decaying density and for a matrix size of $128 \times 128 \times 128$, $k_{max} = 320\,m^{-1}$, $G_{max} = 40$ mT/m and $S_{max} = 200$ T/m/s. This shot is then rotated to fill the regions of equal elevation angle, as depicted in (Fig. 4.2**d**). For example, (Fig. 4.3**a**) displays a complete 3D SPARKLING

trajectory using this method for a radially decaying density and a total of $n_s = 60$ shots[1]. An individual shot was highlighted in black. For comparison, (Fig. 4.3**b**) displays the corresponding radial trajectory with 60 shots, showing the gain in k-space coverage offered by the SPARKLING method, especially when looking at the individual spoke in black.

4.2.3 Selection of the target density

In view of the long computation time required for 3D images, the target density was retrospectively selected among a set of 6 radially decaying densities. We consider here a radial isotropic density of the form $\nu : k \mapsto \frac{1}{|k|^d}$, which decays with a decay rate d and is going to be truncated by the method introduced in the last chapter 3.3.3 based on the threshold parameter τ and give the density π. Two parameters of the density were varied here: the decay rate $d \in \{2, 3\}$ and the plateau threshold $\tau \in \{0.5, 0.75, 1\}$. (Fig. 4.4) shows the 6 tested densities for $N = 320$. To rank the different densities, evenly

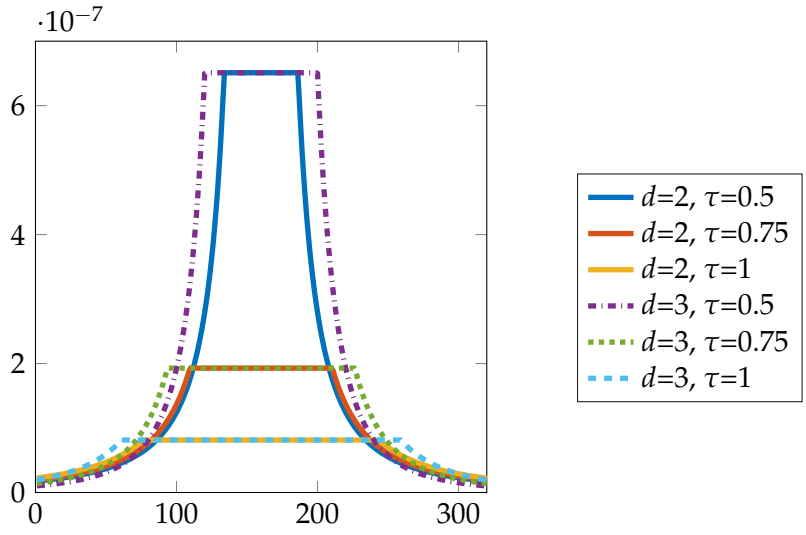

FIGURE 4.4: The 6 tested densities for $N = 320$.

spaced samples were drawn along each density by using Lloyd's algorithm, also known as Voronoi iteration (Lloyd, 1982). Lloyd's method allows to quickly produce a distribution of points with blue noise characteristics, i.e. to produce a locally uniform coverage (criterion (ii) of the previous Chapter). The initial positions of the m samples were determined with an i.i.d. drawing along the considered density. Then, LLoyd's algorithm was applied as follows:

- The Voronoi diagram of the m samples is computed.
- The centroid of each cell of the Voronoi diagram is computed.
- Each sample is then moved to the centroid of its Voronoi cell.

This process was repeated 10 times. (Fig. 4.5) illustrates the output of the algorithm for $m = 1000$ samples in 2D and 3D. Lloyd's algorithm allowed to spread the samples:

[1]Trajectories with only 60 shots are displayed here for better visualization.

the clusters that were present in the initial iid sampling were disrupted and void region were filled. It can be noted that the process is not perfect (even after more iterations) as some bunches of clusters are still visible.

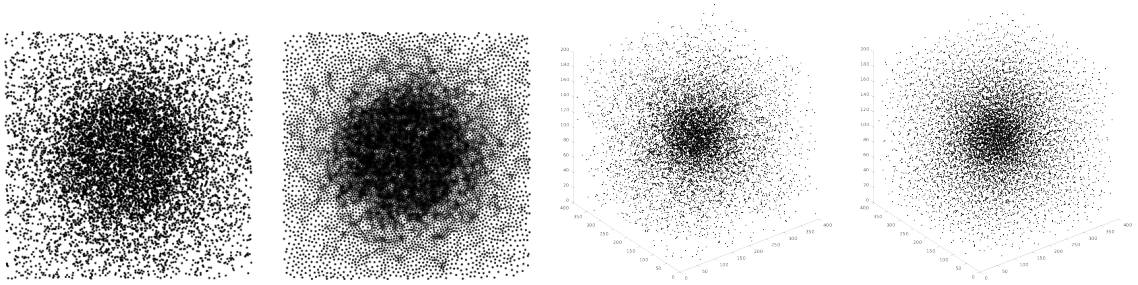

(a) 2D iid samples **(b)** 2D Lloyd samples **(c)** 3D iid samples **(d)** 3D Lloyd samples

FIGURE 4.5: Results of Lloyd's algorithm performed on iid samples in 2D and 3D.

Once the 3D samples are produced for $m = 10^6$ and all densities, the corresponding retrospectively generated Fourier data of a 3D baboon brain image are reconstructed using nonlinear 3D reconstructions[2]. The density which gives the best image quality both visually and in terms of pSNR is selected and will be used as a 3D target density for the SPARKLING trajectories. For instance, in the case of $N = 320$, we selected the density with $d = 3$ and $\tau = 0.75$.

4.2.4 Acquisitions

3D acquisitions were performed on a 7 Tesla MR scanner (Siemens Healthineers, Erlangen, Germany) with a 1Tx/32Rx head coil (Nova Medical, Wilmington, MA, USA). The maximum gradient amplitude and slew rate for this system were 40 mT/m and 200 T/m/s, respectively. A 3D Gradient Recalled Echo (GRE) sequence was used. The imaging parameters are summarized in (Table 4.1).

TABLE 4.1: Parameters used for 3D GRE sequence.

Parameters	Values
TR	40 ms
TE	20 ms
FA	15°
T_{obs}	15.36 ms
BWr	200 kHz

4.2.5 Image reconstruction

Images were reconstructed using the Matlab algorithm presented in the previous Chapter 3, which was extended to handle 3D matrices. The NFFT was replaced with the GPU nufft to speed up the reconstruction time. Yet, the reconstruction time remained quite

[2]Although the optimal density might change as a function of the number of samples, we assumed here that the hierarchy between the different density remains unchanged for the considered number of samples which usually varied between 1 and 20 million.

long, especially for treating 32ch-receiver coil data, reaching about 4 hours for $N = 256$ and 400 iterations, including the calculation of the Lipschitz constant (needed to calculated the step size), with a NVIDIA GPU card GM204GL Quadro M4000 (1664 cores, global memory 8 GB). In practice, time was saved by avoiding the calculation of the Lipschitz constant and using a "realistic" value.

4.3 *Ex vivo* results

4.3.1 Experimental setup

Prospective acquisitions were performed on an *ex vivo* baboon brain for different setups. First, for an isotropic resolution of 0.6 mm, various 3D sampling strategies are compared:

- 3D SPARKLING sampling:
  - regular stack-of-sparkling
  - z-variable-density stack-of-sparkling
  - fully 3D SPARKLING
- 3D Poisson disk strategy as introduced by Lustig et al (Vasanawala et al., 2010) referred to as *PD-lines*:
  2D Poisson disk samples with a deterministic sampling of the k-space center were produced with our algorithm by removing the constraints on speed and acceleration. The size of the deterministically sampled region and the radially decaying rate of the density outside this region were selected by doing a grid-search on retrospectively subsampled reconstructions of a brain phantom image.
- 3D radial trajectories as presented in Chapter 1 (Larson et al., 2008) (Fig. 1.8).
- Cartesian iPAT with GRAPPA reconstruction available on the scanner (Siemens product sequence):
  - iPAT 4x1 (24 reference lines)
  - iPAT 2 (24 references lines) with Partial Fourier 6/8 (phase and encode)
  - iPAT 8x1 (32 reference lines)

Since the previous chapter on 2D imaging already compared the performance of 2D SPARKLING against radial and variable-density spiral trajectories, we did not investigate here the stack-of-stars nor the stack-of-spirals. We expect the relative performance of 2D sampling patterns to remain the same when they are stacked into 3D trajectories.

Finally, a very high resolution of 0.3 mm in the axial plane with a slice thickness of 1.5 mm was performed, similar to the protocols presented in the literature (Abosch et al., 2010; Schmidt et al., 2017; Moenninghoff et al., 2015). (Table 4.2) summarizes the studied protocols and the different acceleration setups. The acceleration factor is calculated as a function of the fully-sampled Cartesian scan; it is the ratio of the number of lines in the reference scan over the number of shots in the accelerated scan.

TABLE 4.2: Parameters used for trajectory design.

FOV (mm^3)	Matrix size	Resolution (mm)	Number of shots n_s	Total scan time (TA)	Acceleration factor $AF = \frac{N \times N_z}{n_s}$
$200 \times 200 \times 140$	$320 \times 320 \times 224$	$0.6 \times 0.6 \times 0.6$	4010	2 min 40 s	18
			2050	1 min 22 s	35
			1040	45 s	69
$200 \times 200 \times 140$	$640 \times 640 \times 96$	$0.3 \times 0.3 \times 1.5$	4085	2 min 43 s	15
			2090	1 min 24 s	30

4.3.2 Results at 0.6 mm isotropic resolution

Different SPARKLING strategies

First, different 3D SPARKLING strategies were compared for an isotropic resolution of 0.6 mm. Regular stack-of-SPARKLING, z-variable stack-of-SPARKLING and fully 3D SPARKLING trajectories were acquired for two different acquisition times: 2 min 40 s and 1 min 22 s. A Cartesian iPAT 4 scan (TA = 14 min 31 s) was also performed and will be considered as the reference image quality. Results in transversal, coronal and sagittal planes are displayed in (Fig. 4.6) for a SPARKLING acquisition time of 2 min 40 s. Each column corresponds to a different sampling method.

For both acceleration factors of 18 and 35, the image quality is well preserved especially in the tree cerebellum visible in the sagittal plane. It can be noticed that the fully 3D SPARKLING results are slightly below the SOS image quality, as they appear more blurry. Regular and z-variable SOS yield similar image quality as is corroborated by the SSIM scores measured on an axial slice taking the iPAT 4 image as a reference. A similar trend was observed for the shorter acquisition of 1 min 22 s (data not shown).

Comparison with existing sampling trajectories

3D SPARKLING trajectories were also compared to 3D radial and Poisson disk sampling strategies for a very acceleration factor of 69, corresponding to an acquisition time of 45 s. Here, a z-variable-density stack-of-SPARKLING was used for SPARKLING acquisitions since it yielded better image quality among the previously tested 3D SPARKLING strategies and has the advantage of supporting high acceleration factor while still well covering the low frequencies very well. Indeed, at this acceleration factor (1140 shots), a regular SOS would only have 5 shots per plane while the z-variable-density SOS presents twice as more shots in the center of the k-space. Moreover, standard GRAPPA-accelerated Cartesian scans were also performed for an iPAT of 4 and an iPAT of 8, lasting respectively 14 min 31 s and 10 min 02 s. Results are displayed in (Fig. 4.7) for coronal, sagittal, axial planes and a magnified central region of the axial image. Each column displays a different strategy.

Of all 69-fold accelerated scans, the SPARKLING method presents the best image quality. For instance, the tree cerebellum in the sagittal slice and the magnified region of the axial slice both appear significantly more blurry in 3D radial than in SPARKLING. Regarding the Poisson disk lines strategy, it is clearly not competitive in this setup as the high acceleration factor translates into a very high subsampling factor in plane as was explained in the previous Chapter. These visual observations are corroborated by the SSIM scores, calculated for a central axial slice with the iPAT 4 image taken as reference.

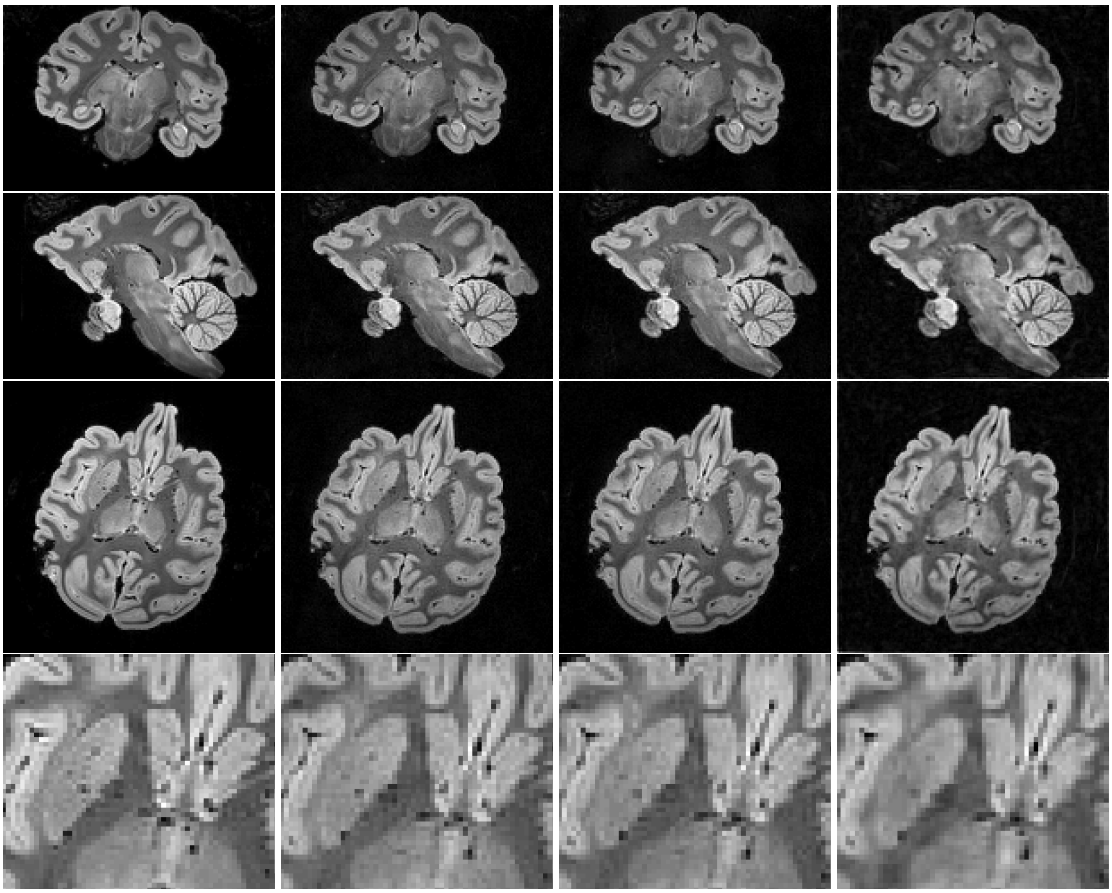

(a) iPAT 4	**(b)** Regular SOS	**(c)** z-variable SOS	**(d)** Fully 3D Sparkling
TA = 14 min 31 s	TA = 2 min 40 s	TA = 2 min 40 s	TA = 2 min 40 s
-	SSIM=0.87	SSIM=0.88	SSIM=0.79

FIGURE 4.6: 0.6 mm isotropic *ex vivo* results comparing different SPARKLING strategies. Column (**a**): iPAT 4. Column (**b**): regular stack-of-sparkling (SOS). Column (**c**): z-variable stack-of-sparkling. Column (**d**): fully 3D SPARKLING for a total number of shots of 4010, i.e., an acquisition time of 2 min 40 s. FOV was $200 \times 200 \times 140$ mm^3.

The SPARKLING image has 0.14 SSIM point more than the radial, and 0.28 SSIM point more than the Poisson disk strategy.

Moreover, it is interesting to compare the iPAT 8 acquisition, although it is significantly longer than the SPARKLING scan (10 min vs. 45 s). As expected, it is quite noisy especially in the central region (see magnified axial slice), but maintains a rather high SSIM score of 0.93. Visually, one may find it more comfortable to work with the SPARKLING image which does not contain so much noise that starts to corrupt the small speckles present in the axial slice of the iPAT 8 image (see magnified region). Let us note that this iPAT 8 acquisition is the maximum in plane acceleration factor achievable using parallel imaging and lasts 10 min. It would be possible to get down to an acquisition time of 45 s by adding a parallel acceleration of 8 along the partition direction and some Partial Fourier 6/8 (phase + slice), but this would surely lead to a very poor image quality.

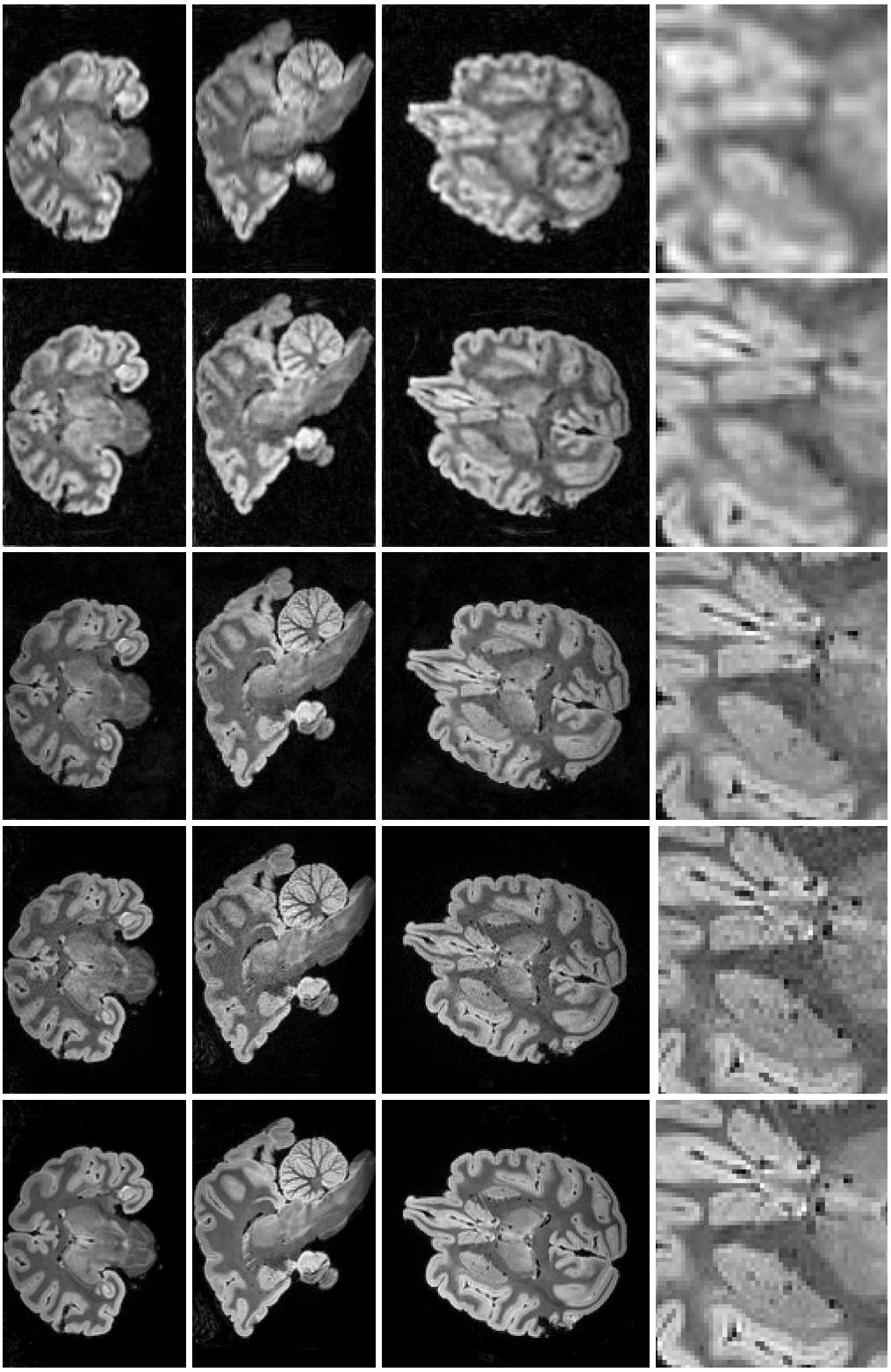

FIGURE 4.7: 0.6 mm isotropic *ex vivo* results comparing z-variable stack-of-sparkling, 3D radial and 3D Poisson disk lines (PD-lines) sampling for a total number of shots of 1140, i.e., an acquisition time of 45 s. FOV was $200 \times 200 \times 140$ mm^3.

4.3.3 Very high in plane resolution

Finally, images were acquired at a very high in plane resolution of 0.3 mm with a slice thickness of 1.5 mm. A standard iPAT 2 PF 6/8 (phase and slice) scan was acquired, which is commonly used in the literature of GRE used for SWI at 7 Tesla (Abosch et al., 2010), and is displayed in (Fig. 4.8**a**). SPARKLING-accelerated acquisitions were also performed for an acquisition time of 2 min 43 s (Fig. 4.8**b**) and 1 min 24 s (Fig. 4.8**c**). We can observe that the SPARKLING reconstructions yield very good image quality although 4 and 10 times faster than the Cartesian scan.

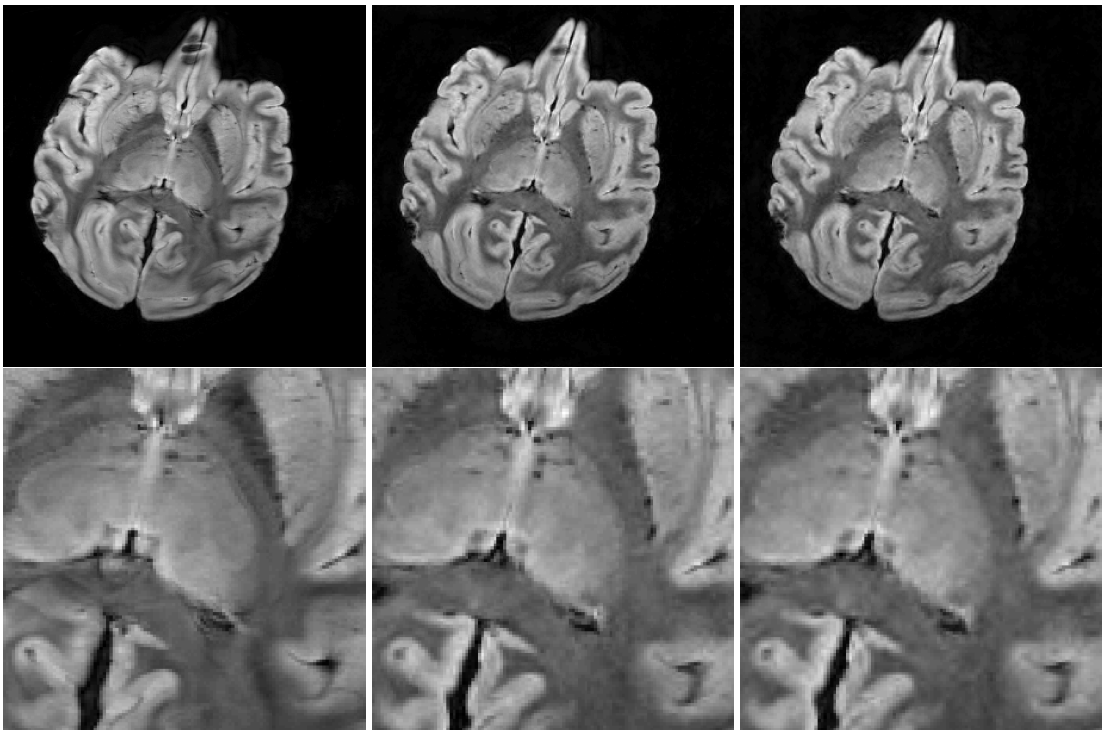

(a) iPAT 2 PF 6/8
TA = 12 min 04 s

(b) SOS
TA = 2 min 43 s

(c) SOS
TA = 1 min 24 s

FIGURE 4.8: *Ex vivo* results of very high in plane resolution of 0.3 mm and 1.5-mm slice thickness for 96 slices. The reference Cartesian scan used iPAT 2 with partial Fourier 6/8 (phase and slice encode) and lasted 12 min 04 s. Regular stack-of-sparkling (SOS) was composed of 2090 shots and 4085 shots, corresponding to acquisition times of 1 min 24 s and 2 min 43 s, respectively. FOV was $200 \times 200 \times 140$ mm^3.

4.4 *In vivo* results

4.4.1 Preliminary results at 7 Tesla

Preliminary *in vivo* results were acquired at 7 Tesla with a regular stack-of-sparkling with 7396 shots and a readout duration of 23 ms and 0.6 mm isotropic resolution. The total acquisition time was 4 min 55 s. Unfortunately, the different setup previously shown for the *ex vivo* study could not be tested yet *in vivo* due to time constraints. (Fig. 4.9) shows the raw image for an axial slice (Fig. 4.9**a**), a minimum intensity projection (mIP) over 10

slices (Fig. 4.9**b**) and a SWI-processed image with a phase mask multiplication of 2 and a mIP over 10 slices (Fig. 4.9**c**). As expected, the mIP process enhances the contrast of the vessels which is further accentuated in the SWI results. Here, the SWI-processing was performed on the whole complex image directly, because it is the solution provided by our reconstruction algorithm. Some off-resonance effects can be distinguished at the top of the image, near the sinuses.

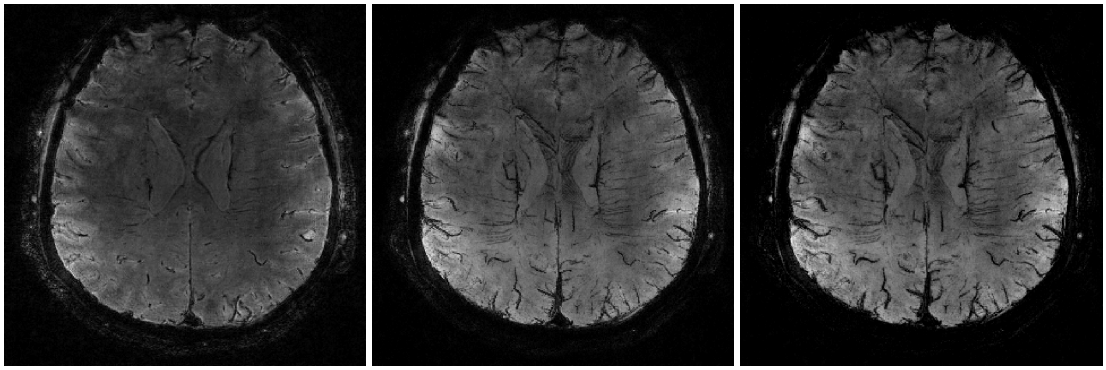

(a) Raw image **(b)** mIP **(c)** SWI + mIP

FIGURE 4.9: Axial slice of an *in vivo* 0.6 mm isotropic brain image. Total acquisition time was TA = 4 min 55 s. (**a**) shows the raw image, (**b**) the minimum intensity projection (mIP) over 10 slices and (**c**), the SWI-processed and mIP image.

4.5 Discussion and conclusions

4.5.1 About the different 3D SPARKLING approaches

Among the three studied approaches of 3D SPARKLING (i.e., regular SOS, z-variable-density SOS and fully 3D SPARKLING), it was observed that the z-variable-density SOS was the most promising. It allows to perform a variable density along the partition direction, thus measuring low frequencies much more than the higher frequencies, in contrast to the regular SOS. Hence, it allows to undersample the data even more.

Regarding the performance of the fully 3D SPARKLING which was significantly behind the SOS strategies, one may propose several explanations. First, the constraint to generate the shots separately introduces some structure in the sampling, which leads to a degraded global distribution of the samples compared to 2D SPARKLING. To examine this, it can be useful to look at all the samples of a 3D SPARKLING trajectory present in a plane of thickness one k-space pixel. These plane sections are displayed in (Fig. 4.10) for different axes and altitudes. Globally, asymmetric structures can be observed in these planes sections, due to the rotation of one SPARKLING-generated shot to fill one latitude of the k-space. In addition, the distribution of the samples is not as neat as it was for 2D SPARKLING, in terms of locally uniformity for instance. Moreover, the center of the k-space seems to be critical as well. Since the samples of different shots are not interacting, the global distribution of the samples in the center is not perfect, with possible holes or overloading. Hence, the fully 3D SPARKLING approach may probably be significantly improved by generating simultaneously all the shots together. This would however require some development efforts and time to reduce significantly the computation time

of the algorithm using fast summations for instance (Potts and Steidl, 2003; Keiner et al., 2009a).

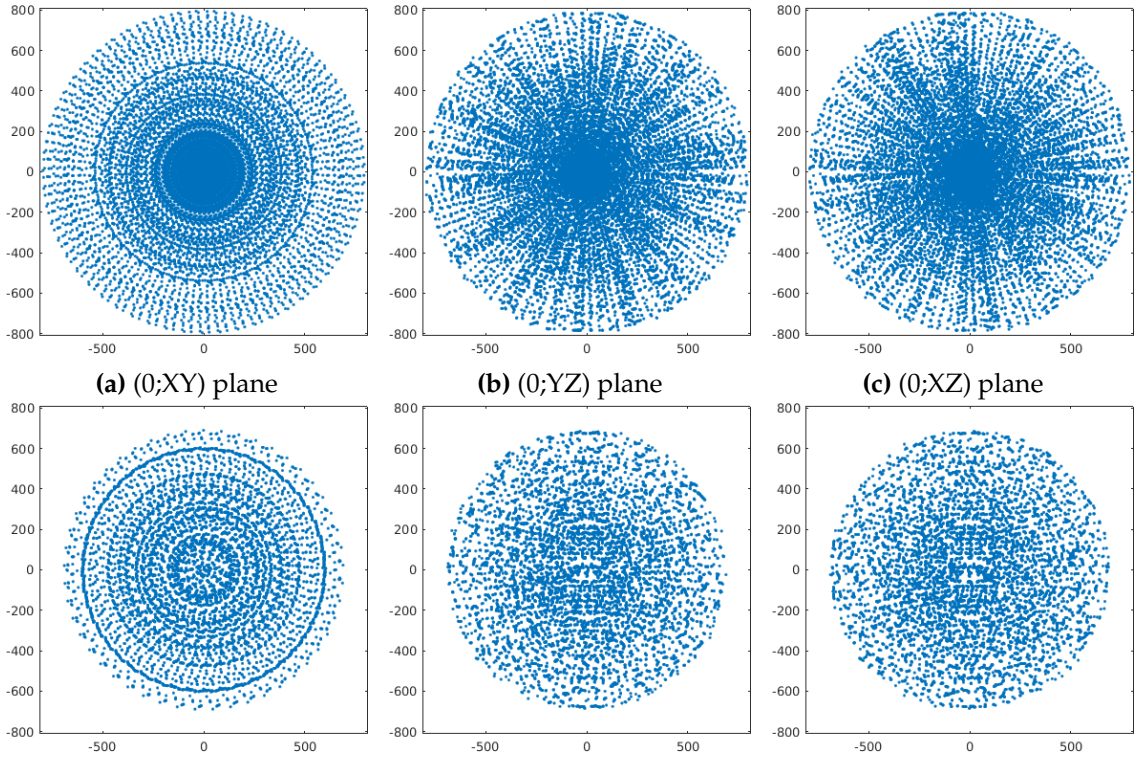

(a) (0;XY) plane **(b)** (0;YZ) plane **(c)** (0;XZ) plane

(d) ($\frac{K_{max}}{2}$;XY) plane - zoom **(e)** ($\frac{K_{max}}{2}$;YZ) plane - zoom **(f)** ($\frac{K_{max}}{2}$;XZ) plane - zoom

FIGURE 4.10: Plane sections of a fully 3D SPARKLING trajectory showing all the samples contained in a plane of thickness one k-space pixel ($1/FOV$). The plane sections are crossing the origin of the k-space or half the maximum spatial frequency $\frac{K_{max}}{2}$ for different directions (top).

4.5.2 About the global performance

***Ex vivo* results**

We used the accelerated 3D SPARKLING trajectories to acquire images at a high isotropic resolution of 0.6 mm for a FOV of $200 \times 200 \times 140$ mm^3. If the iPAT 4 acquisition is considered as a reference scan, the proposed method allowed to divide the acquisition time by a factor of 20, reducing the scan time from 14 min 31 s to 45 s, while maintaining very good image quality. Compared to the fully sampled Cartesian, this acceleration factor would reach 80. For the studied imaging protocol, we also compared the SPARKLING method to other 3D methods such as 3D radial and the Poisson-disk-lines (PD-lines) proposed by Lustig et al., for the same acquisition time of 45 s. The proposed method performed significantly better than these two techniques which both appear very blurry, because of the inefficiency of their sampling lines which are too few at this acceleration rate to produce correct images. Interestingly, this shows that in 3D, the PD-lines method is not adapted to all imaging scenarios using compressed sensing: it may be interesting for short readouts but for longer readouts applications such as SWI it is not as efficient as the SPARKLING approach. Hence, for sufficiently long readouts that enable

the SPARKLING trajectories to wiggle significantly, our method leads to better image quality than PD-lines in the framework of compressed sensing.

For a very high in plane resolution of 0.3 mm, a slice thickness of 1.5 mm and a FOV of $200 \times 200 \times 140$ mm^3, the SPARKLING method was also able to significantly reduce the acquisition time. Compared to the standard sequence used in the context of high resolution SWI (iPAT 2 Partial Fourier 6/8) which lasted 12 min 04 s, the proposed method yielded a very similar image quality in only 1 min 24 s. Perhaps, the acceleration could be pushed even further and enable to reduce the acquisition time below one minute while still presenting diagnostic image quality.

In vivo results

Unfortunately, the extensive *ex vivo* study could not be reproduced *in vivo* due to time constraints. We however hope to gather these results for the PhD defense. One *in vivo* experiment at an isotropic resolution of 0.6 mm with a regular stack-of-sparkling was performed *in vivo* for an acquisition time of less than 5 minutes, while an iPAT 4 scan would have lasted 14 min 31 s. These preliminary *in vivo* results showed the expected image quality at this resolution although some off-resonance effects could be distinguished near the sinuses. Regarding SWI, improvements could be expected by applying the SWI-processing coil by coil, if all coil images are provided by the reconstruction method.

Chapter 5

Correcting the side effects of ADC filtering in MR image reconstruction

5.1 Motivation

We saw in Chapter 1, Section 1.2, how the receive chain detects and processes the received MR signal. One important step of the ADC involves band-limiting and decimation of the *temporal* digital signal to reduce its bandwidth while avoiding aliasing. However, this filtering may have deleterious consequences if the final bandwidth does not permit to respect at least the *spatial* Nyquist criterion along one shot. This may occur in the case of trajectories traversing the k-space at maximum speed or when the SNR does not allow a very high sampling rate. In this situation, the MR sampling can no longer be approximated by a simple discrete Fourier model. The true signal model should describe the accumulation of Fourier information along the k-space path traversed between two consecutive samples.

(Fig. 5.1) shows the detrimental consequences of the ADC filtering for a SPARKLING trajectory which does not respect the Nyquist rate along individual shots. Here, the images were reconstructed using a gridding method and the imaged object was an *ex vivo* human brain. A zoom of the central part of a SPARKLING sampling which was not constrained to respect criterion (iii) is displayed in (Fig. 5.1**a**). This non-Cartesian trajectory is composed of 64 symmetric shots of 512 samples each, for an image size of 512×512 and a field-of-view of $20\,\text{cm} \times 20\,\text{cm}$. (Fig. 5.1**a**) shows that the center of the k-space is sampled at Nyquist rate (1 sample/pixel). Nevertheless, when examining an individual segment and their samples (blue curve in Fig. 5.1**a**), we can notice that the distance between consecutive samples on a given segment is sometimes 6 times larger than the size of a k-space pixel $\Delta k_0 = 1/\text{FOV}$ (represented by the Cartesian grid). This large gap is responsible for creating severe artifacts in the reconstructed image displayed in (Fig. 5.1**e**). Indeed, it is possible to oversample the SPARKLING sampling in (Fig. 5.1**a**) by a factor 6, which is represented in the zoom in (Fig. 5.1**b**). Consecutive k-space samples are now approximately at a one-pixel distance from each other. Using this sampling, the reconstructed image in (Fig. 5.1**f**) does not suffer from the previously observed artifacts. By picking only 1 sample out of 6 from the latter 6-fold oversampled SPARKLING sampling, as depicted in (Fig. 5.1**c**), the selected samples (red squares) therefore correspond to the first SPARKLING sampling in (Fig. 5.1**a**). However in this case, the reconstructed image (Fig. 5.1**g**) is still artifact-free as in (Fig. 5.1**f**). Although the samples' coordinates are the same in (Fig. 5.1**c**) and (Fig. 5.1**a**), they were allocated different data values: the first measurements result from an averaging of the MR signal over a long portion of k-space curve (sometimes long of several k-space pixels) while the second measurements

were acquired on a shorter k-space path smaller than 1 pixel. To verify this assumption, one can artificially recreate the filtered measurements corresponding to (Fig. 5.1**a**) by averaging the 6-fold oversampled SPARKLING acquisition over groups of 6 samples. This operation is represented in (Fig. 5.1**d**), where the averaged value over a group of 6 samples (in different colors) is allocated to the first sample in time (red squares). In this case, the resulting image in (Fig. 5.1**h**) presents the same artifacts as in (Fig. 5.1**e**).

In this chapter, we will show how it is possible to recover the artifact-free image in (Fig. 5.1**f**) from the averaged measurements of (Fig. 5.1**a**) just by considering the appropriate signal model and reconstruction.

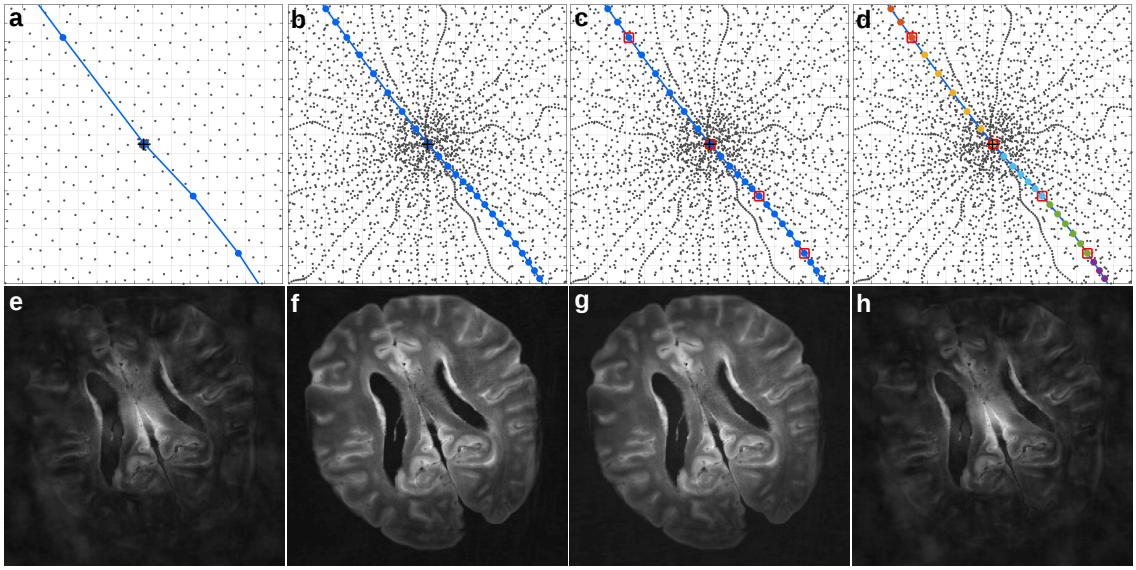

FIGURE 5.1: **Effect of samples localization in k-space (criterion (iii))**. **a**, A 15-pixel wide zoom on the central part of a SPARKLING sampling trajectory which does not respect criterion (iii). It is composed of 64 symmetric segments of 512 samples each, for an image size of 512×512 and a field-of-view (FOV) of $20\,\text{cm} \times 20\,\text{cm}$, with an individual segment highlighted in blue and samples represented by bullets. **b**, Zoom corresponding to the SPARKLING sampling in **a** oversampled by a factor of 6. **c**, Zoom of the SPARKLING sampling in **b** where 1 sample out of 6 (red squares) is kept for reconstruction. **d**, Zoom of the SPARKLING sampling in **b** where data values are averaged by groups of 6 samples (represented in different colors) and the resulting mean is assigned to the the first (in time) sample of each group (red squares). **e**, **f**, **g** and **h** show the images reconstructed from sampling **a**, **b**, **c** and **d** respectively. The size of a k-space pixel is given by $\Delta k_0 = 1/\text{FOV}$.

5.2 Introduction

The standard acquisition model in MRI states that the continuous Fourier transform of an image $u : \Omega \to \mathbb{C}$ is sampled on a set of discrete points in what is commonly called the *k-space*. The space $\Omega \subset \mathbb{R}^d$ is the field of view, with $d = 2$ or $d = 3$ denoting the space dimension. The particularity of MRI is that these samples are measured along several parametrized curves $\lambda : [0, T] \mapsto R^d$, called k-space trajectories or shots. According to this model, given a sampling period Δt and letting $\hat{u}$ denote the Fourier transform of the

image u, the measured samples are modeled as (Fessler, 2010):

$$y_j = \hat{u}(\lambda(j\Delta t)), \tag{5.1}$$

where $j \in \mathbb{N}$ denotes the index of the measurement. Most commonly, these points lie on a grid, which is filled by parallel Cartesian lines (Lauterbur, 1973), but non-Cartesian sampling such as spiral trajectories (Meyer et al., 1992) may also be used for their greater sampling efficiency and are becoming increasingly popular with the advent of compressed sensing (Lustig et al., 2007a).

Nevertheless, the model expressed in Eq. (5.1) does not account for the analog-to-digital converter (ADC), which converts the continuous signal $f(t) = \hat{u}(\lambda(t))$ into discrete values. The model that will be used to describe this effect is a linear time invariant filter of the type:

$$y_j = (h \star f)(j\Delta t), \tag{5.2}$$

where $\star$ denotes a convolution operator and h is a filter that depends on the ADC technology. The main point of this chapter is to show that neglecting the filtering effect in model (5.2) can have a dramatic impact on the reconstruction quality and to propose numerical algorithms to handle it. We will pay special attention to two typical situations: a simple integrator ADC and more advanced band-limiting filters which are typically used in modern MRI scanners.

- **Integration effect**. The earliest ADCs were simply integrating ADCs, meaning that the ADC simply *integrates* the Fourier transform $\hat{u}$ over a the k-space path. This model reads as $y_j = \int_{(j-1)\Delta t}^{j\Delta t} \hat{u}(\lambda(t))\, dt$ and can be cast into Eq. (5.2) by choosing $h = \mathbf{1}_{[0,\Delta t]}$. The interest of choosing a large sampling period Δt is that the signal-to-noise ratio (SNR) increases since more signal is averaged over time (Hoult, 1978), which is a typical reasoning in MRI physics. We will see later that this improvement might not compensate the downsides that come along with it.

- **Band-limiting filtering**. On most MR scanners, the ADC bandwidth is fixed and much higher than the desired receiver bandwidth (Ansorge and Graves, 2016). The ADC rate reaches several megahertz, while the receiver bandwidth usually ranges from about 5 to 100 kHz (Graessner, 2013). To produce the measurements at the desired sampling rate, band-limiting filtering is applied on the digitized data before decimation. This band-limiting step is introduced both to avoid aliasing of the temporal signal f when subsampling it and to reduce the noise. A perfect band-limiting filter takes the form $h(t) = \mathrm{sinc}(t/\Delta t)$[1].

To the best of our knowledge, the effects of ADC filtering on image reconstructions have not yet been described or studied in the literature.

The higher complexity of the model may be a possible explanation for this omission, since Eq. (5.2) no longer represents a Fourier transform, preventing a straightforward application of standard tools such as the fast Fourier transform. Furthermore, this effect might go unnoticed when using standard Cartesian acquisitions which are usually oversampled by a factor of 2 in the readout direction compared to the Nyquist rate. We will see later that the classical model in that case is sufficient to reconstruct high quality images. However, in situations where faster trajectories are used, as is the case of spiral

[1]The cardinal sinc function is defined on $\mathbb{R}$ by: $sinc(x) = \frac{sin(x)}{x}$

sampling and/or when the use of oversampling is not possible due to low signal-to-noise-ratio (SNR), significant artifacts may appear.

In section 5.3, we first show how the classical approximation in Eq. (5.1) can lead to detrimental artifacts in the reconstructed images, even in the case of Cartesian sampling at Nyquist rate. Depending on the trajectories, intensity modulations, space-varying blurs and image deformations can be observed when ignoring ADC filtering.

In many situations, the filter h is not provided by the manufacturer and correcting the effect hence requires its estimation. In section 5.4, we propose a reverse engineering technique based on the design of specific sequences and numerical algorithms to estimate the applied filter h.

In section 5.5, we propose numerical algorithms to handle the ADC filtering effect for linear and nonlinear reconstructions methods. These are based on a combination of numerical integration methods and of the nonuniform Fast Fourier transform.

In section 5.6, the proposed algorithms are tested against simulated and real data, showing significant improvements in the reconstruction quality, especially when using the novel trajectories designed in the framework of compressed sensing.

5.2.1 Notation

In this paper, we assume that the image domain is $\Omega = [-1/2, 1/2]^2$. We chose to work in 2D to simplify the exposition, but an extension to 3D is direct. Similarly, the domain can be shifted and inflated to account for a different field of view with straightforward scaling arguments. Notice that with the choice $\Omega = [-1/2, 1/2]^2$, Shannon's sampling theorem (Shannon, 1948) suggests to take samples on a Cartesian grid, with a grid size of length 1.

The space $L^2(\Omega)$ is defined as the set of measurable functions u with finite L^2 norm, i.e. $\|u\|_{L^2}^2 := \int_\Omega |u|^2(x)\,dx < +\infty$. The canonical Hermitian product on $\mathbb{C}^n$ and $L^2(\Omega)$ is denoted $\langle \cdot, \cdot \rangle$. Let $u : \Omega \to \mathbb{C}$ denote a magnetic resonance image in $L^2(\Omega)$. Its Fourier transform is defined for all $\xi \in \mathbb{R}^2$ by:

$$\hat{u}(\xi) = \int_\Omega \exp(-2\imath\pi\langle x, \xi\rangle) u(x)\,dx.$$

The Dirac delta function at 0 is denoted by δ and the Dirac delta function at a position x is denoted δ_x.

Given two functions f and g, the tensor product of f and g is defined by $(f \otimes g)(x, y) = f(x)g(y)$ for all x, y. We recall that the Fourier transform preserves the tensor form: $\mathcal{F}(f \otimes g) = \mathcal{F}(f) \otimes \mathcal{F}(g)$.

5.3 The deleterious consequences of filtering

The aim of this section is to explain the ADC filtering effects on the reconstruction of signals and when it is important to account for them. We start by the simple case of Cartesian trajectories and then turn to more general sampling patterns.

5.3.1 The case of Cartesian sampling

The filtering effect in the case of Cartesian sampling with constant speed s can be understood by an analytical argumentation. In that case, for each sampling point, the filtering

is performed along the readout direction only. A convenient way to formalize this observation is to introduce the following tensor product filter $\hat{\mu} = g \otimes \delta$, where $g(t) = h(t/s)$ and to observe that the acquisition model then reads:

$$y_{i,j} = (\hat{u} \star \hat{\mu})(i\Delta\xi, j\Delta\xi) \tag{5.3}$$

where $(i,j) \in \{-n/2, n/2-1\}^2$ describe the set of samples indices, and $n \in \mathbb{N}$ describes the number of samples in each k-space direction.

Now, by not accounting for the filtering effect, the best we can hope for is to reconstruct an image u^* of the form $u^* = \mathcal{F}^{-1}(\hat{u} \star \hat{\mu}) = u \cdot \mu$, where μ is defined by:

$$\mu = \mathcal{F}^{-1}(g \otimes \delta) = \mathcal{F}^{-1}(g) \otimes \mathcal{F}^{-1}(\delta) = \mathcal{F}^{-1}(g) \otimes \mathbf{1}.$$

Depending on the filter h, different effects can be expected.

Integration In the case of an integration filter, we have $h = \mathbf{1}_{[0,\Delta t]}$, where Δt is the sampling period. Then $g = \mathbf{1}_{[0,\Delta\xi]}$, where $\Delta\xi = s\Delta t$ is the length of the segment over which the Fourier transform is integrated. Hence, $\mathcal{F}^{-1}(g)$ is a sinc filter, and the filtering effect hence produces an image modulated by a sinc. Depending on the integration length $\Delta\xi$, this effect will either just lower the contrast at the image boundaries, or create low frequency oscillations.

Sinc By using a sampling period Δt, the standard Shannon-Nyquist sampling theorem states that it is impossible to reconstruct frequencies beyond the interval $I = [-\frac{1}{2\Delta t}, \frac{1}{2\Delta t}]$. Hence, to avoid aliasing effects, one may be tempted to use a perfect band-limiting filter of the type $\hat{h} = \mathbf{1}_I$. In that case, we would get $h(t) = \mathrm{sinc}\left(\frac{t}{\Delta t}\right)$. The filtering effect in that case would simply crop the image in one direction on the interval I.

We now propose to simulate the effect using 4 different Cartesian sequences with $\Delta\xi \in \{\frac{1}{2}, 1, 2, 4\}$. The value $\Delta\xi = 1/2$ corresponds to the most standard Cartesian trajectory in MRI (oversampling factor of 2 along the readout direction). The value $\Delta\xi = 1$ corresponds exactly to the Shannon's limit sampling rate for an image supported on $[-1/2, 1/2]^2$. For the simulation, our measurements are created by incorporating the filtering effect as expressed in Eq. (5.3). For example, in the integration case with $\Delta\xi = 2$, each sample results from the integration of two consecutive samples acquired at $\Delta\xi = 1$. The reconstruction algorithm is based on a standard inverse discrete Fourier transform (which does not account for any filtering effects). Figs. 5.2-5.3 show the results for the integration and the sinc filtering respectively as well with a cross section of the images. The modulation due to the integration filtering can be seen on the cross sections for all values of $\Delta\xi$. On the contrary, the effect of the sinc filtering can be seen only for $\Delta\xi \in \{2, 4\}$, with a dramatic effect: the disk is cropped with an irreversible loss of information.

Overall this experiment highlights the fact that larger distances between consecutive samples in the k-space result in a more pronounced filtering effect.

For more general trajectories, it seems hard to give an analytical description of the filtering effects. From a mathematical viewpoint, it amounts to studying integral operators with kernels defined as measures supported on one dimensional curves. To the best of our knowledge, very little is currently known for such operators. Hence we restrict ourselves to provide experimental simulations with spiral trajectories, which are one of the most widespread non-Cartesian trajectories.

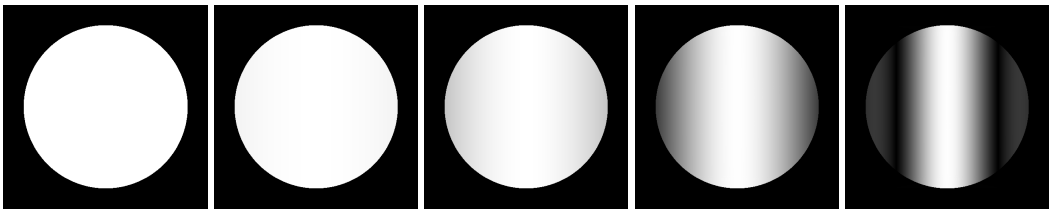

(a) Ground truth **(b)** $\Delta\xi = 1/2$ **(c)** $\Delta\xi = 1$ **(d)** $\Delta\xi = 2$ **(e)** $\Delta\xi = 4$

FIGURE 5.2: The integration effect with a Cartesian sampling. Note: the images might be complex valued, and we only display their modulus. This explains why negative oscillations are seen as positive values.

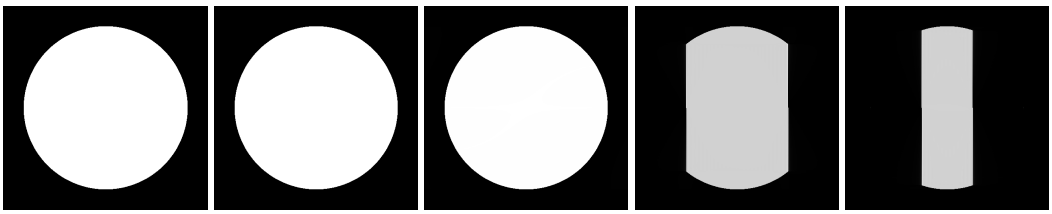

(a) Ground truth **(b)** $\Delta\xi = 1/2$ **(c)** $\Delta\xi = 1$ **(d)** $\Delta\xi = 2$ **(e)** $\Delta\xi = 4$

FIGURE 5.3: The sinc filtering effect with Cartesian sampling. Note: in that experiment, some ringing appears on the boundaries, explaing why the cropped images are darker.

Fig. 5.4 shows a sampling pattern made of 200 interleaved spirals, which were designed using the method proposed in (Lee et al., 2003). Each spiral is depicted with a different color going continuously from blue to green. The number of samples is equal to 153600, while the reference image contains 512×512 pixels. Hence this experiment corresponds to a subsampling factor of 1.7. Notice that while the distance between consecutive samples is about 1 pixel in the k-space center, it reaches about 5 pixels in the outer part, meaning that the filtering effect will have a higher impact on high frequencies. Images of a brain phantom (Guerquin-Kern et al., 2012a) were reconstructed using a standard nonlinear reconstruction algorithm described in Section 5.5.3. Fig. 5.5 shows the consequences of the integration and the sinc filtering on the images acquired with the spiral trajectory. When integration effects occur (Fig. 5.5**b**), the reconstructed image suffers from severe artifacts including a space varying blur, some contrast losses, a slight rotation (visible on ly by switching from one image to the next) and a modulation. In the case of band-limiting filtering (Fig. 5.5**c**), the image quality degrades even more: a magnified region shows the loss of resolution as compared to the ground truth (Fig. 5.5**a**).

5.4 Validation of the filtering model

To the best of our knowledge, the forward model proposed in Eq. (5.2) has not been studied in the literature previously. The way the signal is digitized and processed depends on the MR receiver hardware, with specifications that are usually not transparent. In the following part, we therefore design a reverse-engineering technique to estimate the filter h and to validate the proposed model.

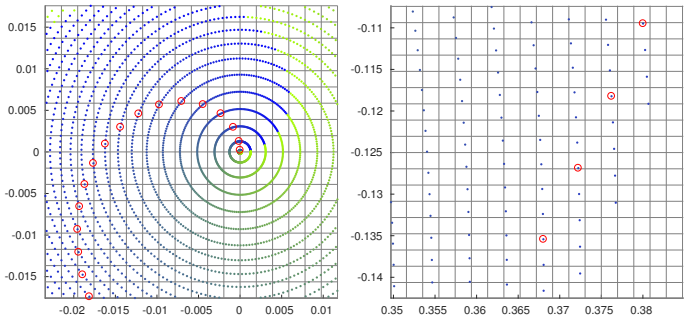

(a) Center **(b)** Boundary

FIGURE 5.4: Two zooms on a sampling pattern made of 200 interleaved spirals. Each spiral has a different color.

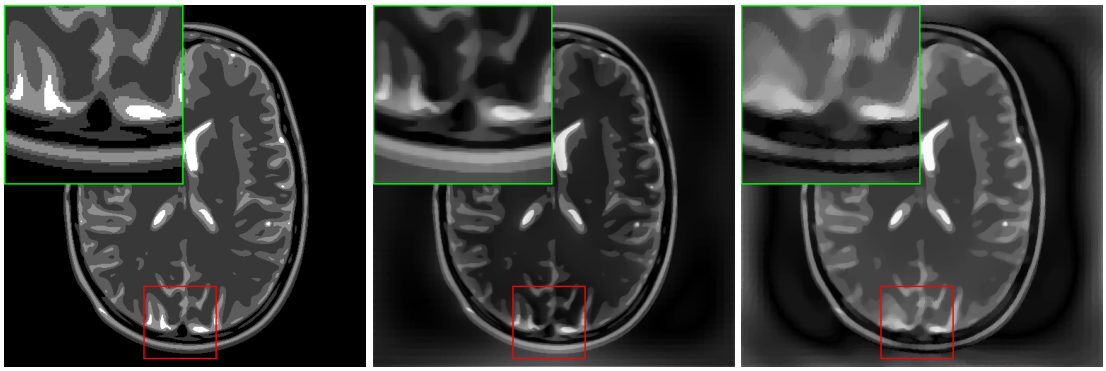

(a) Ground truth **(b)** Recon (integration) **(c)** Recon (sinc filtering)

FIGURE 5.5: Example of reconstruction of an image sampled along the spirals of Fig. 5.4. The reconstruction algorithm does not account for the integration effect.

5.4.1 A filter estimation procedure

We introduce a methodology to verify model (5.2) and to estimate the ADC filter. The principle reads as follows:

- Set a sampling period δt, a downsampling factor $p \in \mathbb{N}$, a number of measurements $m \in p\mathbb{N}$ and a trajectory $\lambda : [0, m\delta t] \to \mathbb{R}^2$.
- Generate a first set of measurements $\boldsymbol{y}_0 \in \mathbb{C}^m$ by sampling $f = \hat{u} \circ \lambda$ with the rate δt.
- Generate a second set of measurements $\boldsymbol{y}_1 \in \mathbb{C}^{m/p}$ by sampling f with the rate $p\delta t$.

In the case of an integrating ADC for instance, the noiseless measurements should then satisfy:

$$\boldsymbol{y}_1[i] = \sum_{j=0}^{p-1} \boldsymbol{y}_0[pi + j]. \tag{5.4}$$

A convenient way to express the model is $\boldsymbol{y}_1 = \boldsymbol{h} \star \boldsymbol{y}_0 \downarrow p$, where $\star$ denotes the convolution product, $\downarrow p$ is the downsampling by a factor p and $\boldsymbol{h} = [1, \dots, 1]/p$ is a constant filter of size p. One way to verify Eq. (5.4) is then to solve the following optimization

problem:

$$\min_{\boldsymbol{h}\in\mathbb{R}^m} \frac{1}{2}\|(\boldsymbol{h}\star\boldsymbol{y}_0\downarrow p)-\boldsymbol{y}_1\|_2^2+\frac{\alpha}{2}\|\mathbf{L}\boldsymbol{h}\|_2^2, \tag{5.5}$$

where $\alpha \geq 0$ is a regularization parameter and $\mathbf{L}$ is a regularizing operator. In all our experiments we set $\mathbf{L}$ to be the discrete first-order derivative and tune α manually.

The underlying idea behind problem (5.5) is to find the best linear time invariant operator that allows to match the two sets of measurements $\boldsymbol{y}_0$ and $\boldsymbol{y}_1$. The least squares in Eq. (5.5) correspond to a *deconvolution* problem, which is highly ill-posed (Tarantola, 2005). Hence we propose to regularize it by adding a Tikhonov regularization. Problem (5.5) can easily be solved with an accelerated projected gradient descent. The interested reader is refered to the first paper on the subject (Nesterov, 2005).

Remark 1 *In practice, the vector of measurements $\boldsymbol{y}_0$ is itself filtered by the ADC and we can only expect this procedure to yield an estimation of the filter valid for the time resolution δt instead of $m\delta t$.*

5.4.2 The experimental setup

All acquisitions were performed on a 7-Tesla MR scanner (Siemens Healthineers, Erlangen, Germany) with a 1Tx/32Rx head coil (Nova Medical, Wilmington, MA, USA). To validate our model, an *ex vivo* baboon brain was imaged using a gradient recalled echo (GRE) sequence to acquire the Cartesian and spiral data corresponding to the experiment described in the previous section 5.3.1.

We validated the model both for Cartesian and spiral sampling.

In the case of Cartesian sampling, we set $\delta t = 10\mu$s with a field-of-view (FOV) of 20×20 cm^2 for a target resolution of 256×256. We then designed three trajectories composed of 256 lines with different sampling periods $\Delta t \in \{\delta t, 4\delta t, 16\delta t\}$, i.e. in the framework of paragraph 5.4.1, $p = 1$, $p = 4$ and $p = 16$. When considering a normalized FOV, those downsampling factors correspond to $\Delta\xi = \frac{1}{4}$, $\Delta\xi = 1$ and $\Delta\xi = 4$ respectively. For the case $p = 16$, we interleaved four sets of trajectories to fill the whole Cartesian grid (yielding a total of $64 \times 4 = 256$ samples), thus measuring enough information to reconstruct the image. Overall, the number of samples per line reached 1024, 256 and 256 for $p = 1$, $p = 4$ and $p = 16$ respectively.

In the case of spiral trajectories, we set $\delta t = 5\mu$s with the same field-of-view (FOV) of 20×20 cm^2. Spirals were designed using the method proposed in (Lee et al., 2003) and were made of 20 shots for a target resolution of 512×512. In that experiment, we studied the cases $p = 1$, $p = 2$ and $p = 8$. For the case $p = 8$, we interleaved 4 spirals to measure as much information as for $p = 2$ (yielding a total of $768 \times 4 = 3072$ samples). Overall, the number of samples per line reached 6144, 3072 and 3072 for $p = 1$, $p = 2$ and $p = 8$ respectively.

5.4.3 Filtering effects on experimental data

In order to validate the proposed model, we first reconstruct the images with Cartesian and spiral sampling using a simple conjugate gradient algorithm. The results are displayed in Fig. 5.6.

In the case of Cartesian trajectories, no filtering effects are observed for $p = 1$ (Fig. 5.6**a**). For $p = 4$, corresponding to a sampling pattern at Shannon's rate (i.e. $\Delta\xi = 1$), two black bands appear at the top and bottom of the image (Fig. 5.6**b**). For the image

on Fig. 5.6**c** corresponding to $p = 16$ (i.e. $\Delta\xi = 4$), four horizontal black bands can be observed and the object is cropped along the readout direction. This perfectly matches the effects described in Section 5.3.1 (Figs. 5.2-5.3). These results strongly suggest that the MR scanner applies a band-limiting filter to the temporal signal. We will provide further evidence of this observation in the next section.

In the case of spiral sampling, the image corresponding to $p = 1$ on Fig. 5.6**d** is near perfectly resolved. For $p = 2$, the image gets slightly more blurry and the contrast is slightly deteriorated. For $p = 8$, the effect gets disastrous, with some parts of the image disappearing and strong rotational blurs.

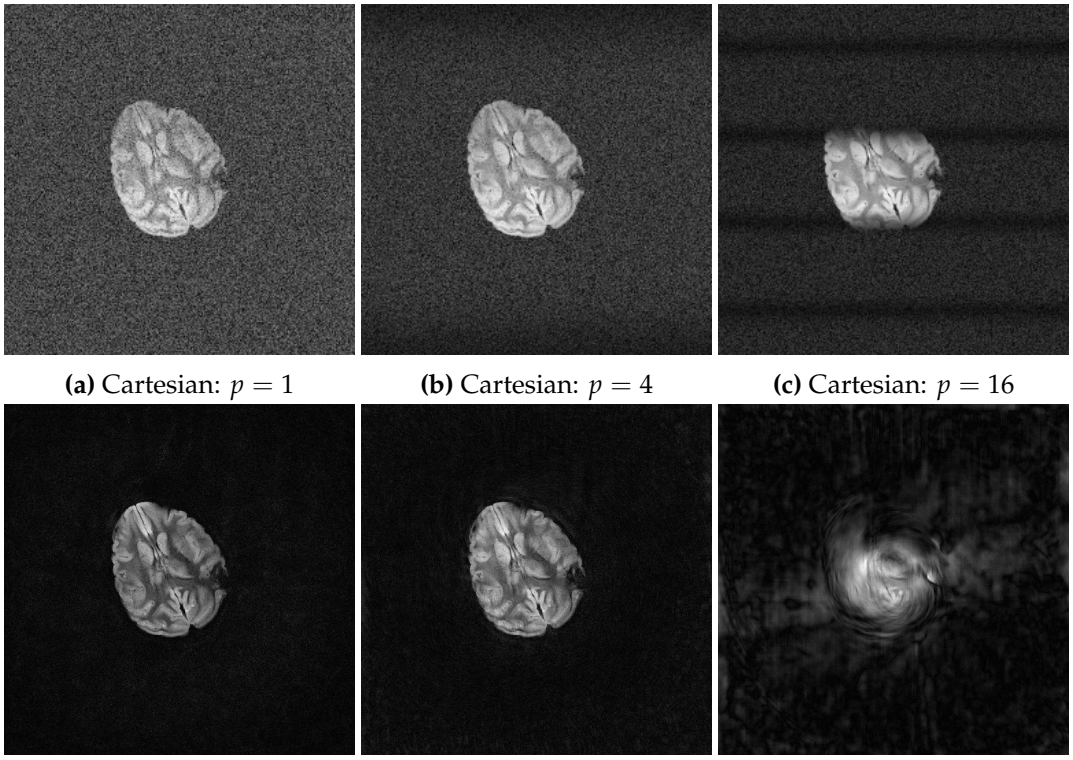

(a) Cartesian: $p = 1$ **(b)** Cartesian: $p = 4$ **(c)** Cartesian: $p = 16$

(d) Spiral: $p = 1$ **(e)** Spiral: $p = 2$ **(f)** Spiral: $p = 8$

FIGURE 5.6: Direct reconstruction results of real data for the Cartesian trajectories (top) and spiral trajectories (bottom) with different sampling periods. Here, we used a change of contrast to better highlight the effect.

5.4.4 Estimation of the filter

Problem (5.5) was solved to estimate the filter $\boldsymbol{h}$ by using both Cartesian and spiral data. We solved the problem for each shot and channel independently and then averaged the result to reduce the noise. Fig. 5.7 shows the mean filter $\boldsymbol{h}$ (red line) for the Cartesian and spiral experiments respectively. In both experiments, a sinc-like function can be identified, which supports that a near perfect band-limiting filter is used on the ADC.

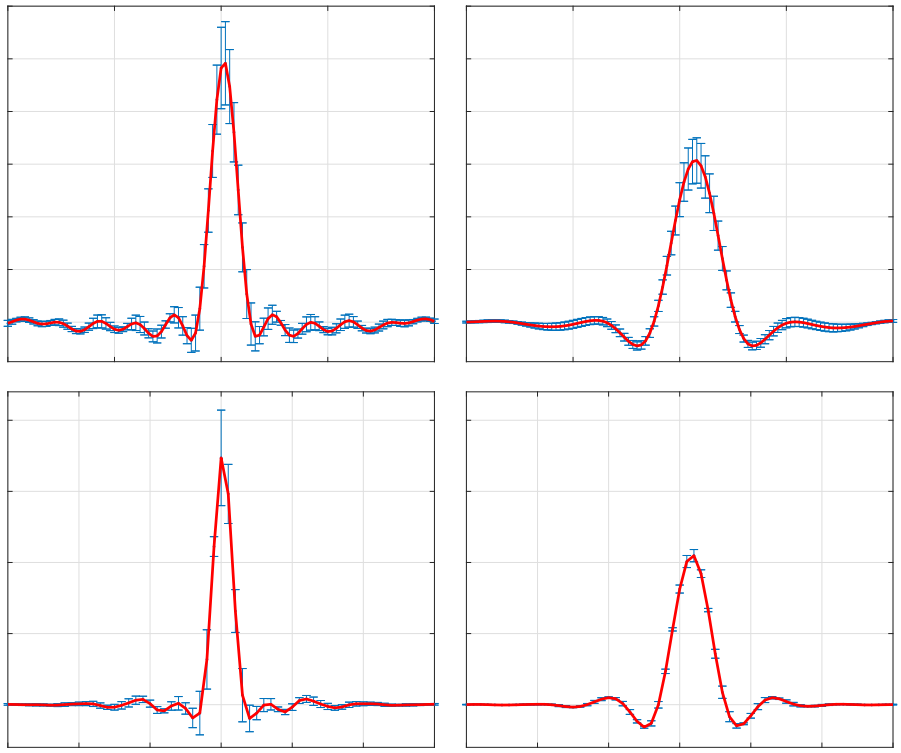

FIGURE 5.7: Mean and standard deviation for the estimated filters using the Cartesian data (top) and spiral data (bottom). For the Cartesian data, we used $p = 4$ (top left) and $p = 16$ (top right). For the spiral data, we used $p = 2$ (bottom left) and $p = 8$ (bottom right).

5.5 Handling the filtering effects in reconstruction algorithms

5.5.1 Discretizing the image

Let $n \in 2\mathbb{N}$ denote a resolution parameter. In this paper, we assume that the true magnetization u can be written as:

$$u = u_d \star \psi, \tag{5.6}$$

where

$$u_d = \sum_{-n/2 \leq i,j < n/2} \mathbf{u}[i,j]\delta_{i/n,j/n} \tag{5.7}$$

is an atomic discretization of the image with $\mathbf{u} \in \mathbb{C}^{n\times n}$ and $\psi : [-\epsilon,\epsilon]^2 \to \mathbb{R}$ is a compactly supported interpolation kernel. The interest of this decomposition lies in the fact that it will allow using nonuniform fast Fourier transforms.

The simplest interpolation kernel ψ is the spline of order 0:

$$\psi(x,y) = \begin{cases} 1 & \text{if } -1/(2n) \leq x,y < 1/(2n), \\ 0 & \text{otherwise.} \end{cases}$$

It will be used in all the experiments of this paper.

Remark 2 *Notice that the model* (5.7) *does not allow to reproduce any function u. An additional error term $\Delta u : \Omega \to \mathbb{C}$ should be added for completeness. We can however show that this term*

can be bounded in L^p under regularity assumptions on u. We refer the interested reader to the following book for more details (DeVore and Lorentz, 1993).

5.5.2 Fast implementation of the forward model

In order to reconstruct the image, nearly any reconstruction algorithm requires an implementation of the forward operator and its adjoint. In this section, we therefore propose a numerical algorithm to evaluate integrals of the form:

$$y_i = \int_{\mathbb{R}} h(i\Delta t - t)\hat{u}(\lambda(t))\, dt. \tag{5.8}$$

It is based on a combination of numerical integration and of the nonuniform Fast Fourier transform.

The NFFT

The atomic structure in (5.7) allows using the non uniform Fast Fourier Transform (NFFT or NUFFT) (Dutt and Rokhlin, 1993; Keiner et al., 2009a) to get a numerical expression of $\hat{u}$ at a set of locations $\boldsymbol{k} = (\boldsymbol{k}[0], \ldots, \boldsymbol{k}[m-1]) \in \mathbb{R}^{m\times 2}$ in the k-space. We let $\boldsymbol{k}_1$ and $\boldsymbol{k}_2$ denote the two spatial components of $\boldsymbol{k}$. The NFFT allows evaluating rapidly with a high precision, all components of $\hat{u}_d(\boldsymbol{k})$, defined by:

$$\hat{u}_d(\boldsymbol{k}[l]) = \sum_{\substack{-n/2\le i<n/2 \\ -n/2\le j<n/2}} \mathbf{u}[i,j] \exp(-2\imath\pi(i\boldsymbol{k}_1[l] + j\boldsymbol{k}_2[l])). \tag{5.9}$$

While a naive implementation of the sum would require $O(mn^4)$ operations, the NFFT reduces the complexity to $O(n^2\log(n) + m|\log(\epsilon)|^2)$, where ϵ is the desired precision. The constants involved in the O depend on the locations of the sampling points $\boldsymbol{k}$.

By using matrix-vector product notations, this can be rewritten as:

$$\hat{u}_d(\boldsymbol{k}) = \boldsymbol{N}_{\boldsymbol{k}}^* \mathbf{u},$$

where $\boldsymbol{N}_{\boldsymbol{k}}^* \in \mathbb{C}^{m\times n^2}$ is the NFFT matrix. Then, to get the values of $\hat{u}$, we simply use the formula: $\hat{u} = \hat{u}_d \odot \hat{\psi}$[2]. Overall, the mapping $(\mathbf{u}, \boldsymbol{k}) \mapsto \hat{u}(\boldsymbol{k}) = \hat{\mathbf{u}}$ is given by:

$$\hat{\mathbf{u}} = \hat{\psi}(\boldsymbol{k}) \odot \boldsymbol{N}_{\boldsymbol{k}}^* \mathbf{u}.$$

Remark 3 *When introducing the interpolating kernel ψ, we need to take special care of boundary conditions. The NFFT assumes periodic boundary conditions. In this work, we simply work with images surrounded by black, as is common in MRI, to avoid creating discontinuities on the boundaries.*

Integration along the curve

In order to compute the integrals (5.8), we propose to use simple numerical integration procedures. Letting $p \in \mathbb{N}$ denote an upsampling parameter, we shall use the following

[2]For two matrices, $\boldsymbol{A}$ and $\boldsymbol{B}$, of the same dimension, $m \times n$, the Hadamard product, $\boldsymbol{A} \odot \boldsymbol{B}$, is a matrix, of the same dimension as the operands, with elements given by $(\boldsymbol{A} \odot \boldsymbol{B})_{i,j} = (\boldsymbol{A})_{i,j}(\boldsymbol{B})_{i,j}$

approximation:

$$y_i = (h \star f)(i\Delta t) \simeq \sum_{j \in \mathbb{Z}} h_j \cdot \hat{u}(\lambda(i\Delta t - j\delta t)), \tag{5.10}$$

where $\delta t = \Delta t / p$ and where the weights h_j can be chosen either by using the estimation procedure proposed in Section 5.4.4 or taken equal to $h(j\delta t)$ if an analytical version of h is available. More advanced Newton-Cotes formula (Ralston and Rabinowitz, 2001) could also be used. The values $\hat{u}(\lambda(i\Delta t - j\delta t))$ can be evaluated efficiently with the NFFT, and the weights h_j only need to be computed once at the start of the algorithm. In practice, we typically use values of p in the range $\{1, \ldots, 8\}$.

The forward model $\boldsymbol{A}$ can now be completely described. Letting $\boldsymbol{k}$ denote the vector of discrete locations with components $\boldsymbol{k}[i] = \lambda(i\delta t)$ for $0 \leq i \leq mp - 1$, it takes the following form:

$$\boldsymbol{A}\mathbf{u} = \mathbf{H}\boldsymbol{\Sigma}_\psi \boldsymbol{N}_{\boldsymbol{k}}^* \mathbf{u},$$

where $\mathbf{H}$ is the operator that computes the sums in Eq. (5.10) and where $\boldsymbol{\Sigma}_\psi : \boldsymbol{z} \mapsto \hat{\psi}(\boldsymbol{k}) \odot \boldsymbol{z}$. The adjoint operator is given by:

$$\boldsymbol{A}^* = \boldsymbol{N}_{\boldsymbol{k}} \boldsymbol{\Sigma}_\psi^* \mathbf{H}^*.$$

Remark 4 *In the case of multiple coils, the forward model can be written as:*

$$\boldsymbol{A}\mathbf{u} = \begin{pmatrix} \mathbf{H}\boldsymbol{\Sigma}_\psi \boldsymbol{N}_{\boldsymbol{k}}^* \boldsymbol{\mathcal{S}}_1 \mathbf{u} \\ \vdots \\ \mathbf{H}\boldsymbol{\Sigma}_\psi \boldsymbol{N}_{\boldsymbol{k}}^* \boldsymbol{\mathcal{S}}_{n_c} \mathbf{u} \end{pmatrix},$$

where $\boldsymbol{\mathcal{S}}_k = \mathrm{diag}(\boldsymbol{s}_k)$ is the diagonal matrix associated to the k-th sensitivity profile and n_c is the total number of receiver coils.

5.5.3 Reconstruction algorithms

Once the forward operator and its adjoint are properly described, most existing algorithms can be used out of the box. In this work, we implemented simple linear reconstructions based on the linear conjugate gradient method and more advanced nonlinear approaches. Other methods such as GRAPPA, SMASH, SENSE or ESPIRIT (Larkman and Nunes, 2007), could be easily modified to account for the integration too.

Estimating the sensitivities

In all the experiments performed in this paper, we first acquire a reference image with a standard Cartesian trajectory sampled at twice Shannon's rate along the readout direction. This allows to simply estimate the sensitivities by using the sum-of-square approach (McKenzie et al., 2002).

Linear reconstructions

One of the simplest ways to reconstruct an image is to solve the following Tikhonov-regularized least squares problem:

$$\min_{\mathbf{u} \in \mathbb{R}^n} \frac{1}{2} \|\boldsymbol{A}\mathbf{u} - \boldsymbol{y}\|_2^2 + \frac{\alpha}{2} \|\mathbf{u}\|_2^2.$$

The optimality conditions for this problem read

$$(\boldsymbol{A}^*\boldsymbol{A} + \alpha I)\mathbf{u} = \boldsymbol{A}^*\boldsymbol{y},$$

which can be solved with an iterative solver. In this paper, we simply use a linear conjugate gradient method (Ralston and Rabinowitz, 2001).

Nonlinear reconstructions

Nonlinear reconstructions are known to yield better results than linear ones, especially in the regime of subsampled data. The whole field of compressed sensing (Lustig et al., 2007a; Candès et al., 2006), which under certain assumptions guarantees exact reconstructions, is based on ℓ^1-regularized problems. In this paper, our nonlinear reconstructions are based on the resolution of the following problem:

$$\min_{\mathbf{u}\in\mathbb{R}^n} \frac{1}{2}\|\boldsymbol{A}\mathbf{u} - \boldsymbol{y}\|_2^2 + \alpha R(\mathbf{u}), \tag{5.11}$$

where $R : \mathbb{C}^{n^2} \to \mathbb{R} \cup \{+\infty\}$ is a regularization term describing some prior information on the image that is sought for. This type of problem can be solved efficiently by using a Douglas-Rachford algorithm (Combettes and Pesquet, 2011). Letting $f(\mathbf{u}) = \frac{1}{2}\|\boldsymbol{A}\mathbf{u} - \boldsymbol{y}\|_2^2$, it reads as follows:

1. *Input:* initial guess $\boldsymbol{v}_0 \in \mathbb{C}^{n^2}$ and parameter $\gamma > 0$.
2. $\mathbf{u}_k = \mathbf{prox}_{\gamma f}(\boldsymbol{v}_k)$.
3. $\boldsymbol{v}_{k+1} = \boldsymbol{v}_k - \mathbf{u}_k + \mathbf{prox}_{\gamma\alpha R}(2\mathbf{u}_k - \boldsymbol{v}_k)$.

The proximal operators $\mathbf{prox}_{\gamma f}$ and $\mathbf{prox}_{\gamma\alpha R}$ are defined by:

$$\mathbf{prox}_{\gamma f}(\boldsymbol{z}) = \underset{\mathbf{u}\in\mathbb{C}^{n^2}}{\arg\min} \frac{\gamma}{2}\|\boldsymbol{A}\mathbf{u} - \boldsymbol{y}\|_2^2 + \frac{1}{2}\|\mathbf{u} - \boldsymbol{z}\|_2^2 \tag{5.12}$$

and by

$$\mathbf{prox}_{\gamma\alpha R}(\boldsymbol{z}) = \underset{\mathbf{u}\in\mathbb{C}^{n^2}}{\arg\min}\, \gamma\alpha R(\mathbf{u}) + \frac{1}{2}\|\mathbf{u} - \boldsymbol{z}\|_2^2. \tag{5.13}$$

The step 2. above can be interpreted as the resolution of the inverse problem using Tikhonov regularization. It can be solved using a linear conjugate gradient algorithm. The step 3. can be interpreted as a *denoising* step. Depending on the prior R, different algorithms can be used. The sequence $(\mathbf{u}_k)_{k\in\mathbb{N}}$ can be proved to converge to a global minimizer of (5.11) if R is a convex closed function with nonempty interior. In this work, we define R as the total variation of the image (Chambolle et al., 2010) and solve the proximal step (5.13) with the method proposed in (Weiss et al., 2009).

Remark 5 *Notice that total variation regularization is a simple prior leading to decent results, but suffering from some defects such as staircasing effect. More advanced denoising methods such as BM3D (Dabov et al., 2007) image can be used instance, as was proposed in the plug-and-play-prior algorithm (Venkatakrishnan et al., 2013).*

5.6 Reconstruction results

In this section, we will demonstrate how the proposed reconstruction algorithms perform on simulated and experimental data compared to traditional approaches.

5.6.1 Simulated data

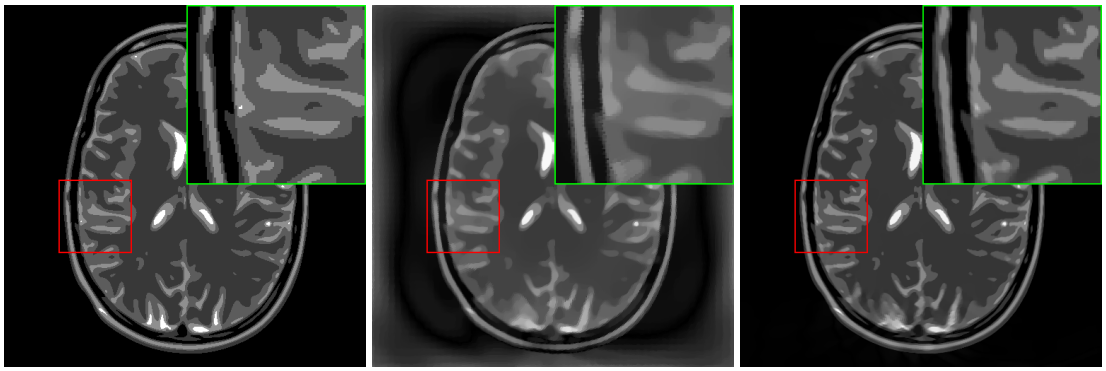

(a) Truth **(b)** Standard reconstruction **(c)** Proposed reconstruction

FIGURE 5.8: Reconstructions of the brain phantom image sampled along the spirals of Fig. 5.4 without (**b**) and with (**b**) accounting for the band-limiting filtering effects.

We first consider the experiment of Section 5.3.1, in which the spiral sampling pattern of Fig. 5.4 was used to simulate measurements of a brain phantom incorporating the band-limiting filtering with $p = 2$. Fig. 5.8**b** displays the brain phantom image reconstructed with the nonlinear algorithm of Section 5.5.3 that does not include the filtering in the forward model. Note that this corresponds to the standard MR reconstruction. We reconstructed the same data with the method proposed in Section 5.5, which accounts for the filtering effect. The result is displayed in Figure 5.8**c**. By looking at the magnified regions, we notice that the proposed reconstruction was able to recover the fine structural details present in the ground truth image (Fig. 5.8**a**), which had disappeared in the standard reconstruction (Fig. 5.8**b**).

Remark 6 *In all experiments, the regularization parameter α of Eq.* (5.11) *was manually tuned so as to produce the best possible result. We had to take it larger for the standard model, otherwise, strong oscillations would have appeared in the reconstructed image, with no significant increase in the level of details.*

To further highlight the gain of resolution offered by the proposed approach, we repeated the same experiment with a synthetic image displayed in Fig. 5.9. Here, we used another four-interleaved spiral which samples the k-space with a variable density decaying as the frequencies get higher. Images reconstructed with the standard method and the proposed approach are displayed in Fig. 5.9**a** and 5.9**b**, respectively. Notice how the resolution is enhanced by including the filtering effect in the forward model.

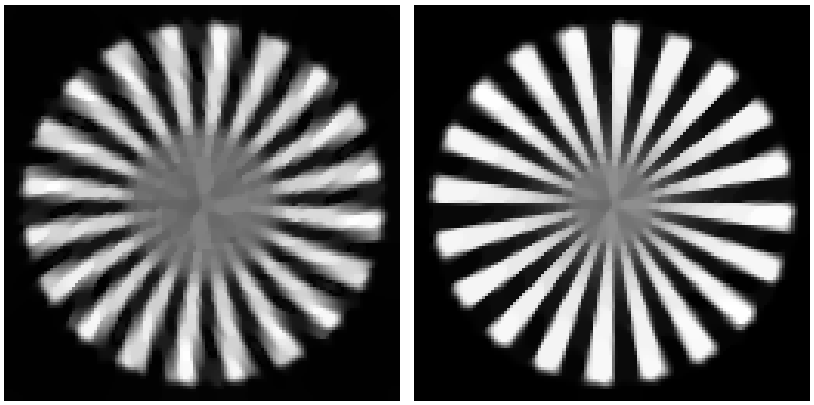

(a) Standard **(b)** Proposed

FIGURE 5.9: Reconstruction with and without the band-limiting filtering accounted for.

5.6.2 Experimental data

The proposed acquisition model and reconstruction schemes were tested on experimental data acquired from both spiral (Lee et al., 2003) and SPARKLING (Boyer et al., 2016; Chauffert et al., 2017; Lazarus et al., 2017) sampling patterns.

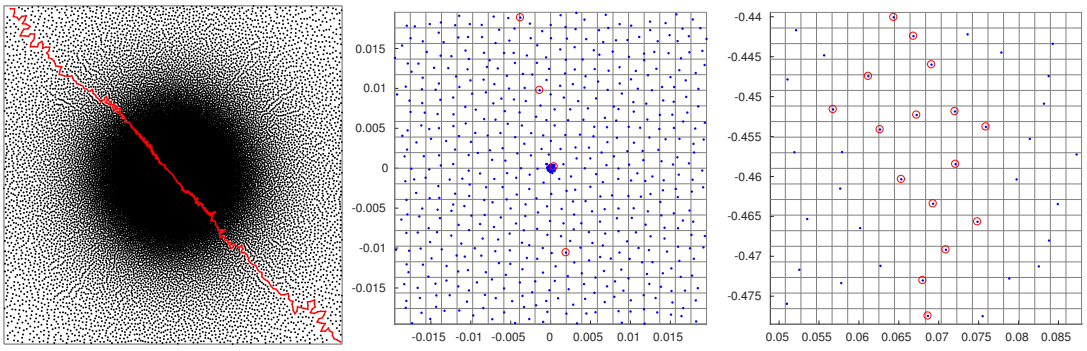

(a) The whole trajectory **(b)** Zoom in the center **(c)** Zoom at the periphery

FIGURE 5.10: Sparkling trajectory and magnified regions of central and peripheral parts.

Spiral sampling

The spiral trajectory used for the acquisition was the same as in Section 5.4.3 for $p = 8$. The reconstruction results are displayed in Fig. 5.11. In this example, we simply used a linear reconstruction algorithm based on the conjugate gradient since the subsampling factor was not large and 32 receiver channels were used. Even though the reconstruction accounting for the filtering effect is not perfect it is clearly far superior to a standard reconstruction.

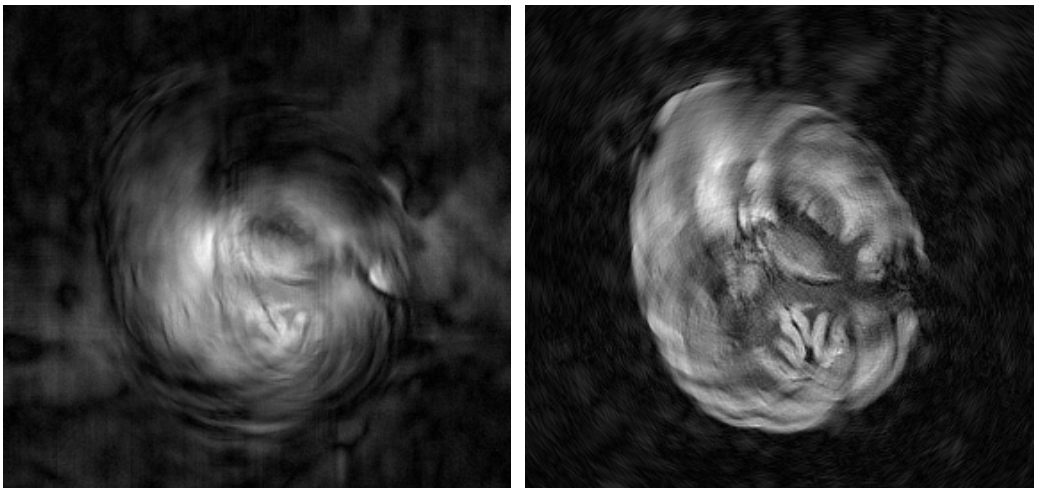

(a) Standard **(b)** Proposed

FIGURE 5.11: Linear reconstructions of an *ex vivo* baboon brain acquired with a spiral trajectory, with (**b**) and without (**b**) the band-limiting filtering accounted for. Acquisitions were prospectively performed on a 7 Tesla MR scanner.

Sparkling sampling

The recently introduced SPARKLING trajectories are novel non-Cartesian trajectories that produce optimal sampling patterns by taking full advantage of the hardware abilities (Boyer et al., 2016; Chauffert et al., 2017; Lazarus et al., 2017).

Remark 7 *This project actually began thanks to these new trajectories. Our first attempts to use those trajectories led to unsatisfactory reconstruction results. We understood after long investigations that the main problem was related to the ADC filtering, which motivated us to do this work. While the results presented for the spiral trajectory were mainly of tutorial value, since we artificially increased the sampling period Δt, the results presented in this paragraph are based on completely realistic data.*

The trajectory used in our experiments consisted of 128 shots composed of 512 samples each for a target resolution of 512×512, corresponding to a subsampling factor of 4. A typical trajectory is displayed in Fig. 5.10. Magnified regions of its center and periphery are displayed in Fig. 5.10**b** and 5.10**c** respectively. As can be seen, the distance between consecutive samples is larger than one pixel, be it in the central region or at the k-space boundary. These large gaps are related to the fact that the trajectory λ goes at the maximal speed offered by the hardware.

An *ex vivo* human brain was imaged and reconstructed with a standard nonlinear reconstruction algorithm and with the proposed method. The results are displayed in Fig. 5.12. Once again, the improvement of quality allowed by the proposed approach is striking, especially in the temporal lobes of the brain.

5.7 Discussion and conclusion

In this work, we illustrated how the anti-aliasing filters implemented in analog-to-digital converters could be detrimental to the good reconstruction of MR images. Depending

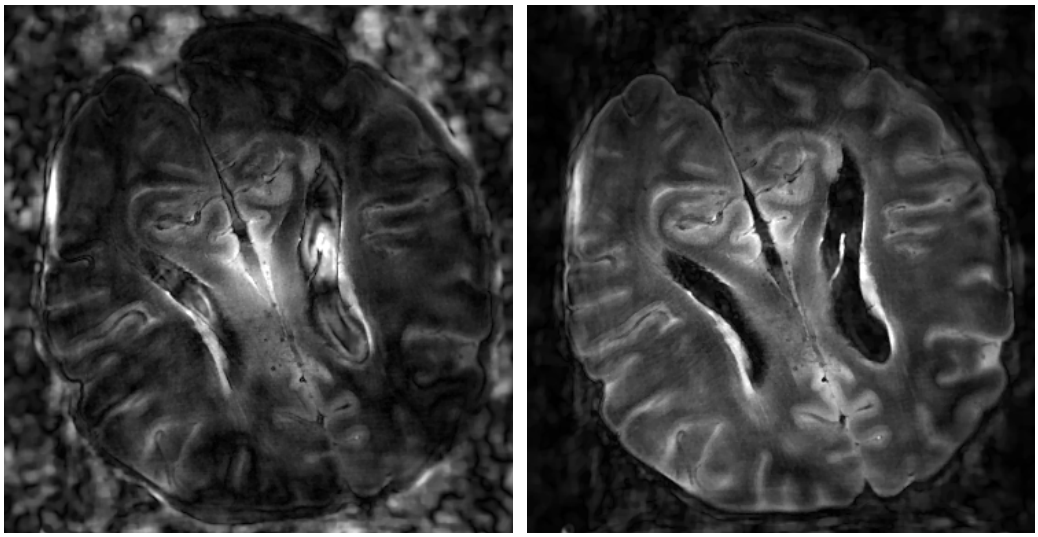

(a) Standard **(b)** Proposed

FIGURE 5.12: Nonlinear reconstructions of *ex vivo* humain brain with a Sparkling trajectory, with (**b**) and without (**b**) the band-limiting filtering accounted for. Acquisitions were prospectively performed on a 7 Tesla MR scanner.

on the speed of the trajectory and on the sampling period, these filters can have dramatic effects, with irreversible loss of information. To the best of our knowledge, these effects were ignored until now in the literature. We proposed novel numerical algorithms to mitigate them, yielding far superior reconstruction results than current approaches for some modern trajectories. This enhanced quality comes at the expense of a higher numerical complexity, with computing times typically multiplied by factors ranging from 2 to 4 compared to standard approaches.

At this point, the reader may wonder why such anti-aliasing filters are actually implemented in practice. While they make perfect sense when the aim is to sample a purely temporal signal $f(t) = \hat{u}(\lambda(t))$ using Shannon's theory, their pertinence becomes less obvious when it comes to the reconstruction of spatial MR images u, especially with modern nonlinear reconstruction algorithms.

Let us consider their pros and cons. On the positive side, filtering allows to *reduce noise* and *increase the signal-to-noise-ratio*, which may sometimes be critical when little signal is available. In addition, it allows to *reduce the number of measurements* and hence leads to faster reconstruction algorithms. Those two arguments are probably the main ones explaining the very existence of these filters. In addition, it is physically impossible to measure pointwise values of f, and the filtering is an effect that cannot be avoided, up to the temporal resolution of the ADC. On the negative side, *applying filters trades temporal resolution for signal-to-noise-ratio*. It is however well known in the field of inverse problems that it is *much harder to gain resolution than signal-to-noise-ratio*. State-of-the-art denoisers are close to being unbeatable (Chatterjee and Milanfar, 2010), while blurring induces an irreversible loss of information.

Overall, we believe that the increase of computational power using massively parallel architectures, makes the arguments supporting the filtering partly irrelevant. We hope that the current manuscript may motivate vendors to use or design different ADCs. For instance, a striking side-result of this work is that the older technology of integrating

ADC is somewhat preferable to more complex band-limiting ADCs, since the integrating filters do not cause an irreversible loss of information (compare Fig. 5.2 and Fig. 5.3). In addition, our analysis suggests to use *time-varying sampling periods*. In the center of the k-space, a lot of signal is usually available, allowing to use very short sampling periods. In contrast, as the sampling trajectory gets more distant to the center, the sampling period should increase to account for the signal decay.

The key factor to know whether a trajectory is acceptable or not for standard reconstruction methods is the maximal distance between consecutive samples. Nearly no effect should be observed below half a pixel, slight effects will be observed between half a pixel and 1.5 pixels, and significant problems should appear beyond. The recent advances in sampling theory advocate the use of more complex trajectories with high speeds (Weiger et al., 2017; Mansfield, 1977; Ahn et al., 1986; Lazarus et al., 2017) that may cross the critical regime of sampling distances. All those arguments make us believe that the proposed analysis and algorithmic framework may play an important role in the future.

Conclusion

Contributions

SPARKLING

In this PhD manuscript, we developed and applied a new optimization-driven method called SPARKLING to design optimal sampling patterns for MRI in the context of compressed sensing to speed up the acquisition time. Perhaps, to conclude this work, we could remind and answer the few questions that were raised in the introduction:

Will the gradient system be able to play out these complex gradient waveforms?
The answer is positive at least on our SIEMENS gradient system. This was directly verified by measuring the actual spatially-resolved phase while playing out a SPARKLING shot, using a local phase measurement method (Schneider et al., 2011). Despite the erratic aspect of the gradient waveform and its slew rate, this experiment proved that the gradient system was very faithful, yielding a NRMSE smaller than 1%.

Furthermore, these non-Cartesian trajectories were successfully used for prospective acquisitions at 7 Tesla both *ex vivo* and *in vivo* on healthy volunteers. For high resolution T_2^*-weighted 2D *in vivo* brain imaging, they were shown to substantially speed up the acquisition time while maintaining very good image quality, which would not be possible if substantial gradient errors occurred. Typically, for a high in-plane resolution of 390 μm, 11 slices could be acquired in just 14 seconds, instead of almost 5 minutes for the fully-sampled Cartesian reference.

Is this method competitive with other non-Cartesian trajectories such as spiral imaging, which is considered as the most efficient sampling?
Most interestingly, our 2D T_2^*-weighted segmented experiments showed that the SPARKLING patterns were as efficient as variable-density spiral trajectories (Lee et al., 2003) in the context of compressed sensing. Because samples are spread out as much as possible along one curve, a SPARKLING shot can cover a large portion of k-space just like spiral. Moreover, in the most accelerated scenarios, the images acquired with a variable-density spiral presented important artifacts of which the SPARKLING images were devoid. This suggests that the SPARKLING trajectories may be a good alternative to segmented spiral imaging, offering more flexible design as well. Compared to radial trajectory – which are admittedly not as efficient as spiral imaging especially in a long-readout setup – SPARKLING-acquired images yielded a visibly superior image quality both in 2D and 3D acquisitions.

How sensitive to imaging and system imperfections are SPARKLING trajectories?
Non-Cartesian trajectories are well-known to be sensitive to imaging and system imperfections including off-resonance effects and physiological motion. In the case of our long-readout experiments, we observed that SPARKLING acquisitions seemed relatively less sensitive to these imperfections than the tested variable-density spirals, and the gap was widening as the acceleration factor increased.

Is SPARKLING interesting for all imaging protocols?
SPARKLING was used successfully both for 2D and 3D imaging at 7 Tesla and 3 Tesla. In 2D, T_2^*- and T_1-weighted images were acquired using this method. In 3D, SPARKLING trajectories allowed to perform T_2^*- and susceptibility-weighted imaging. Limitations will be discussed below.

Other contributions

In this work, we also gave a theoretical introduction of the application of compressed sensing in MRI and highlighted the current limitations in the theory. Based on simulations and prospective experiments, an empirical study allowed to gave some qualitative and quantitative guidelines on the degree of acceleration applicable in a given setup of resolution and SNR. Our objective was to show to the MR community, with a T_2^*-weighted image example, that depending on the input SNR and the target resolution there is only a restricted range where compressed sensing can radically reduce the acquisition time. To our knowledge, it is the first time that an extensive study is done on the relationship existing between input SNR and acceleration factor in the context of compressed sensing. Our findings confirm in particular that the benefit is much higher when targeting high resolution as long as the input SNR can be maintained. It also highlights that beyond a certain threshold for a given acceleration, no more improvement can be expected regardless of the input SNR.

Finally, we proposed a new acquisition model and the adapted nonlinear reconstructions that take into account the ADC filtering effects. Our approach thus incorporates the implicit averaging that is performed when sampling along continuous k-space curves. Simulations and prospective acquisitions allowed to evaluate these model-based algorithms. In particular, they enabled to correct almost perfectly the important artifacts that were present in an image acquired with a SPARKLING trajectory. Hence, the proposed reconstruction could serve as an efficient safeguard against ADC filtering effects for very fast trajectories typically.

Limitations

Although T_1-weighted images were acquired with a variable-density SPARKLING trajectory, it is quite obvious that SPARKLING's best results were obtained for rather long readouts. When the time and the hardware constraints allow it, the output trajectory is able to substantially wiggle around the initial support, thus increasing the sampling efficiency while distributing along the target density. We gave earlier a practical rule for best usage of SPARKLING: the ratio of the number of gradient steps per shot to the image size should be as high as possible. As regards high resolution, long-readout scenarios will maximize this ratio and thus optimize SPARKLING performance, while short-readout acquisitions allow for less departure from simple geometric trajectories. In the latter case, a radial initialization will not be drastically transformed by the proposed algorithm because the constraints do not permit it. In the most extreme case, at maximum speed on a line for instance, we expect little room for improvement. When considering lower resolutions however, our method can still be promising. Hence, there exists a limited regime where the SPARKLING method can substantially improve sampling patterns.

Regarding 3D SPARKLING, it was observed that the fully 3D implementation of the method (as opposed to stacks) did not perform as well as expected. This is most probably due to the fact that all the shots are not generated together, so that the global distribution of all the samples do not look as neat as in 2D SPARKLING. This limitation is due to the development time it would have a taken to code an efficient algorithm.

Perspectives

Many more studies and developments could be imagined in the framework of SPARKLING. For instance, trajectories with anisotropic densities adapted to specific organs could be designed. Since the Fourier content of a knee does not have the same structure as the k-space of a brain, the target density could be changed depending on the object to image.

Although SPARKLING images looked correct without any correction of imaging imperfections, it would be interesting to correct for instance static field inhomogeneities or trajectory errors and see the improvement in image quality. To this end, we intent to use a multi-frequency interpolation method (Man et al., 1997) to handle field inhomogeneities based on a field map. Regarding dynamic phase correction, a Skope camera was recently acquired at NeuroSpin and will hopefully be quickly used to monitor SPARKLING acquisitions. In this setup, it would be interesting to do again the comparison with spiral trajectories.

Regarding the improvement of the method, the 3D algorithm would benefit from some development regarding the calculation of the summation term with the help of NFFT-based fast summation. This may enable to generate multiple shots at once. This work will be addressed soon in the SILICOSMIC research project owing to a close collaboration with La *Maison de la Simulation* at CEA.

Closing remarks

All in all, we provided a flexible optimization-based tool to generate more exotic and pertinent k-space trajectories. We applied this tool successfully to MRI, where it could be used for many other applications, but this elegant framework could also serve other scientific fields (e.g., electronic microscopy) and, perhaps, more artistic purposes.

Résumé en français

Afin d'augmenter significativement la résolution spatio-temporelle des images IRM acquises à très haut champ magnétique, une possibilité consiste à accroître la vitesse d'acquisition en sous-échantillonnant massivement l'espace de Fourier (ou k-space). La théorie récente du Compressed Sensing ou de l'échantillonnage compressif apporte une solution théorique élégante à ce problème et permet de plus de réduire les distorsions dans les images, mais les conditions de sa mise en oeuvre pratique (échantillonnage aléatoire indépendant) la rendent peu utilisée en pratique en IRM en raison des contraintes physiques d'acquisition (trajectoires d'échantillonnage continues voire plus régulières, gradients bornés, vitesse de commutation limitée, ...). Dans ce contexte, des travaux théoriques récents (Boyer et al., 2016) ont permis de produire, dans un cadre simulé ou rétrospectif, des trajectoires d'échantillonnage satisfaisant les contraintes d'acquisition tout en minimisant le temps d'acquisition. Cette technique, rebaptisée SPARKLING (Spreading Projection Algorithm for Rapid K-space sampLING), s'appuie sur un algorithme de projection qui permet de générer des schémas d'échantillonnage optimaux pour l'IRM en alliant efficacité et une distribution des échantillons adaptée à la théorie de l'échantillonnage compressif. Cette méthode a été appliquée sur la plateforme d'imagerie clinique à 7 Teslas de NeuroSpin et a permis d'accélérer significativement l'imagerie haute résolution pondérée en T_2^*. Ses performances ont été comparées aux techniques standards d'imagerie non-cartésiennes (radial, spiral). La méthode a également été étendue à l'imagerie 3D à travers plusieurs stratégies.

Chapitre 1

Ce premier chapitre rappelle les fondamentaux de l'IRM et introduit les outils qui seront utilisés dans les chapitres suivants. Il commence par expliquer l'origine du signal mesuré en IRM, la façon dont il est mesuré et comment il est manipulé par le biais de séquences de gradients de champ magnétique pour produire des images de l'intérieur du corps humain. L'accent est mis sur l'encodage entre l'image et sa transformée de Fourier discrète, appelée dans le jargon de l'IRM «k-space »ou espace-k, où k désigne la fréquence spatiale. L'échantillonnage de l'espace-k se fait le long de courbes régulières et de manière segmentée pour l'IRM anatomique car le signal que l'on mesure décroît vers zéro très rapidement. Il faut donc plusieurs segments, aussi appelés *shots* en anglais, pour remplir l'espace de Fourier de l'objet imagé et lui appliquer une transformée de Fourier inverse pour obtenir l'image. Un état de l'art des différentes méthodes d'échantillonnage en IRM est présenté pour l'imagerie 2D et 3D. Aussi, des outils nécessaires à la reconstruction de données non-Cartésiennes sont détaillés. Enfin l'intérêt des hauts champs magnétiques est discuté. Ils permettent notamment d'utiliser le gain en signal-sur-bruit pour augmenter la résolution. Cependant, plus la résolution de l'image est grande, plus le nombre de données à acquérir pour remplir la grille de l'espace-k est grand, et donc

plus le temps d'acquisition augmente. Cette constatation nous amène au chapitre suivant qui introduit l'Échantillonnage compressif et son application en IRM pour réduire le temps d'acquisition.

Chapitre 2

Ce chapitre introduit l'Échantillonnage compressif et explique tout d'abord sa théorie, et dans quelles conditions elle s'applique. l'Échantillonnage compressif nous dit qu'il est possible de sous-échantillonner[3] des signaux compressibles (i.e., parcimonieux dans une certaine représentation), et toujours être capable de les reconstruire fidèlement si des reconstructions adaptées sont utilisées. Si cette théorie est bien établie dans le cadre des mesures aléatoires gaussiennes, elle l'est beaucoup moins quand il s'agit de l'IRM, où l'échantillonnage et le signal sont structurés. Dans le cas de l'IRM par exemple, les mesures doivent être plus fréquentes dans les basses fréquences que dans les hautes fréquences: on parle d'échantillonnage à densité variable. Après avoir discuté les limites actuelles de la théorie de l'Échantillonnage compressif en IRM, il est entrepris d'étudier sa zone d'applicabilité de manière empirique. En effet, la théorie est aujourd'hui incapable de prédire le facteur de sous-échantillonnage R utilisable pour une certaine situation, alors que ceci serait extrêmement utile à la communauté de l'IRM. Ainsi, pour un contraste T_2^*, une méthodologie est présentée et appliquée pour déterminer quantitativement le facteur de sous-échantillonnage maximal R_{max} qui permet d'assurer une certaine

[3] c'est-à-dire de mesurer le signal à une fréquence d'échantillonnage au-dessous de celle dictée par le théorème de Nyquist-Shannon.

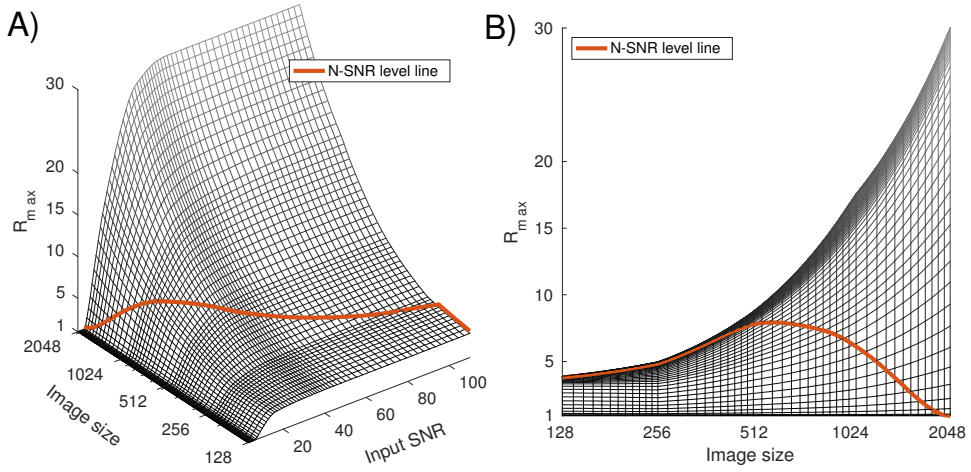

FIGURE 1: Résultats empiriques de la variation du facteur d'accélération maximal R_{max} permettant d'assurer une qualité d'image exprimée par $SSIM \leq 0.9$ en fonction de la taille de l'image (*image size*) et le rapport signal-sur-bruit (RSB) des données (input *SNR* sur l'axe de la figure). A) Vue 3D et B) projection 2D du graphe sur le plan $(R_{\max}, N)$. La ligne orange représente la relation expérimentale entre la taille de l'image et le RSB pour une séquence donnée pour le scanner 7 Teslas de NeuroSpin. Elle a été projetée sur la surface R_{max} pour permettre de lire directement quels sont les facteur de sous-échantillonnage permis en pratique: seuls les facteurs situés *sous* cette ligne orange permettent de préserver la qualité d'image souhaitée (voir B)).

qualité d'image en fonction de la résolution de l'image (N) et du niveau de bruit dans les données (input SNR). La qualité d'image est quantifié par la métrique de la similarité en structure ou SSIM qui varie entre 0 et 1, où 1 correspond au meilleur score (Wang et al., 2002). Ces résultats sont montrés sur la figure 1.

Chapitre 3

Après avoir mieux compris la zone d'applicabilité de l'échantillonnage compressif, est présenté le coeur de cette thèse, à savoir la conception et l'utilisation de nouvelles trajectoires d'échantillonnage adaptées à l'échantillonnage compressif. La méthode repose sur un algorithme d'optimisation présentée dans (Boyer et al., 2016) qui permet de générer des courbes d'échantillonnage avec une densité contrôlée et un étalement optimal des échantillons tout en respectant les contraintes de l'IRM en termes de vitesse et d'accélération maximale. Le schéma en figure 2 explique le procédé de la méthode, baptisée SPARKLING pour Spreading Projection Algortihm for Radid K-space samplING, et comment elle permet d'améliorer les trajectoires existantes, notamment leur fonction d'étalement de point (PSF pour *point spread function* en anglais).

Dans ce chapitre, cet outil a été utilisé pour générer des trajectoires 2D avec une densité variable optimisée pour une haute résolution planaire de 390 μm. Les résultats *in vivo* acquis avec une séquence écho de gradients à 7 teslas pour un contraste T_2^* sont présentés sur la figure 3. Tout d'abord, on peut observer que la méthode SPARKLING demeure très proche de la référence cartésienne échantillonnée à Nyquist, malgré son temps d'acquisition 20 fois plus court. En revanche, l'acquisition spirale à densité variable (Lee et al., 2003) présente beaucoup d'artefacts qui sont probablement dûs à l'inhomogénéité du champ magnétique et/ou à des erreurs de trajectoire. Enfin, la méthode radiale, beaucoup trop accélérée est floue et présente des artefacts de stries. Ces expériences nous ont permis de valider les performances de la méthode SPARKLING: des trajectoires non seulement efficaces mais aussi avec une densité variable maîtrisée permettent une application optimale de l'échantillonnage compressif. La méthode présentée semble également être relativement plus robuste aux imperfections de l'acquisition comparée à la spirale très sensible (Yudilevich and Stark, 1987).

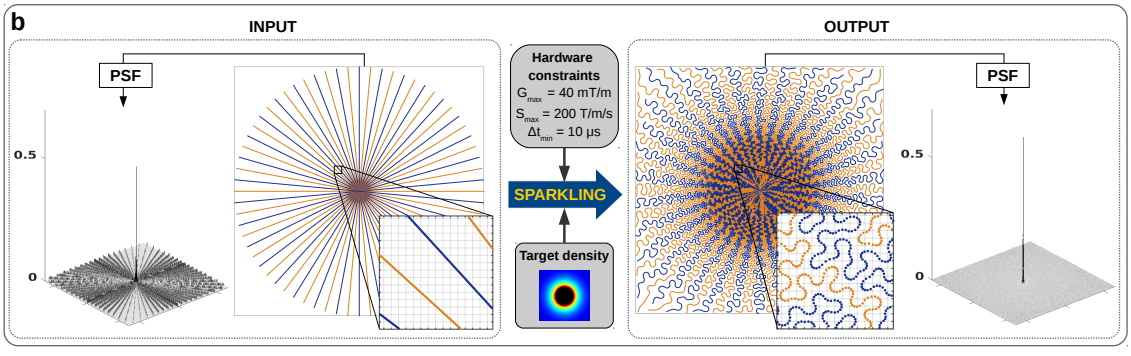

FIGURE 2: **Génération des trajectoires SPARKLING**. L'amplitude maximale du gradient et sont slew rate sont $G_{max} = 40\,\mathrm{mT/m}$ et $S_{max} = 200\,\mathrm{T/m/s}$ respectivement. La durée de chaque segment était de 30.72 ms. La méthode SPARKLING appliquée sur des lignes radiales pour une densité variable pour $N = 512$ et 34 segments symétriques ($AF = 15$, $R = 2.5$).

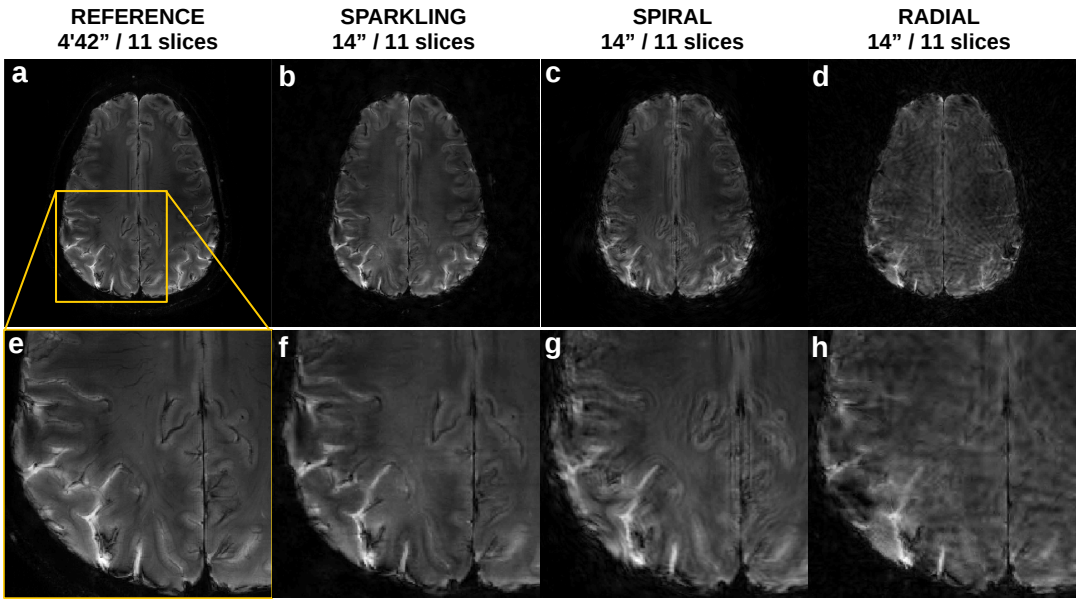

FIGURE 3: **Validation *in vivo* des trajectoires SPARKLING à densité variable pour un facteur d'accélération de 20 et comparison avec les stratégies spirale et radiale**. Des acquisitions pondérées en T_2^* réalisées sur un scanner 7 teslas à une resolution de 390 μm $\times$ 390 μm $\times$ 3 mm. **a**,**e**, Référence cartésienne échantillonnées à Nyquist pour un temps d'acquisition de 4 min 42 s et un zoom sur une région d'intérêt dans le cortex parieto-occipital (boite jaune). **b**,**f**, Image et zoom reconstruits à partir d'une acquisition SPARKLING accélérée 20 fois qui durait 14 s. **c**,**g**, Image et zoom reconstruits à partir d'une acquisition spirale accélérée 20 fois qui durait 14 s. **d**,**h**, Image et zoom reconstruits à partir d'une acquisition radiale accélérée 20 fois qui durait 14 s. (La reconstruction des images n'incluait aucune correction.)

Chapitre 4

Au vue des performances prometteuses de la méthode SPARKLING en 2D, l'approche a été étendue à l'imagerie 3D. Plusieurs approches ont été explorées. Tout d'abord, comme il est coutûme de faire pour les trajectoires radiale et spirale, une trajectoire 3D peut se réaliser en empilant des trajectoires SPARKLING 2D. C'est ce qu'on appelle en IRM «stack-of-Sparkling» (SOS). En outre, l'algorithme SPARKLING a été étendu en 3D avant de réaliser des trajectoires «complètement 3D». Les trois différentes stratégies SPARKLING sont présentées en figure 4. Deux SOS sont considérées: l'une régulière en figure 4**a** nommée «SOS régulier»et l'autre à densité variable selon la troisième direction en figure 4**b** nommée «z-vd SOS». Enfin, une trajectoire complètement 3D nommée «SPARKLING 3D» est étudiée en figure 4**c**.

Ces différentes méthodes ont été comparées sur un cerveau de babouin *ex vivo* et il a été observé que la stratégie z-vd SOS était la plus prometteuse parmi les trois méthodes étudiées, surtout pour des facteurs d'accélération importants. C'est pour cela que cette dernière a été utilisée pour une série de comparaison à d'autres stratégies 3D usuelles et à facteur d'accélération important dont les résultats apparaissent en figure 5. Il a été montré que la méthode permettait de réduire un temps d'acquisition de 14 min (iPAT

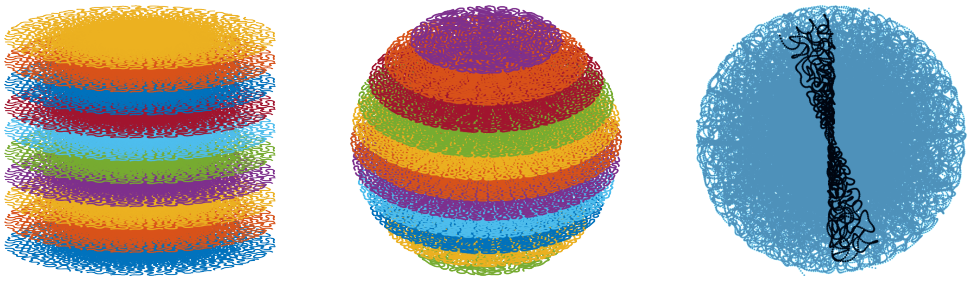

(a) SOS régulier **(b)** z-vd SOS **(c)** SPARKLING 3D

FIGURE 4: Trois différentes trajectoires SPARKLING tridimensionnelles. (a), SOS régulier: empilement de la même trajectoires SPARKLING. 11 plans sont représentés et forment un cylindre. (b), z-vd SOS: empilement de trajectoires SPARKLING dont la densité et le nombre de shots varient en fonction de l'altitude. 11 plans sont représentés et forment une boule. (c), 3D SPARKLING: une trajectoire complètement 3D pour 60 segments.

4^4) à seulement 45 secondes, tout en préservant la qualité de l'image pour une résolution isotrope de 0.6 mm et une tranche de $20 \times 20 \times 14\,\text{cm}^3$. Comme on peut le voir sur la figure 5, l'approche SPARKLING donne des résultats bien meilleurs que le radial 3D ou l'approche Poisson disk proposé dans (Vasanawala et al., 2010). Aussi, de la très haute résolution de 0.3 mm dans le plan a été testée avec notre approche qui s'est montrée à nouveau très prometteuse (résultats non montrés). Enfin, des résultats préliminaires ont été faits *in vivo* sur un volontaire sain, qui sont en accord avec les résultats *ex vivo*.

Chapitre 5

Dans ce dernier chapitre, on considère un modèle d'acquisition qui prend en compte les effets de filtrage réalisé au cours de la réception du signal en IRM. En effet, il faut se souvenir qu'on échantillonne une courbe régulière parcourue continûment dans l'espace de Fourier. Chaque mesure résulte ainsi d'une sorte de moyennage de l'information de Fourier parcourue pendant le temps d'échantillonnage. Lors de la conversion du signal analogique en signal digital, il est en fait réalisé une série de filtrage à passe-bande qui peuvent corrompre le signal. C'est équivalent à appliquer un filtre de convolution à chaque segment. C'est ce filtrage que nous intégrons dans notre modèle d'acquisition et dans notre modèle de reconstruction afin de tenter de corriger les artefacts introduits par le modèle classique de la transformée de Fourier discrète. Nous montrons ainsi sur des données simulées et expérimentales que nous arrivons à améliorer la qualité des images reconstruites grâce à ce modèle plus précis, surtout dans les cas où la distance dans l'espace-k est de l'ordre de grandeur ou plus grande qu'un pixel à Nyquist. Un exemple de l'amélioration apportée par notre la méthode est montrée en figure 6 pour une trajectoire SPARKLING.

[4] l'iPAT qui veut dire *integrated parallel accceleration technique*, utilise l'imagerie parallèle avec une reconstruction GRAPPA (Griswold et al., 2002).

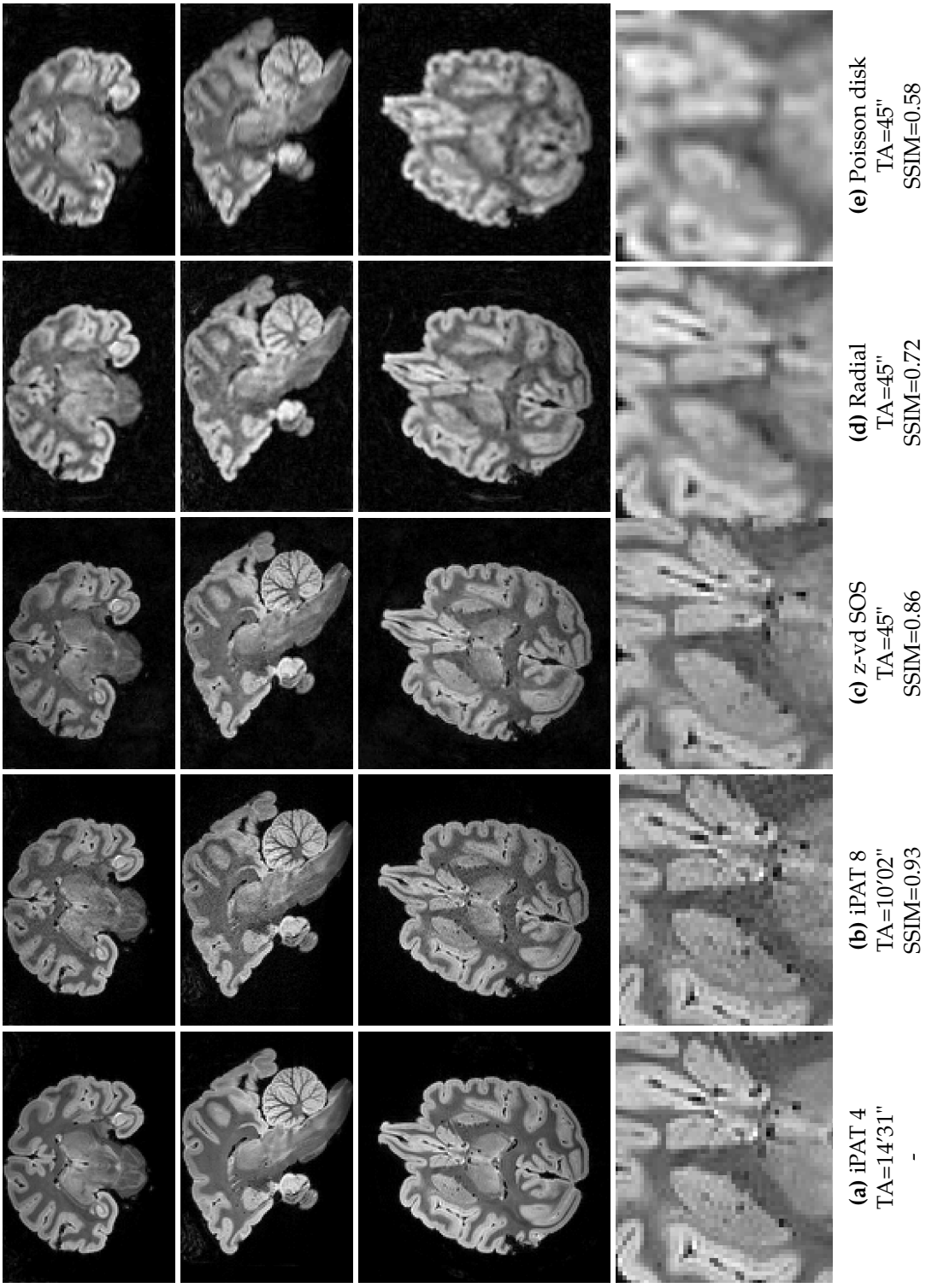

FIGURE 5: Résultats *ex vivo* pour une résolution isotrope de 0.6 mm comparant les stratégies z-vd stack-of-sparkling, radiale 3D et l'approche 3D Poisson disk pour un 1140 segments, i.e., un temps d'acquisition de 45 secondes. Le champ de vue est de $200 \times 200 \times 140\,\mathrm{mm}^3$.

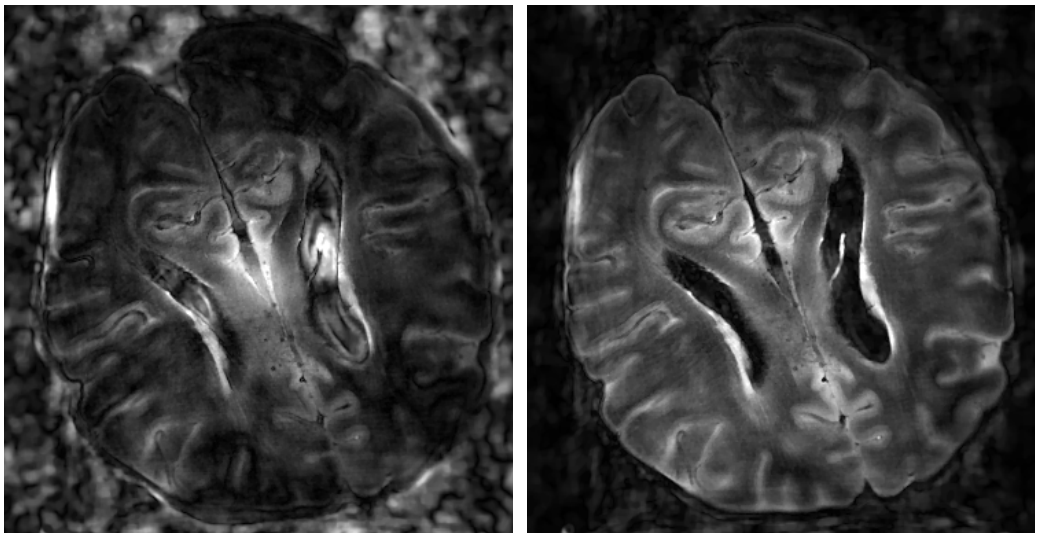

(a) Reconstruction standard **(b)** Reconstruction proposée

FIGURE 6: Reconstructions non-linéaires d'un cerveau humain *ex vivo* avec une trajectoire SPARKLING, avec (a) et sans (b) prendre en compte l'effet de filtrage de l'ADC. Les acquisitions ont été réalisées prospectivement sur un scanner 7 teslas.

Appendix A

Mathematical details on the SPARKLING algorithm

A.1 Mathematical model

Let $\Omega = [0,1]^d$ denote the Fourier domain with d the dimension. Let $\pi : \Omega \to \mathbb{R}$ denote a target probability density function. Following our previous work, we aim at solving:

$$\min_{\boldsymbol{k}\in\Omega^N} \frac{1}{N^2} \sum_{1\leq i,j\leq N} H(\boldsymbol{k}[i] - \boldsymbol{k}[j]) - \frac{1}{N} \sum_{i=1}^{N} \int_\Omega H(x - \boldsymbol{k}[i])\pi(x)\, dx, \tag{A.1}$$

where H is a well chosen function, typically $H(x) = \|x\|_2$.

Let

$$F_r(\boldsymbol{k}) = \frac{1}{N^2} \sum_{1\leq i,j\leq N} H(\boldsymbol{k}[i] - \boldsymbol{k}[j]) \tag{A.2}$$

and

$$F_a(\boldsymbol{k}) = \frac{1}{N} \sum_{i=1}^{N} \int_\Omega H(x - \boldsymbol{k}[i])\pi(x)\, dx. \tag{A.3}$$

The main issue to solve (A.1) is to compute these functions and their derivatives.

A.2 Evaluating F_a and its gradient

We assume that:

$$\pi = \left(\sum_{0\leq i,j\leq n-1} \boldsymbol{\pi}[i,j]\delta_{i/n,j/n} \right) \star \psi, \tag{A.4}$$

where ψ is an interpolation function, typically, a bilinear kernel.

Then, notice that for radial functions H, we have

$$F_a(\boldsymbol{k}) = \frac{1}{N} \sum_{i=1}^{N} (H \star \pi)(\boldsymbol{k}[i]), \tag{A.5}$$

where $\boldsymbol{k}[i] \in \Omega$ does not necessarily belong to the grid. The main difficulty is thus to quickly evaluate $(H \star \pi)(x)$ and its derivatives off the grid.

This can be done as follows. First, we can construct a discrete filter

$$\boldsymbol{\phi}[i,j] = (\psi \star H)(i/n, j/n) \tag{A.6}$$

for $-n \leq i, j \leq n$.

Notice that

$$\begin{aligned}(\pi \star H)(x) &= \left(\sum_{0 \leq i,j \leq n-1} \boldsymbol{\pi}[i,j] \delta_{i/n, j/n} \right) \star (\psi \star H)(x) \\ &= \sum_{0 \leq i,j \leq n-1} \boldsymbol{\pi}[i,j] (\psi \star H)(x - (i/n, j/n))\end{aligned}$$

Now, for x belonging to the grid, i.e. $x = (i'/n, j'/n)$, with $(i', j') \in \mathbb{N}^2$, the above expression can be simplified as

$$(\pi \star H)(x) = (\boldsymbol{\pi} \star \boldsymbol{\phi})(i', j'), \tag{A.7}$$

where - this time - $\star$ denotes the discrete convolution. Hence, it is possible to precompute $\boldsymbol{\pi} \star \phi$ on a discrete grid with fast Fourier transforms, this yields the values of $(\pi \star H)$ on a grid. If the kernel $\psi \star H$ is sufficiently smooth, then, so is $\pi \star H$ and its values can be evaluated off the grid by using interpolation functions.

A.3 Evaluating F_r and its gradient

The problem addressed here is to compute:

$$\partial_i F(\boldsymbol{k}) = \frac{1}{N^2} \sum_{j=1}^{N} \nabla H(\boldsymbol{k}[j] - \boldsymbol{k}[i]). \tag{A.8}$$

This can be done by direct calculation, but at the price of a large complexity of $O(N^2)$. This is the most straightforward approach and can be done in C++ as was done for the 3D version of the algorithm.

On the other hand, the summation can be calculated faster using NFFT-based fast summations (Fenn and Steidl, 2004). This was done for the 2D version of the SPARKLING algorithm.

Bibliography

[1] Aviva Abosch et al. "An assessment of current brain targets for deep brain stimulation surgery with susceptibility-weighted imaging at 7 tesla". In: *Neurosurgery* 67.6 (2010), pp. 1745–1756 (cit. on pp. 83, 89, 93).

[2] Anatole Abragam. *The principles of nuclear magnetism*. 32. Oxford university press, 1961 (cit. on p. 7).

[3] Ben Adcock and Anders C Hansen. "Generalized sampling and infinite-dimensional compressed sensing". In: *Foundations of Computational Mathematics* (2015), pp. 1–61 (cit. on p. 37).

[4] Ben Adcock et al. "Breaking the coherence barrier: A new theory for compressed sensing". In: *arXiv preprint arXiv:1302.0561* (2013) (cit. on pp. 37, 40).

[5] Ben Adcock et al. "Breaking the coherence barrier: A new theory for compressed sensing". In: 5 (2017) (cit. on p. 56).

[6] Nii Okai Addy, Holden H Wu, and Dwight G Nishimura. "Simple method for MR gradient system characterization and k-space trajectory estimation". In: *Magnetic Resonance in Medicine* 68.1 (2012), pp. 120–129 (cit. on p. 27).

[7] Jan Aelterman et al. "Augmented Lagrangian based reconstruction of non-uniformly sub-Nyquist sampled MRI data". In: *Signal Processing* 91.12 (2011), pp. 2731–2742 (cit. on p. 37).

[8] C. B. Ahn, J. H. Kim, and Z. H. Cho. "High-Speed Spiral-Scan Echo Planar NMR Imaging-I". In: *IEEE Transactions on Medical Imaging* 5.1 (1986), pp. 2–7 (cit. on pp. 16, 56, 114).

[9] Akram Aldroubi and Karlheinz Gröchenig. "Nonuniform sampling and reconstruction in shift-invariant spaces". In: *SIAM review* 43.4 (2001), pp. 585–620 (cit. on p. 63).

[10] Marcus T Alley, Gary H Glover, and Norbert J Pelc. "Gradient characterization using a Fourier-transform technique". In: *Magnetic Resonance in Medicine* 39.4 (1998), pp. 581–587 (cit. on p. 27).

[11] Dennis Amelunxen et al. "Living on the edge: Phase transitions in convex programs with random data". In: *Information and Inference* (2014), iau005 (cit. on p. 40).

[12] R. Ansorge and M. J. Graves. *The Physics and Mathematics of MRI*. Morgan & Claypool Publishers, 2016, 3.3 The transmit–receive chain (cit. on pp. 21, 62, 64, 99).

[13] A. Arunachalam, A. Samsonov, and W. F. Block. "Self-calibrated GRAPPA method for 2D and 3D radial data". In: *Magnetic resonance in medicine* 57.5 (2007), pp. 931–938 (cit. on p. 16).

[14] David Atkinson et al. "Sampling and reconstruction effects due to motion in diffusion-weighted interleaved echo planar imaging". In: *Magnetic Resonance in Medicine: An Official Journal of the International Society for Magnetic Resonance in Medicine* 44.1 (2000), pp. 101–109 (cit. on p. 83).

[15] Luca Baldassarre et al. “Learning-based compressive subsampling”. In: *IEEE Journal of Selected Topics in Signal Processing* 10.4 (2016), pp. 809–822 (cit. on p. 80).

[16] AV Barger et al. “Single breath-hold 3D contrast-enhanced method for assessment of cardiac function”. In: *Magnetic resonance in medicine* 44.6 (2000), pp. 821–824 (cit. on p. 19).

[17] Christoph Barmet, Nicola De Zanche, and Klaas P Pruessmann. “Spatiotemporal magnetic field monitoring for MR”. In: *Magnetic resonance in medicine* 60.1 (2008), pp. 187–197 (cit. on pp. 24, 29).

[18] Josephine Barnes et al. “A meta-analysis of hippocampal atrophy rates in Alzheimer’s disease”. In: *Neurobiology of aging* 30.11 (2009), pp. 1711–1723 (cit. on pp. 1, 34, 55).

[19] Jonathan Barzilai and Jonathan M Borwein. “Two-point step size gradient methods”. In: *IMA journal of Numerical Analysis* 8.1 (1988), pp. 141–148 (cit. on p. 62).

[20] Amir Beck and Marc Teboulle. “A fast iterative shrinkage-thresholding algorithm for linear inverse problems”. In: *SIAM Journal on Imaging Sciences* 2.1 (2009), pp. 183–202 (cit. on p. 44).

[21] CJ Bergin, JM Pauly, and A Macovski. “Lung parenchyma: projection reconstruction MR imaging”. In: *Radiology* 179.3 (1991), pp. 777–781 (cit. on p. 56).

[22] Matt A Bernstein, Kevin F King, and Xiaohong Joe Zhou. *Handbook of MRI pulse sequences*. Burlington MA Elsevier Google Scholar, 2004 (cit. on pp. 7, 9, 11–13, 21, 26, 62, 64).

[23] Jérémie Bigot, Claire Boyer, and Pierre Weiss. “An analysis of block sampling strategies in compressed sensing”. In: *IEEE Transactions on Information Theory* 62.4 (2016), pp. 2125–2139 (cit. on pp. 37, 40).

[24] Berkin Bilgic et al. “Wave-CAIPI for highly accelerated 3D imaging”. In: *Magnetic resonance in medicine* 73.6 (2015), pp. 2152–2162 (cit. on p. 19).

[25] A Bilgin et al. “Randomly perturbed radial trajectories for compressed sensing MRI”. In: *Proceedings of the 16th annual meeting of ISMRM*. Toronto, Canada, 2008, p. 3152 (cit. on pp. 56, 58).

[26] Bernd Bittersohl et al. “Feasibility of T 2* mapping for the evaluation of hip joint cartilage at 1.5 T using a three-dimensional (3D), gradient-echo (GRE) sequence: A prospective study”. In: *Magnetic Resonance in Medicine* 62.4 (2009), pp. 896–901 (cit. on p. 80).

[27] Fernando E Boada et al. “Fast three dimensional sodium imaging”. In: *Magnetic Resonance in Medicine* 37.5 (1997), pp. 706–715 (cit. on p. 19).

[28] Peter Börnert and Dye Jensen. “Coronary artery imaging at 0.5 T using segmented 3D echo planar imaging”. In: *Magnetic resonance in medicine* 34.6 (1995), pp. 779–785 (cit. on p. 19).

[29] Peter Börnert et al. “Improvements in spiral MR imaging”. In: *Magnetic Resonance Materials in Physics, Biology and Medicine* 9.1 (1999), pp. 29–41 (cit. on p. 80).

[30] C. Boyer et al. “On the generation of sampling schemes for Magnetic Resonance Imaging”. In: *SIAM Journal on Imaging Sciences* 9.4 (2016), pp. 2039–2072 (cit. on pp. 3, 37, 40, 53, 56, 59, 61, 111, 112, 119, 121).

[31] Claire Boyer, Pierre Weiss, and Jérémie Bigot. "An algorithm for variable density sampling with block-constrained acquisition". In: *SIAM Journal on Imaging Sciences* 7.2 (2014), pp. 1080–1107 (cit. on p. 37).

[32] Claire Boyer, Jérémie Bigot, and Pierre Weiss. "Compressed sensing with structured sparsity and structured acquisition". In: *Applied and Computational Harmonic Analysis* (2017) (cit. on pp. 40, 41).

[33] Claire Boyer et al. "HYR^{2}PICS: Hybrid regularized reconstruction for combined parallel imaging and compressive sensing in MRI". In: *Biomedical Imaging (ISBI), 2012 9th IEEE International Symposium on*. IEEE. 2012, pp. 66–69 (cit. on p. 72).

[34] Felix A Breuer et al. "Zigzag sampling for improved parallel imaging". In: *Magnetic resonance in medicine* 60.2 (2008), pp. 474–478 (cit. on p. 18).

[35] Ethan K Brodsky, Alexey A Samsonov, and Walter F Block. "Characterizing and correcting gradient errors in non-cartesian imaging: Are gradient errors linear time-invariant (LTI)?" In: *Magnetic resonance in medicine* 62.6 (2009), pp. 1466–1476 (cit. on pp. 27, 67).

[36] E. J. Candès, J. Romberg, and T. Tao. "Robust uncertainty principles: exact signal reconstruction from highly incomplete frequency information". In: *IEEE Transactions on information theory* 52.2 (2006), pp. 489–509 (cit. on pp. 1, 55, 109).

[37] L. Chaari et al. "A wavelet-based regularized reconstruction algorithm for SENSE parallel MRI with applications to neuroimaging". In: 15.2 (2011), pp. 185–201 (cit. on p. 53).

[38] A. Chambolle et al. "An introduction to total variation for image analysis". In: *Theoretical Foundations and Numerical Methods for Sparse Recovery* 9.263-340 (2010), p. 227 (cit. on p. 109).

[39] Hersh Chandarana et al. "Free-breathing contrast-enhanced multiphase MRI of the liver using a combination of compressed sensing, parallel imaging, and golden-angle radial sampling". In: *Investigative radiology* 48.1 (2013) (cit. on p. 58).

[40] Hersh Chandarana et al. "Free-breathing radial 3D fat-suppressed T1-weighted gradient echo sequence: a viable alternative for contrast-enhanced liver imaging in patients unable to suspend respiration". In: *Investigative Radiology* 46.10 (2011), pp. 648–653 (cit. on p. 19).

[41] Yulin V Chang et al. "3d-accelerated, stack-of-spirals acquisitions and reconstruction of arterial spin labeling MRI". In: *Magnetic Resonance in Medicine* 78.4 (2017), pp. 1405–1419 (cit. on p. 19).

[42] P. Chatterjee and P. Milanfar. "Is Denoising Dead?" In: *IEEE Transactions on Image Processing* 19.4 (2010), pp. 895–911 (cit. on pp. 64, 113).

[43] N. Chauffert et al. "A projection algorithm for gradient waveforms design in Magnetic Resonance Imaging". In: *IEEE Transactions on Medical Imaging* 35.9 (Sept. 2016), pp. 2026–2039 (cit. on pp. 37, 60, 62).

[44] N. Chauffert et al. "A Projection Method on Measures Sets". In: *Constructive Approximation* 45.1 (2017), pp. 83–111 (cit. on pp. 60–62, 111, 112).

[45] N. Chauffert, P. Ciuciu, and P. Weiss. "Variable density compressed sensing in MRI. Theoretical vs. heuristic sampling strategies". In: *Proc. of 10th IEEE ISBI conference*. San Francisco, USA, 2013, pp. 298–301 (cit. on p. 43).

[46] N. Chauffert et al. “Variable density sampling with continuous trajectories. Application to MRI”. In: *SIAM Journal on Imaging Sciences* 7.4 (2014), pp. 1962–1992 (cit. on p. 37).

[47] Zang-Hee Cho. *Foundations of medical imaging*. Wiley-Interscience, 1993 (cit. on pp. 21, 62, 64).

[48] I. Y. Chun, B. Adcock, and T. M. Talavage. “Efficient Compressed Sensing SENSE pMRI Reconstruction With Joint Sparsity Promotion”. In: 35.1 (2016), pp. 354–368. ISSN: 0278-0062. DOI: 10.1109/TMI.2015.2474383 (cit. on p. 53).

[49] Harvey E Cline, Xuli Zong, and Neville Gai. “Design of a logarithmic k-space spiral trajectory”. In: *Magnetic Resonance in Medicine* 46.6 (2001), pp. 1130–1135 (cit. on pp. 62, 64).

[50] P. L. Combettes and J.-C. Pesquet. “Proximal Splitting Methods in Signal Processing”. In: *Fixed-Point Algorithms for Inverse Problems in Science and Engineering*. Springer, 2011, pp. 185–212 (cit. on p. 109).

[51] Mandy Conijn et al. “Visualization of cerebral microbleeds with dual-echo T2*-weighted magnetic resonance imaging at 7.0 T”. In: *Journal of Magnetic Resonance Imaging* 32.1 (2010), pp. 52–59 (cit. on p. 35).

[52] Andrew Thomas Curtis and Christopher Kumar Anand. “Random volumetric MRI trajectories via genetic algorithms”. In: *Journal of Biomedical Imaging* 2008 (2008), p. 6 (cit. on pp. 20, 59).

[53] K. Dabov et al. “Image denoising by sparse 3D transform-domain collaborative filtering”. In: *IEEE Transactions on Image Processing* 16.8 (2007), pp. 2080–2095 (cit. on p. 109).

[54] Brian M Dale, Jonathan S Lewin, and Jeffrey L Duerk. “Optimal design of k-space trajectories using a multi-objective genetic algorithm”. In: *Magnetic resonance in medicine* 52.4 (2004), pp. 831–841 (cit. on p. 20).

[55] Ingrid Daubechies and Ron DeVore. “Approximating a bandlimited function using very coarsely quantized data: A family of stable sigma-delta modulators of arbitrary order”. In: *Annals of mathematics* 158.2 (2003), pp. 679–710 (cit. on pp. 62, 64, 65).

[56] Fernando De Goes et al. “Blue noise through optimal transport”. In: *ACM Transactions on Graphics (TOG)* 31.6 (2012), p. 171 (cit. on p. 56).

[57] François De Guio et al. “Loss of venous integrity in cerebral small vessel disease: a 7-T MRI study in cerebral autosomal-dominant arteriopathy with subcortical infarcts and leukoencephalopathy (CADASIL)”. In: *Stroke* 45.7 (2014), pp. 2124–2126 (cit. on pp. 35, 80).

[58] Nicola De Zanche et al. “NMR probes for measuring magnetic fields and field dynamics in MR systems”. In: *Magnetic Resonance in Medicine* 60.1 (2008), pp. 176–186 (cit. on p. 68).

[59] Ralf Deichmann et al. “Optimization of 3-D MP-RAGE sequences for structural brain imaging”. In: *Neuroimage* 12.1 (2000), pp. 112–127 (cit. on pp. 77, 79).

[60] Bénédicte MA Delattre et al. “Spiral demystified”. In: *Magnetic Resonance Imaging* 28.6 (2010), pp. 862–881 (cit. on p. 17).

[61] Christian Denk and Alexander Rauscher. "Susceptibility weighted imaging with multiple echoes". In: *Journal of Magnetic Resonance Imaging* 31.1 (2010), pp. 185–191 (cit. on p. 80).

[62] R. A. DeVore and G. G. Lorentz. *Constructive Approximation*. Springer-Verlag Berlin Heidelberg, 1993 (cit. on p. 107).

[63] Mark AZ Dippé and Erling Henry Wold. "Antialiasing through stochastic sampling". In: *ACM Siggraph Computer Graphics* 19.3 (1985), pp. 69–78 (cit. on p. 56).

[64] David L Donoho. "Compressed sensing". In: *IEEE Transactions on Information Theory* 52.4 (2006), pp. 1289–1306 (cit. on pp. 1, 55).

[65] A. Dutt and V. Rokhlin. "Fast Fourier Transforms for Nonequispaced Data". In: *SIAM Journal on Scientific computing* 14.6 (1993), pp. 1368–1393 (cit. on pp. 32, 107).

[66] Jeff H Duyn. "The future of ultra-high field MRI and fMRI for study of the human brain". In: *Neuroimage* 62.2 (2012), pp. 1241–1248 (cit. on pp. 1, 34, 55).

[67] Jeff H Duyn and Yihong Yang. "Fast spiral magnetic resonance imaging with trapezoidal gradients". In: *Journal of Magnetic Resonance* 128.2 (1997), pp. 130–134 (cit. on p. 17).

[68] Jeff H Duyn et al. *Simple correction method fork-space trajectory deviations in MRI*. 1998 (cit. on pp. 28, 29).

[69] Hadrien Dyvorne et al. "Abdominal 4D flow MR imaging in a breath hold: combination of spiral sampling and dynamic compressed sensing for highly accelerated acquisition". In: *Radiology* 275.1 (2014), pp. 245–254 (cit. on p. 58).

[70] William A Edelstein et al. "Spin warp NMR imaging and applications to human whole-body imaging". In: *Physics in Medicine and Biology* 25.4 (1980), p. 751 (cit. on p. 56).

[71] Shereen M El-Metwally et al. "Rapid cardiac MRI using random radial trajectories". In: *Radio Science Conference, 2008. NRSC 2008. National*. IEEE. 2008, pp. 1–7 (cit. on pp. 58, 59).

[72] Christian Federau and Daniel Gallichan. "Motion-correction enabled ultra-high resolution in-vivo 7T-MRI of the brain". In: *PloS one* 11.5 (2016), e0154974 (cit. on pp. 1, 36, 55).

[73] Li Feng et al. "Golden-angle radial sparse parallel MRI: Combination of compressed sensing, parallel imaging, and golden-angle radial sampling for fast and flexible dynamic volumetric MRI". In: *Magnetic Resonance in Medicine* 72.3 (2014), pp. 707–717 (cit. on pp. 1, 19, 37, 58).

[74] Li Feng et al. "XD-GRASP: Golden-angle radial MRI with reconstruction of extra motion-state dimensions using compressed sensing". In: *Magnetic Resonance in Medicine* 75.2 (2016), pp. 775–788 (cit. on pp. 37, 58).

[75] M. Fenn and G. Steidl. "Fast NFFT based summation of radial functions". In: *Sampling Theory in Signal and Image Processing* 3 (2004), pp. 1–28 (cit. on p. 128).

[76] J. A. Fessler. "Model-Based Image Reconstruction for MRI". In: *IEEE Signal Processing Magazine* 27.4 (2010), pp. 81–89 (cit. on p. 99).

[77] J. A. Fessler and B. P. Sutton. "Nonuniform fast Fourier transforms using min-max interpolation". In: *IEEE Transactions on Signal Processing* 51.2 (2003), pp. 560–574 (cit. on p. 32).

[78] Anisia Florescu et al. "A Majorize-Minimize Memory Gradient method for complex-valued inverse problems". In: *Signal Processing* 103 (2014), pp. 285–295 (cit. on p. 37).

[79] Josa M Frischer et al. "Susceptibility-weighted imaging at 7 T: improved diagnosis of cerebral cavernous malformations and associated developmental venous anomalies". In: *NeuroImage: Clinical* 1.1 (2012), pp. 116–120 (cit. on pp. 35, 80).

[80] Amanda K Funai et al. "Regularized field map estimation in MRI". In: *IEEE transactions on medical imaging* 27.10 (2008), pp. 1484–1494 (cit. on p. 28).

[81] Urs Gamper, Peter Boesiger, and Sebastian Kozerke. "Compressed sensing in dynamic MRI". In: *Magnetic resonance in medicine* 59.2 (2008), pp. 365–373 (cit. on p. 37).

[82] Gary H Glover and Christine S Law. "Spiral-in/out BOLD fMRI for increased SNR and reduced susceptibility artifacts". In: *Magnetic resonance in medicine* 46.3 (2001), pp. 515–522 (cit. on pp. 18, 35).

[83] Gary H Glover et al. "Simple analytic spiral K-space algorithm". In: *Magnetic Resonance in Medicine* 42.2 (1999), pp. 412–415 (cit. on p. 17).

[84] GH Glover and JM Pauly. "Projection reconstruction techniques for reduction of motion effects in MRI". In: *Magnetic Resonance in Medicine* 28.2 (1992), pp. 275–289 (cit. on p. 56).

[85] Nadine N Graedel et al. "Motion correction for functional MRI with three-dimensional hybrid radial-Cartesian EPI". In: *Magnetic resonance in medicine* 78.2 (2017), pp. 527–540 (cit. on p. 19).

[86] J. Graessner. "Bandwidth in MRI". In: *Magnetom Flash* 2 (2013), pp. 3–8 (cit. on p. 99).

[87] Mark A Griswold et al. "Generalized autocalibrating partially parallel acquisitions (GRAPPA)". In: *Magnetic Resonance in Medicine* 47.6 (2002), pp. 1202–1210 (cit. on pp. 55, 75, 123).

[88] M. Guerquin-Kern et al. "Realistic analytical phantoms for parallel magnetic resonance imaging". In: *IEEE Transactions on Medical Imaging* 31.3 (2012), pp. 626–636 (cit. on p. 102).

[89] Matthieu Guerquin-Kern et al. "A fast wavelet-based reconstruction method for magnetic resonance imaging". In: *IEEE transactions on medical imaging* 30.9 (2011), pp. 1649–1660 (cit. on p. 37).

[90] Matthieu Guerquin-Kern et al. "Realistic analytical phantoms for parallel magnetic resonance imaging". In: *IEEE Transactions on Medical Imaging* 31.3 (2012), pp. 626–636 (cit. on pp. 43, 44).

[91] Paul T Gurney, Brian A Hargreaves, and Dwight G Nishimura. "Design and analysis of a practical 3D cones trajectory". In: *Magnetic Resonance in Medicine* 55.3 (2006), pp. 575–582 (cit. on p. 19).

[92] E Mark Haacke et al. "In vivo validation of the BOLD mechanism: a review of signal changes in gradient echo functional MRI in the presence of flow". In: *International Journal of Imaging Systems and Technology* 6.2-3 (1995), pp. 153–163 (cit. on p. 33).

[93] E Mark Haacke et al. *Magnetic resonance imaging: physical principles and sequence design*. Vol. 82. Wiley-liss New York: 1999 (cit. on pp. 7, 10, 13).

[94] E Mark Haacke et al. "Susceptibility weighted imaging (SWI)". In: *Magnetic resonance in medicine* 52.3 (2004), pp. 612–618 (cit. on pp. 33, 80).

[95] Axel Haase et al. "FLASH imaging. Rapid NMR imaging using low flip-angle pulses". In: *Journal of Magnetic Resonance (1969)* 67.2 (1986), pp. 258–266 (cit. on pp. 22, 23).

[96] Justin P Haldar. "Low-rank modeling of local-space neighborhoods (LORAKS) for constrained MRI". In: *IEEE Transactions on Medical Imaging* 33.3 (2014), pp. 668–681 (cit. on p. 37).

[97] Justin P Haldar, Diego Hernando, and Zhi-Pei Liang. "Compressed-sensing MRI with random encoding". In: *IEEE Transactions on Medical Imaging* 30.4 (2011), pp. 893–903 (cit. on p. 37).

[98] S. J. Holdsworth et al. "Fast susceptibility-weighted imaging with three-dimensional short-axis propeller (SAP)-echo-planar imaging". In: *Journal of Magnetic Resonance Imaging* 41.5 (2015), pp. 1447–1453 (cit. on p. 83).

[99] DJ Holland et al. "Compressed sensing reconstruction improves sensitivity of variable density spiral fMRI". In: *Magnetic Resonance in Medicine* 70.6 (2013), pp. 1634–1643 (cit. on p. 58).

[100] Kieren G Hollingsworth et al. "Investigating the quantitative fidelity of prospectively undersampled chemical shift imaging in muscular dystrophy with compressed sensing and parallel imaging reconstruction". In: *Magnetic Resonance in Medicine* 72.6 (2014), pp. 1610–1619 (cit. on p. 45).

[101] Kieren Grant Hollingsworth. "Reducing acquisition time in clinical MRI by data undersampling and compressed sensing reconstruction". In: *Physics in medicine and biology* 60.21 (2015), R297 (cit. on p. 38).

[102] D. I. Hoult. "The NMR receiver: A description and analysis of design". In: *Progress in Nuclear Magnetic Resonance Spectroscopy* 12.1 (1978), pp. 41–77 (cit. on p. 99).

[103] David I Hoult and RE Richards. "The signal-to-noise ratio of the nuclear magnetic resonance experiment". In: *Journal of magnetic resonance* 213.2 (2011), pp. 329–343 (cit. on p. 10).

[104] Pablo Irarrazabal and Dwight G Nishimura. "Fast three dimensional magnetic resonance imaging". In: *Magnetic Resonance in Medicine* 33.5 (1995), pp. 656–662 (cit. on p. 19).

[105] John I Jackson et al. "Selection of a convolution function for Fourier inversion using gridding (computerised tomography application)". In: *IEEE Transactions on Medical Imaging* 10.3 (1991), pp. 473–478 (cit. on p. 31).

[106] John I Jackson, Dwight G Nishimura, and Albert Macovski. "Twisting radial lines with application to robust magnetic resonance imaging of irregular flow". In: *Magnetic Resonance in Medicine* 25.1 (1992), pp. 128–139 (cit. on pp. 18, 56).

[107] Oliver Jeromin, Marios S Pattichis, and Vince D Calhoun. "Optimal compressed sensing reconstructions of fMRI using 2D deterministic and stochastic sampling geometries". In: *Biomedical engineering online* 11.1 (2012), p. 1 (cit. on p. 45).

[108] Peter Jezzard, Stuart Clare, et al. "Sources of distortion in functional MRI data". In: *Human Brain Mapping* 8.2-3 (1999), pp. 80–85 (cit. on p. 74).

[109] Kevin M Johnson. "Hybrid radial-cones trajectory for accelerated MRI". In: *Magnetic Resonance in Medicine* 77.3 (2017), pp. 1068–1081 (cit. on p. 20).

[110] Hong Jung et al. "k-t FOCUSS: A general compressed sensing framework for high resolution dynamic MRI". In: *Magnetic Resonance in Medicine* 61.1 (2009), pp. 103–116 (cit. on p. 37).

[111] Lars Kasper et al. "Rapid anatomical brain imaging using spiral acquisition and an expanded signal model". In: *NeuroImage* (2017) (cit. on p. 80).

[112] J. Keiner, S. Kunis, and D. Potts. "Using NFFT 3—A Software Library for Various Nonequispaced Fast Fourier Transforms". In: *ACM Transactions on Mathematical Software (TOMS)* 36.4 (2009), p. 19 (cit. on pp. 62, 95, 107).

[113] Jens Keiner, Stefan Kunis, and Daniel Potts. "Using NFFT 3—a software library for various nonequispaced fast Fourier transforms". In: *ACM Transactions on Mathematical Software (TOMS)* 36.4 (2009), p. 19 (cit. on pp. 32, 44, 73).

[114] Dong-hyun Kim, Elfar Adalsteinsson, and Daniel M Spielman. "Simple analytic variable density spiral design". In: *Magnetic Resonance in Medicine* 50.1 (2003), pp. 214–219 (cit. on p. 17).

[115] Anja G van der Kolk et al. "Clinical applications of 7T MRI in the brain". In: *European journal of radiology* 82.5 (2013), pp. 708–718 (cit. on pp. 1, 34, 55).

[116] Felix Krahmer and Rachel Ward. "Stable and robust sampling strategies for compressive imaging". In: *IEEE transactions on image processing* 23.2 (2014), pp. 612–622 (cit. on p. 40).

[117] Christopher Kumar Anand, Andrew Thomas Curtis, and Rakshit Kumar. "Durga: A heuristically-optimized data collection strategy for volumetric magnetic resonance imaging". In: *Engineering Optimization* 40.2 (2008), pp. 117–136 (cit. on pp. 20, 59).

[118] Gitta Kutyniok and Wang-Q Lim. "Optimal compressive imaging of Fourier data". In: *arXiv preprint arXiv:1510.05029* (2015) (cit. on p. 80).

[119] Christian Langkammer et al. "Fast quantitative susceptibility mapping using 3D EPI and total generalized variation". In: *Neuroimage* 111 (2015), pp. 622–630 (cit. on p. 80).

[120] D. J. Larkman and R. G. Nunes. "Parallel magnetic resonance imaging". In: *Physics in Medicine & Biology* 52.7 (2007), R15 (cit. on p. 108).

[121] Andrew C Larson, Orlando P Simonetti, and Debiao Li. "Coronary MRA with 3D undersampled projection reconstruction TrueFISP". In: *Magnetic resonance in medicine* 48.4 (2002), pp. 594–601 (cit. on p. 19).

[122] Andrew C Larson et al. "Self-gated cardiac cine MRI". In: *Magnetic resonance in medicine* 51.1 (2004), pp. 93–102 (cit. on p. 16).

[123] Peder EZ Larson, Paul T Gurney, and Dwight G Nishimura. "Anisotropic field-of-views in radial imaging". In: *IEEE Transactions on Medical Imaging* 27.1 (2008), pp. 47–57 (cit. on pp. 19, 89).

[124] P. C. Lauterbur. *Image Formation by Induced Local Interactions: Examples Employing Nuclear Magnetic Resonance*. Nature Publishing Group, 1973 (cit. on pp. 15, 16, 56, 99).

[125] Christine S Law and Gary H Glover. "Interleaved spiral-in/out with application to functional MRI (fMRI)". In: *Magnetic Resonance in Medicine* 62.3 (2009), pp. 829–834 (cit. on p. 70).

[126] C. Lazarus et al. "SPARKLING: Novel Non-Cartesian Sampling Schemes for Accelerated 2D Anatomical Imaging at 7T Using Compressed Sensing". In: *25th annual meeting of the International Society for Magnetic Resonance Imaging*. 2017 (cit. on pp. 111, 112, 114).

[127] J. H. Lee et al. "Fast 3D imaging using variable-density spiral trajectories with applications to limb perfusion". In: *Magnetic Resonance in Medicine* 50.6 (2003), pp. 1276–1285 (cit. on pp. 17, 18, 70, 102, 104, 111, 115, 121).

[128] Paul Leopardi. "A partition of the unit sphere into regions of equal area and small diameter". In: *Electronic Transactions on Numerical Analysis* 25.12 (2006), pp. 309–327 (cit. on p. 85).

[129] D. Liang et al. "Accelerating SENSE using compressed sensing". In: *Magnetic Resonance in Medicine* 62.6 (2009), pp. 1574–1584 (cit. on p. 53).

[130] Richard S Likes. *Moving gradient zeugmatography*. US Patent 4,307,343. 1981 (cit. on p. 13).

[131] Wei Lin et al. "Respiratory motion-compensated radial dynamic contrast-enhanced (DCE)-MRI of chest and abdominal lesions". In: *Magnetic resonance in medicine* 60.5 (2008), pp. 1135–1146 (cit. on p. 19).

[132] Bo Liu, Yi Ming Zou, and Leslie Ying. "SparseSENSE: application of compressed sensing in parallel MRI". In: *Information Technology and Applications in Biomedicine, 2008. ITAB 2008. International Conference on*. IEEE. 2008, pp. 127–130 (cit. on p. 72).

[133] Duan-duan Liu et al. "Under-sampling trajectory design for compressed sensing MRI". In: *Engineering in Medicine and Biology Society (EMBC), 2012 Annual International Conference of the IEEE*. IEEE. 2012, pp. 73–76 (cit. on pp. 20, 59).

[134] Stig Ljunggren. "A simple graphical representation of Fourier-based imaging methods". In: *Journal of Magnetic Resonance (1969)* 54.2 (1983), pp. 338–343 (cit. on p. 13).

[135] Stuart Lloyd. "Least squares quantization in PCM". In: *IEEE transactions on information theory* 28.2 (1982), pp. 129–137 (cit. on p. 87).

[136] M. Lustig, D. Donoho, and J. M. Pauly. "Sparse MRI: The application of compressed sensing for rapid MR imaging". In: *Magnetic Resonance in Medicine* 58.6 (2007), pp. 1182–1195 (cit. on pp. 99, 109).

[137] Michael Lustig, Seung-Jean Kim, and John M Pauly. "A fast method for designing time-optimal gradient waveforms for arbitrary k-space trajectories". In: *IEEE transactions on medical imaging* 27.6 (2008), pp. 866–873 (cit. on pp. 58, 59).

[138] Michael Lustig et al. "Compressed sensing MRI". In: *IEEE Signal Processing Magazine* 25.2 (2008), pp. 72–82 (cit. on pp. 44, 79).

[139] Michael Lustig et al. "Faster imaging with randomly perturbed, under-sampled spirals and ℓ_1 reconstruction". In: *Proceedings of the 13th annual meeting of ISMRM*. Miami Beach, FL, USA, 2005, p. 685 (cit. on pp. 56, 58).

[140] Michael Lustig, David Donoho, and John M Pauly. "Sparse MRI: The application of compressed sensing for rapid MR imaging". In: *Magnetic Resonance in Medicine* 58.6 (2007), pp. 1182–1195 (cit. on pp. 1, 37, 41, 55).

[141] Julian Maclaren et al. "Measurement and correction of microscopic head motion during magnetic resonance imaging of the brain". In: *PloS One* 7.11 (2012), e48088 (cit. on pp. 1, 36, 55).

[142] Caterina Mainero et al. "In vivo imaging of cortical pathology in multiple sclerosis using ultra-high field MRI". In: *Neurology* 73.12 (2009), pp. 941–948 (cit. on pp. 66, 73).

[143] Lai-Chee Man, John M Pauly, and Albert Macovski. "Multifrequency interpolation for fast off-resonance correction". In: *Magnetic resonance in medicine* 37.5 (1997), pp. 785–792 (cit. on p. 117).

[144] Louis W Mann et al. "Accelerating MR imaging liver steatosis measurement using combined compressed sensing and parallel imaging: a quantitative evaluation". In: *Radiology* 278.1 (2015), pp. 247–256 (cit. on p. 45).

[145] P. Mansfield. "Multi-planar image formation using NMR spin echoes". In: *Journal of Physics C: Solid State Physics* 10.3 (1977) (cit. on pp. 9, 16, 56, 114).

[146] Graeme F Mason et al. "A Method to measure arbitrary *k*-space trajectories for rapid MR imaging". In: *Magnetic Resonance in Medicine* 38.3 (1997), pp. 492–496 (cit. on p. 80).

[147] C. A. McKenzie et al. "Self-calibrating parallel imaging with automatic coil sensitivity extraction". In: *Magnetic Resonance in Medicine* 47.3 (2002), pp. 529–538 (cit. on p. 108).

[148] Marion I Menzel et al. "Accelerated diffusion spectrum imaging in the human brain using compressed sensing". In: *Magnetic Resonance in Medicine* 66.5 (2011), pp. 1226–1233 (cit. on p. 57).

[149] C. H. Meyer et al. "Fast spiral coronary artery imaging". In: *Magnetic Resonance in Medicine* 28.2 (1992), pp. 202–213 (cit. on pp. 16, 56, 99).

[150] Roberto Mir et al. "Fast three-dimensional k-space trajectory design using missile guidance ideas". In: *Magnetic Resonance in Medicine* 52.2 (2004), pp. 329–336 (cit. on pp. 20, 59).

[151] C. Moenninghoff et al. "Diffuse axonal injury at ultra-high field MRI". In: *PLoS One* 10.3 (2015), e0122329 (cit. on pp. 83, 89).

[152] C. Moenninghoff et al. "Imaging of brain metastases of bronchial carcinomas with 7 T MRI–initial results". In: *RöFo-Fortschritte auf dem Gebiet der Röntgenstrahlen und der bildgebenden Verfahren*. Vol. 182. 09. © Georg Thieme Verlag KG Stuttgart· New York. 2010, pp. 764–772 (cit. on p. 83).

[153] Christoph Moenninghoff et al. "Imaging of adult astrocytic brain tumours with 7 T MRI: preliminary results". In: *European radiology* 20.3 (2010), pp. 704–713 (cit. on p. 35).

[154] J. P. Mugler and J. R. Brookeman. "Rapid three-dimensional T1-weighted MR imaging with the MP-RAGE sequence". In: *Journal of Magnetic Resonance Imaging* 1.5 (1991), pp. 561–567 (cit. on p. 23).

[155] J. P. Mugler and J. R. Brookeman. "Three-dimensional magnetization-prepared rapid gradient-echo imaging (3D MP RAGE)". In: *Magnetic Resonance in Medicine* 15.1 (1990), pp. 152–157 (cit. on p. 23).

[156] KRISHNA S Nayak and Dwight G Nishimura. "Randomized trajectories for reduced aliasing artifact". In: *Proceedings of the 6th Annual Meeting of ISMRM*. Sydney, Australia, 1998, p. 670 (cit. on p. 67).

[157] Y. Nesterov. "Smooth minimization of non-smooth functions". In: *Mathematical Programming* 103.1 (2005), pp. 127–152 (cit. on p. 104).

[158] Douglas C Noll. "Multishot rosette trajectories for spectrally selective MR imaging". In: *IEEE Transactions on Medical Imaging* 16.4 (1997), pp. 372–377 (cit. on p. 18).

[159] Robert J Ogg et al. "The correlation between phase shifts in gradient-echo MR images and regional brain iron concentration". In: *Magnetic resonance imaging* 17.8 (1999), pp. 1141–1148 (cit. on p. 33).

[160] Yong Pang, Xiaohua Jiang, and Xiaoliang Zhang. "Sparse parallel transmission on randomly perturbed spiral k-space trajectory". In: *Quantitative imaging in medicine and surgery* 4.2 (2014), p. 106 (cit. on pp. 58, 59).

[161] Nikolaos G Papadakis et al. "A general method for measurement of the time integral of variant magnetic field gradients: application to 2D spiral imaging". In: *Magnetic resonance imaging* 15.5 (1997), pp. 567–578 (cit. on p. 29).

[162] Jinil Park et al. "A radial sampling strategy for uniform k-space coverage with retrospective respiratory gating in 3D ultrashort-echo-time lung imaging". In: *NMR in Biomedicine* 29.5 (2016), pp. 576–587 (cit. on p. 19).

[163] Davide Piccini et al. "Spiral phyllotaxis: the natural way to construct a 3D radial trajectory in MRI". In: *Magnetic resonance in medicine* 66.4 (2011), pp. 1049–1056 (cit. on p. 19).

[164] James G Pipe. "An optimized center-out k-space trajectory for multishot MRI: comparison with spiral and projection reconstruction". In: *Magnetic Resonance in Medicine: An Official Journal of the International Society for Magnetic Resonance in Medicine* 42.4 (1999), pp. 714–720 (cit. on p. 18).

[165] James G Pipe et al. "A new design and rationale for 3D orthogonally oversampled *k*-space trajectories". In: *Magnetic Resonance in Medicine* 66.5 (2011), pp. 1303–1311 (cit. on p. 19).

[166] James G Pipe et al. "Motion correction with PROPELLER MRI: application to head motion and free-breathing cardiac imaging". In: *Magnetic Resonance in Medicine* 42.5 (1999), pp. 963–969 (cit. on pp. 18, 56).

[167] Daniel Potts and Gabriele Steidl. "Fast summation at nonequispaced knots by NFFT". In: *SIAM Journal on Scientific Computing* 24.6 (2003), pp. 2013–2037 (cit. on pp. 62, 95).

[168] Klaas P Pruessmann et al. "SENSE: sensitivity encoding for fast MRI". In: *Magnetic Resonance in Medicine* 42.5 (1999), pp. 952–962 (cit. on p. 55).

[169] JC Pruessner et al. "Volumetry of hippocampus and amygdala with high-resolution MRI and three-dimensional analysis software: minimizing the discrepancies between laboratories". In: *Cerebral Cortex* 10.4 (2000), pp. 433–442 (cit. on pp. 1, 34, 55).

[170] Gilles Puy, Pierre Vandergheynst, and Yves Wiaux. "On variable density compressive sampling". In: *IEEE Signal Processing Letters* 18.10 (2011), pp. 595–598 (cit. on p. 40).

[171] Gilles Puy et al. "Spread spectrum magnetic resonance imaging". In: *IEEE transactions on medical imaging* 31.3 (2012), pp. 586–598 (cit. on p. 37).

[172] A. Ralston and P. Rabinowitz. *A First Course in Numerical Analysis*. Courier Corporation, 2001 (cit. on pp. 108, 109).

[173] Saiprasad Ravishankar and Yoram Bresler. "Adaptive sampling design for compressed sensing MRI". In: *Engineering in Medicine and Biology Society, EMBC, 2011 Annual International Conference of the IEEE*. IEEE. 2011, pp. 3751–3755 (cit. on pp. 20, 59).

[174] Paul J Reber et al. "Correction of off resonance-related distortion in echo-planar imaging using EPI-based field maps". In: *Magnetic Resonance in Medicine* 39.2 (1998), pp. 328–330 (cit. on p. 28).

[175] JR Reichenbach et al. "High-resolution blood oxygen-level dependent MR venography (HRBV): a new technique". In: *Neuroradiology* 43.5 (2001), pp. 364–369 (cit. on p. 33).

[176] Jurgen R Reichenbach et al. "Small vessels in the human brain: MR venography with deoxyhemoglobin as an intrinsic contrast agent." In: *Radiology* 204.1 (1997), pp. 272–277 (cit. on p. 33).

[177] Bogdan Roman, Anders Hansen, and Ben Adcock. "On asymptotic structure in compressed sensing". In: *arXiv preprint arXiv:1406.4178* (2014) (cit. on pp. 39, 40).

[178] Sebastian Sabat et al. "Three dimensional k-space trajectory design using genetic algorithms". In: *Magnetic Resonance Imaging* 21.7 (2003), pp. 755–764 (cit. on p. 20).

[179] Christian Schmaltz et al. "Electrostatic halftoning". In: *Computer Graphics Forum*. Vol. 29. 8. Wiley Online Library. 2010, pp. 2313–2327 (cit. on p. 61).

[180] Manuel A Schmidt et al. "Ultra high-field SWI of the substantia nigra at 7T: reliability and consistency of the swallow-tail sign". In: *BMC neurology* 17.1 (2017), p. 194 (cit. on pp. 83, 89).

[181] Johannes T Schneider et al. "Robust spatially selective excitation using radiofrequency pulses adapted to the effective spatially encoding magnetic fields". In: *Magnetic resonance in medicine* 65.2 (2011), pp. 409–421 (cit. on pp. 3, 27, 29, 115).

[182] Matthias Seeger et al. "Optimization of k-space trajectories for compressed sensing by Bayesian experimental design". In: *Magnetic resonance in medicine* 63.1 (2010), pp. 116–126 (cit. on pp. 20, 59).

[183] CE Shannon. "A Mathematical Theory of Communication". In: *The Bell System Technical Journal* 27.3 (1948), pp. 379–423 (cit. on p. 100).

[184] Peter J Shin et al. "Calibrationless parallel imaging reconstruction based on structured low-rank matrix completion". In: *Magnetic Resonance in Medicine* 72.4 (2014), pp. 959–970 (cit. on p. 73).

[185] Travis B Smith and Krishna S Nayak. "MRI artifacts and correction strategies". In: *Imaging in Medicine* 2.4 (2010), pp. 445–457 (cit. on p. 74).

[186] Hee Kwon Song and Lawrence Dougherty. "Dynamic MRI with projection reconstruction and KWIC processing for simultaneous high spatial and temporal resolution". In: *Magnetic resonance in medicine* 52.4 (2004), pp. 815–824 (cit. on p. 19).

[187] Juan Spiniak et al. "Undersampling k-space using fast progressive 3D trajectories". In: *Magnetic Resonance in Medicine* 54.4 (2005), pp. 886–892 (cit. on p. 59).

[188] R Jason Stafford. "High Field MRI: Technology, Applications, Safety, and Limitations". In: *46th AAPM Annual Meeting, American Association of Physicists in Medicine*. 2004 (cit. on p. 35).

[189] Daniel Stucht et al. "Highest resolution in vivo human brain MRI using prospective motion correction". In: *PloS One* 10.7 (2015), e0133921 (cit. on pp. 1, 36, 55).

[190] Bradley P Sutton, Douglas C Noll, and Jeffrey A Fessler. "Fast, iterative image reconstruction for MRI in the presence of field inhomogeneities". In: *IEEE transactions on Medical Imaging* 22.2 (2003), pp. 178–188 (cit. on p. 80).

[191] Hao Tan and Craig H Meyer. "Estimation of *k*-space trajectories in spiral MRI". In: *Magnetic Resonance in Medicine* 61.6 (2009), pp. 1396–1404 (cit. on pp. 56, 62, 64, 80).

[192] A. Tarantola. *Inverse Problem Theory and Methods for Model Parameter Estimation*. Vol. 89. SIAM, 2005 (cit. on p. 104).

[193] A. B Taylor, J. M Hendrickx, and F. Glineur. "Exact worst-case convergence rates of the proximal gradient method for composite convex minimization". In: *preprint arXiv:1705.04398* (2017) (cit. on p. 73).

[194] Tanja Teuber et al. "Dithering by differences of convex functions". In: *SIAM Journal on Imaging Sciences* 4.1 (2011), pp. 79–108 (cit. on p. 62).

[195] Siemens Healthineers. "Compressed Sensing Supplement". In: *MAGNETOM Flash* 2016.66 (Apr. 2016), pp. 1–60 (cit. on p. 37).

[196] Daniel R Thedens et al. "Fast magnetic resonance coronary angiography with a three-dimensional stack of spirals trajectory". In: *Magnetic resonance in medicine* 41.6 (1999), pp. 1170–1179 (cit. on p. 19).

[197] Jens M Theysohn et al. "7 tesla MRI of microbleeds and white matter lesions as seen in vascular dementia". In: *Journal of magnetic resonance imaging* 33.4 (2011), pp. 782–791 (cit. on p. 83).

[198] Bradley P Thomas et al. "High-resolution 7T MRI of the human hippocampus in vivo". In: *Journal of Magnetic Resonance Imaging* 28.5 (2008), pp. 1266–1272 (cit. on p. 34).

[199] C Triantafyllou et al. "Comparison of physiological noise at 1.5 T, 3 T and 7 T and optimization of fMRI acquisition parameters". In: *Neuroimage* 26.1 (2005), pp. 243–250 (cit. on p. 35).

[200] Chi-Ming Tsai and Dwight G Nishimura. "Reduced aliasing artifacts using variable-density *k*-space sampling trajectories". In: *Magnetic Resonance in Medicine* 43.3 (2000), pp. 452–458 (cit. on p. 67).

[201] Martin Uecker et al. "Image reconstruction by regularized nonlinear inversion-joint estimation of coil sensitivities and image content". In: *Magnetic Resonance in Medicine* 60.3 (2008), pp. 674–682 (cit. on p. 73).

[202] Muhammad Usman et al. “Motion corrected compressed sensing for free-breathing dynamic cardiac MRI”. In: *Magnetic resonance in medicine* 70.2 (2013), pp. 504–516 (cit. on p. 37).

[203] Giuseppe Valvano et al. “Variable density randomized stack of spirals (VDR-SoS) for compressive sensing MRI”. In: *Magnetic Resonance in Medicine* 76.1 (2016), pp. 59–69 (cit. on p. 19).

[204] S Johanna Vannesjo et al. “Retrospective correction of physiological field fluctuations in high-field brain MRI using concurrent field monitoring”. In: *Magnetic resonance in medicine* 73.5 (2015), pp. 1833–1843 (cit. on pp. 1, 24, 29, 36, 55, 68).

[205] Signe J Vannesjo et al. “Gradient system characterization by impulse response measurements with a dynamic field camera”. In: *Magnetic resonance in medicine* 69.2 (2013), pp. 583–593 (cit. on pp. 26–28, 67, 80).

[206] Orestis Vardoulis et al. “Single breath-hold 3D measurement of left atrial volume using compressed sensing cardiovascular magnetic resonance and a non-model-based reconstruction approach”. In: *Journal of Cardiovascular Magnetic Resonance* 17.1 (2015), p. 1 (cit. on p. 37).

[207] Shreyas S Vasanawala et al. “Improved pediatric MR imaging with compressed sensing”. In: *Radiology* 256.2 (2010), pp. 607–616 (cit. on pp. 57, 89, 123).

[208] S. V. Venkatakrishnan, C. A Bouman, and B. Wohlberg. “Plug-and-Play priors for model based reconstruction”. In: *Global Conference on Signal and Information Processing (GlobalSIP) IEEE*. 2013, pp. 945–948 (cit. on p. 109).

[209] Fredy Visser et al. “High-resolution magnetization-prepared 3D-FLAIR imaging at 7.0 Tesla”. In: *Magnetic resonance in medicine* 64.1 (2010), pp. 194–202 (cit. on p. 34).

[210] Haifeng Wang et al. “Smoothed random-like trajectory for compressed sensing MRI”. In: *Engineering in Medicine and Biology Society (EMBC), 2012 Annual International Conference of the IEEE*. IEEE. 2012, pp. 404–407 (cit. on pp. 56, 58).

[211] Y Wang et al. “Artery and vein separation using susceptibility-dependent phase in contrast-enhanced MRA”. In: *Journal of Magnetic Resonance Imaging* 12.5 (2000), pp. 661–670 (cit. on p. 33).

[212] Zhou Wang et al. “Image quality assessment: from error visibility to structural similarity”. In: *IEEE Transactions on Image Processing* 13.4 (2004), pp. 600–612 (cit. on p. 45).

[213] Zhou Wang, Alan C Bovik, and Ligang Lu. “Why is image quality assessment so difficult?” In: *Acoustics, Speech, and Signal Processing (ICASSP), 2002 IEEE International Conference on*. Vol. 4. IEEE. 2002, pp. IV–3313 (cit. on p. 121).

[214] M. Weiger et al. “A high-performance gradient insert for rapid and short-T2 imaging at full duty cycle”. In: *Magnetic Resonance in Medicine* (2017) (cit. on p. 114).

[215] Markus Weiger et al. “A high-performance gradient insert for rapid and short-T2 imaging at full duty cycle”. In: *Magnetic resonance in medicine* 79.6 (2018), pp. 3256–3266 (cit. on p. 80).

[216] P. Weiss, L. Blanc-Féraud, and G. Aubert. “Efficient Schemes for Total Variation Minimization Under Constraints in Image Processing”. In: *SIAM Journal on Scientific Computing* 31.3 (2009), pp. 2047–2080 (cit. on p. 109).

[217] Christian Windischberger et al. "Robust field map generation using a triple-echo acquisition". In: *Journal of magnetic resonance imaging* 20.4 (2004), pp. 730–734 (cit. on p. 28).

[218] Stefanie Winkelmann et al. "An optimal radial profile order based on the Golden Ratio for time-resolved MRI". In: *IEEE Transactions on Medical Imaging* 26.1 (2007), pp. 68–76 (cit. on p. 57).

[219] Sam TS Wong and Mark S Roos. "A strategy for sampling on a sphere applied to 3D selective RF pulse design". In: *Magnetic Resonance in Medicine* 32.6 (1994), pp. 778–784 (cit. on p. 19).

[220] B Wu et al. "Applying compressed sensing in parallel MRI". In: *Proceedings of the 16th Annual Meeting of ISMRM*. Vol. 1480. Toronto, Canada, 2008 (cit. on p. 72).

[221] Dmitriy A Yablonskiy, Alexander L Sukstanskii, and Joseph JH Ackerman. "Image artifacts in very low magnetic field MRI: the role of concomitant gradients". In: *Journal of Magnetic Resonance* 174.2 (2005), pp. 279–286 (cit. on p. 26).

[222] Ernest N Yeh et al. "Inherently self-calibrating non-Cartesian parallel imaging". In: *Magnetic Resonance in Medicine* 54.1 (2005), pp. 1–8 (cit. on p. 73).

[223] Eitan Yudilevich and Henry Stark. "Spiral sampling in magnetic resonance imaging - the effect of inhomogeneities". In: *IEEE Transactions on Medical Imaging* 6.4 (1987), pp. 337–345 (cit. on pp. 80, 121).

[224] Marco Zanforlin et al. "SSIM-based video admission control and resource allocation algorithms". In: *Modeling and Optimization in Mobile, Ad Hoc, and Wireless Networks (WiOpt), 2014 12th International Symposium on*. IEEE. 2014, pp. 656–661 (cit. on p. 45).

[225] Tao Zhang et al. "Clinical performance of contrast enhanced abdominal pediatric MRI with fast combined parallel imaging compressed sensing reconstruction". In: *Journal of Magnetic Resonance Imaging* 40.1 (2014), pp. 13–25 (cit. on p. 42).

[226] T Zhao et al. "An improved analytical solution for variable density spiral design". In: *Proceedings 16th Scientific Meeting, International Society for Magnetic Resonance in Medicine, Toronto*. 2008, p. 1342 (cit. on p. 17).

[227] Jaco JM Zwanenburg et al. "Fast high resolution whole brain T2* weighted imaging using echo planar imaging at 7 T". In: *Neuroimage* 56.4 (2011), pp. 1902–1907 (cit. on p. 35).

université PARIS-SACLAY
ÉCOLE DOCTORALE
Physique et ingénierie : électrons, photons, sciences du vivant (EOBE)

Titre : L'échantillonnage compressif en IRM: conception optimisée de trajectoires d'échantillonnage pour accélérer l'IRM

Mots clés : Imagerie par Résonance Magnétique, IRM, Compressed Sensing, Accéleration, SPARKLING

Résumé : L'imagerie par résonance magnétique (IRM) est l'une des modalités d'imagerie les plus puissantes et les plus sures pour examiner le corps humain. L'IRM de haute résolution devrait aider à la compréhension et le diagnostic de nombreuses pathologies impliquant des lésions submillimétriques ou des maladies telles que la maladie d'Alzheimer et la sclérose en plaque. Bien que les systèmes à haut champ magnétique soient capables de fournir un rapport signal-sur-bruit permettant d'augmenter la résolution spatiale, les longs temps d'acquisition et la sensibilité au mouvement continuent d'entraver l'utilisation de l'IRM de haute résolution. Malgré le développement de méthodes de correction du mouvement et du bruit physiologique, le long temps d'acquisition reste un obstacle majeur à l'IRM de haute résolution, en particulier dans les applications cliniques.
Au cours de la dernière décennie, la nouvelle théorie du compressed sensing (CS) a proposé une solution prometteuse pour réduire le temps d'examen en IRM. Après avoir expliqué la théorie du compressed sensing, ce projet de thèse propose une étude empirique et quantitative du facteur de sous-échantillonnage maximum réalisable grâce au CS pour l'imagerie pondérée en T_2^*.
En outre, l'application de CS en IRM repose généralement sur l'utilisation de courbes d'échantillonnage simples telles que les lignes droites, spirales ou des légères variations de ces formes élémentaires qui ne tirent pas pleinement parti des degrés de liberté offerts par le hardware et ne peuvent être facilement adaptées à une distribution d'échantillonnage arbitraire. Dans cette thèse, j'ai introduit une méthode appelée SPARKLING, qui permet de surmonter ces limitations en adoptant une approche radicalement nouvelle de la conception de l'échantillonnage de l'espace-k. L'acronyme SPARKLING signifie Spreading Projection Algorithm for Rapid K-space sampLING. C'est une méthode flexible inspirée des techniques de stippling qui génère automatiquement, grâce à un algorithme d'optimisation, des courbes d'échantillonnage non cartésiennes optimisées et compatibles avec les contraintes hardware de l'IRM en termes d'amplitude de gradient maximale et d'accélération maximale. Ces courbes d'échantillonnage sont conçues pour répondre à des critères clés pour un échantillonnage optimal : une distribution contrôlée des échantillons et une couverture de l'espace-k localement uniforme. Avant de s'engager dans des acquisitions, nous avons vérifié que notre système de gradient était bien capable d'exécuter ces trajectoires complexes. Nous avons implémenté une méthode de mesure de phase et avons observé une très bonne adéquation entre trajectoires prescrites et mesurées.
Enfin, en alliant une efficacité d'échantillonnage avec le compressed sensing et l'imagerie parallèle, les trajectoires SPARKLING ont permis de réduire jusqu'à 20 fois le temps d'acquisition d'un examen IRM T_2^* par rapport aux acquisitions cartésiennes de référence, sans détérioration de la qualité d'image. Ces résultats experimentaux ont été obtenus à 7 Tesla pour de l'imagerie cérébrale *in vivo*. Par rapport aux stratégies d'échantillonnage non-cartésiennes usuelles (spirale et radiale), la technique proposée a également permis d'obtenir une qualité d'image supérieure. Enfin, l'approche proposée a été étendue à l'imagerie 3D et appliquée à 3 Tesla pour laquelle des résultats préliminaires ex vivo à une résolution isotrope de 0.6 mm suggèrent la possibilité d'atteindre des facteurs d'accélération très élevés jusqu'à 60 pour la pondération T_2^* et l'imagerie pondérée en susceptibilité.

Title : Compressed Sensing in MRI: optimization-based design of k-space filling curves for accelerated MRI

Keywords : Magnetic Resonance Imaging, MRI, Compressed Sensing, k-space trajectories, Acceleration, SPARKLING

Abstract : Magnetic resonance imaging (MRI) is one of the most powerful and safest imaging modalities for examining the human body. High-resolution MRI is expected to aid in the understanding and diagnosis of many neurodegenerative pathologies involving submillimetric lesions or morphological alterations, such as Alzheimer's disease and multiple sclerosisAlthough high-magnetic-field systems can deliver a sufficient signal-to-noise ratio (SNR) to increase spatial resolution, long scan times and motion sensitivity continue hindering the utilization of high resolution MRI. Despite the development of corrections for bulk and physiological motion, lengthy acquisition times remain a major obstacle to high-resolution acquisition, especially in clinical applications.
In the last decade, the newly developed theory of compressed sensing (CS) offered a promising solution for reducing the MRI scan time. After having explained the theory of compressed sensing, this PhD project proposes an empirical and quantitative analysis of the maximum undersampling factor achievable with CS for T_2^*-weighted imaging.
Furthermore, the application of CS to MRI commonly relies on simple sampling patterns such as straight lines, spirals or slight variations of these elementary shapes, which do not take full advantage of the degrees of freedom offered by the hardware and cannot be easily adapted to fit an arbitrary sampling distribution. In this PhD thesis, I have introduced a method called SPARKLING, that may overcome these limitations by taking a radically new approach to the design of k-space sampling. The acronym SPARKLING stands for Spreading Projection Algorithm for Rapid K-space sampLING. It is a versatile method inspired from stippling techniques that automatically generates optimized non-Cartesian sampling patterns compatible with MR hardware constraints on maximum gradient amplitude and slew rate. These sampling curves are designed to comply with key criteria for optimal sampling: a controlled distribution of samples and a locally uniform k-space coverage. Before engaging into experiments, we verified that our gradient system was capable of executing the complex gradient waveforms. We implemented a local phase measurement method and we observed a very good adequacy between prescribed and measured k-space trajectories. Finally, combining sampling efficiency with compressed sensing and parallel imaging, the SPARKLING sampling patterns allowed up to 20-fold reductions in MR scan time, compared to fully-sampled Cartesian acquisitions, for T_2^*-weighted imaging without deterioration of image quality, as demonstrated by our experimental results at 7 Tesla on *in vivo* human brains. In comparison to existing non-Cartesian sampling strategies (spiral and radial), the proposed technique also yielded superior image quality. Finally, the proposed approach was also extended to 3D imaging and applied at 3 Tesla for which preliminary results on *ex vivo* phantoms at 0.8 mm isotropic resolution suggest the possibility to reach very high acceleration factors up to 60 for T_2^*-weighting and susceptibility-weighted imaging.

Université Paris-Saclay
Espace Technologique / Immeuble Discovery
Route de l'Orme aux Merisiers RD 128 / 91190 Saint-Aubin, France